Dynamic optimization in multi-states systems for automobile energy efficiency

Djamaleddine Maamria

ParisTech
INSTITUT DES SCIENCES ET TECHNOLOGIES
PARIS INSTITUTE OF TECHNOLOGY

MINES ParisTech

Ecole doctorale n° 432 : Sciences des Métiers de l'ingénieur

Doctorat ParisTech

T H È S E

pour obtenir le grade de docteur délivré par

l'École nationale supérieure des Mines de Paris

Spécialité « Mathématique et Automatique »

présentée et soutenue publiquement par

Djamaleddine MAAMRIA

le 06 novembre 2015

Méthodes d'optimisation dynamique de systèmes à plusieurs états pour l'efficacité énergétique automobile

Dynamic optimization in multi-states systems for automobile energy efficiency

Directeur de thèse : **Nicolas PETIT**
Maitre de thèse : **François CHAPLAIS**
Co-encadrement de la thèse : **Antonio SCIARRETTA**

Jury

M. J. Frédéric BONNANS,	Directeur de Recherche, Inria, Ecole Polytechnique	Rapporteur
M. Yann CHAMAILLARD,	Professeur, PRISME ,Université d'Orléans	Rapporteur
M. T-Marie GUERRA,	Professeur, LAMIH, Université de Valenciennes	Examinateur
M. Theo HOFMAN,	Maître assistant, Eindhoven University of Technology	Examinateur
M. Nicolas PETIT,	Professeur, CAS, MINES ParisTech	Examinateur
M. François CHAPLAIS,	Ingénieur de recherche, CAS, MINES ParisTech	Examinateur
M. Antonio SCIARRETTA,	Expert, IFPEn	Examinateur

MINES ParisTech
Centre Automatique et Systèmes, Unité Mathématiques et Systèmes
60 boulevard Saint-Michel, 75006 Paris

THÈSE

Résumé :

La gestion énergétique (EMS) pour véhicules hybrides a pour objectif de déterminer la répartition de puissance entre les différentes sources d'énergie de manière à minimiser la consommation de carburant et/ou les émissions polluantes. L'objectif de cette thèse est de développer un EMS en prenant en compte des températures internes (la température du moteur et/ou la température du système de post-traitement). Dans une première partie et en utilisant une connaissance préalable du cycle de conduite, le calcul d'un EMS est formulé comme un problème de commande optimale. Ensuite, le principe du minimum de Pontryagin (PMP) est utilisé pour résoudre ce problème d'optimisation. En se basant sur les résultats numériques obtenus, un compromis entre les performances de la stratégie de commande et de la complexité du modèle utilisé pour la calculer est établi. Les différents problèmes étudiés dans cette thèse sont des exemples des simplifications successives de modèle qui peuvent être regroupées dans le concept des perturbations régulières en contrôle optimal sous contrainte de commande discuté ici. Dans une deuxième partie, la formulation de l'ECMS a été généralisée pour inclure les dynamiques thermiques. Ces extensions définissent des stratégies sous-optimales que nous avons testées numériquement et expérimentalement.

Mots-clés : Superviseur énergétique, véhicule électrique hybride, commande optimale, PMP, perturbation régulière, généralisation de l'ECMS.

Abstract:

Energy management system (EMS) for hybrid vehicles consists on determining the power split between the different energy sources in order to minimize the overall fuel consumption and/or pollutant emissions of the vehicle. The objective of this thesis is to develop an EMS taking into account the internal temperatures (engine temperature and/or catalyst temperature). In a first part and using a prior knowledge of vehicle driving cycle, the EMS design is formulated as an optimal control problem. Then, the PMP is used to solve this optimization problem. Based on the obtained numerical results, some trade-off between performance of the control strategy and complexity of the model used to calculate this strategy is established. The various problems studied in this thesis are examples of successive model simplifications which can be recast in the concept of regular perturbations in optimal control under input constraints discussed here. In a second part, the feedback law of ECMS is generalized to include thermal dynamics. This defines sub-optimal feedback strategies which we have tested numerically and experimentally.

Keywords: Energy management, hybrid electric vehicle, optimal control, Pontryagin minimum principle, regular perturbation, ECMS extensions.

Remerciements

Je voudrais tout d'abord remercier très sincèrement mon maître de thèse M. François Chaplais et mon promoteur M. Antonio Sciarretta de m'avoir fait confiance pour cette thèse et de m'avoir toujours poussé à être plus précis et rigoureux. J'ai beaucoup appris pendant cette thèse et surtout à votre contact.

Je remercie ensuite mon directeur de thèse M. Nicolas Petit pour ses conseils scientifiques, son soutien, sa disponibilité et sa grande réactivité. Sa vision sur mon travail, toujours pertinente, et ses conseils efficients, ont été déterminants dans l'avancement de mes travaux. Au-delà de ses conseils scientifiques, j'ai été extrêmement sensible à ses qualités humaines d'écoute et de compréhension tout au long de ma thèse.

Je souhaite remercier Frédéric Bonnans ainsi que Yann Chamaillard qui ont accepté d'être les rapporteurs de cette thèse. Je remercie également Thierry Marie Guerra et Theo Hofman qui m'ont fait l'honneur de participer au jury de ma soutenance. Vos questions et commentaires m'ont aidé à améliorer ce manuscrit.

Je remercie également le département Contrôle, Signal et Système à IFP Energies nouvelles pour m'avoir accueillie pendant ces trois ans. J'adresse également mes sincères remerciements à Laurent Thibault et Frédéric Lippens pour leurs aides, conseils et le temps qui ont consacré afin de bien mener les essais au banc. Merci aux collègues que j'ai côtoyés quotidiennement et qui ont contribué à rendre ce travail convivial: Prakach, Nicolas, Carole, Fabrice, Alexandre, Giovani, Ayoub, Caroline, Luiz, Jianning et Florine.

Un merci également à l'ensemble du Centre Automatique et Systèmes (CAS) de MINES ParisTech, permanents et doctorants. Travailler au CAS fut un privilège. Ce lieu offre aux jeunes chercheurs un environnement de travail fantastique.

Je remercie également mes amis Sofiane, Djawad, Khaled, Seif, Zaki, Zohir, Farid et Mounir sur lesquels je peux toujours compter.

Je remercie ma famille : mes parents, mes grands-parents, mes soeurs (Leila, Meriem et Imene), mes oncles (Omar et Lazhari) et particulièrement mon grand frère Issam pour m'avoir toujours encouragé et conseillé pour arriver là où je suis aujourd'hui.

Contents

Acronyms

AFR	Air Fuel Ratio
ATS	After-Treatment System
DOC	Diesel Oxidation Catalyst
DP	Dynamic Programming
DPF	Diesel Particulate Filter
ECMS	Equivalent Consumption Minimization Strategy
EM	Electric Machine
EMS	Energy Management System
FHDS	Federal Highway Driving Cycle
FTP	Federal Test Procedure
FUDS	Federal Urban Driving Cycle
HEV	Hybrid Electric Vehicle
HiL	Hardware-in-the-Loop
HV	Hybrid Vehicle
ICE	Internal Combustion Engine
IPM	Interior Penalty Method
LTI	Linear Time Invariant
NEDC	New European Driving Cycle
OCP	Optimal Control Problem
PMP	Pontryagin Minimum Principle
SCR	Urea Selective Catalytic Reduction
SOC	State Of Charge
TPBVP	Two Point Boundary Value Problem
WLTC	Worldwide harmonized Light vehicles Test Cycle

Nomenclature

Variable	Signification	Unit
v	Vehicle speed	[m/s]
α	Vehicle acceleration	[m/s^2]
F_a	Aerodynamics drag force	[N]
F_r	Rolling friction force	[N]
F_g	Uphill driving force	[N]
F_t	Traction force	[N]
m	Vehicle mass	[kg]
m_{rot}	Equivalent mass of the rotation parts	[kg]
g	Gravitational acceleration	[m/s^2]
T_t	Torque requested at the wheel	[Nm]
T_{eng}	Engine torque	[Nm]
T_{el}	Electric machine torque	[Nm]
ω_{wh}	Rotational speed at the wheel	[rpm]
ω_{eng}	Engine speed	[rpm]
ω_{el}	Electric machine speed	[rpm]
R_{gb}	Gear-box ratio	[−]
R_{el}	Motor-to-wheel transmission ratio	[−]
η_{gb}	Gear-box efficiency	[−]
ξ	State of charge of the battery	[%]
U_{ocv}	Open equivalent circuit voltage of the battery	[V]
R_b	Equivalent internal resistance	[Ω]
I_b	Battery current	[A]
Q_0	Battery nominal capacity	[C]
η_c	Battery charging efficiency	[−]
θ_e	Engine temperature	[°C]
θ_c	Catalyst temperature	[°C]
H_{lhv}	Lower heating value of the fuel	$[J/kg]$
P_m	Electric power requested by the electric machine	[W]
P_f	Fuel power consumed by the engine	[W]
P_b	Battery power	[W]
P_e	Engine power	[W]
P_d	Traction power at the wheels	[W]

Chapter 1

Introduction

Contents

1.1 The focus on energy efficiency for automotive vehicles

The announced depletion of fossil fuel sources, climate change due to pollution and an increase in overall energy demands are major challenges for the automotive industry. More generally, energy efficiency is increasingly becoming a major concern, and a subject of attention from major international organizations around the world. In 2006, the European Parliament stated that energy efficiency is a relevant reaction in the face of environmental concerns and rising energy prices [52, 61]. Later, in 2012, the EU established a set of binding measures, called the "2012 Energy Efficiency Directive", to help it reach its 20% energy efficiency target by 2020. Under this directive, all EU countries are required to use energy efficiently at all stages of the energy chain, from production to final consumption. Similar concerns are also present in USA (President Obama speech 2015 announcing the Clean Power Plan, "A historic step in the fight against climate change" [67]). However, energy-saving technologies are still vastly underdeveloped.

In the automotive industry, the European Commission established a strategy for clean and efficient vehicles with a threefold aim. First, it sets out medium- to long-term objectives to promote a new industrial approach, based on clean and efficient vehicles to boost the competitiveness of the European automotive industry. Second, the strategy promotes alternative propulsion technologies in a global perspective of worldwide mobility systems. Third, the strategy encourages the creation of a green economy and supports the decarbonization of the transportation system.

Besides the development of alternative fuel sources, the main research directions towards improving energy efficiency in the automotive field are focussed on fuel efficiency, with a particular emphasis on decreasing carbon dioxide (CO_2) emissions. To improve efficiency, it is important to understand that there are three stages involved in the conversion of fossil fuels to a useful work at the wheels. Each stage induces losses in the overall efficiency.

1. Well-to-tank (W2T): The energy contained in one of the available primary energy carriers (fossil hydrocarbons, nuclear energy, coal, etc.) is transmitted to an energy carrier that is suitable for on-board storage–that is, to the fuel (examples are gasoline, hydrogen).

2. Tank-to-vehicle (T2V): The fuel obtained from the first stage is then converted by the propulsion system into a mechanical energy which, in part, may be stored as a kinetic or a potential energy.

3. Vehicle-to-meters (V2M): This step involves the conversion of the mechanical energy produced in the previous step into a work used to power the vehicle. Energy losses during this phase are related to certain vehicle parameters: rolling resistance, aerodynamics drag and friction of the non-rotating components. These losses depend also on the driving profile.

More details about the definition of these stages are given in [33]. Hybridization [4, 26, 33] is a solution suggested to optimize the energy conversion during stage 2 (T2V)[1]. Next, we will describe this technology, which is the main scope of this thesis.

1.2 Hybridization and hybrid electric vehicles (HEV)

Generally, hybrid vehicles are characterized by two or more prime movers and power sources. Several techniques for storing energy are considered: rotational energy in a flywheel, pressure in a hydraulic system, and electricity in a battery or a super-capacitor. The term "hybrid vehicle" usually refers to a vehicle that combines an engine and an electric machine. A more appropriate term for such a combination is "hybrid electric vehicle" (HEV). One of the main motivations for developing HEVs is the possibility of combining the advantages of electric vehicles – in particular, zero local emissions – with the advantages of the internal combustion engine (ICE)-based vehicles, namely, high energy and power density.

A HEV achieves improved efficiency by employing several techniques, among them: stop-start [86, 91] and regenerative breaking. In common (non hybrid) cars, the vehicle kinetic energy is thermally dissipated via the brake discs. In hybrid and electric vehicles, a portion of the dissipated energy can be recovered using a kinetic energy recovering system (KERS), and it is stored in a battery. Furthermore, the advantage of an electric machine over an internal combustion engine is its efficiency at low speeds, where the former can provide maximum torque at low speeds. In principle, HEVs can benefit from the best of both technologies: electric drives and internal combustion.

According to their architecture, HEVs are classified into three main categories: series, parallel and combined.

[1]Driver support system, or eco-driving, is among the solutions proposed to improve energy conversion during the V2M stage. See the Appendix H for more details.

- In the series configuration, traction is obtained via a powerful electric machine. The internal combustion engine drives an electric generator to recharge the battery or to power the electric machine. Series HEV may be considered as purely electric vehicles with an additional ICE based energy path. Cadillac ELR and BMW I3 are examples of production series hybrids.

- *Parallel HEVs* are considered to be ICE-based vehicles that possess an additional electrical path. In this configuration, both the engine and the electric machine provide the needed traction power either separately or together. This provides an additional *degree of freedom* towards fulfilling the power requirements of the vehicle, and allows some optimization to be performed. This is the architecture studied in this thesis. Examples of parallel hybrids in the market are the 3008 Hybrid 4 (PSA) and BMW I8.

- An intermediate configuration between series and parallel hybrids is the combined hybrid configuration. This is mostly a parallel hybrid, but it contains some features of a series configuration. Toyota Prius is an example of a series-parallel HEV.

More details about this classification are given in [4, 33]. To maximize the benefits of hybridization, two approaches can be used:

- At the design level by optimizing the structure and the components of the propulsion system and their assembly (assuming that the fuel type and the vehicle parameters are fixed) [51, 73, 84].

- At the control level by optimizing the control algorithms of the various sub-systems and their coordination (assuming that the propulsion system configuration and the vehicle parameters are fixed). The aim of this approach is to maximize the performance of the system [19, 66, 73]. This is the topic covered in this thesis.

1.3 Energy management systems (EMS) of parallel HEV

In conventional propulsion systems, the driver requests (e.g. action on the accelerator or the brake which is converted into a torque request) are handled by an on-board computer. When the driver acts on the accelerator pedal, the torque request to be provided by the engine is regulated by the engine control unit (ECU). When the brake pedal is depressed, either the brake circuit is mechanically activated (coupled braking), or an intermediate controller converts the pedal position into a braking torque request that is split between the front and the rear braking circuits. Purely electric vehicles have similar behaviors with the electric machine acting as the sole prime mover [4, 33].

For parallel HEV, the interpretation step of the driver request is conceptually the same as for conventional vehicles. However, the additional degree of freedom yield by hybridization can be exploited. The presence of an additional energy source gives some flexibility as to how the traction power requested by the driver may be satisfied: using only the engine, using only the electric machine or using a combination thereof. For this task, a supervisory controller is needed, which must determine how the powertrain components should operate and how the energy split between different sources should be organized. This controller is referred to as an "energy management system" (EMS) [33]. Its role in the on-board control system is presented in Figure 1.1.

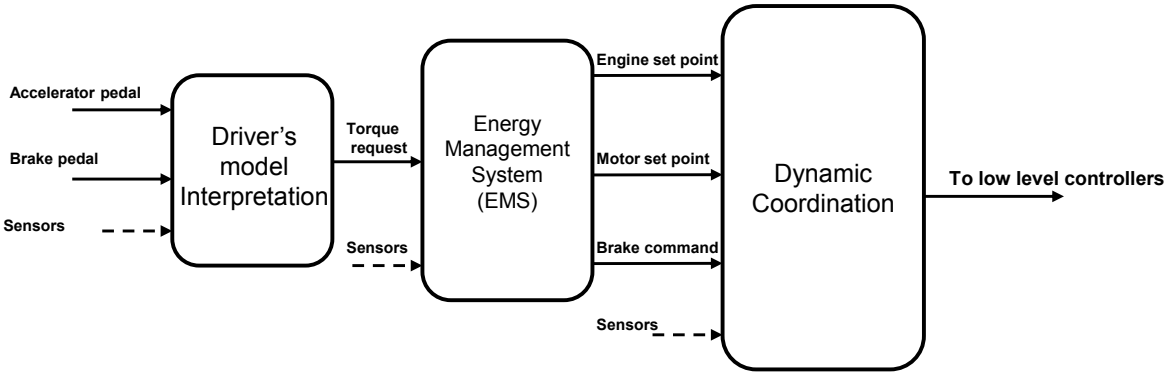

Figure 1.1: Flowchart of an HEV supervisory controller. The EMS determines the distribution of a torque request.

The strategies implemented in an EMS may be classified into two categories. Type I, usually called heuristic or rule-based, represents the method used in most prototypes and mass-production hybrids. Strategies derived from optimal control (Type II) are seen as an innovative approach. They are currently the subject of much research efforts and, are gradually being introduced into the automotive industry. A brief description of these two approaches are given in the next sections.

1.3.1 Heuristics (rule-based) EMS

This kind of controller implements intuitive rules and correlations inspired by *a priori* knowledge of the behavior and the efficiency of the propulsion system [18, 20, 29, 56]. For example, one of the main rules suggests to use the engine only when its efficiency is relatively high (generally for high loads), while in less favorable conditions the electric mode should be preferred and the engine should be turned off.

The main advantage of these algorithms is that the rules are intuitive, so they are well-accepted by engineers and end-users, and give relatively satisfactory results if they are carefully tuned. They do not require any knowledge of future driving conditions, which simplifies their implementation for real-time applications. Unfortunately, they are only appropriate for simple systems, and their performance in real driving conditions (which are usually different from those used to tune the rules) is not guaranteed. Moreover, rule-based strategies are sub-optimal by definition. All these reasons have motivated the development of (model-based) optimal controllers.

1.3.2 Optimal (model-based) EMS

The (relative) weaknesses of the heuristic EMS discussed above have spurred the development of model-based optimal controllers. These strategies are based on the definition of a cost function to be minimized or maximized for a dynamic system that represents the vehicle dynamics. Various objectives can be considered: fuel consumption, pollutant emissions, battery aging, drivability concerns or any combination of these [2, 17, 44, 56, 71, 72, 74, 77, 81, 92]. For energy management problems, a HEV can be described by

quasistatic models. The state vector usually includes only the state of charge (SOC) of the battery [33].

Whether future driving conditions are, or are not known, defines two sub-categories. In the first category, the vehicle is assumed to follow a prescribed driving cycle defined by the vehicle speed profile that is to be tracked, over a finite time horizon. The calculated optimal strategy anticipates what will happen from the current time to the end of the driving cycle. Knowing future conditions is possible when the vehicle is operated along regulatory driving cycles, or for public transportation vehicles that have prescribed driving profiles and right-of-ways. In all other cases, driving profiles may be vastly uncertain.

In the second category, where future driving conditions are unknown, the control strategy is calculated from available information in real-time, in the form of a feedback. As it is impossible to find an optimal strategy under such conditions, the obtained strategy is sub-optimal. Predictive control [13, 36] and the equivalent consumption minimization strategy (ECMS) [16, 37] are among the methods used to deal with unmodeled uncertainties.

1.4 Considered problems and proposed solutions

In this thesis, we wish to develop an EMS for a parallel HEV by taking into account the impact of internal temperatures (engine temperature and/or catalyst temperature) on fuel consumption and pollutant emissions in addition to the SOC dynamics. Indeed, these additional variables have a strong impact, as can be observed in Figure 1.2 and Figure 1.3. Accounting for these variables yields a three-states dynamical system (with a single input), and two outputs of interest (fuel consumption and pollutants). To be implementable in real conditions, this EMS has to take the form of a feedback, as future driving conditions will not be known. Currently [16], the ECMS is able to deal only with a single state variable (the battery SOC).

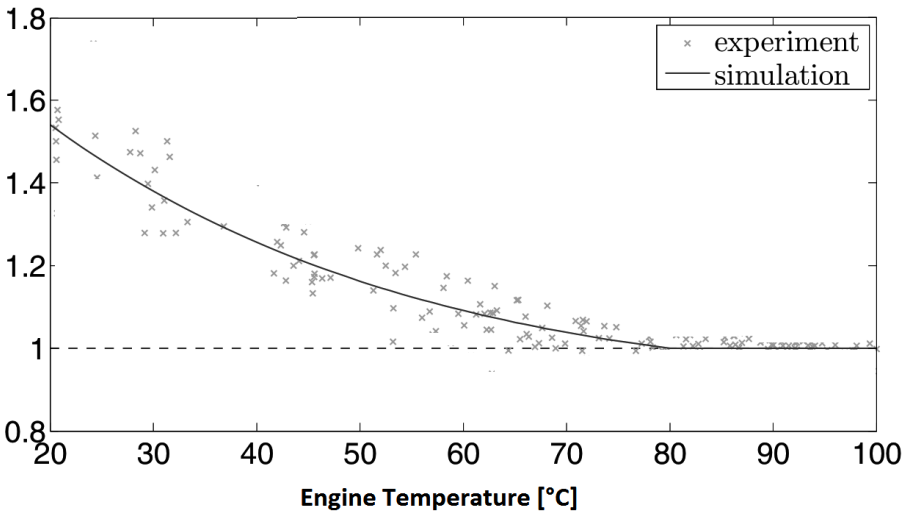

Figure 1.2: Typical excess fuel consumption of the engine as a function of engine temperature [87].

Because of an increase in the state-space dimension (by including the new thermal dynamics), it seems very costly to try to develop a rule-based EMS. Indeed, the complexity of establishing rules that could cover all possible cases would be very high. What we wish

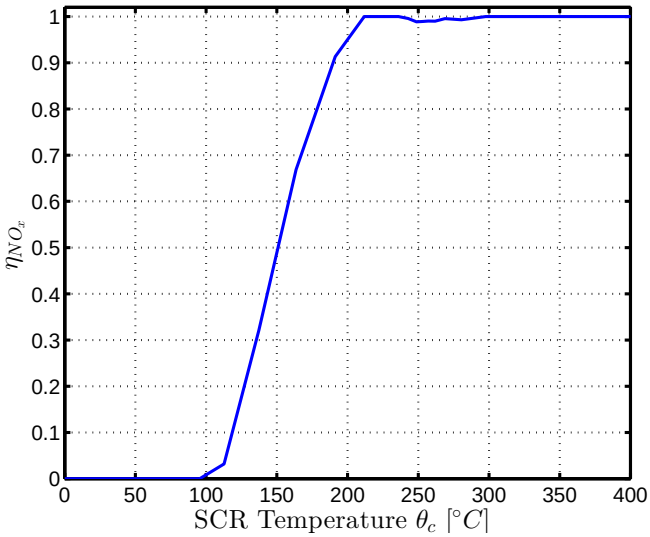

Figure 1.3: Typical catalyst conversion efficiency as a function of catalyst temperature

to develop is a generalization of the ECMS strategy which combines the results of optimal control (the control variable minimizes at all times the Hamiltonian of the system) and a feedback loop (the adjoint variable is calculated as the output of a feedback controller on the state variables). Thus, a significant extension is needed to address the problem under consideration. Furthermore, because it is a sub-optimal strategy by construction, it is not known whether ECMS can achieve a sufficient level of performance with respect to pollutant emissions while keeping fuel consumption within acceptable limits. We visually display this situation in Figure 1.4.

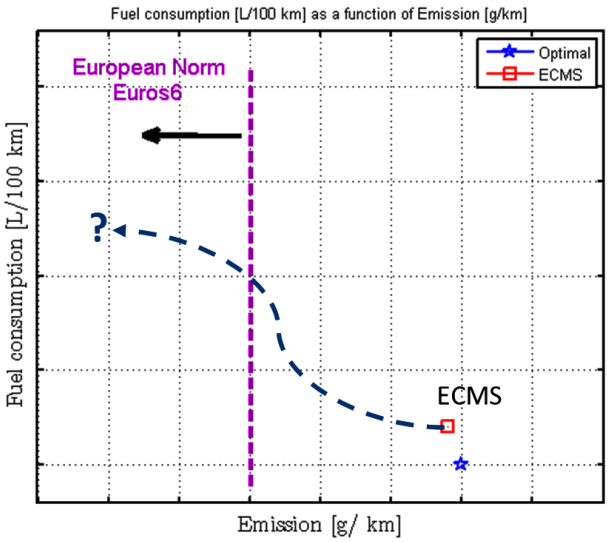

Figure 1.4: Fuel consumption [L/100 km] as a function of emissions [g/km]. The blue point corresponds to the optimal strategy that minimizes the fuel consumption via the PMP. The application of existing single-state ECMS has to be done in order to establish attainable performance.

At first sight, it is not clear which state(s) should be considered in the analysis. As

each state increases the complexity of the control design task, we wish to establish some trade-off between performance and complexity.

To solve this problem, we proceed in two steps. In the first step, we solve a collection of optimal control problems for the various dynamics under consideration (one, two or three states). To make a fair comparison between the obtained solutions, the resulting control strategies are applied to the full model with three state variables. We consider a weighted sum of the overall fuel consumption and emissions over a known time horizon that corresponds to a known driving cycle. In these cases, all information are known. The results quantify the maximum benefit of considering additional states. Typical results are illustrated in Figure 1.5.

Part I of this thesis focuses on offline solutions of energy management problems for a gasoline engine fitted with an after-treatment system. The driving cycle is assumed to be known in advance. In Chapter 3, the single-state energy management problem, which is usually considered in the literature, is presented. It focuses solely on minimizing the fuel consumption. We solve it using the Pontryagin minimum principle (PMP). This problem is extended to include state constraints on the SOC.

In Chapter 4, we present possible extension of this simple problem to account for pollutant emissions. This extension includes thermal dynamics of the engine and the after-treatment system. We use this work to produce a figure similar to Figure 1.5.

In Chapter 5 of Part II, we explore the general concept of regular perturbations in optimal control problems under input constraints. The various problems studied in Part I are examples of successive model simplifications which can be recast in this concept.

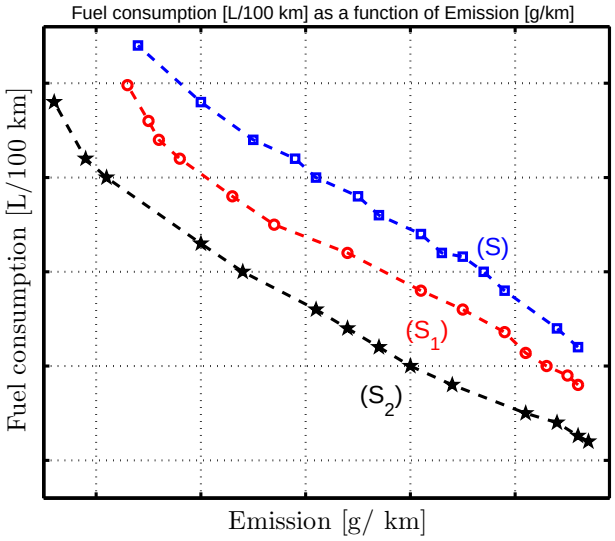

Figure 1.5: Simulation of control strategies solution of several OCP (with one, two and three states) for various cost functions. The strategies (S), (S_1) and (S_2) are the solutions of one, two and three states OCP, respectively.

In the second step detailed in Part III, we will generalize the feedback law of ECMS by using correlations between the state and their corresponding adjoint states, which can be observed along extremal calculated in the first step. This defines a sub-optimal feedback strategy which we test numerically and experimentally. Typical results are illustrated in Figure 1.6.

In Chapter 6, a brief study of the stability properties and the robustness of ECMS is proposed. Then, extensions of this strategy are proposed to include thermal dynamics in the optimization problem. Simulation results stress that the obtained performance is sufficient to satisfy the environmental norms while keeping fuel consumption sub-optimality with reasonable bounds.

Finally, in Chapter 7, we apply our methodology to an experimental test bench consisting of a diesel engine fitted with a diesel oxidation catalyst (DOC), a diesel particulate filter (DPF) and an urea selective catalytic reduction (SCR) system. These experimental tests validate the assertion that a simple control strategy is actually sufficient to reduce NO_x emissions.

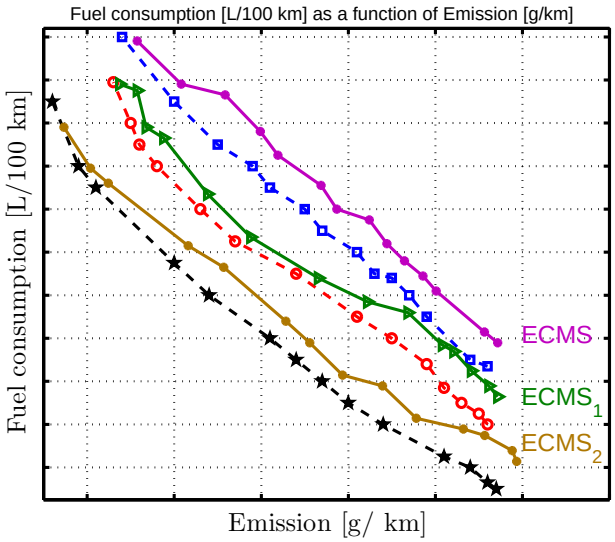

Figure 1.6: Generalized ECMS strategies with one, two or three states. The real-time strategies ($ECMS_1$) and ($ECMS_2$) are the extensions of ECMS for two and three states OCP, respectively.

1.5 Thesis contributions

The two-steps approach, described above, suggests interesting investigation that constitute, with the application results, the contribution of the thesis. These contributions are twofold:

1. **Perturbations in optimal control under input constraints:** in this thesis, the results of Bensoussan [7], which consider regular perturbations in optimal control, is extended to include input constraints. We show that perturbation terms of magnitude ε appearing in the dynamics and the cost function lead to an improvement of $K\varepsilon^2$ in the optimal cost. This is an improvement over the earlier result which only proved (in the constraint-free case) the existence of K; here the constant K is (conservatively) estimated from the solution of the optimal control problem for $\varepsilon = 0$. This result, which is handy for practical applications, is proven by means of the interior penalty method (IPM) proposed in [47]. A possible extension to include state constraints, which are more difficult to handle in the presence of modeling errors, is discussed and illustrated via a numerical example. This results allow us

to assess the quantitative impact of model reduction for OCP. It brings an answer to the informal question "Is it worth considering extra complexity in my model in order to optimize the obtained performance?". This result is used in the first step of our controller design.

2. **Generalized ECMS:** Three extensions of the ECMS are proposed to include thermal dynamics in the optimization problem. These extensions are based on the parametrization of the relations between the adjoint state variables and their corresponding states (which are assumed to be measured, or at least estimated) independently of the driving cycles. The proposed real-time strategies are capable of handling some degrees of uncertainty in the future driving scenarios. They are designed to handle more than one state, which is necessary for further applications.

The works presented in this thesis have been the subject of the following publications:

1. D. Maamria, F. Chaplais, N. Petit and A. Sciarretta, "Comparison of several strategies for HEV energy management system including engine and catalyst temperatures", in Proc. of the American Control Conference 2015.

2. D. Maamria, F. Chaplais, N. Petit and A. Sciarretta, "On the impact of model simplification in input constrained optimal control: application to HEV energy-thermal management", in Proc. of the 53rd IEEE Conference on Decision and Control, 2014.

3. D. Maamria, F. Chaplais, N. Petit and A. Sciarretta, "Numerical optimal control as a method to evaluate the benefit of thermal management in hybrid electric vehicles", in Proc. of the 2014 IFAC World Congress.

Chapter 2

Introduction (version française)

Contents

2.1 Efficacité énergétique dans l'automobile

L'épuisement annoncé des sources fossiles, le changement climatique dû à la pollution et à l'augmentation de la demande globale d'énergie sont parmi les défis majeurs pour l'industrie automobile. De manière golbale , l'efficacité énergétique est devenue de plus en plus une préoccupation majeure pour les grandes organisations internationales. En 2006, le parlement européen a déclaré que l'efficacité énergétique est une réaction pertinente face aux préoccupations environnementales et la hausse des prix de l'énergie [52, 61]. Plus tard, en 2012, l'UE a établi un ensemble de mesures intitulé "2012 Energy Efficiency Directive", afin de l'aider à atteindre l'objectif de 20% d'efficacité énergétique en 2020. Tous les pays de l'UE ont été invités à optimiser l'utilisation de leurs ressources énergétiques, de la production à la consommation. Des préoccupations similaires sont présentes également aux Etats-Unis (discours d'Obama en 2015 annonçant le plan Power Clean, «*une étape historique dans la lutte contre le changement climatique*» [67]).

Dans l'industrie automobile, la commission européenne a établi une stratégie pour des véhicules propres et efficaces avec trois objectifs. Premièrement, elle a fixé des lignes directrices à moyen et à long termes pour promouvoir une nouvelle approche industrielle, fondée sur des véhicules propres pour stimuler la compétitivité de l'industrie automobile européenne. Deuxièmement, la stratégie promeut des technologies de propulsion alternatives dans une perspective globale. Troisièmement, la stratégie encourage la création d'une économie verte et apporte son soutien à la dé-carbonisation des moyens de transport.

Les orientations principales de la recherche, visant à améliorer l'efficacité énergétique dans le monde de l'automobile, sont axées sur la minimisation de la consommation de carburant, avec un accent particulier sur la réduction des émissions de dioxyde de carbone (CO_2). Pour cela, il est important de comprendre qu'il existe trois étapes essentielles dans la conversion des énergies fossiles à un travail utile au niveau des roues. Chaque étape induit des pertes dans le bilan global.

1. Puits-au-réservoir (W2T) : L'énergie contenue dans l'une des sources primaires (hydrocarbures, énergie nucléaire, charbon, etc.) est transformée à une autre forme d'énergie qui est appropriée pour le stockage à bord. Nous citons comme exemple le carburant (essence et hydrogène).

2. Réservoir-au-véhicule (T2V) : Le carburant issu de la première étape est ensuite converti par un système de propulsion en une énergie mécanique qui, en partie, peut être stockée sous une forme cinétique ou potentielle.

3. Véhicule-au-mètres (V2M) : Cette étape implique la conversion de l'énergie mécanique produite à l'étape précédente en un travail pour propulser le véhicule. Les pertes d'énergie durant cette phase sont liées essentiellement aux caractéristiques du véhicule : résistance aux pneus; résistance aérodynamique et les frottements des parties non-tournantes. Ces pertes dépendent également de la vitesse du véhicule.

Plus de détails sur ces étapes sont donnés dans [33]. L'hybridation [4, 26, 33] représente une des solutions proposées pour optimiser la conversion d'énergie à l'étape 2 (T2V)[1]. Par la suite, nous décrivons cette technologie, qui constitue l'application principale de cette thèse.

2.2 Hybridation et véhicule électrique hybride

Les véhicules hybrides sont caractérisés par la présence de deux voir plusieurs sources d'énergie à bord du véhicule. L'énergie peut être stockée sous une forme mécanique (rotative) dans un volant d'inertie, sous une forme de pression dans un système hydraulique, et sous une forme électrique dans une batterie ou un super-condensateur. Le terme «véhicule hybride» est généralement associé à la configuration d'un véhicule qui combine un moteur thermique et une machine électrique. Le terme le plus approprié pour une telle combinaison est «véhicule électrique hybride» (HEV). L'une des motivations principales pour le développement des HEVs est la possibilité de combiner les avantages des véhicules purement électriques en particulier, zéro émission, avec ceux des moteurs thermiques, à savoir, une densité de puissance et d'énergie élevée.

Les performances énergétiques d'un HEV ont été améliorées par rapport à un véhicule conventionnel en utilisant plusieurs techniques, telles que : le système stop-start [86, 91] et le freinage récupératif. Pour les voitures conventionnelles, l'énergie cinétique du véhicule, lors d'une phase de freinage, est thermiquement dissipée dans les disques de frein. Dans les véhicules hybrides et électriques, une partie de cette énergie peut être récupérée à l'aide d'un système de récupération d'énergie cinétique (KERS), et elle sera stockée dans une batterie.

[1] l'éco-conduite, est parmi les solutions proposées pour améliorer la conversion d'énergie au cours de l'étape V2M. Voir l'Annexe H pour plus de détails.

D'un point de vue architectural, les HEVs sont généralement classés en trois catégories : série, parallèle et combiné.

- Dans la configuration série, la traction du véhicule est assurée par une machine électrique puissante. Le moteur thermique entraîne une génératrice pour recharger la batterie ou pour alimenter la machine électrique. Cette configuration peut être considérée comme un véhicule purement électrique avec un apport d'énergie supplémentaire par le moteur thermique. Cadillac ELR et BMW I3 sont des exemples de véhicules hybrides série disponibles sur le marché.

- *Les hybrides parallèles* sont considérés comme des véhicules conventionnels (avec un moteur thermique) qui possèdent une source électrique supplémentaire. Dans cette configuration, le moteur thermique et la machine électrique peuvent fournir la puissance de traction nécessaire soit séparément, soit ensemble. Ce qui donne un *degré de liberté supplémentaire* pour satisfaire la demande de puissance de la part du conducteur. Cette architecture est étudiée dans cette thèse. La 3008 Hybrid 4 (PSA) et BMW i8 sont des exemples d'hybrides parallèles commercialisées.

- Une configuration intermédiaire entre l'hybride série et l'hybride parallèle est la configuration combinée. Cette configuration est principalement de type parallèle, mais elle possède des caractéristiques d'un hybride série. Toyota Prius est parmi les exemples de cette configuration.

Plus de détails sur cette classification sont donnés dans [4, 33]. Pour profiter des avantages de l'hybridation, on distingue deux approches :

- Au niveau de la conception : optimisation de la structure et les composants du système de propulsion en supposant que le type de carburant et les paramètres du véhicule sont fixés [51, 73, 84].

- Au niveau du contrôle : optimisation des algorithmes de commande des différents sous-systèmes. Dans ce cas, la configuration du système et les paramètres du véhicule sont fixés. L'objectif de cette approche, qui est le sujet principal traité dans cette thèse, est de maximiser les performances du système [19, 66, 73].

2.3 Gestion énergétique pour un véhicule hybride de type parallèle

Dans un système de propulsion conventionnel (thermique), la demande du conducteur est traitée par un ordinateur à bord, connu sous le nom ECU : Engine Control Unit (par exemple une action sur l'accélérateur ou le frein est convertie en une demande de couple). Lorsque le conducteur agit sur la pédale d'accélération, la demande de couple à fournir par le moteur thermique est régulée par l'ECU. Lorsque la pédale de frein est enfoncée, soit le circuit de freinage est mécaniquement activé (freinage couplé), soit un dispositif intermédiaire convertit la position du pédale en une demande de couple de freinage qui est divisée entre les circuits de freinage avant et arrière. Les véhicules purement électriques ont un comportement similaire avec la machine électrique comme actionneur principal [4, 33].

Pour un HEV de type parallèle, l'étape d'interprétation de la demande du conducteur est typiquement la même. Cependant, le degré de liberté supplémentaire résultant de l'hybridation peut être exploité. En effet, la présence d'une source d'énergie supplémentaire laisse une liberté à la manière dont la puissance de traction demandée par le conducteur peut être satisfaite : en utilisant uniquement le moteur thermique ou la machine électrique, ou par une combinaison des deux. Pour réaliser cette tâche, un contrôleur haut-niveau est nécessaire et il doit déterminer comment les différents composants du groupe motopropulseur doivent fonctionner. Ce contrôleur est souvent appelé "système de supervision énergétique" (EMS) [33]. Son rôle est schématisé dans Figure 1.1.

Les stratégies de contrôle implémentées dans un EMS peuvent être classées en deux catégories. Les stratégies de Type I, généralement appelé stratégies heuristiques, sont utilisées dans la plupart des prototypes hybrides disponibles sur le marché. Les stratégies dérivées du contrôle optimal (de Type II) sont considérées comme une solution innovante. Actuellement, elles attirent beaucoup d'attention de la part de la communauté scientifique et elles sont progressivement introduites dans l'industrie automobile. Ces deux approches seront décrite dans les sections ci-dessous.

2.3.1 EMS heuristique

Ce type de contrôleur est basé sur des règles et des corrélations inspirées par une connaissance *a priori* du comportement et de l'efficacité du système de propulsion [18, 20, 29, 56]. Par exemple, une des règles principales suggère l'utilisation du moteur thermique seulement lorsque son efficacité est relativement élevée (en général pour des charges élevées), alors que dans des conditions moins favorables, le mode électrique devrait être préféré et le moteur thermique sera éteint.

L'avantage principal de ce type d'algorithmes est que les corrélations sont intuitives, de sorte qu'elles sont bien acceptées par les ingénieurs et les utilisateurs finaux. Ils donnent des résultats relativement satisfaisants s'ils sont soigneusement réglés. Ils ne nécessitent aucune connaissance des conditions futures de conduite, ce qui simplifie leur mise en œuvre pour des applications en temps réel.

L'inconvénient majeur de ce type d'algorithmes est qu'ils sont adaptés pour des systèmes simples, et leurs performances dans des conditions de conduite réelles (qui sont généralement différentes de celles utilisées pour calibrer la stratégie de commande) ne sont pas garanties. Toutes ces raisons ont poussé le développement des contrôleurs optimaux basés sur des modèles (model based approach).

2.3.2 EMS optimal

Les faiblesses (relatives) de l'EMS heuristique discutées ci-dessus ont motivé le développement des contrôleurs optimaux. Ce type de stratégie est basé sur la définition d'une fonction coût à minimiser ou à maximiser pour un système dynamique qui représente la dynamique du véhicule. Différentes fonctions coût peuvent être considérées : consommation du carburant, émissions polluantes, vieillissement de la batterie, agrément de conduite ou toute combinaison de ces quantités [2, 17, 44, 56, 71, 72, 74, 77, 81, 92]. Pour les problèmes de la gestion d'énergie, un HEV peut être décrit par des modèles quasi-statiques. Le vecteur d'état ne comprend généralement que l'état de charge (SOC) de la batterie [33].

En fonction de la connaissance des conditions futures de conduite, on distingue deux sous-catégories. Dans la première catégorie, le véhicule est supposé suivre un cycle de conduite prédéfini sur un horizon de temps fini. La stratégie optimale calculée anticipe ce qui se passe de l'instant actuel jusqu'à la fin du cycle de conduite. La connaissance des conditions futures est seulement possible lorsque le véhicule opère sur des cycles de conduite normalisés, ou pour des véhicules qui ont des trajets prescrits. Dans tous les autres cas, le profil de vitesse est incertain.

Dans la deuxième catégorie, où les conditions futures de conduite ne sont pas connues, la stratégie de commande doit être calculée à partir des informations disponibles en temps réel, sous la forme d'un feedback. Comme il est impossible dans ces conditions de calculer une stratégie optimale, la stratégie obtenue sera sous-optimale. La commande prédictive [13, 36] et l'ECMS (Equivalent Consumption Minimization Strategy) [16, 37] font partie des méthodes utilisées pour faire face aux incertitudes dans les conditions de conduite.

2.4 Problèmes considérés et solutions proposées

Dans cette thèse, nous souhaitons développer un EMS pour un HEV de type parallèle en prenant en compte l'impact des températures internes (du moteur et/ou du système de dépollution) sur la consommation du carburant et les émissions polluantes. En effet, ces variables supplémentaires ont un impact significatif, comme on peut le constater sur les Figures 1.2 et 1.3 et la prise en compte de leurs dynamiques conduit à un système dynamique à trois états avec une seule entrée de commande, et deux sorties d'intérêt (consommation du carburant et émissions polluantes). Pour implémenter ce régulateur dans des conditions réelles de conduite, l'EMS doit prendre la forme d'un feedback des in- formations disponibles en temps réel. Actuellement, l'ECMS [16] est en mesure de prendre en compte une seule variable d'état (le SOC de la batterie).

À cause de l'augmentation du nombre de variables d'état, il nous semble très coûteux de développer un EMS fondé sur des règles et des corrélations heuristiques. En effet, la complexité d'établir un tel contrôleur, qui pourrait couvrir tous les cas possibles, serait très élevée. Notre objectif est de développer une généralisation de l'ECMS qui combine les résultats du contrôle optimal (l'entrée de commande minimise l'Hamiltonien associé au problème de commande optimale considéré) et une boucle de rétroaction (la variable adjointe est calculée comme la sortie d'un contrôleur de type PID sur les variables d'état). En outre, parce que ce genre de stratégie est sous-optimal par construction, on ne sait pas si l'ECMS, dans sa formulation originale, peut atteindre un niveau de performance suffisant en ce qui concerne les émissions polluantes, tout en gardant l'excès en consommation du carburant dans des limites acceptables. Nous illustrons cette situation dans la Figure 1.4.

A première vue, on ne sait pas quelle(s) variable(s) d'état doit (doivent) être considérée dans l'analyse. Comme chaque état augmente la complexité de la tâche de conception de commande, nous souhaitons établir un certain compromis entre les performances des stratégies et la complexité des modèles utilisés pour les calculer. Pour réponde à cette question, nous procédons en deux étapes. Dans la première étape, nous résolvons une collection de problèmes de contrôle optimal pour différents niveaux de modélisation (un, deux ou trois états). Pour faire une comparaison équitable entre les solutions obtenues, les stratégies de contrôle qui en résultent sont appliquées au modèle complet avec trois variables d'état. Nous considérons une somme pondérée de la consommation du carburant

et les émissions polluantes sur un horizon temporel prédéfini qui correspond à un cycle de conduite. Les résultats obtenus quantifient le bénéfice de la prise en compte des états supplémentaires. Des résultats types sont illustrés dans la Figure 1.5.

La Partie I de cette thèse est consacrée pour les solutions optimales des problèmes de gestion d'énergie pour un hybride parallèle équipé avec d'un moteur essence et un système de post-traitement de type catalyseur trois-voies. Le cycle de conduite est supposé être connu à l'avance.

Dans le chapitre 3, le problème de la gestion d'énergie mono-état (considérant seulement le SOC), généralement considéré dans la littérature, est présenté. La fonction coût à minimiser est la consommation de carburant. Nous résolvons le problème de commande optimale associé en utilisant le principe du minimum de Pontryagin (PMP). Ce problème est étendu pour inclure des contraintes d'état sur le SOC.

Dans le chapitre 4, nous présentons une extension possible du problème mono-état pour réduire les émissions polluantes. Cet extension permet de prendre en compte les dynamiques thermiques du moteur et du système de post-traitement. Nous utilisons les résultats numériques de cet étape pour produire une figure similaire à Figure 1.5.

Dans le chapitre 5 de la partie II, nous explorons le concept des perturbations régulières dans les problèmes de contrôle optimal sous contrainte de commande. Les différents problèmes étudiés dans la Partie I sont des exemples de simplifications successives des modèles qui peuvent être refondues dans ce concept général.

Dans la deuxième étape décrite dans la Partie III, nous proposons une généralisation de l'ECMS en utilisant des corrélations entre les états thermiques et ses variables adjointes. Ces relations sont observées sur les trajectoires optimales calculées dans la première étape. Cela définit un feedback sous-optimal que nous testons numériquement et expérimentalement. Des résultats types attendus sont illustrés dans la Figure 1.6.

Dans le chapitre 6, une étude des propriétés de stabilité et de robustesse de l'ECMS est proposée. Ensuite, des extensions de cette stratégie sont proposées pour inclure les dynamique thermique dans le problème d'optimisation. Les résultats obtenus montrent que les performances obtenues sont satisfaisantes notamment pour satisfaire la norme sur les émissions polluantes tout en gardant la sous-optimalité sur la consommation du carburant avec des limites acceptables.

Enfin, dans le chapitre 7, nous appliquons notre méthodologie à un banc d'essai constitué d'un moteur diesel équipé d'un catalyseur d'oxydation diesel (DOC), d'un filtre à particules diesel (DPF) et d'un système de réduction sélective catalytique par l'urée (SCR). Les tests expérimentaux réalisés valident l'affirmation selon laquelle une stratégie de contrôle simple est suffisante pour réduire les NO_x.

2.5 Contributions de la thèse

L'approche en deux étapes, décrites ci-dessus, suggère une étude qui constitue, avec les résultats de l'application en chapitre 7, les contributions de la thèse. Ces contributions sont de deux ordres :

1. **Perturbations dans les problèmes de commande optimale sous contrainte de commande :** Le résultat obtenu par Bensoussan [7] sur les perturbations régulières dans le contrôle optimal est étendu pour inclure des contraintes de commande. Nous montrons que les termes d'ordre ε apparaissant dans la dynamique et

la fonction coût conduisent à une sous-optimalité de l'ordre $K\varepsilon^2$ dans le coût optimal. Le paramètre K est estimé à partir de la solution du problème d'optimisation pour $\varepsilon = 0$. Ce résultat, qui est très utile pour des applications pratiques, est prouvé par le biais de la méthode de points intérieurs (IPM) proposée dans [47]. Une extension possible pour inclure les contraintes d'état, qui sont plus difficiles à gérer dans la présence des erreurs de modélisation, est discutée et illustrée par un exemple numérique. Ce résultat nous permet d'évaluer quantitativement l'impact de réduction de modèle dans les problèmes d'optimisation. Il apporte une réponse à la question informelle suivante : : *«Est-il utile de considérer une complexité supplémentaire dans mon modèle afin d'optimiser les performances obtenues?»*.

2. **Généralisation de l'ECMS :** Trois extensions possibles de l'ECMS sont proposées pour inclure les dynamiques thermiques dans l'optimisation. Ces extensions sont basées sur la paramétrisation de la relation entre les états adjoints et leurs états associés (qu'on suppose mesurés ou au moins estimés) indépendamment des conditions de conduite. Les stratégies temps réel proposées sont capables de gérer certains degrés d'incertitudes dans les futurs scénarios de conduite. Elles sont conçues pour prendre en considération plus qu'une seule variable dynamique.

Les travaux présentés dans cette thèse ont fait l'objet des publications suivantes :

1. D. Maamria, F. Chaplais, N. Petit and A. Sciarretta, "Comparison of several strategies for HEV energy management system including engine and catalyst temperatures", in Proc. of the American Control Conference 2015.

2. D. Maamria, F. Chaplais, N. Petit and A. Sciarretta, "On the impact of model simplification in input constrained optimal control: application to HEV energy-thermal management", in Proc. of the 53rd IEEE Conference on Decision and Control, 2014.

3. D. Maamria, F. Chaplais, N. Petit and A. Sciarretta, "Numerical optimal control as a method to evaluate the benefit of thermal management in hybrid electric vehicles", in Proc. of the 2014 IFAC World Congress.

Part I

Optimal control for EMS of parallel HEV
Contrôle optimal pour EMS d'un HEV de type parallèle

Chapter 3

Optimal single-state problem

Chapitre 3 Pour les véhicules hybrides, un contrôleur *haut-niveau* est nécessaire pour déterminer comment les composants du groupe motopropulseur doivent fonctionner, afin de satisfaire la demande de puissance du conducteur. L'objectif principal de ce contrôleur est la réduction de la consommation d'énergie, particulièrement en présence des contraintes : agrément de conduite et limitations physiques des composants. Le calcul de ce contrôleur peut être formulé comme un problème de commande optimale. Dans ce chapitre, l'architecture du véhicule hybride choisie dans ce travail de thèse est détaillée. Ensuite, le problème de la commande optimale pour calculer ce contrôleur est formulé. Puis, certains aspects théoriques et numériques, ainsi que les résultats sont discutés.

Contents

Hybrid vehicles (HV) are characterized by two or more motors and power sources. Regardless of the type of HV, a supervisory controller is needed to determine how the powertrain components should operate, in order to satisfy the power demand of the driveline in the most convenient way. The main objective of this controller is the reduction of the energy consumption, typically in the presence of various constraints due to drivability requirements and the physical limitations of the components [4, 33]. The design of this controller can be formulated as an optimal control problem (OCP).

The architecture of the chosen hybrid electric vehicle (HEV) to be investigated in this thesis is detailed in this chapter. An optimal control problem is formulated. Then, some theoretical and numerical aspects are discussed. Finally, numerical results are presented.

3.1 System modeling

The modeling methodology is adopted from [33], resulting in a quasistatic model of the various components.

3.1.1 Reference parallel architecture

The system considered here is a parallel HEV equipped with an internal combustion engine. The architecture is depicted in Figure 3.1. The electric machine allows the power assistance, including the purely electric drive, and the battery recharging. The transmission ratio of the electric machine to the wheels is constant. Additionally, a battery is used as an energy storage system for the electric energy. The architecture choice is not restrictive, as the methodology presented in this thesis could be transposed to other cases of interest (series or combined HEV).

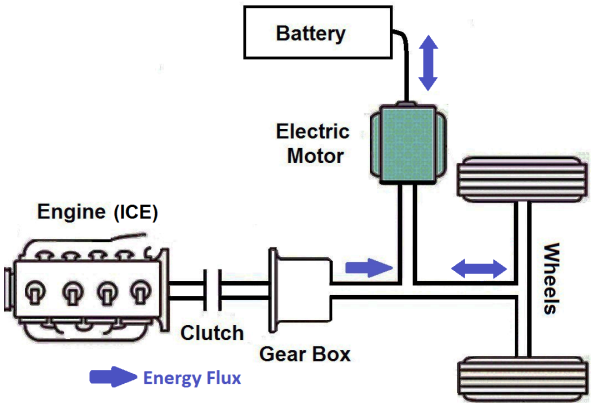

Figure 3.1: A parallel HEV architecture

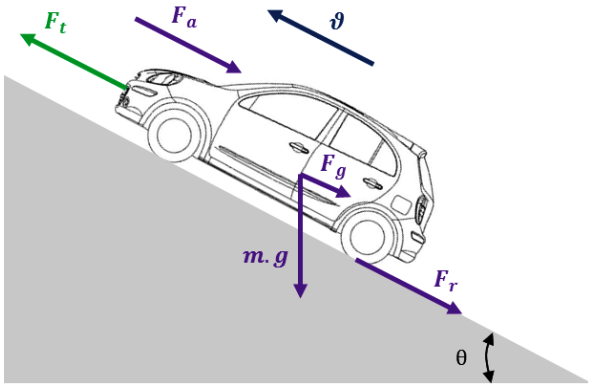

Figure 3.2: Schematic representation of the forces acting on the vehicle

3.1.2 Longitudinal vehicle dynamics

Figure 3.2 shows the forces acting on the vehicle body. The vehicle is modeled in a vertical plan. Assuming that the vehicle speed $v(t)$, the acceleration $\alpha(t)$ and the road grade $\theta(t)$

are known, the traction force $F_t(t)$ required by the driving cycle is given, according to Newton's law of motion, by

$$F_t(t) = (m + m_{rot}) \cdot \alpha(t) + F_a(t) + F_r(t) + F_g(t),$$

where F_a is the aerodynamic drag force, F_r is the rolling friction force, F_g is the uphill driving force and m is the total vehicle mass. The term m_{rot}

$$m_{rot} = \frac{n_{tire} \cdot j_{tire} + j_{rot}}{r_{tire}^2}$$

is an equivalent mass of the rotating parts. It accounts for the overall inertia of the wheels $n_{tire} \cdot j_{tire}$ and for that of the traction machines j_{rot}. The expressions of the applied forces are

$$F_g(t) = m \cdot g \cdot \sin(\theta(t)),$$
$$F_a(t) + F_r(t) = c_0 + c_1 \cdot v + c_2 \cdot v^2,$$

where g is the gravitational acceleration and $c_i,\ i = \{0, 1, 2\}$ are the coefficients of the road load equation (this model is employed in [33, 66, 73]). This model considers only the forces in the longitudinal direction. All latitudinal forces, variations of friction parameters during curves, wind forces, and other disturbances are neglected. The traction force $F_t(t)$ has to be provided by prime movers.

3.1.3 Transmission model

The driver's torque request and the vehicle speed are directly calculated from the driving cycle which is described by the wheel speed profile, elevation profiles and the gear-box ratio as functions of time. The resulting torque value $T_t(t)$ can be positive (traction) or negative (braking). As the considered HEV is of parallel type, the engine torque T_{eng} and the torque of the electric machine T_{el} are related to the torque required at the wheel $T_t(t) = r_{tire} \cdot F_t(t)$ by the torque balance

$$r_{tire} \cdot F_t(t) = R_{el} \cdot T_{el}(t) + \eta_{gb} \cdot R_{gb}(t) \cdot T_{eng}(t), \tag{3.1}$$

where R_{el} is the constant motor-to-wheel transmission ratio, R_{gb} is the gear-box ratio, r_{tire} is the wheel radius and η_{gb} is the constant gear-box efficiency. Similarly, the rotational speed of the ICE and of the electric machine are related to the rotational speed at the wheel ω_{wh} by

$$\begin{aligned} \omega_{eng}(t) &= R_{gb}(t) \cdot \omega_{wh}(t), \\ \omega_{el}(t) &= R_{el} \cdot \omega_{wh}(t). \end{aligned}$$

3.1.4 Engine model

The fuel consumption of the engine, neglecting the effects of engine temperature, is given by a quasistatic map as a function of the effective engine torque T_{eng} and the engine rotational speed ω_{eng}

$$\dot{m}_{fuel} = c(T_{eng}, \omega_{eng}).$$

The fuel power can be written

$$P_f = c(T_{eng}, \omega_{eng}) \cdot H_{lhv},$$

where H_{lhv} denotes the lower heating value of the fuel. The maximum allowed engine torque is given as a function of ω_{eng}.

3.1.5 Electric machine model

The electric machine[1] is modeled by a quasistatic map describing either the electric power or its efficiency. The electric power consumed (in traction mode) or supplied to the battery (in recuperation mode) is of the form

$$P_m = \Gamma(T_{el}, \omega_{el}),$$

where Γ is the electric power map of the electric machine. It represents the requested power from the battery to provide the needed torque T_{ele} at the speed ω_{el}. This map often includes the losses in the electric machine (mechanical, copper and iron losses) [8, 24, 90] and losses in the power converters. The electric machine torque is limited by speed-dependent upper and lower bounds of the form

$$T_{emin}(\omega_{el}) \leq T_{el} \leq T_{emax}(\omega_{el}).$$

3.1.6 Battery model

The battery is usually represented by an equivalent circuit model comprising a voltage source U_{ocv} in series with an electric resistance R_b, both of which vary with certain parameters such as ξ, the state of charge (SOC) of the battery (which describes the capacity remaining in the battery expressed as a percentage of its nominal capacity) and the battery temperature [4, 33]. The open-circuit voltage U_{ocv} represents the equilibrium potential of the battery. The internal resistance R_b can be experimentally evaluated as a function of the SOC and, possibly, the battery temperature. It depends on the sign of the current I_b (charging or discharging phase) [33]. Kirchhoff's law for the equivalent circuit yields

$$U_b = U_{ocv}(\xi) - R_b(\xi) I_b,$$

which relates two unknowns, the battery current I_b and the voltage U_b. A second equation is given by the definition of the battery power: $P_b = I_b U_b$. This power equals the electric machine power P_m. Thus, the formula of the current I_b is given by [33]

$$I_b = \frac{1}{2R_b(\xi)} \left(U_{ocv}(\xi) - \sqrt{U_{ocv}^2(\xi) - 4R_b(\xi)P_b} \right).$$

Due to the limitation of the battery, the current I_b is not defined if the power P_b is greater than $U_{ocv}^2(\xi)/4/R_b(\xi)$. In practice, this limit is never reached [4]. The power delivered by the battery is limited by the constraints of the current I_b and the battery voltage

$$P_{b,min}(t) \leq P_b(t) \leq P_{b,max}(t).$$

The definitions of $P_{b,min}$ and $P_{b,max}$ are given in [33]. The SOC dynamics is given in the discharging case by

$$\frac{d\xi}{dt} = -\frac{I_b}{Q_0}.$$

In the charging case, the evaluation of the SOC must take into account the fact that a fraction of the current I_b is not transformed into charge. This fraction is due to irreversible,

[1] The term electric machine is used for the combined unit consisting of the electric machine and its power electronics.

parasitic reactions taking place in the battery [33]. The SOC dynamics, in this case, is given by

$$\frac{d\xi}{dt} = -\eta_c \frac{I_b}{Q_0},$$

where Q_0 is the nominal battery capacity and η_c is the charging efficiency. In practice, the current I_b depends on ξ, but this dependency is neglected in the control model as commonly assumed in the literature [40, 80] (it has been shown [80] that neglecting this dependance does not have a substantial impact on the optimal fuel consumption). In order to simplify the notation, the dynamics of ξ considering a given initial condition ξ_0 is written as

$$\frac{d\xi}{dt} = f(T_{el}, t), \ \xi(0) = \xi_0. \tag{3.2}$$

3.2 Optimal energy management problem statement

As discussed above, the main task of an EMS for a parallel HEV is to find the most convenient way to split the power at the wheel, requested by the driver, between the engine and the electric machine to minimize the overall energy use. The calculation of such controller can be formulated as an OCP. Details about this formulation are given in following sections.

3.2.1 Cost function

The simplest cost function to be minimized is the fuel consumption over a given driving cycle of a duration T. Pollutant emissions can be included in the performance index by considering a trade-off between the two quantities [33, 64]. A general expression for the cost is given by

$$J(u) = \int_0^T L(u, x, w)dt,$$

where L combines the fuel consumption rate and the emission rates of the regulated pollutants, u is the control variable (engine torque $u = T_{eng}$) and x is the state variable. The variable w includes the speed ω_{wh} and the torque T_t at the wheels requested by the driver. These two parameters may be seen as disturbances in the case when future driving conditions are unknown (online optimization). When the driving cycle is known in advance (offline optimization), w is a known function of time.

Drivability concerns can also be introduced into the performance index. For example, the cost function might include an anti-jerk term, which consists of the engine acceleration squared [92], or a term related to gear shifting multiplied by an arbitrary weighting factor [44].

The vehicle is assumed to follow a prescribed driving cycle and all fast dynamics taking place in the powertrain are neglected. The considered cost function is the fuel consumption

$$J_0(u) = \int_0^T c(u(t), \omega_{eng}(t))dt,$$

where c is the fuel consumption rate for a warm engine described in Section 3.1.4.

3.2.2 Dynamics

The nature of the state variables is related to the dynamics of the considered system, which generally include mechanical, thermal, electrical, and electrochemical subsystems. For the purpose of energy management, HEV can be described by quasistatic models [33]. Thus, the number of state variables decreases, and the state vector includes only integral quantities such as the SOC [33]. The SOC dynamics is given by equation (3.2).

One operational constraint reflecting *charge-sustaining* (final SOC equals its initial value) or *charge-depleting* (final SOC is nearly its minimal value) operations requires that the final value of ξ should be equal to a target value ξ_{ref}, where

$$\xi(T) = \xi_{ref}. \tag{3.3}$$

This final condition allows a fair comparison of various strategies by guaranteeing the same level of battery energy at the end of the driving cycle. In fact, the fuel consumption and the final value of the SOC are related:

- if the final SOC is greater than its target value, the fuel consumption will be higher than when the final constraint is satisfied;
- if the final SOC is lower than its target value, the fuel consumption will be lower than when the final constraint is satisfied.

3.2.3 Input and state constraints

The engine torque u and the electric machine torque T_{el} are constrained and the bounds depend on the motors speed; thus they are functions of time as the driving cycle is assumed known in advance:

$$\begin{aligned} T_{min}(t) \leq & u(t) \leq T_{max}(t), \\ T_{emin}(t) \leq & T_{el}(t) \leq T_{emax}(t). \end{aligned}$$

In Figure 3.3, an example of the upper and the lower bounds on the engine and the electric machine torques are given for the new European driving cycle (NEDC). As has mentioned above, these bounds depend on the driving cycle to follow.

By combining these two equations with torque balance in equation (3.1), only one constraint on the input control u is considered. This constraint defines a set U^{ad} of the form

$$U^{ad} = \{u \in L^{\infty}([0,T],\mathbb{R}) \text{ s.t. } u_{min}(t) \leq u(t) \leq u_{max}(t),\ t \in [0,T]\}. \tag{3.4}$$

As the energy available in the battery is limited and in order to maximize the life expectancy of the battery, the OCP may include some instantaneous constraints on the state ξ. These are of the form

$$\xi_{\min} \leq \xi(t) \leq \xi_{\max}. \tag{3.5}$$

Gathering all the facts discussed above, the OCP, being considered in this chapter, is defined as follows

$$\min_{u \in U^{ad}} J_0(u), \tag{3.6}$$

under the final constraint (3.3), the instantaneous constraints (3.5), the state dynamics (3.2) and U^{ad} is defined in equation (3.4). This optimization problem is solved below using the PMP [40, 74].

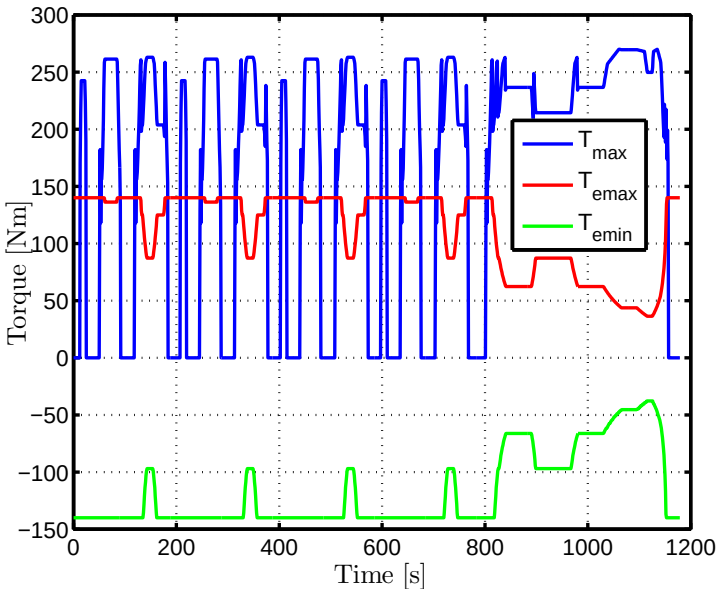

Figure 3.3: Torque constraints [Nm] for NEDC

3.3 Recalls on optimal control theory

The optimal control problems (OCP) we treat in this thesis are of the form

$$\min_{u \in U^{ad}} \left[\int_0^T l(u(t), x(t), w(t)) dt \right], \tag{3.7}$$

where l is a continuously differentiable locally Lipschitz function of its arguments and the variable w is a function of time representing the disturbance terms (for the EMS, w characterizes the driving cycle). $x \in \mathbb{R}^n$ and $u \in \mathbb{R}^m$ $(m \leq n)$ are the state and the control variables of the following nonlinear dynamics with prescribed initial conditions x_0

$$\dot{x} = h(x, u, w), \ x(0) = x_0, \tag{3.8}$$

where h is a smooth real-valued function of its arguments. On the considered time horizon T, which is assumed to be fixed without loss of generality, the control variable u can be chosen in a set U^{ad} (a subset of L^∞)

$$U^{ad} = \{u \in L^\infty([0,T], \mathbb{R}^m) \text{ s.t. } u(t) \in C, \ t \in [0,T]\}, \tag{3.9}$$

in which C is a bounded closed convex set of $\mathbb{R}^m$. The optimal control problem consists in finding the control u that minimizes the cost (3.7). To solve these unconstrained optimal control problems, two main approaches are usually used: Pontryagin's minimum principle (PMP) and dynamic programming (DP). In this thesis, we are interested in PMP methods. We now recall it.

3.3.1 Pontryagin minimum principle (PMP)

The minimum principle [68] states necessary conditions for optimality. It is based on a variational approach and it converts the optimal control problem into a two-point

boundary-value problem (TPBVP). If (u, x) is an optimal solution for the problem (3.7, 3.8, 3.9), then there exists a function p called adjoint state variable, such that almost everywhere on $[0, T]$

$$\begin{aligned} \dot{x} &= h(x, u(t)),\ x(0) = x_0, \\ \dot{p} &= -\frac{\partial H}{\partial x}(x(t), u(t), p(t)),\ p(T) = 0, \\ u(t) &\in \arg\min_{v \in C} H(x(t), v, p(t)), \end{aligned}$$

where H is the Hamiltonian defined by

$$H(x(t), u(t), p(t)) = l(u(t), x(t)) + p^T(t) h(x(t), u(t)).$$

The Hamiltonian H has to be minimized by $u(t)$ at each time $t \in [0,\ T]$. The equations giving p and the optimal control u are usually called stationarity conditions. Dynamic programming can be also used to solve this kind of optimal control. The interested reader is referred to [9, 14].

3.3.2 Interior point methods for state constraints

More generally, beside the input constraints (3.9), the general OCP described by (3.7) could include state constraints that are difficult to handle. Methods used to deal with state constraints include the interior penalty method (IPM). The main advantage of this approach is that the solution of the constrained OCP is determined from the simple stationarity conditions. There is no need to know in advance the sequence of constrained/unconstrained arc and switching points [50]. This is of practical importance when implementing numerical methods based on the PMP.

Historically, these methods, IPM, have been introduced for finite dimensional constrained optimization by Fiacco and MacCormick [27] in the late 1960s. They were very successful in the mid-1980s thanks to Karmarkar's work [35] in which it was shown that the proposed interior point algorithm is significantly (50 times) faster than the simplex method for a linear programming (LP) problem. They have been generalized in [47] to a class of optimal control problems of the form (3.7) with state constraints of the form $g(x(t)) \leq 0$ for all $t \in [0, T]$.

The algorithm presented in [47] demonstrates how to solve this class of optimal control problem as a sequence of unconstrained problems. The idea consists of introducing penalties on the state and on the control input with a penalty weight r in the cost function. This modification defines a new unconstrained problem after an adequate change of variable. Then, it has be shown that the solution of the new unconstrained problem converges to the solution of the initial problem under constraints when r goes to zero and the solutions approach the constraints from the interior. The new cost function parametrized by the penalty weight r is

$$\min_{u \in U^{ad}} \left[\int_0^T \left[l(u(t), x(t)) + r \cdot \gamma_g(g(x(t))) \right] dt \right], \tag{3.10}$$

where γ_g is a penalty function satisfying the following conditions:

- for $x < 0$, $\gamma_g(x)$ is continuously differentiable, convex, and increasing;

- $\gamma_g(x) \geq 0$ if $x < 0$ and $\gamma_g(x) = 0$ if $x \geq 0$;
- $\lim_{x \to 0} \gamma_g(x) = +\infty$.

To satisfy these conditions, a possible choice of γ_g is

$$\gamma_g(x) = \begin{cases} (-x)^{-n_g}, & \text{for } x < 0, \\ 0, & \text{otherwise,} \end{cases} \tag{3.11}$$

where the parameter $n_g > 1$ [50].

Proposition 1 *[47] If u is constrained and γ_g is properly chosen, then:*

- *If the cost in (3.10) is finite, then the state x satisfies $g(x) < 0$;*
- *the modified cost (3.10) decreases and $r \cdot \gamma_g(g(x(t))) \to 0$ when r tends to zero;*
- *when r tends to zero, the optimal value of the modified cost (3.10) converges to the optimal value of (3.7) with the satisfaction of the state constraints $g(x(t)) \leq 0$.*

3.4 Optimal solution

3.4.1 System specifications and driving cycle

The specifications of the HEV are summarized in Table 3.1. The ICE is a gasoline engine. Its fuel consumption rate as a function of the engine rotational speed and the engine torque is given in Figure 3.4.

Table 3.1: Vehicle characteristics

Vehicle weight	1932 kg
ICE max. power	92 kW
Electric machine max. power	42 kW
Battery capacity	2000 Wh

Figure 3.5 shows the electric power P_m and the speed dependent torque limits of the electric machine used in the vehicle. The open-circuit voltage U_{ocv} and the internal resistance R_b are given in Figures 3.6 and 3.7. These data are gotten from [15, 17].

The NEDC driving cycle is considered. The speed requested at the wheel and the gear-box ratio (for the thermal mode) are given in Figures 3.8 and 3.9.

3.4.2 Determination of optimal solution

3.4.2.1 Without instantaneous SOC constraints (3.5)

The Hamiltonian H_0 associated to the OCP (3.6) is defined by

$$H_0(u, t, \lambda) = c(u, t) + \lambda f(u, t), \tag{3.12}$$

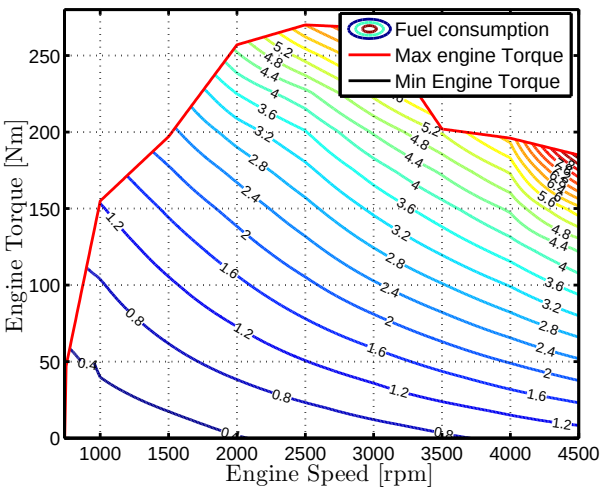

Figure 3.4: Engine fuel map $c(.)$ [g/s]

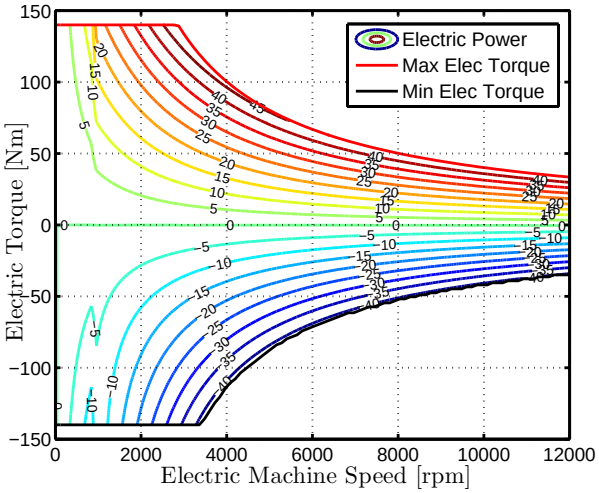

Figure 3.5: Electric power map P_m [kW]

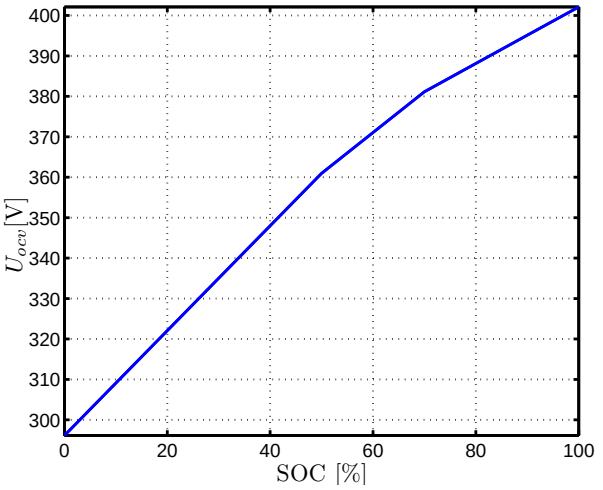

Figure 3.6: Battery open-circuit voltage U_{ocv} [V]

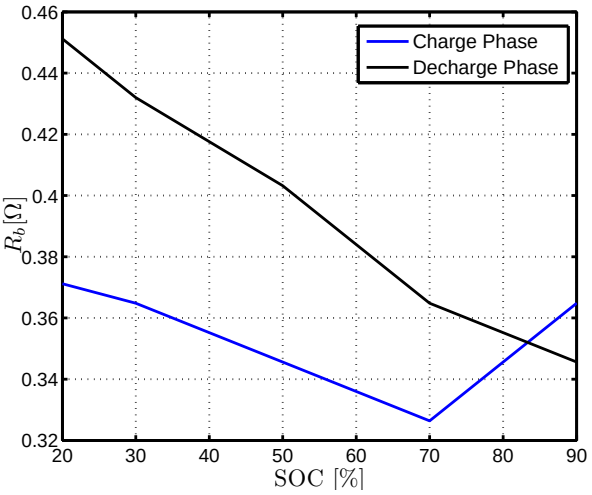

Figure 3.7: Battery internal resistance R_b [Ω]

where λ is the adjoint variable associated to ξ. For a given control u, the dynamics of λ is defined by

$$\frac{d\lambda}{dt} = -\frac{\partial H_0}{\partial \xi}(u, t, \lambda) = 0. \tag{3.13}$$

The PMP states that, if u_0^* is an optimal control, then, for every time t, $u_0^*(t)$ minimizes the Hamiltonian in the set defined by (3.4) along the optimal state and costate trajectories

$$u_0^*(t) \in \arg\min_{u \in U^{ad}} H_0(u, t, \lambda(t)). \tag{3.14}$$

Equations (3.2, 3.3, 3.13, 3.14) constitute a two-point boundary-value problem (TPBVP), denoted by (P_0), where the final condition $\lambda(T)$ is unknown, as the final SOC is constrained. From (3.13), λ is a constant and its value should be chosen to satisfy the final constraint (3.3).

In most practical cases of EMS design for HEV, the relationship between λ and $\xi(T)$ is monotonic. In particular, if λ chosen lower than its optimal value, $\xi(T)$ will be higher than ξ_{ref} and, conversely if λ is higher than its optimal value, $\xi(T)$ will be lower than

Table 3.2: HEV parameters

Parameter	Symbol	Value
Constant coefficient of the road load	c_0	$133,7343$ N
Linear coefficient of the road load	c_1	$1,8374$ N/(m/s)
Quadratic coefficient of the road load	c_2	$0,5398$ N/(m/s)^2
Wheel radius	r_{tire}	$0,3173$ m
Number of wheels	n_{tire}	4
Inertia of each wheel	j_{tire}	1.1 kg$\cdot$ m^2
Battery nominal capacity	Q_0	18000 C
Motor-to-wheel transmission ratio	R_{el}	11
Gear-box efficiency	η_{gb}	0.95
Battery charging efficiency	η_c	0.95
Fuel lower heating value	H_{lhv}	42600000 J/kg
Lower SOC value	ξ_{min}	0.4
Upper SOC value	ξ_{max}	0.8

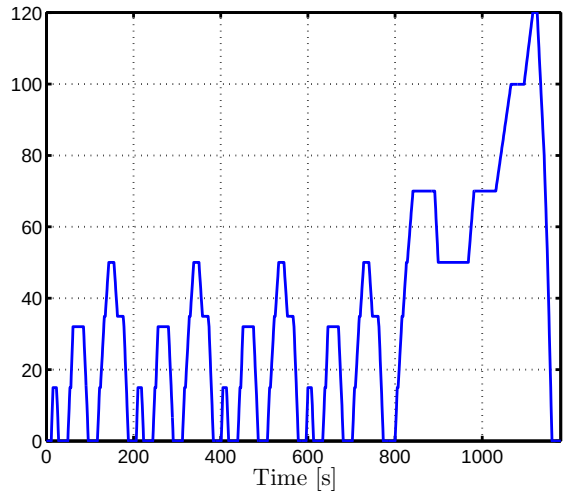

Figure 3.8: Wheel speed [km/h] for NEDC

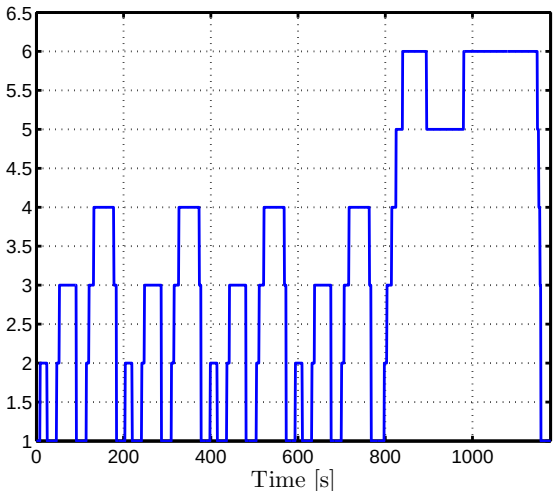

Figure 3.9: Gear-box ratio for NEDC

ξ_{ref}. Based on this property, λ can be iteratively determined by correcting the previous estimation in accordance with the sign of $(\xi(T) - \xi_{ref})$ after each iteration [33]. A more detailed study of this relationship has been conducted in [21].

Generally in the literature of EMS, an equivalence factor (that is positive and dimensionless) denoted by s is usually used [74] instead of using λ (that is negative). The relationship between these two parameters is given by

$$s(t) = -\frac{H_{lhv}}{Q_0 \cdot U_{ocv}}\lambda(t). \tag{3.15}$$

The stationarity condition of the PMP is expressed on the quantity $\tilde{H}_0$ (which is in power units) given in (3.16). It is the sum of the consumed fuel power and the inner (electrochemical) battery power

$$\tilde{H}_0(u,t,s) = c(u,t) \cdot H_{lhv} + s(t) \cdot I_b(t) \cdot U_{ocv}(t). \tag{3.16}$$

3.4.2.2 With instantaneous SOC constraints

To take the SOC constraints into account, the algorithm proposed in [47] is used. Consistently with Section 3.3.2, a new cost function parametrized by the penalty weight r is defined

$$\bar{J}_0(u, r) = \int_0^T [c(u, t) + r \cdot \gamma(\xi)]\, dt,$$

where the penalty γ is of the form (3.11). For simplicity, and as the SOC trajectories are always below ξ_{max} for the considered driving cycles, only the constraint $\xi(t) \geq \xi_{min}$ is considered. The new Hamiltonian H_{0r} associated to this OCP is

$$H_{0r}(u, t, \xi, \lambda, r) = c(u, t) + r \cdot \gamma(\xi) + \lambda f(u, t).$$

The dynamics of λ is then given by

$$\dot{\lambda} = -\frac{\partial H_{0r}}{\partial \xi}(u_0^r(t), t, \xi, \lambda, r) = \frac{r.n_g}{(\xi(t) - \xi_{min})^{n_g+1}}, \tag{3.17}$$

where $\lambda(T)$ is free as the final SOC is constrained. The optimal control $u_0^r(t)$ minimizes the Hamiltonian in the set defined by (3.4)

$$u_0^r(t) \in \arg\min_{u \in U^{ad}} H_{0r}(u, t, \xi, \lambda(t), r). \tag{3.18}$$

Equations (3.2, 3.3, 3.17, 3.18) constitute a TPBVP denoted by (P_0^r). The parameter n_g is set at 1.1. The weight r is initialized with $r_0 = 10^{-6}$ for NEDC and is then decreased.

3.4.3 Numerical results

3.4.3.1 Without instantaneous SOC constraints

The only unknown parameter in the TPBVP (P_0) is the value of the adjoint state λ (which is constant). Its value is determined by using a dichotomy as the relation between λ and $(\xi(T) - \xi_{ref})$ is monotonic. The obtained SOC trajectory is given in Figure 3.11 (black curve). It satisfies the instantaneous constraints given by the relation (3.5).

The engine and the electric machine torques for the time interval $t \in [0,\ 200]$ s are depicted in Figure 3.10. In this part of the driving cycle, the vehicle speed is low and the use of the engine is limited to the acceleration phases. In the deceleration phases, the engine is not used and the electric machine recovers the kinetic energy (represented by a negative electric machine torque) to recharge the battery. In the case of a constant vehicle speed, the torque requested at the wheels will be constant and this demand will be satisfied by the electric machine.

The adjoint state λ is constant, but its value and the obtained control strategy both depend on the prescribed driving cycle. This solution can be used as a reference of comparison for evaluating any sub-optimal real-time strategy.

3.4.3.2 With instantaneous SOC constraints

For each value of r in a decreasing sequence, the TPBVP (P_0^r) is solved. The state and costate trajectories are shown in Figures 3.11 and Table 3.3 summarizes the obtained fuel

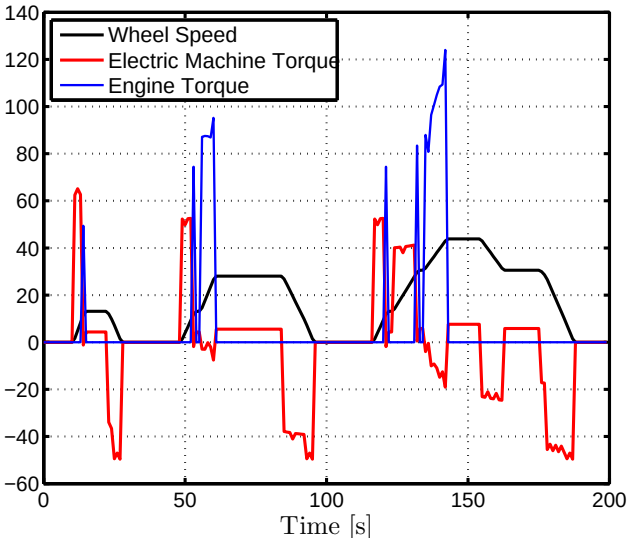

Figure 3.10: Torque trajectories in [Nm] for NEDC in the unconstrained case for the time interval [0, 200] s.

consumption for NEDC. For this driving cycle, the state constraints are never active and the SOC trajectories converge to the unconstrained trajectory when r decreases.

As shown in Figure 3.11, when r decreases, the SOC trajectory approaches the constraint-free optimal state trajectory from the interior (the SOC trajectories for different values of r remain inside the domain defined by the constraints. In Figure 3.13, for a different driving cycle, the trajectories approach the constraints from the interior). The parameter r has to be decreased to small values to avoid causing too much sub-optimality and change in the optimal trajectory. The parameter r also has some impact on the history of the SOC (the use of the engine and the electric machine):

- For high values of r, the control strategy recharges the battery at the beginning of the driving cycle by preferring the use of the engine: in order to minimize the term $r \cdot \gamma(.)$, $\xi(t)$ has to be far from its lower bound (ξ_{min}) and thus the term $\gamma(\xi)$ is small.

- When r tends to zero, the control strategy has more flexibility. The SOC trajectory can move nearer to the constraints and the term $\gamma(\xi)$ increases. This variation is offset by decreasing r: there is a compensation effect between decreasing the value of r and the growth of the penalty value.

From Table 3.3, the fuel consumption decreases when r tends to zero and the difference in terms of fuel consumption between the various solutions (for different values of r) is less than 2% (for example, the difference in terms of fuel consumption between the solutions corresponding to $r = 5e^{-7}$ and $r = 8e^{-9}$ is less than 1.1%). This quantification means that having *an acceptable* distance from the constraints leads to an acceptable sub-optimal fuel consumption.

As appears in Figure 3.11, for the NEDC (which is the main focus in the thesis), the SOC constraints are never active (the unconstrained strategy does not violate it). To illustrate the usefulness of the interior penalty approach in the presence of active state constraints, another driving cycle, for which the constraint $\xi(t) \geq \xi_{min}$ is active, is

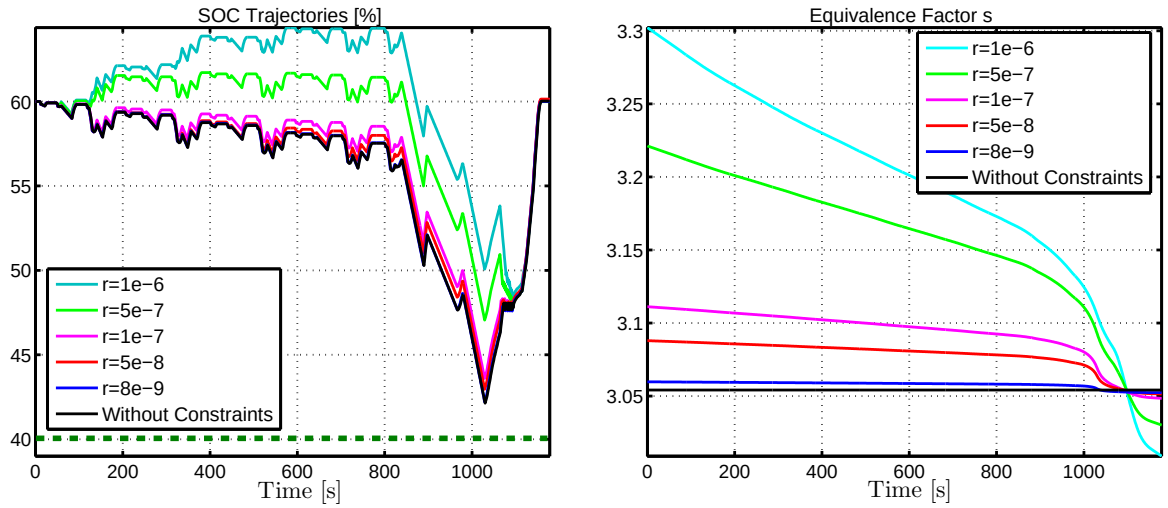

Figure 3.11: Optimal SOC [%] trajectories (left) and s trajectories (right) for NEDC in the constrained case

Table 3.3: $J_0(u_0^r)$ [L/100 km] for NEDC in the constrained case

r	$J_0(u_0^r)$	$100 \cdot \min(\xi(t) - \xi_{min})$
$1e^{-6}$	4.48	8.23
$5e^{-7}$	4.45	7.05
$1e^{-7}$	4.41	3.59
$5e^{-8}$	4.402	2.95
$8e^{-9}$	**4.39**	**2.21**
Without constraints	**4.385**	/

considered. This new cycle is a combination of two driving cycles: FHDS (federal highway driving cycle) and NEDC. The wheel speed and the gear-box ratio (for the thermal mode) for this new cycle are given in Figures 3.12. The weight r is initialized with $r_0 = 5 \cdot 10^{-7}$. The obtained solutions (for decreasing values of r) are compared to the solution without state constraints in terms of fuel consumption in Table 3.4.

Plots of Figure 3.13 report the SOC and its associated equivalence factor s trajectories in the unconstrained case and for decreasing values of r. The behavior of the SOC when r tends to zero has the same tendency as for the NEDC: $\xi(t)$ approaches the state constraints from the interior. When r tends to zero, the minimum distance between the SOC and its lower bound decreases and after a certain threshold of r for which $\xi(t)$ is very close to ξ_{min}, a jump in the value of the equivalence factor s appears.

The results given in Table 3.4 show that the difference in fuel consumption for different values of r is less than 2% compared to the control strategy without constraints. It is relevant to note that having *an acceptable* distance from the state constraint does not cause a substantial impact on fuel consumption (this remark is discussed in Section 5.9 from a theoretical viewpoint).

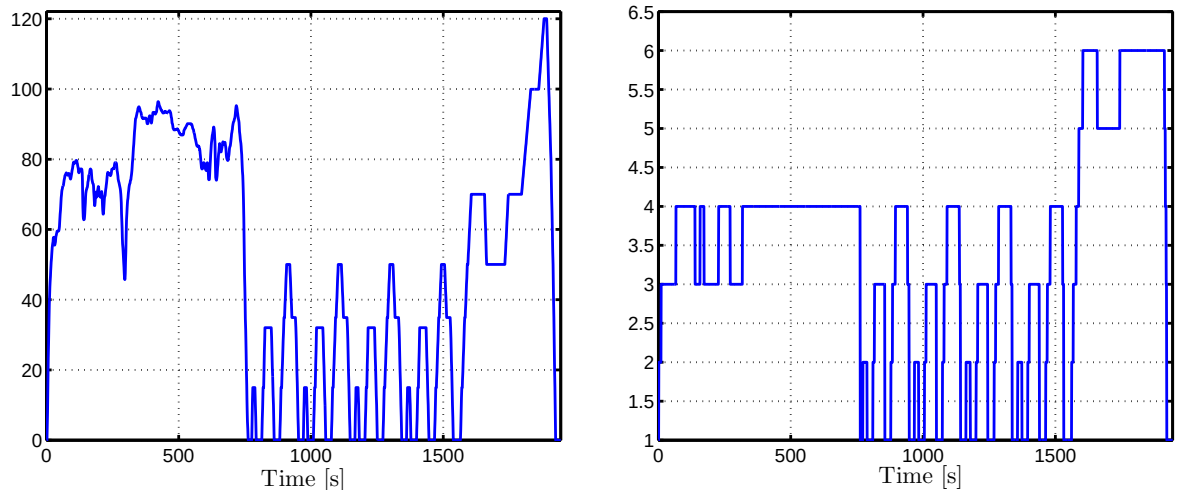

Figure 3.12: Wheel speed [km/h] (left) and gear-box ratio (right) for the combined cycle

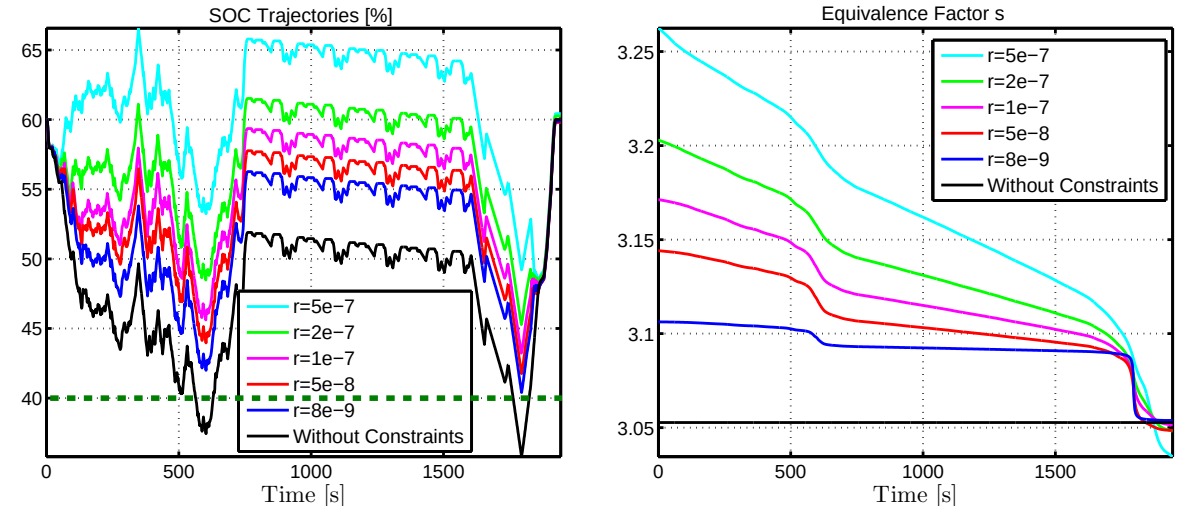

Figure 3.13: Optimal SOC [%] trajectories (left) and s trajectories (right) for the combined cycle in the constrained case

Table 3.4: $J_0(u_0^r)$ [L/100 km] for the combined cycle in the constrained case

r	$J_0(u_0^r)$	$100 \cdot \min(\xi(t) - \xi_{min})$
$5e^{-7}$	4.85	8.23
$2e^{-7}$	4.83	5.27
$1e^{-7}$	4.80	3.22
$5e^{-8}$	4.78	1.75
$8e^{-9}$	**4.76**	**0.27**
Without constraints	**4.75**	/

3.5 Conclusion

In this chapter, the single-state energy management problem for a parallel hybrid electric vehicle aiming at minimizing the fuel consumption has been addressed and formulated as an OCP. The obtained OCP has been solved using the PMP and the control strategy has

been extended to include instantaneous state constraints on the SOC by using the interior penalty approach. The obtained control strategies depend on the prescribed driving cycle and they can be used as a reference of comparison for real-time strategies.

It is to be noted that optimal solutions does not reach the state constraints. So, they will now be left-out from the discussion.

Chapter 4

Optimal EMS including thermal dynamics

Chapitre 4 Dans la plupart des études sur la gestion d'énergie pour un véhicule électrique hybride, la consommation du carburant du moteur thermique représente la fonction coût à minimiser. L'état de charge de la batterie (SOC) est généralement la seule variable d'état considérée dans l'optimisation. Récemment, et pour des raisons pratiques, étendre un tel problème d'optimisation en considérant des nouvelles fonctions coût (émissions polluantes, vieillissement de la batterie ou toute combinaison de ceux-ci) et des variables d'état supplémentaires (températures du moteur, de la batterie et du système de dépollution) a suscité un grand intérêt de la part de la communauté scientifique. Ces extensions augmentent le niveau de complexité des problèmes d'optimisation ainsi que le temps nécessaire pour les résoudre, quel que soit la méthode numérique utilisée [34]. Dans ce chapitre, une extension de l'EMS mono-état, décrit dans le chapitre 3, pour réduire les émissions polluantes en incluant les températures du moteur et du système de post-traitement est présentée et discutée.

Contents

In most studies investigating optimal energy management problems for HEV, the fuel consumption over a fixed time window corresponding to a given driving cycle is the cost function to be minimized. The battery SOC is usually the only state variable considered because of the final constraint reflecting the charge-sustaining or depleting operations. Recently, and for practical reasons, extending such optimization problem by considering new cost functions (pollutant emissions, battery aging or any combination thereof) and additional state variables (engine, battery and the after-treatment system temperatures) has attracted interest from researchers. These extensions, while interesting in terms of their application, significantly raise the level of complexity of the optimization problem and thereby increase the time needed to solve it offline, regardless the numerical methods used [34].

In this chapter, a possible extension of the single-state EMS (presented in Chapter 3) by including engine and after-treatment system temperatures is presented and discussed.

4.1 State of the art

4.1.1 Engine temperature

One frequent but unstated (hidden) assumption in numerous studies dealing with EMS for HEV is that the engine is at thermal equilibrium. However, from an engine modeling viewpoint, engine temperature is an important factor that influences both the fuel consumption and the pollutant emissions [39]. A low powertrain temperature has a negative impact on fuel consumption and transmission efficiency. These are due to the higher frictional losses in the engine resulting from increased hydrodynamic viscosity effects together with the need for a richer air-fuel mixture to overcome poor combustion [3, 59, 83]. These problems are particularly true for HEV, as the engine is subject to stop-start phases, and its temperature may drop. On the pollutant side, the after-treatment system is only activated beyond a catalyst temperature threshold, and its efficiency is relatively poor at low temperatures. For these reasons, it seems necessary to quantify the benefits of including engine temperature in EMS, aiming at minimizing fuel consumption.

Little recent researches have been conducted with the aim of including thermal states in the optimization problem formulation of EMS: these are referred to as thermal management systems [43, 55, 81]. The study in [43] was a first attempt to include engine temperature dynamics in the optimization problem and to quantify the corresponding gain in terms of fuel consumption. [55] presented a general framework for optimal energy-thermal management in which optimal strategies based on PMP were compared with heuristic rule-based strategies. Very promising benefits in fuel economy and reduction of pollutant emissions were reported. The PMP solution outperforms the tested heuristic strategy of 6% in fuel economy for a warm-start cycle. For a cold-start cycle, the benefit of the PMP was 4.5%. If emissions are considered, about 20% reduction was obtained with the PMP in a cold-start cycle.

Works in [87, 88] described a study of the effect of engine temperature on the fuel consumption for conventional and hybrid vehicles with cold and warm start. One of the

main conclusions relevant to the hybrid vehicle studied was that the optimal controls calculated for a warm engine start and a cold engine start were so similar that the difference in fuel consumption could not be quantified.

4.1.2 After-treatment system temperature

The design of an EMS aimed at minimizing fuel consumption can also be extended to take the pollutant emissions into account, since minimizing the fuel consumption does not directly ensure pollutant emissions reduction. The emission rate not only depends on the engine operating point (load and speed), but also on the engine and catalyst temperatures. The catalyst temperature is an important factor because:

- the catalyst is activated only beyond a certain threshold temperature, while its efficiency is relatively poor at low temperatures (see Figure 4.2);
- as the engine can be turned off for varying durations, engine and catalyst temperatures may decrease, which can significantly increases the pollutant emissions out of the after-treatment system.

To properly manage this situation, the optimization should include a new thermal state (catalyst temperature) in addition to the SOC and the engine temperature, and that requires a third adjoint variable associated to the catalyst temperature.

Only few studies have included the catalyst temperature θ_c in the calculation of an EMS aiming at minimizing a trade-off between fuel consumption and pollutant emissions. In [15, 55, 81], PMP-based optimization techniques, including three-way catalyst converter dynamics with emissions as objective, were presented along with numerical comparisons. In [57, 58], the integration of the three-way catalyst converter in a gasoline-HEV EMS was discussed using numerical comparisons between three control strategies, and a simplified control model to reduce NO_x emissions was suggested. The missing point in these studies is the comparison of the proposed solution to the optimal solution of the multi-state problem (two or three state variables).

In this chapter, we present a possible extension of the single state EMS to account for the CO emissions. This extension includes thermal dynamics of the engine and the after-treatment system. The associated three-states optimization problem is solved. After, a trade-off between model complexity and the optimality of the solutions is analyzed.

4.2 Model with thermal dynamics

The HEV is considered to be equipped with an after-treatment system. Four pollutants are regulated in accordance with the current standards: hydrocarbons (HC), carbon monoxide (CO), nitrogen oxides (NO_x), and particulate matter (PM). Since the HEV has a gasoline engine, the critical pollutants are mostly CO and HC. NO_x emissions and particulate matter are less crucial in gasoline engines. The choice of CO emissions in the cost function is not restrictive, the same approach can be applied to other pollutant emissions.

4.2.1 Impact of thermal variables on the cost function

The cost function (4.1) to be minimized is a weighted sum of the fuel consumption rate and the CO emission rate out of the after-treatment system, over a fixed time window

corresponding to a driving cycle of a duration T:

$$J_2(u) = \int_0^T [(1-\alpha) \cdot c_f(u,t,\theta_e) + \alpha \cdot m_{CO}(u,t,\theta_e,\theta_c)]dt, \tag{4.1}$$

where $0 \leq \alpha \leq 1$ is a weighting factor for adjusting the relative importance of the two quantities $c_f(.)$ and $m_{CO}(.)$, θ_e is the engine temperature and θ_c is the after-treatment system temperature. The time variable t accounts for the dependence of the fuel consumption on the engine speed related to the wheel speed, which is assumed to be tracked.

The quantity $c_f(u,t,\theta_e)$ is the fuel consumption rate when the engine is cold. It can be written as

$$c_f(u,t,\theta_e) = c(u,t)e(\theta_e), \tag{4.2}$$

where the function $c(.)$ is the fuel consumption rate for a warm engine. The correction

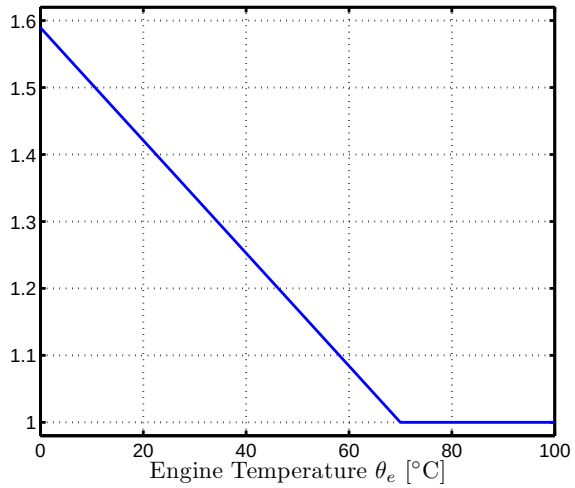

Figure 4.1: Correction factor of fuel consumption

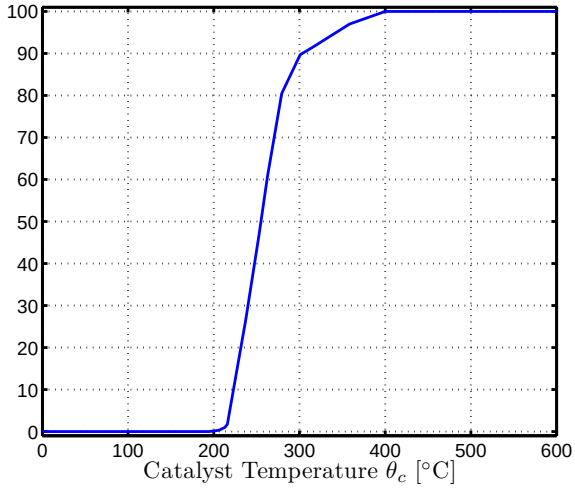

Figure 4.2: Catalyst conversion efficiency [%]

factor $e(\theta_e)$ of the fuel consumption with respect to θ_e is a decreasing function, always greater or equal to one. It represents an extra-consumption factor that takes into account the increase of friction and, as a consequence, the increase of fuel injected per cycle at low temperatures. In the case of a warm engine, $e(\theta_e) = 1$. This function can be any decreasing (not necessarily smooth) function with asymptotic value of one. The simple form shown in Figure 4.1 has been extracted from engine control maps given by car manufacturers.

Similarly, the emission rate of CO out of the after-treatment system $m_{CO}(.)$ is of the form

$$m_{CO}(u,t,\theta_e,\theta_c) = m_{CO,h}(u,t) \cdot e_{CO}(\theta_e) \cdot (1 - \eta_{CO}(\theta_c)),$$

where $m_{CO,h}$ is the emission rate out of the engine when the engine is warm, given by a quasi-steady map as a function of the engine speed and the engine torque. The correction factor $e_{CO}(.)$ is a decreasing function of θ_e and is always greater or equal to one (it is similar to e given in Figure 4.1). The quantity η_{CO} is the after-treatment conversion efficiency for CO emissions, which depends on the catalyst temperature θ_c (see Figure 4.2).

4.2.2 Dynamics

In addition to the dynamics of the SOC given by equation (3.2), the engine temperature θ_e, and the after-treatment system temperature (ATS) θ_c must be taken into account.

4.2.2.1 Engine temperature

The variable θ_e represents the coolant temperature. A typical ICE cooling system consists of a thermostat, a coolant temperature sensor, a radiator, and a coolant circulation pump [41]. An engine cooling system can be viewed as an energy storage device comprising the coolant, the engine oil and the engine block. The energy level can be expressed as the temperature of the system. There is typically one source of energy (i.e., combustion energy) and several forms of energy loss. A part of the combustion energy produces engine power and the remaining part is transferred to the ambient air, the engine block, the oil and the engine coolant. The energy transfers take place in the different engine subsystems can described as follows: the engine converts a significant part of the fuel power (P_{f}) (i.e., chemical energy flux) into an effective mechanical power (P_{eng}), whereas another part leaves the engine in the form of exhaust gases ($P_{\text{th,exh}}$) and convection in the ambient air ($P_{\text{th,out}}$) [26, 87]. $P_{\text{th,aux}}$ represents the power drained by the auxiliaries (considered to be constant in our case).

The heat losses from the engine block to the ambient air stem mainly from convective heat transfer; therefore, the radiation and the conduction heat transfer mode can be neglected [41], leading to

$$P_{\text{th,out}} = G_e \cdot (\theta_e - \theta_0),$$

where G_e is an equivalent conductance (the inverse of a resistance) and θ_0 is the ambient temperature. Defining an equivalent engine temperature θ_e, an energy balance across the system yields

$$C_e \frac{d\theta_e}{dt} = P_{\text{comb}} - P_{\text{th,out}} - P_{\text{th,aux}} - P_{\text{th,exh}} - P_{\text{eff}},$$

where C_e is an equivalent thermal capacity. This equation can be written in the form [55]

$$C_e \frac{d\theta_e}{dt} = P_{\text{th,e}}(u, t, \theta_e) - G_e \cdot (\theta_e - \theta_0) - P_{\text{th,aux}},$$

where the term $P_{\text{th,e}} = P_{\text{comb}} - P_{\text{th,exh}} - P_{\text{eff}}$ represents the sum of friction power dissipated into heat and thermal power transferred from the engine to the coolant, and is given by a look-up table as a function of the speed, the torque and the temperature of the engine. The external cooling system (thermostat) is not modeled here; rather, the temperature θ_e is considered to be limited by a maximum value θ_w, at which the thermostat is activated.

To simplify the notation, the dynamics of θ_e considering a given initial condition θ_0 is written as

$$\frac{d\theta_e}{dt} = g(u, t, \theta_e), \quad \theta_e(0) = \theta_0. \tag{4.3}$$

4.2.2.2 Catalyst temperature

The variable θ_c represents the (spatially averaged) catalyst temperature [25, 81]. The considered model is a zero-dimensional model based on physical equations. Figure 4.3 shows a simplified heat transfer balance taking place in the after-treatment system.

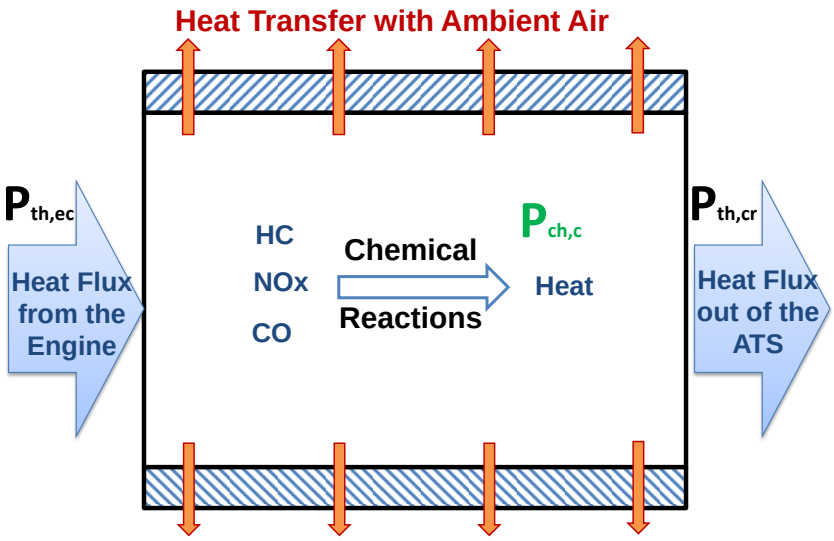

Figure 4.3: Energy flows in the after-treatment system (ATS)

Based on the energy balance presented above, the after-treatment system temperature variation can be written as

$$C_c(\theta_c) \cdot \frac{d\theta_c}{dt} = P_{th,ec} - P_{th,cr} - G_c \cdot (\theta_c - \theta_0) + P_{ch,c},$$

where C_c is an equivalent thermal capacity of the catalyst depending on θ_c, G_c in an equivalent conductance of the catalyst and θ_0 is the ambient temperature. The term $G_c \cdot (\theta_c - \theta_0)$ represents the heat flux exchanged with ambient air (mainly governed by convection). The term $P_{ch,c}$ is the rate of heat released by the chemical reactions. It depends on θ_e and θ_c as presented in [55]

$$P_{ch,c} = -\sum_j h_j \cdot \eta_j(\theta_c) \cdot m_{j,h}(u,t) e_j(\theta_e),$$

where $j = \{CO, HC, NOx\}$, and h_j is the heat generated (enthalpy) by the oxidation of the j^{th} pollutant. The quantity $m_{j,h}$ is the emission rate out of the engine for each j and it is given by a look-up table as a function of the engine speed and torque. The correction factors e_j have the same form as $e(.)$ given in Figure 4.1. The term $P_{th,ec}$ is the heat flux (enthalpy) from the engine to the after-treatment system, and $P_{th,cr}$ is the heat flux (enthalpy) out of the after-treatment system. These quantities are defined by [25]

$$\begin{aligned} P_{th,ec} &= m_{exh} \cdot c_{exh}(\theta_{exh}) \cdot \theta_{exh}, \\ P_{th,cr} &= m_{exh} \cdot c_c(\theta_c) \cdot \theta_c, \\ m_{exh} &= c_f(u,t,\theta_e) \cdot (\frac{AFR_{st}}{\phi} + 1), \end{aligned}$$

where AFR_{st} is the Air/Fuel Ratio of a stoichiometric mixture; ϕ is the equivalence ratio, and c_{exh} and c_c are the specific heat capacities, which are functions of the catalyst temperature θ_c and the gas temperature at the input of the after-treatment system, denoted by θ_{exh} respectively [55]. This latter temperature equals the exhaust temperature gas and is given by a static map of the engine speed and the engine torque.

In order to simplify the notations, the dynamics of θ_c considering a given initial condition $\theta_{c,0}$ is written as

$$\frac{d\theta_c}{dt} = k(u, t, \theta_e, \theta_c), \quad \theta_c(0) = \theta_{c,0}. \tag{4.4}$$

4.2.3 Constraints

The control u is constrained to belong to U^{ad} defined by the relation (3.4).

4.2.4 OCP summary

In summary, the OCP, denoted by (OCP_2), is defined

$$(OCP_2) \quad \min_{u \in U^{ad}} J_2(u),$$

under the boundary constraint (3.3), the dynamics (3.2, 4.3, 4.4) and U^{ad} is defined in equation (3.4). The corresponding optimal strategy is denoted by (S_2).

When $\alpha = 0$, only the fuel consumption is minimized and the catalyst temperature θ_c is neglected from the optimization problem. This case is detailed in Appendix B.

4.3 PMP solution and numerical solving

The Hamiltonian H_2 is defined by

$$H_2(u, t, \theta_e, \theta_c, \lambda, \mu, \rho) = L(u, t, \theta_e, \theta_c) + \lambda f(u, t) + \mu g(u, t, \theta_e) + \rho k(u, t, \theta_e, \theta_c), \tag{4.5}$$

where λ, μ, ρ are the adjoint variables associated to ξ, θ_e and θ_c respectively, and L is given by

$$L(u, t, \theta_e, \theta_c) = (1 - \alpha) \cdot c(u, t, \theta_e) + \alpha \cdot m_{CO}(u, t, \theta_e, \theta_c).$$

The adjoint states $\lambda(t)$, $\mu(t)$ and $\rho(t)$ are defined by

$$\begin{cases} \dfrac{d\lambda}{dt} = -\dfrac{\partial H_2}{\partial \xi} = 0, \\ \dfrac{d\mu}{dt} = -\dfrac{\partial H_2}{\partial \theta_e} = -\dfrac{\partial L}{\partial \theta_e}(u_2^*, t, \theta_e, \theta_c) - \mu \dfrac{\partial g}{\partial \theta_e}(u_2^*, t, \theta_e) - \rho \dfrac{\partial k}{\partial \theta_e}(u_2^*, t, \theta_e, \theta_c), \\ \dfrac{d\rho}{dt} = -\dfrac{\partial H_2}{\partial \theta_c} = -\dfrac{\partial L}{\partial \theta_c}(u_2^*, t, \theta_e, \theta_c) - \rho \dfrac{\partial k}{\partial \theta_c}(u_2^*, t, \theta_e, \theta_c), \end{cases} \tag{4.6}$$

with

$$\mu(T) = 0, \ \rho(T) = 0, \tag{4.7}$$

since the final temperatures $\theta_e(T)$ and $\theta_c(T)$ are free and the final time T is fixed. On the other hand, the final value of λ is not constrained since the final SOC is fixed.

If u_2^* is an optimal control, then, for every t, $u_2^*(t)$ minimizes the Hamiltonian in the set defined by (3.4) along the optimal states and corresponding adjoint states trajectories

$$u_2^* \in \arg\min_{u \in U^{ad}} H_2(u, t, \theta_e, \theta_c, \lambda, \mu, \rho). \tag{4.8}$$

Equations (3.2, 3.3, 4.6, 4.7, 4.8) constitute a TPBVP. Many numerical methods can be used to solve this TPBVP. Among these are Dynamic Programming (DP), which in our case leads to numerical difficulties and memory-management issues, due to the grid size of three-dimensional state variables.

To solve our TPBVP, the collocation method could be employed. It is implemented in Matlab through the routines `bvp4c` and `bvp5c` [82]. It appears that solving this problem with these routines leads to numerical instabilities and the solutions they produce are not sufficiently accurate. Therefore, a specifically tailored single shooting-related method is used.

Classically, the idea of this algorithm is to consider the initial conditions of the adjoint states (λ_0, μ_0, ρ_0) as unknown variables and the vector function which associates $[\xi(T) - \xi(0)]$, $\mu(T)$ and $\rho(T)$ to $(\lambda_0, \mu_0, \rho_0)$

$$
\begin{cases}
\dfrac{d\xi}{dt} = f(u_2^*, t), \quad \xi(0) = \xi_0, \\
\dfrac{d\theta_e}{dt} = g(u_2^*, t, \theta_e), \quad \theta_e(0) = \theta_{e,0}, \\
\dfrac{d\theta_c}{dt} = k(u_2^*, t, \theta_e, \theta_c), \quad \theta_c(0) = \theta_{c,0}, \\
\dfrac{d\lambda}{dt} = 0, \quad \lambda(0) = \lambda_0, \\
\dfrac{d\mu}{dt} = -\dfrac{\partial L}{\partial \theta_e}(u_2^*, t, \theta_e, \theta_c) - \mu \dfrac{\partial g}{\partial \theta_e}(u_2^*, t, \theta_e) - \rho \dfrac{\partial k}{\partial \theta_e}(u_2^*, t, \theta_e, \theta_c), \quad \mu(0) = \mu_0, \\
\dfrac{d\rho}{dt} = -\dfrac{\partial L}{\partial \theta_c}(u_2^*, t, \theta_e, \theta_c) - \rho \dfrac{\partial k}{\partial \theta_c}(u_2^*, t, \theta_e, \theta_c), \quad \rho(0) = \rho_0.
\end{cases}
$$

Then, the problem is re-cast into finding zeros of this function from $\mathbb{R}^3$ into $\mathbb{R}^3$. This is achieved using Newton's method implemented in the popular `fsolve` Matlab function. The solution given by `bvp4c` (which is not accurate enough, as noted above) is used to initialize the `fsolve` algorithm.

Due to the absence of analytical expressions of the cost function and some variables which are involved in the state dynamics, u_2^* is determined as follows: first, u is discretized into a finite number of possible values (a grid) satisfying the condition (3.4). Then the Hamiltonian H_2 is evaluated for each value and the one minimizing H_2 is taken as an optimal value for u. From a theoretical viewpoint, this approach is consistent with the fact that PMP is applicable in the case of discrete input control. However, a good mesh of possible values must be considered to reach a good level of performance.

Implementing such a method requires special care in the present situation. In particular, the discrete nature of the set for which the control is sought after makes it quite risky to rely on automatic finite difference schemes (that are usually very convenient in other situations) to calculate the Jacobian matrix. If the value of the finite difference parameter is set too small, the estimated derivatives are simply zero, as no change is seen in the function. If it is set too high, then the estimate is biased by second-order terms. For these reasons, the finite difference parameter was carefully tuned.

4.4 Simplified strategies

Two simplifications are now considered. They are based on simplifying the factors $e(.)$, $e_{CO}(.)$ and $\eta_{CO}(.)$. When the two simplifications are used, one gets back to an OCP covering the OCP of Chapter 3.

4.4.1 First simplification

The first simplification is to assume that the engine is warm and its temperature θ_e is always greater than $\theta_h = 80$ °C. This assumption is equivalent to neglecting the influence of θ_e in the case of a cold-start of the engine. This can be formulated as

$$e_{CO}(\theta_e) = 1, \ e(\theta_e) = 1.$$

The cost function, in this case, becomes

$$J_1(u) = \int_0^T \left[(1-\alpha)c_h(u,t) + \alpha m_{CO,h}(u,t)(1-\eta_{CO}(\theta_c))\right] dt.$$

As J_1 is independent of θ_e, only the dynamics of the SOC and θ_c (two states instead of three considered earlier) have to be considered in the optimization problem with the final constraint on the SOC (3.3). In summary, the OCP, denoted by (OCP_1), is

$$(OCP_1) \quad \min_{u \in U^{ad}} J_1(u),$$

under the boundary constraint (3.3), the dynamics (3.2, 4.4) and U^{ad} is defined in equation (3.4). The control strategy obtained from (OCP_1) is denoted by (S_1). The Hamiltonian H_1 associated to (OCP_1) is given by

$$H_1(u,t,\theta_c,\lambda,\rho) = (1-\alpha)c_h(u,t) + \alpha m_{CO,h}(u,t)(1-\eta_{CO}(\theta_c)) + \lambda f(u,t) + \rho k(u,t,\theta_h,\theta_c).$$

This formula can be derived from the expression of H_2 as follows

$$H_1(u,t,\theta_c,\lambda,\rho) = H_2(u,t,\theta_e = \theta_h,\theta_c,\lambda,\mu(t) = 0,\rho).$$

4.4.2 Second simplification

Another possible simplification is to assume that the catalyst is never activated and its efficiency η_{CO} is zero. In this case, the cost function is

$$J(u) = \int_0^T \left[(1-\alpha)c_h(u,t) + \alpha m_{CO,h}(u,t)\right] dt.$$

This simplification is equivalent to minimizing the CO emissions out of the engine. On the other hand, assuming that the catalyst is activated (its efficiency is $\eta_{CO} = 1$) would lead to a cost function depending only on the fuel consumption rate and no reduction of pollutant emissions can be considered.

As the fuel consumption and the pollutant emissions are both independent of θ_c, the number of state variables is reduced from two to one. Only the dynamics of SOC, given

by (3.2), has to be considered with the final constraint (3.3). In summary, the OCP, denoted by (OCP), is

$$(OCP) \quad \min_{u \in U^{ad}} J(u),$$

under the boundary constraint (3.3), the dynamics (3.2) and U^{ad} is defined in equation (3.4). This OCP, in the case $\alpha = 0$, is equivalent to the OCP described in Chapter 3. The control strategy obtained from (OCP) is denoted by (S). The Hamiltonian H associated to the (OCP) is given by

$$H(u, t, \lambda) = (1 - \alpha)c_h(u, t) + \alpha m_{CO,h}(u, t) + \lambda f(u, t).$$

This formula can be derived from the expression of H_1 as follows

$$H(u, t, \lambda) = H_1(u, t, \theta_c = \theta_{c,0}, \lambda, \rho(t) = 0).$$

4.4.3 Heuristics strategies

For completeness, two additional heuristic strategies from the literature are considered.

- The first strategy, noted by (HS_2), is a pseudo-solution of the OCP_2 where $\mu(t) \equiv \rho(t) \equiv 0$ are imposed in the Hamiltonian H_2 (see [55]). The only unknown variable λ is determined to satisfy the final constraint on ξ.
- The second strategy, noted by (HS_1), is the strategy suggested in [57, 58]: the impact of the engine temperature on the fuel consumption and the CO emissions is neglected (which is equivalent to assuming that the engine is warm and $\mu(t) \equiv 0$) and $\rho(t)$ is set to zero in the Hamiltonian H_1. The only unknown variable λ is determined to satisfy the final constraint on ξ.

All these strategies are summarized in Table 4.1. The unknown which must be determined and the formula synthesizing the control law are detailed. The nature of the solution (optimal or heuristic) is also reported.

Table 4.1: Control strategies description

Strategy	Unknown	Control	Opt/Heur
(S_2)	3 (λ, μ, ρ)	$u_2^*(t) = \arg\min_{u \in U^{ad}} H_2(u, t, \theta_e, \theta_c, \lambda, \mu, \rho)$	Opt.
(S_1)	2 (λ, ρ)	$u_1^*(t) = \arg\min_{u \in U^{ad}} H_1(u, t, \theta_c, \lambda, \rho)$	Opt.
(S)	1 (λ)	$u^*(t) = \arg\min_{u \in U^{ad}} H(u, t, \lambda)$	Opt.
(HS_2)	1 (λ)	$u_2^h(t) = \arg\min_{u \in U^{ad}} H_2(u, t, \theta_e, \theta_c, \lambda, \mu(t) \equiv 0, \rho(t) \equiv 0)$	Heur.
(HS_1)	1 (λ)	$u_1^h(t) = \arg\min_{u \in U^{ad}} H_1(u, t, \theta_c, \lambda, \rho(t) \equiv 0)$	Heur.

4.5 Numerical results

For the comparison between the different strategies, the simulation of the control strategies are carried out using the full model (3.2, 4.3, 4.4) with cold start conditions.

4.5.1 System parameters

The engine parameters are listed in Table 4.2. The correction factor $e(\theta_e)$ is given by

$$e(\theta_e) = \begin{cases} -a_0\theta_e + b_0, \ \theta_c \leq \theta_e \leq \theta_w, \\ 1, \ \theta_e > \theta_w, \end{cases}$$

where a_0 and b_0 are positive constants that have been identified from experimental data. Similarly, the correction factor $e_{CO}(.)$ is approximated by

$$e_{CO}(\theta_e) = \begin{cases} -a_1\theta_e + b_1, \ \text{if } \theta_c \leq \theta_e \leq \theta_w, \\ 1, \ \text{if } \theta_e > \theta_w, \end{cases}$$

where a_1 and b_1 are positive constants. Look-up tables for CO emissions $m_{CO,h}$ and the exhaust temperature θ_{exh} are given in Figures 4.4 and 4.5, respectively. They are derived from experimental engine tests. The after-treatment system parameters are listed in Table 4.3.

Table 4.2: Engine parameters

Parameter	Value
a_0	0.0084 [° C]$^{-1}$
b_0	1.59
C_e	10^5 J/kg
G_e	14.3 s^{-1}
θ_w	70 °C
θ_c	−30 °C

Table 4.3: After-treatment system parameters

Parameter	Value
a_1	0.0126 [°C]$^{-1}$
b_1	1.8842
C_c	5355 J/kg
G_c	0.30 s^{-1}
θ_{act}	200 °C
AFR_{st}	14.5

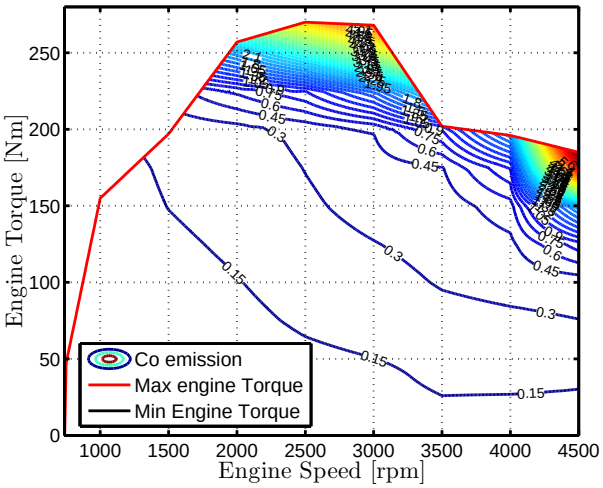

Figure 4.4: CO map $m_{CO,h}$ [g/s]

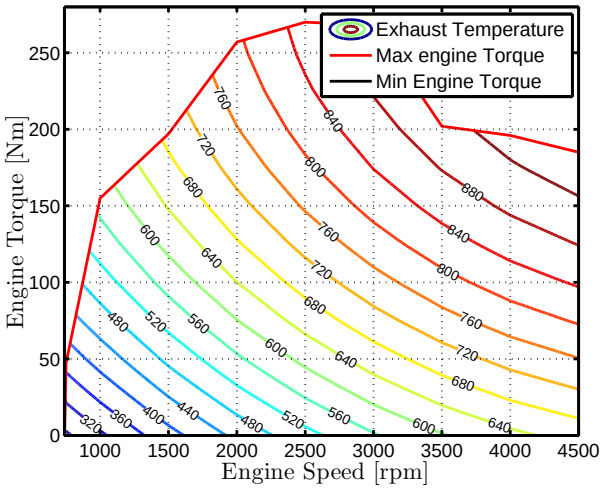

Figure 4.5: Exhaust temperature map θ_{exh} [°C]

4.5.2 Results

To ease the reading, the engine and the catalyst temperatures trajectories for $\alpha = 0.8$, simulated using all the strategies described above, are given in Figures 4.6 and 4.7, respectively. From Figure 4.6, the engine temperature trajectories for the three strategies

(S_2, S_1, S) remain close whereas the engine temperature trajectories are little further from the optimal trajectory when the strategies (HS_2, HS_1) are employed. Figure 4.7 shows that the optimal control u_2^* improves the catalyst efficiency by warming it up promptly, which decreases the pollutant emissions out of the catalyst. The price to be paid for achieving this improvement is increased fuel consumption due to greater use of the engine.

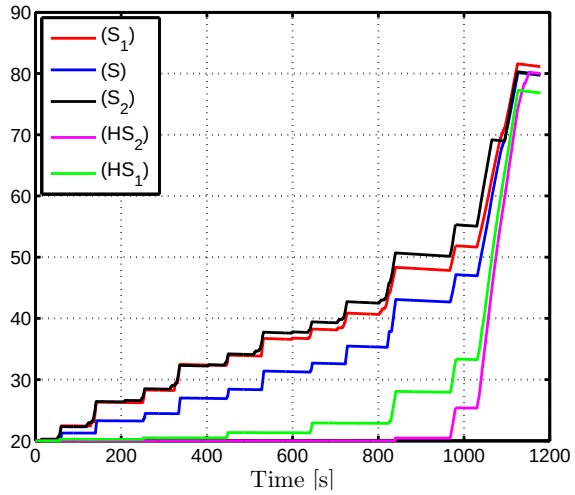

Figure 4.6: Histories of simulated engine temperature θ_e [°C] obtained from optimal input calculated for $\alpha = 0.8$

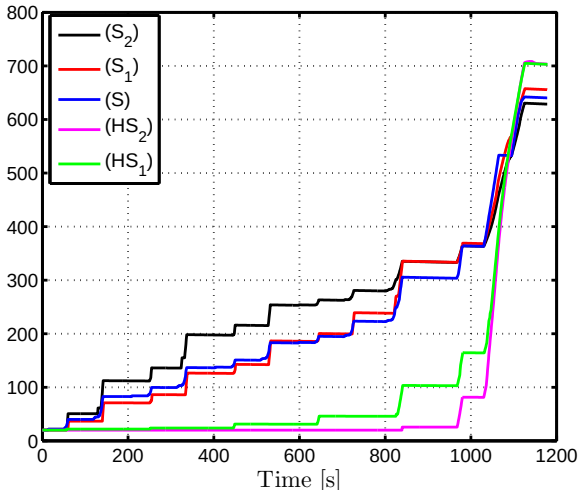

Figure 4.7: Histories of simulated catalyst temperature θ_c [°C] obtained from optimal input calculated for $\alpha = 0.8$

Another remark is that the strategies (HS_2, HS_1) in the first part of the driving cycle use only the electric machine by discharging the battery. Due to the final constraint on the SOC for the charge-sustaining operation, these two control strategies are forced to use the engine in order to bring the final SOC at the end of the driving cycle to its desired value.

Figure 4.8 details the variation of the fuel consumption as a function of CO emissions for various values of α. For each control strategy, each point is obtained as follows: the value of α is fixed and the strategies (S_2, S_1, S, HS_2, HS_1) are simulated. The corresponding fuel consumption and CO emissions are presented.

As Figure 4.8 shows it, the five strategies allow the reduction of CO emissions below 1 g/km (which corresponds to the European norm Euro 6 for CO emissions); the main difference between them lies in the fuel consumption. The solutions corresponding to the strategies (S_2), (S_1) and (HS_2) agree very close in terms of CO emissions reduction. To further reduce CO emissions using strategies (S, HS_1), the value of α must be increased (recalling that when α in increased, more importance is given to CO emissions in the cost function) at the expense of increased fuel consumption.

Note that the decrease of CO emissions is not obtained by deteriorating combustion efficiency (ignition timing advance) as it is done in common strategies used for conventional vehicles to satisfy the European norm requirements (this solution lowers the engine performance in order to send more heat to the exhaust). The only degree of freedom used here is the torque split between the engine and the electric machine.

Figure 4.8 shows that the single state models corresponding to the strategies (S, HS_2, HS_1) satisfy the requirements of the European norm Euro 6, but the difference in the fuel

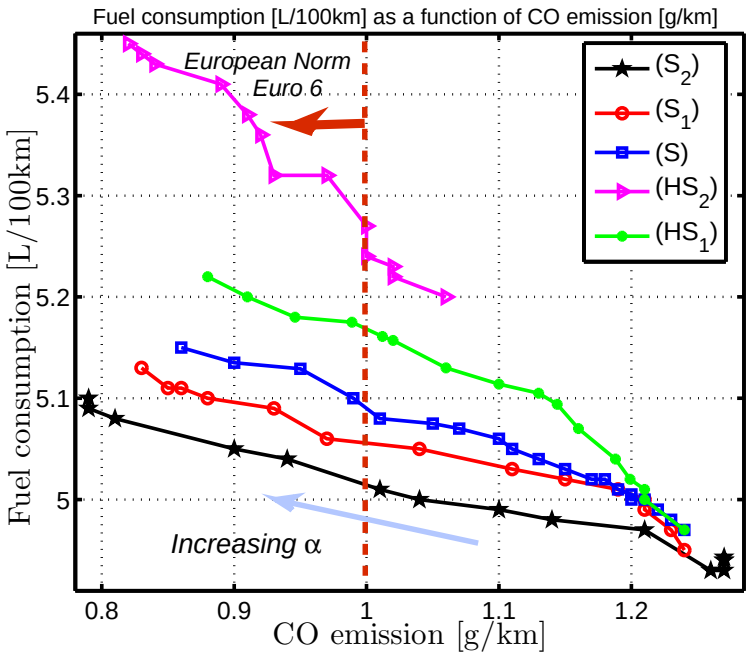

Figure 4.8: Optimal fuel consumption [L/100 km] as a function of CO emissions [g/km] for NEDC

consumption is relatively negligible only for the strategy (S):

- Strategy (HS_2) is far from the optimal fuel consumption (the difference is more than 5%).
- Strategy (HS_1) is close to the optimal fuel consumption (sub-optimality is less than 2%).
- Strategy (S) is better than strategy (HS_1) suggested in [57, 58] as it gives a quasi-optimal fuel consumption compared to the optimal strategy.

Therefore, the single-state strategy (S) is a promising candidate to generate a control trajectory which satisfies the European norm Euro 6 for the CO emissions, with close-to-optimal fuel consumption. The simplified model used in this strategy will serve as a benchmark for finding a suitable real-time energy management strategy. For example, the ECMS as it is presented in the literature can be used to solve this single-state problem.

The European norms have been evaluated for the NEDC. Similar analysis and additional numerical results are given in Appendix C for other four driving cycles. These numerical results support the suggested simplification for EMS calculation.

4.6 Conclusion

In this chapter, an extension of the energy management problem aiming at minimizing fuel consumption has been considered to include pollutant emissions reduction. This extension requires the introduction of the engine and the after-treatment system temperatures. The corresponding OCP has been solved using the PMP, and the obtained results have been discussed.

The complexity of the model used to calculate optimal strategies minimizing a trade-off between fuel consumption and CO emissions is analyzed. The presented numerical results show that the single-state model, considering only the SOC dynamics, is actually sufficient to calculate control trajectories allowing the CO emissions to be reduced with an acceptable extra-fuel consumption compared to the three-states optimal strategy.

Interestingly, similar conclusions have been made in studies focussed on other objectives in [63, 76], where the authors have quantified the impact of battery temperature θ_{bat} on the EMS, aiming at minimizing a trade-off between fuel consumption and battery aging [80]. The comparison in [76] of single state (SOC only) vs. two states (SOC + θ_{bat}) solutions has shown that the first solution is sufficient in most cases, the exception being battery aging minimization.

Part II

Theoretical aspects of model reduction in optimal control
Aspects théoriques de la réduction de modèle dans les problèmes de commande optimale

Chapter 5

Perturbation in optimal control under input constraints

Chapitre 5 Dans ce chapitre, nous discutons quelques résultats généraux sur les perturbations régulières dans les problèmes de contrôle optimal sous contrainte de commande suite aux études sur la gestion de l'énergie décrites dans le chapitre 4. L'objectif était de quantifier l'apport de la prise en compte des températures (du moteur et du système de post-traitement) dans la minimisation de la consommation de carburant et les émissions polluantes. En se basant sur les résultats présentés dans [45], l'effet de la température du moteur peut être ignorée de ce problème. Le résultat général établi dans ce chapitre explique ces observations numériques. Plus précisément, les perturbations du grandeur ε apparaissant dans le coût et la dynamique conduisent à une sous-optimalité d'ordre $O(\varepsilon^2)$ sur le coût optimal.

Contents

Following our studies on the energy management system described in Chapter 4, we develop here some general results on the topic of perturbation in optimal control problems. Earlier, we have quantified the benefit of taking engine and after-treatment system temperatures into account in the minimization of fuel consumption and pollutant emissions. Based on simulation results presented in [45], it seems that the engine temperature state could be ignored from this problem. Similar observations were given in [87, 88]. Our own investigations in Chapter 4 also concur. The general result based on regular perturbation established in this chapter explains and support these numerical observations. It states that, even in input-constraint cases, perturbation of magnitude ε in the problem definition gives an $O(\varepsilon^2)$ difference in optimal cost value.

Prior to establishing a general result, we first recall the state of the art about regular perturbations in optimal control. Then, a problem is formulated and the theoretical contributions are discussed. Finally, three illustrative examples are presented.

5.1 State of the art

From theoretical and numerical viewpoints, the number of state variables and the occurrence of constraints greatly affect the resolution of OCP. This observation holds for all methods, from dynamic programming [9], PMP based methods [68, 70], or direct formulations (e.g. collocation methods) [34]. The presence of modeling uncertainties adds another level of difficulty in the design of optimal controllers from the robustness viewpoint. Such uncertainty arises when some aspects of the system model are not completely known and/or when physical phenomena are neglected for reasons of simplification. One of the methods used to study the impact of modeling uncertainties on optimal solutions is perturbation theory.

Perturbations are mainly classified into two types: singular and regular. Only the latter type is discussed in this chapter. Parameter variation in regular perturbation does not produce a change of the model structure, nor its dimension.

It has been shown in [7, 23] (and references therein) how, under certain assumptions, perturbation terms appearing in the dynamics and the cost of an unconstrained OCP affect the optimality of the solution and the state trajectories. More precisely, if the error in the right hand-side of the dynamics and the cost function between the nominal model (which is generally used to calculate an optimal control) and the perturbed model (considered to represent the real system) are of magnitude ε, then the error in the optimal state trajectories and the control is bounded by a linear function in ε. As a consequence, the induced sub-optimality in the cost is bounded by a quadratic function ($K\varepsilon^2$). The proposed results in [7, 23] are concerned only with the existence of K[1].

[1]Interestingly, in the case of singular perturbation, the same question has been investigated in [7, 23, 89].

In real situations, however, most OCPs have to include input and also very often state constraints (which we leave out of the discussion). Several recent works have proposed to deal with these constraints by means of unconstrained representation of the variables, for example by saturation functions [30, 31, 32] or by using a method based on interior penalties [47, 48, 49].

In this chapter, the proposed method is grounded on the results of Bensoussan [7] about the robustness of cost, control and state with respect to model errors, and the results of [47] which shows how to solve an OCP under constraints as a sequence of problems without constraints. We combine the two approaches and we show that, here also, the error in the cost function is bounded by $K\varepsilon^2$ [46]. A secondary but important objective in this chapter is to (at least roughly) estimate the value of K as a function of the system parameters. Once K is estimated, its value can be used as a tool to analyze the cost of the simplifying the original OCP.

5.2 Problem formulation and main result

Consider the OCP

$$\min_u \left[J_\varepsilon(u) = \int_0^T L_\varepsilon(x,u)dt \right], \tag{5.1}$$

where L_ε is C^1, T is a fixed parameter, $\varepsilon \in [0,\ 1]$ is a parameter scaling the error terms (perturbation) in the cost function and the state dynamics in (5.2), and $x \in \mathbb{R}^n$ and $u \in \mathbb{R}^m$ are the state and the control variables of the following nonlinear dynamics with prescribed initial conditions X_0

$$\frac{dx}{dt} = f_\varepsilon(x,u),\ x(0) = X_0. \tag{5.2}$$

The control u is constrained to belong to the set $U^{ad} \subset L^\infty[0,T]$ of the functions of the form

$$u_{min} \leq u(t) \leq u_{max},\quad a.e.\ \ t \in [0,T]. \tag{5.3}$$

This study can be extended to the case of a cost $J_\varepsilon(.)$ with a terminal cost function. For convenience, the notation $\sigma \triangleq [x,u]$ is used. For a variable X, $\partial_z X$ indicates the partial derivative of X with respect to z, $z = x,\ u$.

Assumption 1 (Model disturbances) *The functions L_ε and f_ε are affine in ε,*

$$L_\varepsilon(\sigma) \triangleq L_0(\sigma) + \varepsilon L_1(\sigma),\ f_\varepsilon(\sigma) \triangleq f_0(\sigma) + \varepsilon f_1(\sigma),$$

where f_0 and L_0 are of class C^1 and L_1, f_1 and their first and second derivatives are assumed to be bounded.

The choice of affine functions in ε is not restrictive and the presented results can be extended to more general formulations.

Assumption 2 (Existence and Uniqueness) *The optimal control problem (5.1) for any $\varepsilon \geq 0$ is supposed to possess a unique solution. u_ε^* denotes the corresponding optimal control and x_ε the corresponding solution of the differential equation (5.2) for $u = u_\varepsilon^*$.*

The objective of the study conducted here is to quantify the induced sub-optimality in the cost (5.1) for $\varepsilon > 0$ by using the nominal control strategy calculated for $\varepsilon = 0$. For this and following the interior penalty approach [48, 49], a penalty function $P(u)$ is introduced into the cost. This function is defined on $]u_{min}, u_{max}[$. It satisfies the following conditions:

- the function $P(.)$ is continuously differentiable, strictly convex, and non-decreasing,
- the penalty $P(.)$ grows unbounded as its argument reaches either u_{min} or u_{max}.

This penalty function is used to define a penalized, constraints-free OCP,

$$\min_{u \in L^\infty[0,T]} \left[J_\varepsilon^r(u) = \int_0^T [L_\varepsilon(\sigma) + rP(u)]dt \right], \ r > 0. \tag{5.4}$$

This approach is very general, see [11] and references therein. As was shown in [27, 48, 49], when r goes to zero, under certain assumptions, the optimal value of the modified cost (5.4) converges to the optimal cost of (5.1) under input constraints and the penalty term $rP(u)$ goes to zero. The main advantage of this method is that, for each value of the weight r, the solution of OCP (5.4) is determined from simple stationarity conditions.

The first step is to establish relationships between the solution of the optimization problem (5.4) for $\varepsilon = 0$ and for $\varepsilon > 0$ under Assumptions 1 and 2. To do this, the stationarity conditions of the penalized problems are formulated.

5.2.1 Stationarity condition for the penalized nominal problem

The nominal problem is obtained for $\varepsilon = 0$. Using the PMP, the following TPBVP is considered.

$$\begin{aligned} \dot{x}_0^r &= f_0(\sigma_0^r), \ x_0^r(0) = X_0, \\ -\dot{p}_0^{rT} &= \partial_x L_0(\sigma_0^r) + p_0^{rT} \partial_x f_0(\sigma_0^r), \ p_0^{rT}(T) = 0, \qquad (5.5) \\ \partial_u L_0(\sigma_0^r) &+ r\partial_u P(u_0^r) + p_0^{rT} \partial_u f_0(\sigma_0^r) = 0, \qquad (5.6) \end{aligned}$$

where p_0^r is the adjoint state associated to x_0^r, and u_0^r is the optimal control. The Hamiltonian associated to this problem is

$$H_0^r(\sigma, p) = L_0(\sigma) + p^T f_0(\sigma) + rP(u).$$

5.2.2 Stationarity condition for the penalized perturbed problem

In the case $\varepsilon > 0$, the TPBVP is given by

$$\begin{aligned} \dot{x}_\varepsilon^r &= f_\varepsilon(\sigma_\varepsilon^r), \ x_\varepsilon^r(0) = X_0, \\ -\dot{p}_\varepsilon^{rT} &= \partial_x L_\varepsilon(\sigma_\varepsilon^r) + p_\varepsilon^{rT} \partial_x f_\varepsilon(\sigma_\varepsilon^r), \ p_\varepsilon^{rT}(T) = 0, \\ \partial_u L_\varepsilon(\sigma_\varepsilon^r) &+ r\partial_u P(u_\varepsilon^r) + p_\varepsilon^{rT} \partial_u f_\varepsilon(\sigma_\varepsilon^r) = 0, \end{aligned}$$

where p_ε^r is the adjoint state associated to x_ε^r. For a given control u_ε^r, the first two lines of the TPBVP are independent of the penalty $P(.)$. The Hamiltonian associated to this problem is

$$H_\varepsilon^r(\sigma, p) = L_\varepsilon(\sigma) + p^T f_\varepsilon(\sigma) + rP(u),$$

which can be written as an affine function of ε as follows

$$H_\varepsilon^r(\sigma, p) = H_0^r(\sigma, p) + \varepsilon H_1(\sigma, p), \tag{5.7}$$

where $H_1(\sigma, p) = L_1(\sigma) + p^T f_1(\sigma)$ is independent of the penalty function.

Assumption 3 (Convexity Condition) *Assume that* $\exists \beta > 0$ *such that*

$$\begin{cases} \partial_{uu} H_0^r(\sigma, p_0^r) \geq \beta I \text{ uniformly in } \sigma, \\ (\partial_{xx} H_0^r - \partial_{xu} H_0^r [\partial_{uu} H_0^r]^{-1} \partial_{ux} H_0^r)(\sigma, p_0^r) \geq 0 \text{ uniformly in } \sigma. \end{cases}$$

These inequalities are known in the calculus of variations as convexity conditions or strengthened Legendre-Clebsch conditions [14]. If $\beta \geq 0$, the inequalities are called Legendre-Clebsch conditions and they represent second-order necessary conditions for optimality. The strengthened Legendre-Clebsch conditions, in contrast to the Legendre-Clebsch conditions, are not necessary.

Denote for any x, u, x_ε^r and u_ε^r,

$$w \triangleq [\sigma \; p], \; \delta x^r = x - x_0^r, \; \delta u^r = u - u_0^r, \; \delta \sigma^r = \sigma - \sigma_0^r,$$
$$\delta x_\varepsilon^r = x_\varepsilon^r - x_0^r, \; \delta u_\varepsilon = u_\varepsilon^r - u_0^r, \; \delta \sigma_\varepsilon^r = \sigma_\varepsilon^r - \sigma_0^r.$$

5.2.3 Main result

The induced sub-optimality is defined as

$$\Delta J = J_\varepsilon(u_0^*) - J_\varepsilon(u_\varepsilon^*).$$

Theorem 1 (Main Result) *There exists a positive constant* K *such that the sub-optimality of* u_0^* *is upper bounded under the form*

$$\Delta J \triangleq J_\varepsilon(u_0^*) - J_\varepsilon(u_\varepsilon^*) \leq K\varepsilon^2 \quad \forall \varepsilon \in [0, 1]. \tag{5.8}$$

5.3 Preliminary results

The proof of Theorem 1 relies on elements of proof found in [7]. In order to estimate an upper bound on ΔJ, the two results given in Propositions 2 and 4 are used. These two general results are based on Taylor expansion and differential calculation. The first step toward the estimation of an upper bound on ΔJ is to write the cost function $J_\varepsilon^r(.)$ in the following form.

Proposition 2 (Second Order Expansion) *For any control* u, $J_\varepsilon^r(u)$ *can be written*

$$J_\varepsilon^r(u) = \int_0^T \left[H_\varepsilon^r(\sigma_0^r, p_0^r) - p_0^{rT} \dot{x}_0^r\right] dt + \varepsilon \int_0^T \left[N^0(t) \cdot \delta u^r + N^1(t) \cdot \delta x^r\right] dt$$
$$+ \int_0^T \int_0^1 \int_0^1 \lambda \partial_{\sigma\sigma} H_\varepsilon^r(\sigma_0^r + \lambda\mu\delta\sigma^r, p_0^r)(\delta\sigma^r)^2 d\lambda d\mu dt, \tag{5.9}$$

where

$$N^0(t) \triangleq \partial_u H_1(\sigma_0^r, p_0^r), \; N^1(t) \triangleq \partial_x H_1(\sigma_0^r, p_0^r). \tag{5.10}$$

As the term $\int_0^T \left[H_\varepsilon^r(\sigma_0^r, p_0^r) - p_0^{rT}\dot{x}_0^r\right] dt$ depends only on the nominal trajectories, it can be seen as a constant term. The second term $\int_0^T \left[N^0(t)\delta u^r + N^1(t)\delta x^r\right] dt$ represents the first-order variation of the cost due to the state and control trajectories variation.

Proof The proof is based on Taylor expansion combined with stationarity conditions. Details are given in Appendix D.1. ■

For a given r, ξ_0^r ts the solution of the differential equation (5.2) for the control u_0^r:

$$\frac{d\xi_0^r}{dt} = f_\varepsilon(\xi_0^r, u_0^r), \;\; \xi_0^r(0) = x_0(0), \tag{5.11}$$

while x_0^r satisfies

$$\frac{dx_0^r}{dt} = f_0(x_0^r, u_0^r), \;\; x_0^r(0) = x_0(0). \tag{5.12}$$

The two trajectories of $\xi_0^r(t)$ and $x_0^r(t)$ have the same control input u_0^r and the same initial conditions. The following proposition gives an upper bound on $\|\xi_0^r(t) - x_0^r(t)\|$.

Proposition 3 *Consider (5.11) and (5.12), the error $\|\xi_0^r(t) - x_0^r(t)\|$ satisfies*

$$\|\xi_0^r(t) - x_0^r(t)\| \leq F_1 q(t)\varepsilon, \tag{5.13}$$

where

$$F_1 = \sup_{t\in[0,T]} \|f_1(\sigma_0^r(t))\|, \;\; q(t) = \frac{1}{\Gamma}(e^{\Gamma t} - 1). \tag{5.14}$$

and Γ is the Lipschitz constant of f_ε.

Proof The proof is given in Appendix D.2. ■

The second step in calculating an upper bound ΔJ is to estimate the error in the state trajectories due to the control input variation and perturbation in the dynamics. This estimation is summarized in the following proposition.

Proposition 4 *There exist positive constants $(\alpha_3,\ \alpha_4)$ and time functions $(\alpha_1,\ \alpha_2)$such that*

$$\|\delta x_\varepsilon^r(t)\|^2 \leq \alpha_1(t) \int_0^T \int_0^1 \int_0^1 \lambda \|z(\lambda,\mu,t)\|^2 \, d\lambda d\mu dt + \alpha_2(t) F_1^2 \varepsilon^2, \tag{5.15}$$

$$\int_0^T \|\delta u_\varepsilon^r(t)\|^2 \, dt \leq \alpha_3 \int_0^T \int_0^1 \int_0^1 \lambda \|z(\lambda,\mu,t)\|^2 \, d\lambda d\mu dt + \alpha_4 F_1^2 \varepsilon^2, \tag{5.16}$$

where the variable z defined by

$$z(\lambda,\mu,t) = \delta u_\varepsilon^r + [\partial_{uu} H_0^r(.)]^{-1} \partial_{ux} H_0^r(.) \delta x_\varepsilon^r \tag{5.17}$$

is well defined because $\partial_{uu} H_0^r(.)$ is assumed to be positive definite from Assumption 3.

Proof The proof is based on first order expansion of the system given the dynamics of δx_ε^r. Details are given in Appendix D.3. ■

5.4 Proof of the Main Result

In contrast to the results presented in Section 5.3 which are general, the propositions presented in this section are specific to the suggested method to calculate the parameter K. To prove the main result, we need the following intermediate upper bounds on $x_\varepsilon^r(t)-x_0^r(t)$ and $u_\varepsilon^r(s)-u_0^r(s)$ for a fixed value of r.

Lemma 1 *There exist positive constants c_x and c_u independent of $rP(.)$, such that*

$$|x_\varepsilon^r(t)-x_0^r(t)|^2 \leq c_x^2\varepsilon^2, \tag{5.18}$$

$$\int_0^T |u_\varepsilon^r(s)-u_0^r(s)|^2\,ds \leq c_u^2\varepsilon^2. \tag{5.19}$$

The proof of this lemma is divided into two parts, each of which is summarized in a proposition. The proof is organized as follows:

1. First, an upper bound on M_0 defined by

$$M_0 \triangleq J_\varepsilon^r(u_0^r) - \int_0^T \left[H_\varepsilon^r(\sigma_0^r,p_0^r) - p_0^{rT}\dot{x}_0^r\right] dt, \tag{5.20}$$

   is calculated. This upper bound is given in Proposition 5.

2. An upper bound on R defined by

$$R \triangleq \int_0^T\int_0^1\int_0^1 \lambda\,\|z(\lambda,\mu,t)\|^2\,d\lambda d\mu dt, \tag{5.21}$$

   is given in Proposition 6 where the inequalities (5.18, 5.19) will be derived.

5.4.1 Upper bound on M_0

An upper bound on M_0 is calculated in the following proposition.

Proposition 5 *There exist positive constants c_0 and c_1 such that*

$$|J_\varepsilon^r(u_0^r) - \int_0^T \left[H_\varepsilon^r(\sigma_0^r,p_0^r) - p_0^{rT}\dot{x}_0^r\right] dt| \leq (c_0F_1^2+c_1)\varepsilon^2. \tag{5.22}$$

These are

$$c_0 = \frac{1}{2}(\sup_{t\in[0,T]}\partial_{xx}H_0^r(.)+m)\int_0^T q^2(t)dt + \frac{1}{2}\sup_{t\in[0,T]}\partial_{xx}H_1(.)\int_0^T q^2(t)dt,$$

$$c_1 = \frac{1}{2m}\int_0^T k_1^2(t)dt,$$

where m is a positive constant, q is given in (5.14) and k_1 is an upper bound on $N^1(t)$ defined in (5.10). In particular, the upper bound in (5.22) is independent of $rP(.)$.

Proof The proof is based on the second-order expansion given in Proposition 2. The upper bound in (5.22) is independent of the penalty, as the input constraints are satisfied. Note that this remark would not be true in the presence of state constraints where the perturbation in the dynamics may lead to the violation of the state constraints. Details of the proof are given in Appendix D.4. ■

5.4.2 Upper bound on R

The following proposition gives an upper bound on R. The proof is based on Proposition 2.

Proposition 6 *There exists a constant c_2 such that*

$$R \leq c_2 \varepsilon^2,$$

where c_2 is independent of the penalty $rP(.)$.

Proof Essentially, the proof is based on the decomposition suggested in Proposition 2 and the convexity conditions given in Assumption 3. The variable z defined in (5.17) will be helpful as it allows the manipulation of diagonal quadratic forms. Details of the proof are given in Appendix D.5. ■

5.4.3 Upper bound on ΔJ

The final step is to find an upper bound of $J_\varepsilon^r(u_0^r) - J_\varepsilon^r(u_\varepsilon^r)$.

Proposition 7 *There exists a constant K such that*

$$J_\varepsilon^r(u_0^r) - J_\varepsilon^r(u_\varepsilon^r) \leq K\varepsilon^2.$$

Proof The upper bound on ΔJ is a consequence of the upper bounds on δx_ε^r, δu_ε^r and R given in (5.18, 5.19, D.20) respectively. The term $J_\varepsilon^r(u_\varepsilon^r) - J_\varepsilon^r(u_0^r)$ can be written

$$J_\varepsilon^r(u_\varepsilon^r) - J_\varepsilon^r(u_0^r) = J_\varepsilon^r(u_\varepsilon^r) - \int_0^T \left[H_\varepsilon^r(w_0^r) - p_0^{rT}\dot{x}_0^r\right] dt - J_\varepsilon^r(u_0^r) + \int_0^T \left[H_\varepsilon^r(w_0^r) - p_0^{rT}\dot{x}_0^r\right] dt,$$

that is

$$\begin{aligned} J_\varepsilon^r(u_0^r) - J_\varepsilon^r(u_\varepsilon^r) &\leq \left| J_\varepsilon^r(u_\varepsilon^r) - \int_0^T \left[H_\varepsilon^r(w_0^r) - p_0^{rT}\dot{x}_0^r\right] dt \right| + \left| J_\varepsilon^r(u_0^r) - \int_0^T \left[H_\varepsilon^r(w_0^r) - p_0^{rT}\dot{x}_0^r\right] dt \right|, \\ &\leq |M_1| + |M_0|, \end{aligned}$$

where M_1 is given by

$$M_1 = J_\varepsilon^r(u_\varepsilon^r) - \int_0^T \left[H_\varepsilon^r(\sigma_0^r, p_0^r) - p_0^{rT}\dot{x}_0^r\right] dt.$$

The upper bound on M_0 is given in (5.22). M_1 can be written using Proposition 2

$$\begin{aligned} M_1 &= \varepsilon \int_0^T \left[N^0 \delta u_\varepsilon^r + N^1 \delta x_\varepsilon^r\right] dt + \int_0^T \int_0^1 \int_0^1 \lambda \partial_{\sigma\sigma} H_0^r(\sigma_0^r + \lambda\mu\delta\sigma_\varepsilon^r, p_0^r)(\delta\sigma_\varepsilon^r)^2 d\lambda d\mu dt \\ &\quad + \varepsilon \int_0^T \int_0^1 \int_0^1 \lambda \partial_{\sigma\sigma} H_1(\sigma_0^r + \lambda\mu\delta\sigma_\varepsilon^r, p_0^r)(\delta\sigma_\varepsilon^r)^2 d\lambda d\mu dt. \end{aligned}$$

An upper bound on M_1 can be written as

$$\begin{aligned} M_1 \leq & \int_0^T \left[\frac{\varepsilon^2}{2m}\left\{(N^0(t))^2 + (N^1(t))^2\right\} + \frac{m}{2}\left\{\|\delta x_\varepsilon^r\|^2 + \|\delta u_\varepsilon^r\|^2\right\}\right] dt \\ & + \int_0^T \int_0^1 \int_0^1 \lambda \left[z^T \partial_{uu} H_0^r(.) z + \delta x_\varepsilon^{rT} \left[\partial_{xx} H_0^r - \partial_{xu} H_0^r [\partial_{uu} H_0^r]^{-1} \partial_{ux} H_0^r\right](.) \delta x_\varepsilon^r\right] dt \\ & + \varepsilon \int_0^T \int_0^1 \int_0^1 \lambda \partial_{\sigma\sigma} H_1(\sigma_0^r + \lambda\mu\delta\sigma_\varepsilon^r, p_0^r)(\delta\sigma_\varepsilon^r)^2 d\lambda d\mu dt. \end{aligned}$$

By using equations (5.18, 5.19, D.20), the upper bound on M_1 is given by

$$M_1 \leq c_3(r)\varepsilon^2,$$

where

$$\begin{aligned} c_3(r) = & \int_0^T \left[\frac{1}{2m}(k_1^2(t)+k_1^2(t)) + \frac{m}{2}c_x^2(t)\right] dt + \frac{m}{2}c_u^2 \\ & + \frac{1}{2}\sup_{s\in[0,T]} \|\partial_{\sigma\sigma}H_1(.)\| \left[F_1^2(\alpha_4+d_2)+(\alpha_3+d_1)c_2\right] + \sup_{s\in[0,T]} \|\partial_{uu}H_0^r(.)\| c_2 \\ & + \sup_{s\in[0,T]} \left\|\partial_{xx}H_0^r - \partial_{xu}H_0^r[\partial_{uu}H_0^r]^{-1}\partial_{ux}H_0^r\right\| \int_0^T c_x^2(t)dt. \end{aligned}$$

The upper bound on ΔJ is of the form

$$J_\varepsilon^r(u_0^r) - J_\varepsilon^r(u_\varepsilon^r) \leq (c_0F_1^2+c_1)\varepsilon^2 + \min\left[c_3(r), (c_0F_1^2+c_1)\right]\varepsilon^2 = K\varepsilon^2.$$

As $(c_0F_1^2+c_1)\varepsilon^2$ is independent of $rP(.)$ and the input constraints are always satisfied when r goes to zero, the upper bound on $J_\varepsilon^r(u_0^r) - J_\varepsilon^r(u_\varepsilon^r)$ is finite and its limit is independent of $rP(.)$. As the penalized cost J_ε^r converges to the optimal value of J_ε under input constraint when r goes to zero (see [27, 47]), there exist a constant K such that

$$J_\varepsilon(u_0) - J_\varepsilon(u_\varepsilon) \leq K\varepsilon^2.$$

The perturbation does not affect the satisfaction of the control constraint, as the latter are independent of the state trajectories. Again, this remark would not be true in the presence of state constraints, since the perturbations affect the state trajectories and may jeopardize satisfying the state constraints. In the presence of state constraints, the approach is different and the parameter r can not go to zero. This concludes the proof. ■

5.5 Estimation of the error factor K

The purpose of the main result, i.e. Theorem 1, is to quantify the sub-optimality induced by modeling errors in the presence of control constraints. This objective can be achieved by estimating the value of K. This estimation is carried out in five steps:

1. Step 1: Calculate the nominal trajectories (state, adjoint state and the nominal control) for $\varepsilon = 0$. This step can be done using the PMP.

2. Step 2: Estimate the coefficients $(\alpha_1,\ \alpha_2,\ \alpha_3,\ \alpha_4)$ giving the upper bounds on the state and the control trajectories

$$\begin{aligned} \|\delta x_\varepsilon^r(t)\|^2 &\leq \alpha_1(t)\int_0^T\int_0^1\int_0^1 \lambda \|z(\lambda,\mu,t)\|^2 d\lambda d\mu dt + \alpha_2(t)F_1^2\varepsilon^2, \\ \int_0^T \|\delta u_\varepsilon^r(t)\|^2 dt &\leq \alpha_3\int_0^T\int_0^1\int_0^1 \lambda \|z(\lambda,\mu,t)\|^2 d\lambda d\mu dt + \alpha_4F_1^2\varepsilon^2, \end{aligned}$$

   where F_1 is the maximum error in the state dynamics, z is defined in (5.17). This estimation can be achieved using the Lipschitz property (in accordance with Appendix D.3) or the first order expansion of the system given the dynamics of $\delta x_\varepsilon^r(t)$.

3. Step 3: Estimate an upper bound on M_0 given by

$$|M_0| \leq (c_0 F_1^2 + c_1)\varepsilon^2,$$

$$\begin{aligned} c_0 &= \frac{1}{2}(\sup_{t\in[0,T]} \partial_{xx} H_0^r(.) + m) \int_0^T q^2(t)dt + \frac{1}{2} \sup_{t\in[0,T]} \partial_{xx} H_1(.) \int_0^T q^2(t)dt, \\ c_1 &= \frac{1}{2m} \int_0^T k_1^2(t)dt, \end{aligned}$$

where m is a positive constant (whose value will be calculated below) and q is given in (5.14).

4. Step 4: Estimate the upper bound on R given by

$$R \leq \frac{2}{\beta} \left(s_{2a} F_1^2 + s_{2b}\right) \varepsilon^2 = c_2 \varepsilon^2,$$

where

$$\begin{aligned} s_{2a} &= c_0 + \left[\frac{m}{2} - \frac{1}{2} \sup_{s\in[0,T]} \|\partial_{\sigma\sigma} H_1(.)\|\right] (\alpha_4 + \int_0^T \alpha_2(s)ds), \\ s_{2b} &= c_1 + \frac{1}{2m} \int_0^T (k_2^2(t) + k_1^2(t))dt, \end{aligned}$$

and m is given by

$$m = \sqrt{\frac{\beta}{\alpha_3 + \int_0^T \alpha_1(s)ds}}.$$

The upper bound on δx_ε and δu_ε become of the form

$$\begin{aligned} \|\delta x_\varepsilon^r(t)\|^2 &\leq \left[\frac{2}{\beta}\alpha_1(t)\left(s_{2a}F_1^2 + s_{2b}\right) + \alpha_2(t)F_1^2\right] \varepsilon^2 = c_x^2(t)\varepsilon^2, \\ \int_0^T \|\delta u_\varepsilon^r(t)\|^2 dt &\leq \left[\frac{2}{\beta}\alpha_3\left(s_{2a}F_1^2 + s_{2b}\right) + \alpha_4 F_1^2\right] \varepsilon^2 = c_u^2 \varepsilon^2. \end{aligned}$$

5. Step 5: Estimate the upper bound on ΔJ of the form $K\varepsilon^2$ where

$$\begin{aligned} K &= c_0 F_1^2 + c_1 + \min\left[c_3, c_0 F_1^2 + c_1\right], \\ c_3 &= \int_0^T \left[\frac{1}{2m}(k_1^2(t) + k_1^2(t)) + \frac{m}{2} c_x^2(t)\right] dt + \frac{m}{2} c_u^2 \\ &\quad + \frac{1}{2} \sup_{s\in[0,T]} \|\partial_{\sigma\sigma} H_1(.)\| \left[F_1^2 \left(\alpha_4 + \int_0^T \alpha_2(s)ds\right) + \left(\alpha_3 + \int_0^T \alpha_1(s)ds\right) c_2\right] \\ &\quad + \sup_{s\in[0,T]} \left\|\partial_{uu} H_0^0(.)\right\| c_2 + \sup_{s\in[0,T]} \left\|\partial_{xx} H_0^0 - \partial_{xu} H_0^0 [\partial_{uu} H_0^0]^{-1} \partial_{ux} H_0^0\right\| \int_0^T c_x^2(t)dt. \end{aligned}$$

The obtained upper bound on ΔJ will be conservative. The inequalities used in the calculation of K can be improved and better results for K can be obtained on a case-by-case basis.

5.6 Illustrative examples

Three illustrative examples are considered: (i) a linear quadratic control problem with input constraints, (ii) a toy nonlinear control problem and (iii) an eco-driving control problem which is more relevant in the context of the thesis. The parameter K is estimated for each example and its value is compared to the real value calculated from the numerical solutions of the nominal and the perturbed problems. The following notations are used:

- The nominal state and costate trajectories for $\varepsilon = 0$: $(y_1,\ y_2,\ \lambda_1,\ \lambda_2)$.
- The solutions of the dynamics equations for the nominal control $u = u_0$ and for $\varepsilon > 0$: $(x_1,\ x_2)$.
- The optimal state and costate trajectories for $\varepsilon > 0$: $(x_1^*,\ x_2^*,\ \lambda_1^*,\ \lambda_2^*)$.
- The error in the state and the control trajectories $\delta X_1 = x_1 - y_1,\ \delta X_2 = x_2 - y_2,\ \delta x_1 = x_1^* - y_1,\ \delta x_2 = x_2^* - y_2,\ \delta u = u_\varepsilon - u_0$.

5.6.1 Linear quadratic (LQ) problem

Consider the following linear quadratic problem

$$J_\varepsilon(u) = \frac{1}{2}\int_0^T ((1+\frac{\varepsilon}{3})u^2 + x_1^2)dt,$$

where $x_1,\ x_2$ and u are the state and the control variables of the following linear system

$$\begin{aligned} \dot{x}_1 &= x_2 - \frac{\varepsilon}{12}x_1,\ x_1(0) = 4, \\ \dot{x}_2 &= -(1-\frac{\varepsilon}{10})x_2 + u,\ x_2(0) = 4. \end{aligned}$$

The parameter ε models the uncertainties (parameters variation) in the model ($\varepsilon \in [0,\ 1]$). The control u is constrained to belong to the set U^{ad} defined by

$$u_{min} \leq u(t) \leq u_{max}.$$

The Hamiltonian H_ε associated to this OCP is given by

$$H_\varepsilon(x_1, x_2, u, \lambda_1, \lambda_2) = H_0(x_1, x_2, u, \lambda_1, \lambda_2) + \varepsilon(-\frac{\lambda_1}{12}x_1 + \frac{\lambda_2}{10}x_2 + \frac{u^2}{6}),$$

where H_0 is the Hamiltonian associated to the nominal problem ($\varepsilon = 0$), and is given by

$$H_0(x_1, x_2, u, \lambda_1, \lambda_2) = \frac{1}{2}(u^2 + x_1^2) + \lambda_1 x_2 + \lambda_2(-x_2 + u).$$

5.6.1.1 Upper bounds on δX_i

The dynamics of δX_1 and δX_2 are given by

$$\begin{aligned} \frac{d(\delta X_1)}{dt} &= \delta X_2 - \frac{\varepsilon}{12}\delta X_1 - \frac{\varepsilon}{12}y_1,\ \delta X_1(0) = 0, \\ \frac{d(\delta X_2)}{dt} &= -(1-\frac{\varepsilon}{10})\delta X_2 + \frac{\varepsilon}{10}y_2,\ \delta X_2(0) = 0. \end{aligned}$$

The transition matrix Φ of this linear system is given by

$$\Phi(t,\tau,\varepsilon) = \begin{bmatrix} \Phi_{11}(t,\tau,\varepsilon) & \Phi_{12}(t,\tau,\varepsilon) \\ \Phi_{21}(t,\tau,\varepsilon) & \Phi_{22}(t,\tau,\varepsilon) \end{bmatrix} = \begin{bmatrix} e^{-\frac{\varepsilon}{12}(t-\tau)} & \frac{60e^{(\frac{\varepsilon}{10}-1)(t-\tau)}-60e^{-\frac{\varepsilon}{12}(t-\tau)}}{11\varepsilon-60} \\ 0 & e^{(\frac{\varepsilon}{10}-1)(t-\tau)} \end{bmatrix}. \quad (5.23)$$

By using (5.23), δX_1 and δX_2 can be bounded as follows

$$\begin{aligned} \|\delta X_1(t)\| &\leq \varepsilon \left| \int_0^t \left[-\frac{1}{12} y_1(\tau)\Phi_{11}(t,\tau,0) + \frac{1}{10} y_2(\tau)\Phi_{12}(t,\tau,0) \right] d\tau \right|, \\ \|\delta X_2(t)\| &\leq \varepsilon \left| \int_0^t \frac{1}{10} y_2(\tau)\Phi_{22}(t,\tau,1) d\tau \right|. \end{aligned}$$

The two upper bounds on δX_1 and δX_2, which depend only on the nominal trajectories, are of the form

$$\|\delta X_1(t)\| \leq \varepsilon\alpha_{21}(t), \ \|\delta X_2(t)\| \leq \varepsilon\alpha_{22}(t),$$

where

$$\alpha_{21}(t) = \left| \int_0^t \left[-\frac{y_1(\tau)}{12} + \frac{y_2(\tau)}{10}\Phi_{12}(t,\tau,0) \right] d\tau \right|, \ \alpha_{22}(t) = \left| \int_0^t \frac{y_2(\tau)}{10}\Phi_{22}(t,\tau,1) d\tau \right|.$$

Note that α_{21} and α_{22} depend only on the nominal trajectories. They are calculated numerically.

5.6.1.2 Upper bounds on δx_i

The dynamics of δx_1 and δx_2 are given by

$$\begin{aligned} \frac{d(\delta x_1)}{dt} &= \delta x_2 - \frac{\varepsilon}{12}\delta x_1 - \frac{\varepsilon}{12} y_1, \ \delta x_1(0) = 0, \\ \frac{d(\delta x_2)}{dt} &= -(1 - \frac{\varepsilon}{10})\delta x_2 + \delta u + \frac{\varepsilon}{10} y_2, \ \delta x_2(0) = 0. \end{aligned}$$

By using the transition matrix $\Phi(t,\tau,\varepsilon)$ given in (5.23), this differential system is solved as

$$\begin{aligned} \delta x_1(t) &= \int_0^t \Phi_{12}(t,\tau,\varepsilon)\delta u(\tau) d\tau + \varepsilon \int_0^t \left[-\frac{1}{12} y_1(\tau)\Phi_{11}(t,\tau,\varepsilon) + \frac{1}{10} y_2(\tau)\Phi_{12}(t,\tau,\varepsilon) \right] d\tau, \\ \delta x_2(t) &= \int_0^t \Phi_{22}(t,\tau,\varepsilon)\delta u(\tau) d\tau + \varepsilon \int_0^t \frac{1}{10} y_2(\tau)\Phi_{22}(t,\tau,\varepsilon) d\tau. \end{aligned}$$

From Cauchy-Schwarz inequality, the upper bounds on $\delta x_1(t)$ and $\delta x_2(t)$ are of the form

$$|\delta x_1(t)| \leq \sqrt{\int_0^t \Phi_{12}^2(t,\tau,0) d\tau} \sqrt{\int_0^t \delta u^2(\tau) d\tau} + \varepsilon\alpha_{21}(t) = \alpha_{11}(t) \sqrt{\int_0^t \delta u^2(\tau) d\tau} + \varepsilon\alpha_{21}(t),$$

$$|\delta x_2(t)| \leq \sqrt{\int_0^t \Phi_{22}^2(t,\tau,1) d\tau} \sqrt{\int_0^t \delta u^2(\tau) d\tau} + \varepsilon\alpha_{22}(t) = \alpha_{12}(t) \sqrt{\int_0^t \delta u^2(\tau) d\tau} + \varepsilon\alpha_{22}(t).$$

The upper bounds on $\delta x_1(t)$ and $\delta x_2(t)$ can be written as

$$|\delta x_1(t)| \leq \alpha_{11}(t)\sqrt{R} + \varepsilon\alpha_{21}(t),$$

$$|\delta x_2(t)| \leq \alpha_{12}(t)\sqrt{R} + \varepsilon\alpha_{22}(t),$$

where

$$\alpha_{11}(t) = \sqrt{\int_0^t \Phi_{12}^2(t,\tau,0)d\tau},\ \ \alpha_{12}(t) = \sqrt{\int_0^t \Phi_{22}^2(t,\tau,1)d\tau},$$

$$R = \int_0^T \delta u^2(\tau)d\tau,\ \ M = \int_0^T \left[H_\varepsilon(y_1,y_2,u_0,\lambda_1,\lambda_2) - \lambda_1\dot{y}_1 - \lambda_2\dot{y}_2\right]dt.$$

In the expressions of α_{11} and α_{12}, the stability of the system (eigenvalues properties) is used to obtain upper bounds independent of ε and T.

5.6.1.3 Upper bound on R

From Proposition 2, $J(u_0)$ can be written in the form

$$J_\varepsilon(u_0) = M + \varepsilon\int_0^T \left[N_1(t)\delta X_1(t) + N_2(t)\delta X_2(t)\right]dt + \frac{1}{2}\int_0^T \delta X_1^2 dt,$$

where $N_1(t) = \dfrac{-\lambda_1(t)}{12}$ and $N_2(t) = \dfrac{\lambda_2(t)}{10}$ and an upper bound on $|J_\varepsilon(u_0) - M|$ is of the form

$$|J_\varepsilon(u_0) - M| \leq \varepsilon^2\int_0^T \left[\frac{\alpha_{21}^2(t)}{2} + \left|\frac{-\lambda_1(t)}{12}\alpha_{21}(t) + \frac{\lambda_2(t)}{10}\alpha_{22}(t)\right|\right]dt = c\varepsilon^2,$$

where c is given by

$$c = \int_0^T \left[\frac{\alpha_{21}^2(t)}{2} + \left|\frac{-\lambda_1(t)}{12}\alpha_{21}(t) + \frac{\lambda_2(t)}{10}\alpha_{22}(t)\right|\right]dt.$$

In this upper bound, c depends only on the nominal trajectories. In the same spirit, and by using Proposition 2, $J(u_\varepsilon)$ can be written in the form

$$J_\varepsilon(u_\varepsilon) = M + \varepsilon\int_0^T \left[N_1(t)\delta x_1(t) + N_2(t)\delta x_2(t) + N_0(t)\delta u\right]dt + \frac{1}{2}\int_0^T (\delta x_1^2 + (1+\frac{\varepsilon}{3})\delta u^2)dt, \tag{5.24}$$

where $N_0 = \dfrac{u_0}{3}$. As u_ε is the optimal control, and from (5.24), we derive

$$c\varepsilon^2 \geq \varepsilon\int_0^T \left[N_1(t)\delta x_1(t) + N_2(t)\delta x_2(t) + N_0(t)\delta u\right]dt + \frac{1}{2}\int_0^T (\delta x_1^2 + (1+\frac{\varepsilon}{3})\delta u^2)dt.$$

By using the decomposition $xy \geq -\frac{x^2}{2m} - \frac{m}{2}y^2$, this inequality can be written

$$\begin{aligned} c\varepsilon^2 \ &\geq\ -\frac{\varepsilon^2}{2m}\int_0^T \left[N_1^2(t) + N_2^2(t) + N_0^2(t)\right]dt - \frac{m}{2}\int_0^T \left[\delta x_1^2(t) + \delta x_2^2(t) + \delta u^2(t)\right]dt \\ &+\ \frac{1}{2}\int_0^T (\delta x_1^2 + (1+\frac{\varepsilon}{3})\delta u^2)dt, \end{aligned}$$

yielding

$$\frac{1}{2}\int_0^T ((1+\frac{\varepsilon}{3})\delta u^2 + (1-m)\delta x_1^2 - m\delta x_2^2 - m\delta u^2)dt \leq c\varepsilon^2 + \frac{\varepsilon^2}{2m}\int_0^T \left[N_1^2(t) + N_2^2(t) + N_0^2(t)\right]dt. \tag{5.25}$$

By using the upper bounds on δx_1 and δx_2, inequality (5.25) becomes of the form

$$\frac{1}{2}\left(1+\frac{\varepsilon}{3}+2(1-m)\int_0^T \alpha_{11}^2(t)dt-2m\int_0^T \alpha_{12}^2(t)dt-m\right)R \\ \leq \varepsilon^2\int_0^T\left[(m-1)\alpha_{21}^2(t)+m\alpha_{22}^2(t)\right]dt+c\varepsilon^2+\frac{\varepsilon^2}{2m}\int_0^T\left[N_1^2(t)+N_2^2(t)+N_0^2(t)\right]dt,$$

where $m>0$ is chosen such that

$$1+2(1-m)\int_0^T \alpha_{11}^2(t)dt-2m\int_0^T \alpha_{12}^2(t)dt-m=\frac{1+2\int_0^T \alpha_{11}^2(t)dt}{2}.$$

The upper bound on R is then of the form

$$R\leq 2\frac{c\varepsilon^2+\frac{\varepsilon^2}{2m}\int_0^T\left[N_1^2(t)+N_2^2(t)+N_0^2(t)\right]dt+\varepsilon^2\int_0^T\left[(m-1)\alpha_{21}^2(t)+m\alpha_{22}^2(t)\right]dt}{1+2(1-m)\int_0^T \alpha_{11}^2(t)dt-2m\int_0^T \alpha_{12}^2(t)dt-m+\frac{\varepsilon}{3}},$$

As $\varepsilon\geq 0$, the upper bound on R becomes

$$R\leq 2\frac{c\varepsilon^2+\frac{\varepsilon^2}{2m}\int_0^T\left[N_1^2(t)+N_2^2(t)+N_0^2(t)\right]dt+\varepsilon^2\int_0^T\left[(m-1)\alpha_{21}^2(t)+m\alpha_{22}^2(t)\right]dt}{1+2(1-m)\int_0^T \alpha_{11}^2(t)dt-2m\int_0^T \alpha_{12}^2(t)dt-m}\triangleq c_1\varepsilon^2,$$

and the upper bounds on $\delta x_1(t)$ and $\delta x_2(t)$ become

$$\begin{aligned}|\delta x_1(t)| &\leq \left(\alpha_{11}(t)\sqrt{c_1}+\alpha_{21}(t)\right)\varepsilon\triangleq c_{x1}(t)\varepsilon,\\ |\delta x_2(t)| &\leq \left(\alpha_{12}(t)\sqrt{c_1}+\alpha_{22}(t)\right)\varepsilon\triangleq c_{x2}(t)\varepsilon.\end{aligned}$$

5.6.1.4 Upper bound on ΔJ

The last step is to find an upper bound on $\Delta J=J_\varepsilon(u_0)-J_\varepsilon(u_\varepsilon)>0$. For this, ΔJ can be written

$$\Delta J=J_\varepsilon(u_0)-J_\varepsilon(u_\varepsilon)\leq \underbrace{\left|J_\varepsilon(u_0)-M\right|}_{\leq c\varepsilon^2}+\left|J_\varepsilon(u_\varepsilon)-M\right|.$$

From (5.24) and by using the state upper bounds, we can write

$$\begin{aligned}|J_\varepsilon(u_\varepsilon)-M| &= \Bigg|\varepsilon\int_0^T\left[N_1(t)\delta x_1(t)+N_2(t)\delta x_2(t)+N_0(t)\delta u(t)\right]dt+\frac{1}{2}\int_0^T\delta x_1^2dt\\ &\quad+\frac{1}{2}\int_0^T(1+\frac{\varepsilon}{3})\delta u^2dt\Bigg|,\\ &\leq \int_0^T\left[\varepsilon^2N_1(t)c_{x1}(t)+\varepsilon^2N_2(t)c_{x2}(t)+\frac{\varepsilon^2}{2m_1}N_0^2(t)\right]dt+\frac{\varepsilon^2}{2}\int_0^T c_{x1}^2(t)dt\\ &\quad+\frac{1}{2}(m_1+1+\frac{\varepsilon}{3})c_1\varepsilon^2,\end{aligned}$$

where m_1 is chosen such that

$$m_1=\sqrt{\frac{\int_0^T N_0^2(t)dt}{c_1}}.$$

Finally, the upper bound on ΔJ is $K\varepsilon^2$ where

$$K = \int_0^T [N_1(t)c_{x1}(t) + N_2(t)c_{x2}(t) + \frac{1}{2m_1}N_0^2(t) + \frac{1}{2}c_{x1}^2(t)]dt + \frac{1}{2}(m_1 + \frac{4}{3})c_1 + c. \quad (5.26)$$

The parameter K depends only on the nominal trajectories for $\varepsilon = 0$ and the upper bounds on $(\delta u,\ \delta x_1,\ \delta x_2)$. The expression of K is similar to the expression given in Section (5.5). The difference is in the estimation of the error on the state trajectories: in the general expression, we have used the Lipschitz constant and here we use the transition matrix of the system describing the dynamics of the error on the state trajectories. The obtained value will be less conservative than the general expression in Section (5.5).

5.6.1.5 Numerical evaluation

The problem parameters are given in Table 5.1. The two TPBVPs associated to the nominal and the perturbed problems are solved for $\varepsilon \in [0,\ 1]$ using Matlab routine `bvp4c` [82]. The error in the cost function given by $\Delta J = J_\varepsilon(u_0) - J_\varepsilon(u_\varepsilon)$ is evaluated numerically.

Table 5.1: LQ problem parameters

Parameter	u_{max}	u_{min}	T
Value	1.7	-1.7	10

The numerical comparison between ΔJ (calculated numerically) and $K\varepsilon^2/15$ (estimated using the expression (5.26)) as functions of ε, is shown in Figure 5.1. The upper bound $K\varepsilon^2/15$ gives a good estimation of the error in the cost when ε is less than 0.6. Otherwise, the estimate is higher than its real value.

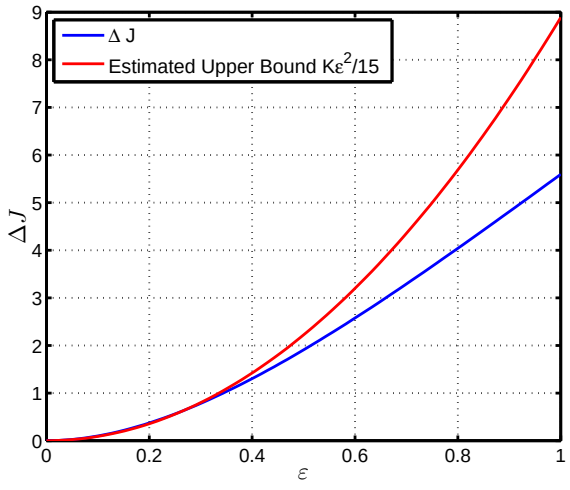

Figure 5.1: $K\varepsilon^2$ for LQ problem

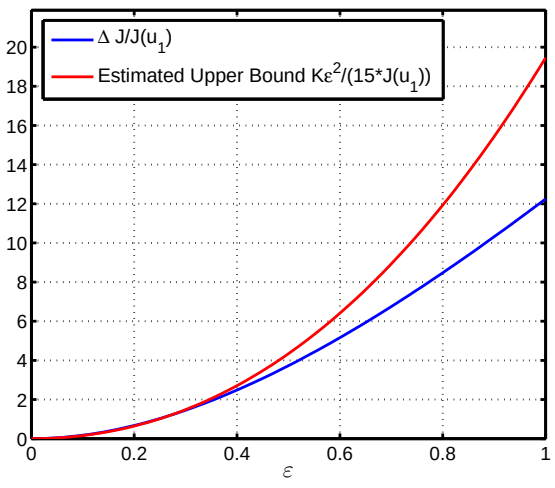

Figure 5.2: Relative error in the optimal cost

The ratio (approx 15) between ΔJ and $K\varepsilon^2$ is due to the conservatism of the calculation method: inequalities manipulation and problem assumptions (global convexity condition in Assumption 3). Additionally, the error in the state $(\delta x_1,\ \delta x_2)$ and the control variable δu are estimated only from the solution of the nominal problem and they are not

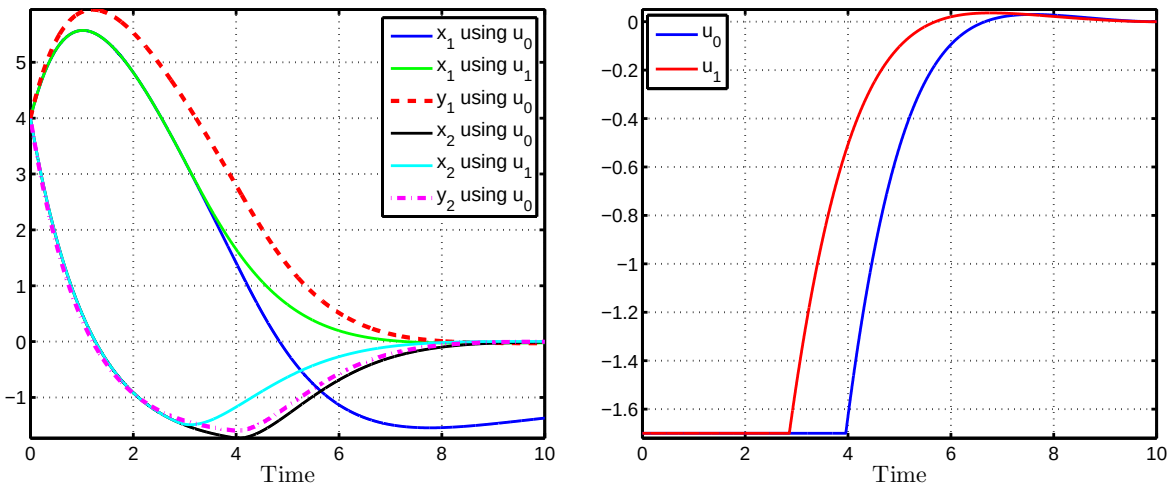

Figure 5.3: State trajectories (left) and optimal controls (right) for $\varepsilon = 1$ in LQ case

exactly calculated. Their estimations are higher than their real values which will lead to a higher value of K, compared to the real error in the cost ΔJ.

The state trajectories determined by using u_0 and u_1 (for $\varepsilon = 1$) and the control trajectories are given in the plots of Figure 5.3. These figures show that the perturbation affects the state and the control trajectories.

5.6.2 Nonlinear (NL) problem

Consider the following quadratic cost function

$$J_\varepsilon(u) = \int_0^T \left(0.3u^2 + 5(1+\frac{\varepsilon}{4})x_1^2\right) dt,$$

where x_1, x_2 and u are the state and the control variables of the following system

$$\begin{aligned} \dot{x}_1 &= (1+\frac{\varepsilon}{5})x_1 - x_1x_2, \ x_1(0) = 4, \\ \dot{x}_2 &= -x_2 + \frac{1}{10}(1+\frac{\varepsilon}{4})u, \ x_2(0) = 5. \end{aligned}$$

The parameter ε models parameters variation in the model ($\varepsilon \in [0,\ 1]$). The control u is constrained to belong to the set defined by

$$u_{min} \leq u(t) \leq u_{max}.$$

The Hamiltonian H_ε associated to this OCP is given by

$$H_\varepsilon(x_1, x_2, u, \lambda_1, \lambda_2) = 0.3u^2 + 5(1+\frac{\varepsilon}{4})x_1^2 + \lambda_1((1+\frac{\varepsilon}{5})x_1 - x_1x_2) + \lambda_2(-x_2 + \frac{1}{10}(1+\frac{\varepsilon}{4})u),$$

where λ_1 and λ_2 are the adjoint state associated to x_1 and x_2 respectively. The Hamiltonian H_ε can be written as an affine function of ε

$$H_\varepsilon(x_1, x_2, u, \lambda_1, \lambda_2) = H_0(x_1, x_2, u, \lambda_1, \lambda_2) + \varepsilon(\frac{5}{4}x_1^2 + \frac{\lambda_1 x_1}{5} + \frac{1}{40}\lambda_2 u).$$

The term H_0 is the Hamiltonian associated to the nominal problem (for $\varepsilon = 0$), and it is given by

$$H_0(x_1, x_2, u, \lambda_1, \lambda_2) = 0.3u^2 + 5x_1^2 + \lambda_1(x_1 - x_1x_2) + \lambda_2(-x_2 + \frac{1}{10}u).$$

The details of the calculation of K are given in Appendix E.1.

5.6.2.1 Numerical evaluation

The problem parameters are given in Table 5.2. The two TPBVPs associated to the nominal and the perturbed problems are solved for $\varepsilon \in [0,\ 1]$ and ΔJ has been evaluated numerically.

Table 5.2: Nonlinear problem parameters

Parameter	u_{max}	u_{min}	T
Value	7.5	-7.5	10

The numerical comparison between ΔJ and $K\varepsilon^2/19.8$ (estimated numerically from equation (E.4)) as functions of ε is given in Figure 5.4. The upper bound $K\varepsilon^2/19.8$ estimate well the error in the cost.

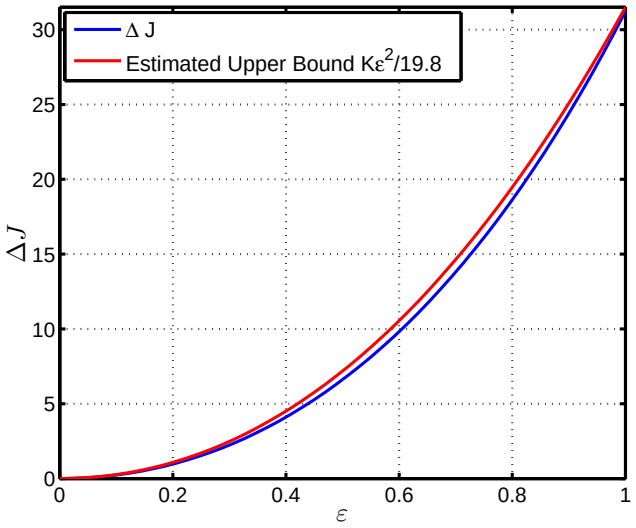

Figure 5.4: $K\varepsilon^2$ for the NL problem

The state trajectories obtained using u_0 and u_ε for different values of ε and the control trajectories are given in Figures 5.5.

5.6.3 Eco-driving problem

The aim of this problem ("eco-driving" problem) is to find a control strategy that minimizes the power consumption of the vehicle within the constraints that the vehicle must

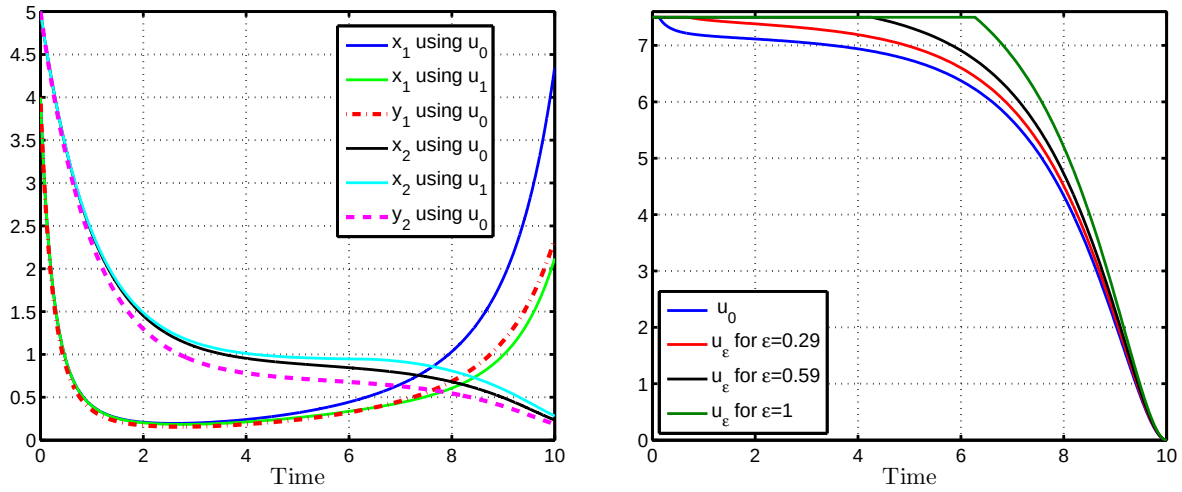

Figure 5.5: State trajectories (left) and optimal controls (right) for $\varepsilon = 1$ for the NL problem

reach a destination point at a distance D in a given time T, with a zero velocity, starting from a given point at rest. This yields the formulation of the following OCP [78].

$$(OCP)\begin{cases} \min\limits_{u} J(u) = \displaystyle\int_0^T (b_1 u x_1 + b_2 u^2)dt + \frac{1}{2}\beta(x_2(T) - D)^2, \\ \dot{x}_1 = h_1 u - h_0, \\ \dot{x}_2 = x_1, \\ x_1(0) = x_1(T) = 0, \\ x_2(0) = 0, \end{cases} \tag{5.27}$$

where x_1 is the vehicle speed, x_2 is the vehicle position, and the parameters b_i and h_i are constants. The objective is to study the effect of the weight β on the optimality of the solution. For this, β is assumed to be of the form

$$\beta = \beta_0 + \varepsilon\beta_1,$$

where β_0 is a nominal value of β, β_1 is the maximum variation of β with respect to its nominal value (β_0 and β_1 are fixed), and $\varepsilon \in [0, 1]$ is a scaling parameter. Two optimization problems can be defined: a nominal problem ($\varepsilon = 0$) and a perturbed problem ($\varepsilon > 0$). For this "eco-driving" problem, the perturbation appears only in the cost function and the estimation of K is more straightforward than the two previous examples (LQ and NL problems). Details of the estimation of K are given in Appendix E.2.

5.6.3.1 Numerical evaluation

The problem parameters are listed in Table 5.3. The nominal and the perturbed TPVBs defined in Appendix E.2 for $\varepsilon \in [0,\ 1]$ are solved using the Matlab routine `bvp4c`.

The induced sub-optimality ΔJ is evaluated numerically. The numerical evaluation of the estimated upper bound on ΔJ as a function of ε given by the relation (E.10) is shown in Figure 5.6.

The quadratic upper bound gives a good estimate of the error when ε is small enough (less than 0.5). The estimation of $K\varepsilon^2$ seems to have the same form as ΔJ, with a ratio

Table 5.3: Eco-driving problem parameters

Parameter	b_1	b_2	h_0	h_1	D	β_0	β_1
Value	1000	1000	0.1	1	10	1000	2000

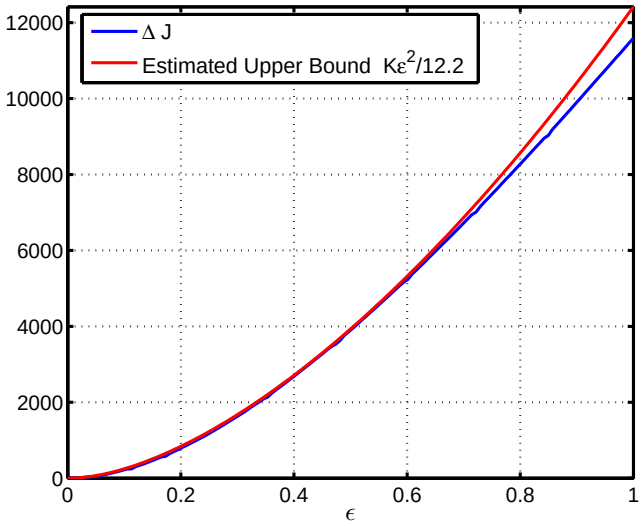

Figure 5.6: Comparison between $K\varepsilon^2$ and ΔJ for the eco-driving problem. The quadratic nature of the error is well observed. The estimation is conservative with a factor of 12.2.

of 12.2 between ΔJ and the estimated $K\varepsilon^2$. The state trajectories for various values of ε are given in Figures 5.7. When ε increases, the maximum speed increases and the final position $x(T)$ tends to its target value D.

5.7 Thermal management problem for HEV

As has been shown in Section 4.1 in the optimal energy management strategy for HEV, neglecting the engine temperature leads to an acceptable sub-optimal fuel consumption. Interestingly, this observation can be justified by Theorem 1. To illustrate this point, the corresponding nominal and perturbed OCP are formulated.

5.7.1 OCP formulation

The cost function under consideration is the fuel consumption given by (B.1). To introduce a perturbation in the cost function, the slope of the correction factor of the fuel consumption $e(.)$ is artificially modified, as shown in Figure 5.8. It is given by an affine function of ε as follows

$$e(\theta_e, \varepsilon) = \begin{cases} \varepsilon_{max}(1 - \dfrac{\theta_e}{\theta_w})\varepsilon + 1, \ \theta_c \leq \theta_e \leq \theta_w, \\ 1, \ \theta_e > \theta_w, \end{cases}$$

where $\varepsilon_{max} = 0.59$, $\varepsilon \in [0,\ 1]$ and $\theta_w = 70°\text{C}$. When $\varepsilon = 0$ (red curve in Figure 5.8), the correction factor is constant and equal to 1 (warm engine start) and the engine temperature can be left out of the equations describing the OCP. When $\varepsilon = 1$ (blue curve

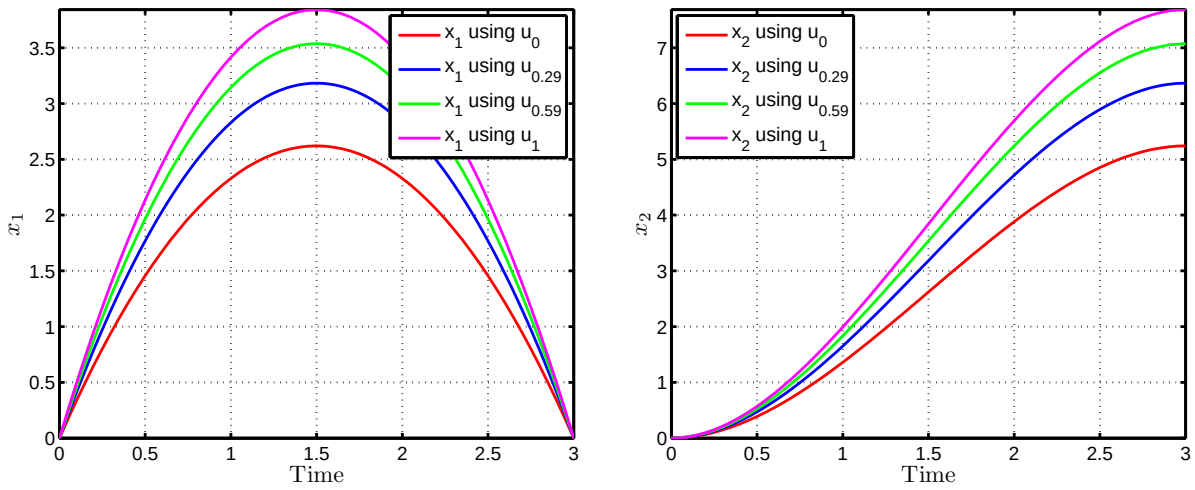

Figure 5.7: Trajectories of x_1 (left) and x_2 (right) for eco-driving problem

in Figure 5.8), the correction factor has maximum sensitivity with respect to the engine temperature (cold engine start). All the curves between the lower ($\varepsilon = 0$) and the upper ($\varepsilon = 1$) boundaries are mathematical extrapolations with no physical interpretation. The

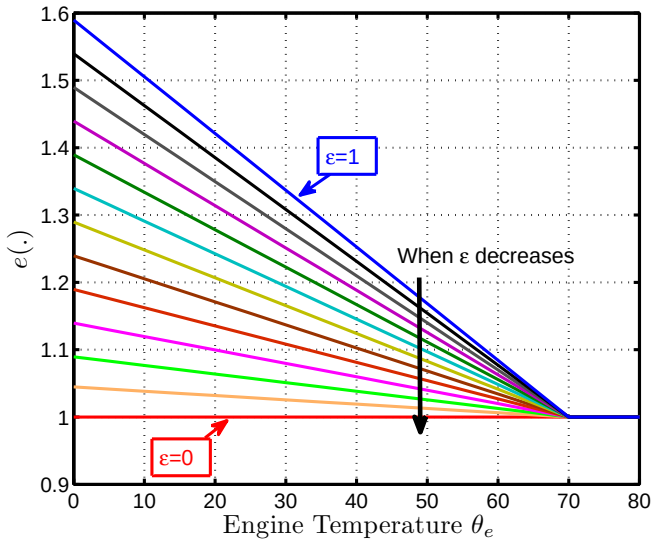

Figure 5.8: Correction factor of the fuel consumption

state variables considered are the SOC and the engine temperature θ_e. Generally, the cost function to be minimized is

$$J_\varepsilon(u) = \beta(\xi(T) - \xi(0))^2 + \int_0^T c(u,t)e(\theta_e, \varepsilon)dt,$$

where β is a parameter used here to include the final constraint on the SOC and is chosen to satisfy the final constraint with a small tolerated error. The perturbed and the nominal

OCP, denoted by (OCP_ε) and (OCP_0) respectively, are defined as

$$(\text{OCP}_\varepsilon) \quad \begin{cases} \min\limits_u \left[J_\varepsilon(u) = \beta(\xi(T) - \xi(0))^2 + \int_0^T c(u,t)e(\theta_e, \varepsilon)dt \right], \\ \dfrac{d\xi}{dt} = f(u,t), \quad \xi(0) = \xi_0, \\ \dfrac{d\theta_e}{dt} = g(u,t,\theta_e), \quad \theta_e(0) = \theta_0, \\ u_{min}(t) \leq u(t) \leq u_{max}(t), \end{cases}$$

$$(\text{OCP}_0) \quad \begin{cases} \min\limits_u \left[J_0(u) = \beta(\xi(T) - \xi(0))^2 + \int_0^T c(u,t)dt \right], \\ \dfrac{d\xi}{dt} = f(u,t), \quad \xi(0) = \xi_0, \\ u_{min}(t) \leq u(t) \leq u_{max}(t). \end{cases}$$

For $\varepsilon = 1$, the (OCP_ε) is obtained from the optimization problem (OCP_2) described in Chapter 4 by setting $\alpha = 0$ (only the fuel consumption is minimized). The (OCP_0) is similar to the problem described by equation (3.6) where the final constraint is taken into account by the final cost.

From an application viewpoint, the problem (OCP_ε), which is considered as the perturbed problem, is the most desirable problem as it is more representative and more accurate than the problem (OCP_0), which is considered as the nominal problem. It is also the most complex.

5.7.2 Numerical evaluation

The details of the estimation of K are given in Appendix E.3. The two problems (OCP_0) and (OCP_ε) for $\varepsilon \in [0,\ 1]$ are solved. The induced sub-optimality ΔJ is evaluated numerically. The quadratic error is observed and evaluated with a conservatism factor of approx 12.

The numerical evaluation of K given by equation (E.17) is shown in Figure 5.9 where ΔJ (calculated numerically) is compared with $K\varepsilon^2$. The quadratic upper bound gives a good estimation of the error when ε is small enough (less than 0.5). For higher values of ε, ΔJ remains below the quadratic conservative estimation of K.

The theorem indicates that the error in the optimal cost between the solutions of the two problems (OCP_0) and (OCP_ε) can not be more than 12%. Numerical studies in Appendix B show that is less than 1%.

5.8 Robustness analysis

Generally, optimal controllers are developed for systems for which the plant model and the cost function are completely specified. Uncertainty arises when some aspects of the system model are not completely known at the time of analysis and design. The typical example is the value of a parameter which may vary according to operating conditions of

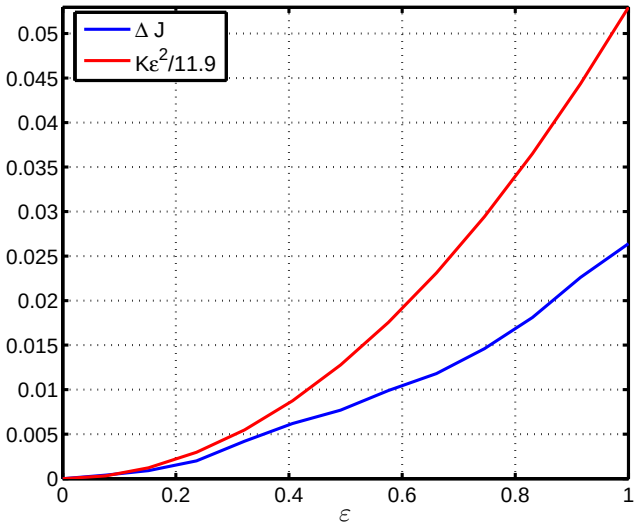

Figure 5.9: Comparison between $K\varepsilon^2$ and ΔJ for the thermal management problem. The quadratic nature of ΔJ is well observed. The estimation is conservative with a factor of 11.9.

the system. The term *uncertainty*, as used here, includes also the result of under-modeling to avoid complex models.

In Section 5.5, the objective was to quantify the error in the optimal cost due to the presence of modeling errors (represented by $\varepsilon \in [0, 1]$). This quantification is given by estimating K from the nominal trajectories. The numerical results presented show that the estimated K is always higher than its real value (the ratio is between 10 and 20 for the considered examples). To decide whether the induced sub-optimality is acceptable or not, the maximum relative error (δ) calculated for $\varepsilon = 1$ by

$$\delta = \frac{K}{J_1(u_0)}$$

is the quantity to be analyzed. If δ is small, the induced sub-optimality is acceptable and the nominal control calculated for $\varepsilon = 0$ is sufficient. The calculated values of δ for the examples considered above are given in Table 5.4. In the last three columns, the OCP considered (LQ and NL problems) have been modified by changing the maximum value of ε (change of scale by replacing ε with the formula shown in brackets in the heading of the corresponding column).

Table 5.4: Maximum relative error and δ values

Problem	Eco-driving	NL	LQ	NL ($\varepsilon/2$)	LQ ($\varepsilon/2$)	LQ ($\varepsilon/4$)
Max error	33%	18%	12%	4.4%	4%	1.1%
δ	3.24	3.08	2.58	0.83	0.66	0.172

In the two first columns of Table 5.4, the induced sub-optimality is important. The value of δ decreases as the relative error decreases. The estimation of K and δ may be used as a tool to analyze the robustness of the nominal strategy addressed by the following question:

> What is the maximum value of ε that would lead to a given maximum desired relative error (δ_{max}) on the optimal cost?

To answer this question, the relative error defined by

$$\delta_1(\varepsilon) = 100\frac{K\varepsilon^2}{J_\varepsilon(u_0)}$$

is used. This quantity, depending on ε, can be estimated numerically, as it depends only on the nominal trajectories and ε (taking into account that this estimated relative error will be 10-20 times greater than its real value) and the maximum value of ε satisfying $\delta_1(\varepsilon) \leq \delta_{max}$ can be calculated. The obtained value will be conservative (less than its real maximum value), since the estimated value of K is always higher than its real value. To illustrate this approach, we consider the following problem for the three OCP described in Section 5.6:

Find the maximum value of ε leading to $\delta_{max} = 4\%$ of the optimal cost.

The values of ε are summarized in Table 5.5 (note that w is the ratio between the estimated and the real value of K).

Table 5.5: Maximum values of ε for $\delta_{max} = 4\%$

Problem	$w = 1$	$w = 10$	$w = 20$
LQ	0.133	0.3903	0.5443
NL	0.106	0.334	0.46
Eco-driving	0.0576	0.2105	0.324

For the LQ problem, the maximum value of ε satisfying the maximum sub-optimality of 4% is in the interval $[0.133, 0.54]$. For $\varepsilon = 0.39$, the real relative error is 2.55% and for $\varepsilon = 0.5443$, the real relative error is 4.62%. The value $\varepsilon = 0.39$ can be considered as a conservative upper bound for modeling errors.

The results in Table 5.5 show that it is possible to estimate a conservative upper bound on the modeling uncertainties leading to a desired maximum relative error in the optimal cost. The conservatism of this estimated bound depends on the ratio between the estimated K and its real value.

5.9 Possible extension: state constraints

In the presence of state constraints of the form $g(x) \leq 0$, the method suggested in Theorem 1 has to be adapted. Generally state constraints are a difficult problem in optimal control. Some perturbation sensitivity results have been addressed in [12]. In fact, for a given value of r, modeling errors in the dynamics may lead to a violation of the state constraints if the nominal control u_0^r is used. The input constraints are still satisfied but it is very difficult to guarantee a priori that u_0^r will satisfy the state constraints. The same notations for the state, adjoint state and the control variables used in Sections 5.2.1 and 5.2.2 are now used below. A penalty function $r\gamma_g(g(x))$ of the form (3.11) is added in the expressions of the Hamiltonian to manage the state constraints for the nominal and the perturbed problems.

For a fixed value of r, u_ε^r is the optimal control for the penalized problem and $c(r)$ is the minimum distance from the constraints

$$g(x_\varepsilon^r) \leq c(r) \leq 0.$$

An estimation of $c(r)$ is given in the following proposition.

Proposition 8 *For a positive constant s and a given $\bar{\gamma}(r)$ such that*

$$\bar{\gamma}(r) \geq \int_{t_1}^{t_2} \gamma_g(g(x(\tau)))d\tau,$$

an estimation of the upper bound on $c(r)$ is given by

$$c(r) \leq -\sqrt[n_g]{\frac{s}{\bar{\gamma}(r)\Gamma(1+s)^{(n_g+1)}}}, \tag{5.28}$$

where the constant $\bar{\gamma}(r)$, depending on r, is an upper bound on the integral of the penalty and it increases when the penalty weight r goes to zero and Γ is a positive constant.

Proof The proof is given in Appendix D.6. ■

The optimal control and the optimal state trajectory, solution of the OCP defined by the new state constraints $g(x) \leq c(r)$, are $(u^*,\ x^*)$. As u^* is the optimal control, we have

$$J_\varepsilon(u^*) \leq J_\varepsilon(u_\varepsilon^r).$$

But, since u_ε^r is the optimal control for the penalized problem, we have

$$J_\varepsilon(u^*) + r\int_0^T \gamma_g(g(x^*(t)))dt \geq J_\varepsilon(u_\varepsilon^r) + r\int_0^T \gamma_g(g(x_\varepsilon^r(t)))dt,$$

yielding

$$0 \leq J_\varepsilon(u_\varepsilon^r) - J_\varepsilon(u^*) \leq r\int_0^T [\gamma_g(g(x^*(t))) - \gamma_g(g(x_\varepsilon^r(t)))]dt. \tag{5.29}$$

This relation shows that the induced sub-optimality and the satisfaction of the constraints are related: if the induced sub-optimality $J_\varepsilon(u_\varepsilon^r) - J_\varepsilon(u^*)$ is high, the error in the state constraints will be high. As γ_g is positive, this inequality can be written

$$0 \leq J_\varepsilon(u_\varepsilon^r) - J_\varepsilon(u^*) \leq r\int_0^T \gamma_g(g(x^*(t)))dt.$$

If the term $r\int_0^T \gamma_g(g(x^*(t)))dt$ is low, the error in the cost will be low. A trade-off between the constraint satisfaction and the optimality of the solution can be made. This point is illustrated in the next section.

By using a particular adjustment between the modeling error and the penalty weight parameter r, we show that it is possible to generate a path of solutions strictly lying in the interior of the state constraints and to have a near-optimal cost value. For a given value of r, x_0^r satisfies the state constraints. This is not guaranteed for the trajectory ξ^r, as its dynamics takes the perturbation into account. To avoid violating the state constraints for ξ^r, the weight r is used as a tuning parameter: for a given ε, the nominal problem is solved for different decreasing values of r and the algorithm is stopped for $r = r_0$ when ξ^{r_0} is close to the constraints. This method ensures that the constraints are satisfied. A central question then arises: how far is the obtained cost function from its optimal value?

To answer this question, the results presented in Section 3.4.3.2 for the state constraints on the SOC are analyzed. From Table 3.4, the difference between the control strategies for $r = 5e^{-7}$ and $r = 8e^{-9}$ is less than 2% in the cost function value whereas the distance from the constraint for $r = 5e^{-7}$ is 8.23. Similar conclusion can be drawn from Tables 3.3, B.2 and B.3. This distance form the constraint will be useful in the presence of error modeling to ensure that the state constraints are satisfied. This point is illustrated in the next section.

5.9.1 Illustrative example

Consider the following LQ problem under state and input constraints

$$\min_{u\in U^{ad}} J_\varepsilon(u) = \int_0^{10} \left[\frac{1}{10}u^2 + (x_1-1)^2\right] dt,$$

where x_1, x_2 and u are the state and the control variables of the following system

$$\dot{x}_1 = x_2, \quad x_1(0) = -1, \tag{5.30}$$
$$\dot{x}_2 = (1+\varepsilon)u, \quad x_2(0) = 0. \tag{5.31}$$

The parameter ε scales the modeling error in the state dynamics. The state x_1 has to satisfy the inequality

$$x_1(t) \leq 0,$$

and the control u is constrained to belong to the set defined by

$$-1 \leq u(t) \leq 1.$$

To solve this problem, we define the modified cost $J_\varepsilon^r(u)$ as

$$J_\varepsilon^r(u) = \int_0^{10} \left[\frac{1}{10}u^2 + (x_1-1)^2 + \frac{r}{(-x_1)^{n_g}}\right] dt.$$

By using the PMP, the optimal control u_ε^r is given by

$$u_\varepsilon^r = \min\left(1, \max\left(-1, -5(1+\varepsilon)\lambda_2\right)\right), \tag{5.32}$$

where λ_1 and λ_2 are the adjoint states of x_1 and x_2 respectively. Their dynamics are

$$\dot{\lambda}_1 = -2(x_1-1) - \frac{r.n_g}{(-x_1)^{n_g+1}}, \quad \lambda_1(10) = 0, \tag{5.33}$$
$$\dot{\lambda}_2 = -\lambda_1, \quad \lambda_2(10) = 0. \tag{5.34}$$

Equations (5.30, 5.31, 5.32, 5.33, 5.34) constitute a TPBVP, which is solved using the Matlab routine `bvp4c`.

The trajectories of x_1 and the variation of costs $J_\varepsilon(u_\varepsilon^r)$ and $J_\varepsilon^r(u_\varepsilon^r)$ for a fixed value of ε are given in Figure 5.10 and 5.11, respectively. Figure 5.10 shows that the state trajectories of x_1 approach the constraints when r goes to zero. Figure 5.11 shows that the costs $J_\varepsilon(u_\varepsilon^r)$ and $J_\varepsilon^r(u_\varepsilon^r)$ decrease when r decreases as expected theoretically, and the difference between these two costs becomes negligible after a certain value of the penalty weight r.

To illustrate the remark given by equation (5.29), the value of ε is fixed ($\varepsilon = 0.09$). The value of $c(r_0)$ calculated from the nominal control is $c(r_0) = 0.0826$ and the value of r from which the state constraints are not satisfied is $r_0 = 0.0148$. For a fixed ε, the results, summarized in Table 5.6, illustrate that when $J_0(.)$ decreases the term $\int_0^T \gamma_g(.)dt$ increases.

The problem of interest is to find a nominal control u_0^r leading to an acceptable sub-optimal cost function while the state constraints are satisfied. For a given ε, the procedure is the following:

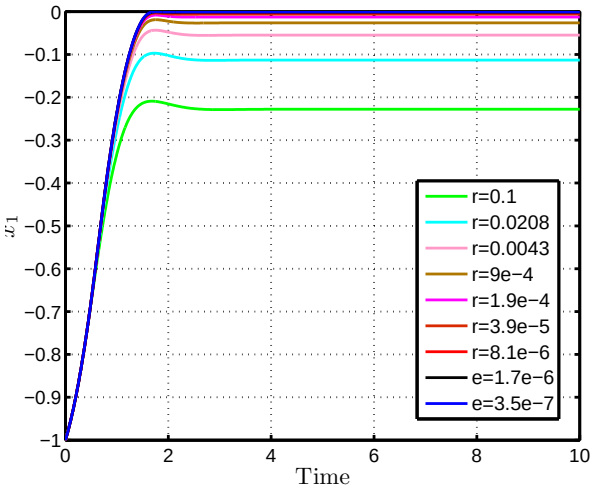

Figure 5.10: x_1 for decreasing values of r

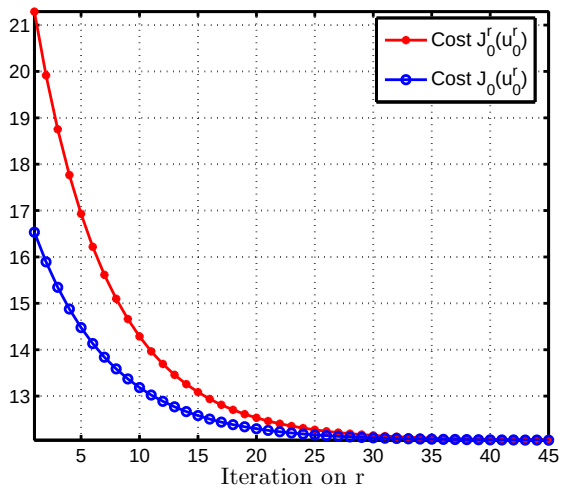

Figure 5.11: Variation of $J_0(u_0^r)$ and $J_0^r(u_0^r)$

Table 5.6: Error in cost function in the case of state constraints

Quantity	$J_0(.)$	$\int_0^{10} \gamma_g(.)dt$	$J_0^{r_0}(.)$
u^*	14.428	132.922	16.395
$u_0^{r_0}$	14.659	114.368	16.352

- solve the nominal and the perturbed problems for different decreasing values of the weight r;
- estimate the error in the state trajectories solution of (5.30, 5.31) using the nominal control u_0^r;
- find the value of the penalty weight, denoted by r_0, such that the state constraint is not satisfied. The error in the state trajectories is evaluated for decreasing values of r and the algorithm is stopped when the state constraint is not satisfied;
- calculate $J_\varepsilon^{r_0}(u_0^{r_0})$, $J_\varepsilon(u_0^{r_0})$, $J_\varepsilon^{r_0}(u_\varepsilon^{r_0})$ and $J_\varepsilon(u_\varepsilon^{r\to 0})$ (the optimal value of the cost function);
- calculate ΔJ_1 and ΔJ_2 given by

$$\Delta J_1 = J_\varepsilon^{r_0}(u_0^{r_0}) - J_\varepsilon^{r_0}(u_\varepsilon^{r_0}),$$

$$\Delta J_2 = \frac{J_\varepsilon(u_0^{r_0}) - J_\varepsilon(u_\varepsilon^{r\to 0})}{J_\varepsilon(u_\varepsilon^{r\to 0})}.$$

Figures 5.12 and 5.13 show the variation of ΔJ_1 and ΔJ_2 as a function of ε. The trajectories of x_1 for $\varepsilon = 0.09$ and for two values of r are given in Figures 5.14 and 5.15.

From Figure 5.12, the error ΔJ_1 in the modified cost function $J_\varepsilon^r(.)$ is bounded by a quadratic form in ε as expected theoretically (as the state constraints are satisfied, the method presented in [7] is applicable). In Figure 5.14, r is chosen such that the state constraints are satisfied by the perturbed trajectories. On the other hand, in Figure 5.15, the penalty weight r has been decreased until state constraint is violated. These two

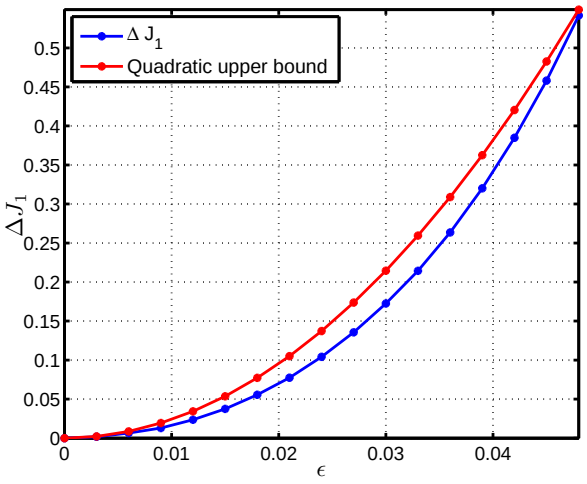

Figure 5.12: ΔJ_1 as a function of ε

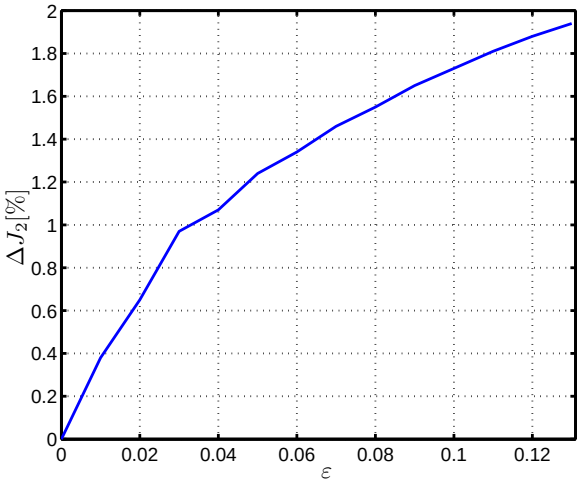

Figure 5.13: ΔJ_2 as a function of ε

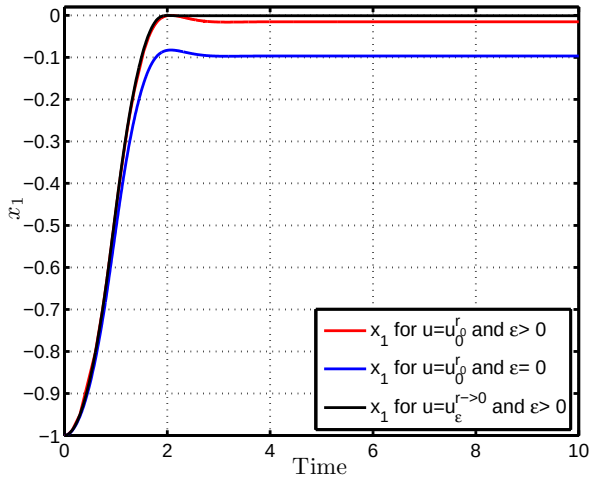

Figure 5.14: x_1 for $\varepsilon = 0.09$ and $r > r_0$

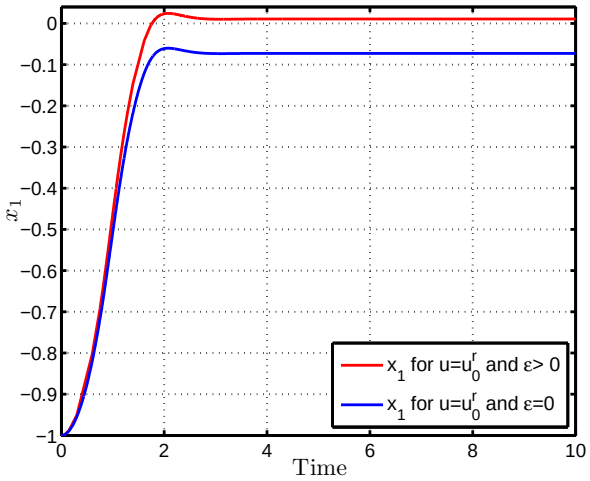

Figure 5.15: x_1 for $\varepsilon = 0.09$ and $r < r_0$

figures illustrate the possibility of handling the state constraint by an appropriate choice of the parameter r.

From the variation of ΔJ_2 (the error in the cost function $J_\varepsilon(.)$) given in Figure 5.13, the induced sub-optimality in the value of J_ε by using the nominal control $u_0^{r_0}$ is less than 2% for $\varepsilon \leq 0.13$. This nominal solution can thus be seen as robust, since the state constraint is satisfied and the sub-optimality is less than 2%.

5.9.2 Discussion

The method presented in the previous section, based on the interior penalty approach, allow a trade-off to be made between the satisfaction of the state constraints and the induced sub-optimality of the nominal control strategy in the presence of perturbation in the dynamics and the cost function. In the interior penalty approach, the difference between the modified cost $J_\varepsilon^r(.)$ and the cost $J_\varepsilon(.)$ decreases when the penalty weight r is reduced. After a certain threshold of r, the difference is negligible as shown in Figure 5.11.

Another possible solution to deal with modeling uncertainty is to calculate a priori

safety distance from the constraint based on dynamics error calculation for any control input. The illustrated solution in the example allow also the determination of this safety distance for the nominal control u_0^r which will be less conservative than the a priori safety distance. After, the same optimal control problem with the new modified state constraints is solved. This approach ensures the constraints satisfaction. The question remains whether the discussed method in the previous numerical example is better than this classical approach in terms of the cost function value.

5.10 Conclusion

Performing the open-loop optimization with the simplified model (plant and cost) and then implementing the optimal trajectory is the most commonly used approach in optimal controller design; however, it is difficult to generate highly accurate models due to the limited quality and quantity of experimental data and models complexity. Thus, in practice, the results of implementing model-based controller often lead to differences between reality and simulation, whatever the model used for process optimization. The method based on the estimation of K presented in this chapter allow induced sub-optimality to be quantified a priori, from the solution of the simplified OCP as demonstrated in the illustrative examples. Estimation of K can be also used to analyze the robustness of nominal controller.

Part III

Real-time strategies
Stratégies temps-réel

Chapter 6

ECMS feedback control

Chapitre 6 Comme il a été mentionné précédemment, les stratégies optimales pour l'EMS obtenues par le PMP nécessitent une parfaite connaissance du cycle de conduite. En une situation réelle, les conditions futures de conduite sont inconnues. Pour des raisons d'implementabilité, la stratégie de contrôle doit être calculée à partir de l'information disponible en temps réel. Une des méthodes utilisées pour faire face à l'incertitude sur les conditions de conduite est l'ECMS. Cette méthode a été utilisée uniquement pour le problème de la gestion d'énergie mono-état en considérant seulement le SOC.

Dans ce chapitre, une description de l'ECMS est donnée avec une étude théorique sur ses propriétés asymptotiques. Ensuite, des extensions possibles de cette stratégie pour inclure les états thermiques (du moteur et du système de dépollution) dans l'optimisation sont présentées et étudiées. Ces extensions sont basées sur la paramétrisation de la relation entre l'état adjoint et l'état, indépendamment des conditions de conduite.

Contents

As it has been mentioned before, optimal strategies obtained by the PMP are determined using full knowledge of the driving cycle. In real situation, the future driving conditions are unknown. For practical applications, the control strategy has to be calculated from the available information in real-time. One of the methods used to deal with driving condition uncertainties is ECMS [64, 74, 79]. This method has thus far been developed only for the single-state energy management problem.

In this chapter, a description of the ECMS is given. We propose a theoretical study about its asymptotic property. Then, extensions to include thermal state variables in the optimization are presented and studied.

6.1 Equivalent consumption minimization strategy (ECMS)

6.1.1 ECMS formulation

The ECMS can be seen as a real-time strategy partially based on optimal control theory [64, 74, 79]. It addresses the single-state EMS described in Chapter 3. In its original formulation, the battery (electric energy) is considered as an auxiliary fuel tank. The control input is selected to minimize the total power drawn from the two tanks (fuel and electric power) by comparing the variation in total energy for the different possible values of the control input at each time t. Combining these two rates (variation in the electric power and the fuel consumed c) into a single cost requires the introduction of a weighting factor λ such that

$$\left(c(u,t) + \lambda(t)\frac{d\xi}{dt}\right)\Delta t.$$

This quantity is then to be minimized at each time t and it is similar to the formula of the Hamiltonian H_0 in equation (3.12) where λ is the adjoint state associated to the SOC. In this formula, λ acts as a weight on the price of the electrical energy, so that:

- if λ is high, the electricity is more expensive, and the thermal mode is preferred;
- if λ is low, the electricity is less expensive and it is preferable to use the electric/power assist mode.

The advantage of this strategy is its dependency on a single parameter, λ. Two information about this parameter are then needed: the initial value λ_0 and its dynamics. From the PMP applied to the single-state OCP, λ is constant on the optimal trajectory, but in the absence of knowledge of the future driving conditions, it is not possible to know the optimal value of λ that would satisfy the final constraint on the SOC. In other words, uncertainties about the future driving conditions are transferred (in an equivalent form) into an uncertainty on the value of λ. The optimal control formula (3.14) still holds. To use it, $\lambda(t)$ is replaced by an online estimation as a function of the available information (in this case, the SOC value) [15, 16, 37]

$$\lambda(t) = \lambda_0 - k_p \cdot (\xi_{ref} - \xi(t)), \tag{6.1}$$

where $\lambda_0 < 0$ is a first guess possibly inspired by offline calculations, and k_p is a tunable positive coefficient. This feedback relation can be interpreted as follows:

- If $\xi(t)$ is greater than ξ_{ref}, the control strategy has to discharge the battery by using the electric machine; the relation (6.1) should reduce $|\lambda(t)|$;
- If $\xi(t)$ is lower than ξ_{ref}, the control strategy has to recharge the battery by using the ICE; the value of $|\lambda(t)|$ should then increase.

In many cases, to favor the convergence of $\xi(t)$ toward ξ_{ref}, an integral term might be appended to the right-hand term of (6.1), regulated by a second positive parameter k_i

$$\lambda(t) = \lambda_0 - k_p \cdot (\xi_{ref} - \xi(t)) - k_i \cdot \int_0^t (\xi_{ref} - \xi(s))ds. \tag{6.2}$$

More complicated feedback have been reported in the literature [60, 62, 81, 85].

6.1.2 Relation between ECMS and linear quadratic regulator

In fact, it is possible to relate the ECMS to the more usual linear quadratic regulator (which allows the calculation of an optimal feedback for linear systems and neighboring optimal control in more complex cases). To establish this relation, the following assumptions are considered:

- The fuel consumption $c(u, \omega_{eng})$ is approximated by a second-order polynomial function in u with the coefficients c_i that depend on the engine rotational speed,

$$c(u, \omega_{eng}) = c_0(\omega_{eng})u^2 + c_1(\omega_{eng})u. \tag{6.3}$$

- The dynamic of the SOC is approximated by an affine function of the control u,

$$f(u, t) = -\alpha_0(\omega_{el})u - \alpha_1(\omega_{el}). \tag{6.4}$$

  This assumption is relevant if the power requested by the electric machine is not important compared to the maximum available power and the losses in the battery are neglected. Otherwise, f is quadratic in u.

- The constraints on the control variable u are neglected, which is equivalent to considering a powerful machine and a large battery.

As the vehicle is assumed to follow a prescribed driving cycle, the parameters $(c_i,\ \alpha_i)$ become functions of time. To take into account the final constraint on the SOC, a final quadratic cost is added to the fuel consumption,

$$J_0^m(u) = \beta \cdot (\xi(T) - \xi_{ref})^2 + \int_0^T c(u, t)dt. \tag{6.5}$$

To satisfy the final constraint (3.3) exactly, β should be infinite, which is not possible from a numerical viewpoint. Thus, a certain error in $(\xi(T) - \xi_{ref})$ must be allowed. The problem (OCP_0) aiming at minimizing (6.5) with the definitions (6.3, 6.4), and in the absence of state and input constraints, is a linear quadratic problem (LQ).

From the PMP, the necessary and sufficient condition for which u_0^* is the optimal control minimizing (6.5) under the dynamics (3.2), is given by

$$u_0^*(\lambda, t) = \frac{\lambda\alpha_0 - c_1}{2c_0}. \tag{6.6}$$

Applied to this problem, DP gives an expression of the costate variable as a function of the state and time. Indeed, $\Im(\xi, t)$ is defined as the optimal cost for the problem (6.5) where the initial time 0 is replaced by $t \in [0, T]$ and the initial state condition is replaced by $\xi(t)$. As the problem is linear quadratic without constraints, its value function $\Im(\xi, t)$, the optimal control and the adjoint state are determined by solving a Riccati differential equation [14].

Since the state only appears in the optimal control problem by the difference $\xi(T) - \xi_{ref}$, a variable x defined by

$$x(t) = \xi_{ref} - \xi(t)$$

is used to simplify the calculations. The form of $\Im$ is quadratic with respect to x such that

$$\Im(x^*, t) = \frac{1}{2} v_0(t) \cdot x^{*2} + v_1(t) \cdot x^* + v_2(t).$$

Then, λ^* is given by

$$\lambda^*(t) = \frac{\partial \Im}{\partial \xi}(x^*, t) = v_0(t) \cdot x^*(t) + v_1(t), \tag{6.7}$$

where x^* is the optimal state trajectory. In this expression, λ^* *is an affine function of* x*, with a time varying gain and a time varying drift.* The parameters v_0 and v_1 are solutions of the time varying differential equations obtained from Riccati equation

$$\begin{aligned} \frac{dv_0}{dt} &= \frac{\alpha_0^2}{2c_0} \cdot v_0^2, \qquad v_0(T) = 2\beta, \\ \frac{dv_1}{dt} &= \left(\frac{\alpha_0 c_1}{2c_0} - \alpha_1 \right) \cdot v_0 + \frac{\alpha_0^2}{2c_0} \cdot v_0 \cdot v_1, \qquad v_1(T) = 0. \end{aligned}$$

These equations are solved backward to compute the optimal control, the state and the costate trajectories. Observe that if $\beta = 0$, the parameters $v_0 = v_1 = 0$, which is intuitive since, in the absence of the final constraint, the optimal strategy is to use the electric energy available in the battery as there is no instantaneous constraint on the SOC.

The expression (6.7) of λ as a function of x is similar to the formula (6.1) where the drift λ_0 and the gain k_p are time varying. This is the analogy one can draw between ECMS and LQ control.

6.1.3 ECMS parameters robustness

The choice of the ECMS parameters is very important to ensure the near-optimality of the resulting control strategy. These parameters are mutually related. They are tied to the driving cycle and to the state constraints (if these have to be considered in the optimization problem).

To investigate the robustness of the ECMS parameters calibration with respect to the variation of the driving conditions, four driving cycles are considered; we proceed as follows:

- Calibrate the ECMS parameters for each driving cycle such that the obtained performance in terms of fuel consumption is close to the optimal strategy.
- Use each combination of the (calibrated) parameters to simulate other driving cycles.

- Compare the obtained fuel consumption to its optimal value.

The results in terms of fuel consumption and satisfaction of the final SOC constraint (expressed by the error $\xi(T) - \xi(0)$) for the ECMS and the optimal strategy calculated by the PMP are summarized in Tables 6.1 and 6.2. It is apparent in these tables that the optimality of the solution is strongly related to the choice of the parameters λ_0 and k_p, and in most of the cases, a trade-off between fuel consumption minimization and final state constraint satisfaction must be done.

Table 6.1: Fuel consumption in [L/100 km] using different combination of ECMS parameters. In each column, a simulation has been made for parameters that are tuned for the cycle shown in the column heading. In each row, the fuel consumption has been computed for the cycle shown for that row. These results are only partial. See Table 6.3.

Tuning	**PMP**	**NEDC**	**FHDS**	**FTP**	**WLTC$_m$**
NEDC	4.385	4.393 (+0.2%)	4.74 (+8.1%)	4.88 (+11.3%)	4.72 (+7.6%)
FHDS	5.10	4.89 (-4.1%)	5.11 (+0.2%)	5.19 (+1.8%)	5.06 (-0.8%)
FTP	4.01	3.72 (-7.2%)	3.93 (-2%)	4.02 (+0.25%)	3.92 (-2.2%)
WLTC$_m$	4.94	4.85 (-1.8%)	5.01 (+1.4%)	5.04 (+2%)	4.94 (+0.1%)

Table 6.2: Percentage difference between final value and target value of ξ ($\xi(T) - \xi(0)$) [%]. These values are to compensate the cost in Table 6.3.

Tuning	**PMP**	**NEDC**	**FHDS**	**FTP**	**WLTC$_m$**
NEDC	0.02	-0.09	5.93	8.04	5.13
FHDS	0.035	-5.82	0.1	2	-1.43
FTP	-0.013	-8.40	-2.66	0.01	-2.84
WLTC$_m$	-0.017	-3.38	2.5	3.33	-0.05

The separate comparison of the fuel consumption and the final constraint satisfaction may introduce some confusions in interpreting the results. In fact, the two quantities are related:

- If the final SOC is below its target value ξ_{ref}, the fuel consumption will be below its optimal value. The battery will be discharged. To fulfill the final constraint on the SOC, the battery will have to be recharged (in the future) using the converted energy by the electric machine. This amount of energy will be provided by the ICE that will lead to a real extra-fuel consumption;

- if the final SOC exceeds its target value ξ_{ref}, the fuel consumption will exceed its optimal value (due to the excessive use of the engine). The battery has been recharged. To bring the SOC to its target value, a future discharge of the battery is required. This discharge will be done using the electric machine which will produce some mechanical power used to propel the vehicle. This mechanical power is equivalent to a real fuel consumption reduction. Indeed, the ICE will have to produce less mechanical power to produce the same power at the wheels. The remained part is produced by the electric machine.

To avoid such awkwardness, the equivalent fuel consumptions (Q_{eq}) is compared for the different parameters combination, as it is commonly done in the literature dealing with EMS for HEV [28, 64, 65, 74]. This equivalent consumption represents the consumed fuel while the final constraint on the SOC is satisfied: the new cost function is the sum of the real fuel consumption rate $c(u,t)$ and the equivalent fuel consumption related to the use of the battery. Indeed, it is clear that the electrical energy and the fuel energy are not directly comparable and a conversion factor is needed. According to [64, 65], this factor is the optimal adjoint state λ[1] determined by the PMP:

$$Q_{eq} = \int_0^T c(u,t)dt + \lambda \cdot (\xi(T) - \xi(0)). \tag{6.8}$$

The values of the obtained equivalent fuel consumption are given in Table 6.3. We emphasize that the purpose of the final constraint on the SOC, in reality, is to make a fair comparison between different control strategies. These results show that all the combinations used lead to a quasi-optimal equivalent fuel consumption Q_{eq}.

Table 6.3: Equivalent fuel consumption (Q_{eq}) in [L/100 km] using different ECMS parameters

Tuning	**PMP**	**NEDC**	**FHDS**	**FTP**	**WLTC$_m$**
NEDC	4.384	4.40 (+0.4%)	4.40 (+0.4%)	4.42 (+0.8%)	4.42 (+0.8%)
FHDS	5.10	5.12 (+0.4%)	5.11 (+0.2%)	5.11 (+0.2%)	5.12 (+0.2%)
FTP	4.01	4.03 (+0.5%)	4.02 (+0.25%)	4.02 (+0.25%)	4.03 (+0.5%)
WLTC$_m$	4.94	4.95 (+0.2%)	4.95 (+0.2%)	4.96 (+0.4%)	4.95 (+0.2%)

6.1.4 ECMS stability analysis

The study presented here is based on assumptions (6.3, 6.4). The variable z is defined by

$$z = \int_0^t x(s)ds.$$

By replacing the formula for u_0^* given by equation (6.6) in ξ dynamics, we can write

$$\frac{d\xi}{dt} = f(u_0^*(\lambda,t),t) = -\lambda\frac{\alpha_0^2}{2c_0} + \frac{\alpha_0 c_1}{2c_0} - \alpha_1 \triangleq -\lambda \cdot D_1(t) + D_2(t), \tag{6.9}$$

where λ is given by the proportional-integral formula in equation (6.2). The parameters λ_0, k_p and k_i in (6.2) are fixed.

If the dynamics (6.9) were a time-invariant equation, and if $\lambda_0 = 0$, then the expression (6.2) would be basically a PID system whose stability could be straightforwardly analyzed using a Laplace domain analysis. This method does not apply to time-varying systems. Instead, a Lyapunov function approach is used [38]. By combining equations (6.9) and (6.2), one gets

$$\dot{x} = -D_1(t) \cdot [\lambda_0 - k_p x - k_i z] + D_2(t). \tag{6.10}$$

[1]This could be established by involving a calculus of marginal cost of the constraints.

The other state variable is

$$y = k_i z - \lambda_0 + G, \qquad G = \frac{D_2}{D_1}.$$

In its state-space form, the system (6.10) is

$$\dot{x} = -D_1(t) \cdot [k_p x + y], \tag{6.11}$$
$$\dot{y} = k_i x + \dot{G}. \tag{6.12}$$

This system is time-variant with a time-varying perturbation G. The term $D_1(t)$ is positive (as c_0 is positive) and can be considered as a positive constant d perturbed by a function of time $\delta(t)$ of the form

$$D_1(t) = d + \delta(t), \tag{6.13}$$

where d may be estimated from the driving cycle data. Typically, it can be taken equal to the mean value of $D_1(t)$. The stability of the previous system (6.11, 6.12) is studied by considering it as successive perturbation of a linear time invariant (LTI) system.

6.1.4.1 LTI system

In the first step, the following LTI system without perturbation is studied

$$\dot{x} = -d \cdot [k_p x + y], \tag{6.14}$$
$$\dot{y} = k_i x. \tag{6.15}$$

The purpose of this analysis is to find a Lyapunov function [38] to be used in the following. The stability of the system (6.14, 6.15) can easily be checked by taking a quadratic Lyapunov function V

$$V = \begin{bmatrix} x & y \end{bmatrix} P \begin{bmatrix} x \\ y \end{bmatrix},$$

where P is a symmetric positive definite matrix solution of the Lyapunov equation

$$A^T P + P A = -I.$$

The matrix A is the dynamic matrix of the system (6.14, 6.15). The matrix P is given by

$$P = \frac{1}{2d} \begin{bmatrix} p_1 & p_2 \\ p_2 & p_3 \end{bmatrix} = \frac{1}{2d} \begin{bmatrix} \frac{1}{k_p} + \frac{k_i}{k_p d} & 1 \\ 1 & \frac{d}{k_p k_i} + \frac{d k_p}{k_i} + \frac{1}{k_p} \end{bmatrix}.$$

The matrix P is definite positive if the gains k_p and k_i are strictly positive

$$k_p > 0, \quad k_i > 0.$$

Details are given in Appendix F.1.

6.1.4.2 Time-varying system without source terms

The next step is to introduce a perturbation term $\delta(t)$ defined in equation (6.13) in the dynamics (6.14, 6.15),

$$\dot{x} = -(d+\delta(t))\cdot[k_p x + y], \tag{6.16}$$
$$\dot{y} = k_i x. \tag{6.17}$$

The objective in this second step is to find sufficient conditions on perturbation term $\delta(t)$ so that the system (6.16, 6.17) remains stable by using the Lyapunov matrix P calculated before. By using Lyapunov theory again, we end up with the following conditions on $\delta(t)$

$$\frac{\delta(t)}{d} < 2\frac{k_p s+1}{(k_p-s)^2}\left(1+\sqrt{1+\frac{(s-k_p)^2}{(sk_p+1)^2}}\right), \tag{6.18}$$
$$\frac{\delta(t)}{d} > \max\left(\frac{-2d}{2d+k_i}, 2\frac{k_p s+1}{(k_p-s)^2}\left(1-\sqrt{1+\frac{(s-k_p)^2}{(sk_p+1)^2}}\right)\right), \tag{6.19}$$

where s is given by

$$s = \frac{1}{k_p} + \frac{k_i}{dk_p}.$$

These bounds are achieved by considering the same Lyapunov function V, calculating its derivative $\dot{V}$ with respect to time and finding conditions on $\delta(t)$ such that $\dot{V} < 0$ independently from x and y. The detail of the calculations is given in Appendix F.2. These strict inequalities are satisfied for $\delta(t) = 0$, and hence for small values of $\delta(t)$.

6.1.4.3 Time-varying system with source terms

In the final step, the following nominal system is considered

$$\dot{x} = -(d+\delta(t))[k_p x + y],$$
$$\dot{y} = k_i x + \dot{G}.$$

This system is equivalent to (6.11, 6.12). Using Lyapunov theory and assuming that $\delta(t)$ satisfies the conditions (6.18, 6.19), there exists a set defined by

$$f_1\left[x+\frac{f_2}{f_1}y-\frac{\dot{G}(t)}{2df_1}\right]^2+(f_3-\frac{f_2^2}{f_1})\left[y-\frac{\dot{G}(t)}{2d}\frac{f_1 s_1-f_2}{f_3 f_1-f_2^2}\right]^2 \leq \frac{\dot{G}^2(t)}{4d^2 f_1}\left[1+\frac{(f_1 s_1-f_2)^2}{f_3 f_1-f_2^2}\right] \tag{6.20}$$

outside of which the Lyapunov function (V) decreases. The functions (f_i) depend on time and they are given by

$$f_1 = 1+\frac{\delta(t)}{d}k_p s,\ \ f_2 = \frac{\delta(t)}{2d}(k_p+s),\ \ f_3 = 1+\frac{\delta(t)}{d}.$$

The following proposition summarizes this result.

Proposition 9 (Stability) *Assume that $\delta(t)$ satisfies the conditions (6.18, 6.19). Then, equation (6.20) defines an ellipse for the variables $(x,\ y)$. The states $x = \xi_{ref} - \xi$ and*

$$y = -\lambda_0 + k_i\int_0^t(\xi_{ref}-\xi(s))ds + \frac{c_1}{\alpha_0} - \frac{2\alpha_1 c_0}{\alpha_0^2}$$

converge to inside this set. Moreover, the origin always belongs to this ellipse. If the term $\dot{G}$ *tends to* 0*, the ellipse converge to the origin of the state space* $(x,\ y)$*.*

Proof See Appendix F.3. ■

This result shows that the closed loop system determined using the ECMS formula (6.2) remains stable, but a priori, not asymptotically. In practice, equations (6.18, 6.19) give upper bounds on $\delta(t)$, which may be used to calculate the gains k_p and k_i ensuring the stability of the system. However, the sub-optimality of the ECMS depends on the choice of the parameters $(\lambda_0,\ k_p,\ k_i)$ as shown in the previous section.

6.1.5 Conclusion

The parameters of the ECMS are sensitive to the driving conditions. The calibration impacts the fuel consumption and the final constraint satisfaction. Separate comparisons introduce a confusion in the results interpretation if the final constraint on the SOC is not fulfilled as explained above. On the other hand, when combined, the results become clear. The error in the equivalent fuel consumption is less than 0.8% comparing to the optimal fuel consumption.

6.2 ECMS extension to include catalyst temperature

In this section, the engine is warm at the beginning of the driving cycle. The impact of the engine temperature θ_e on fuel consumption and CO emissions is negligible. Only the catalyst temperature θ_c needs to be considered in the optimization problem.

6.2.1 Formulation of ECMS$_1$

To extend the ECMS, we aim at finding a relationship between the adjoint state ρ (associated to θ_c defined in Section 4.3) and the catalyst temperature θ_c (which is assumed to be measured or at least estimated). Ideally, this relation has to be robust against the driving conditions variation.

For convenience, an equivalence factor that is positive and dimensionless, denoted by q, is used instead of using ρ (which is negative). The relationship between the two parameters is given by

$$q(t) = -\frac{H_{lhv}}{C_c}\rho(t).$$

Figure 6.1 shows the relationship between q and θ_c on the optimal trajectories calculated using the PMP for $\alpha = 0.6$. Similar behaviors are obtained for other driving cycles for $\alpha \in [0,\ 1[$. Three intervals are distinguished:

- $\theta_c \leq 200°\text{C}$: the cost function is independent of θ_c. The dynamics of q is given by

$$\dot{q}(t) = -q(t) \cdot \frac{\partial P_{cat}(t)}{\partial \theta_c}(u, t, 80, \theta_c). \tag{6.21}$$

- $200°\text{C} \leq \theta_c \leq 400°\text{C}$: the cost function depends on θ_c and an additional term related to the derivative of η_{CO} modified the dynamics of q in (6.21).

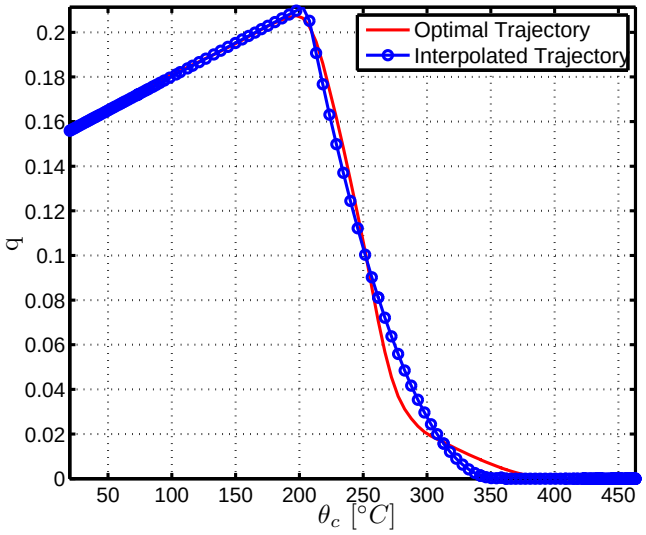

Figure 6.1: Equivalence factor q as a function of θ_c for $\alpha = 0.6$ for FUDS

- $\theta_c \geq 400$°C: the cost function becomes again independent of θ_c; q is equal to zero as the final temperature $\theta_c(T)$ is free.

The relationship between q and θ_c is not monotonic, but this does not cause any problem because q is calculated from θ_c (assumed to be measured) and not the reverse. The proposed relationship between q and θ_c is of the form

$$q(\theta_c) = \begin{cases} d_1\theta_c + d_2, \text{ if } \theta_c \leq 200°\text{C}, \\ d_3\theta_c^2 + d_4\theta_c + d_5, \text{ if } 200°\text{C} < \theta_c \leq 400°\text{C}, \\ 0, \text{ if } \theta_c > 400°\text{C}, \end{cases} \tag{6.22}$$

where the parameters d_i have to be identified from the optimal trajectories calculated by the PMP. The threshold 200°C, beyond which the behavior of the equivalence factor q changes, is the activation temperature of the after-treatment system. The threshold 400°C is the temperature beyond which the efficiency of the after-treatment system reaches its maximum value. For the equivalence factor s associated to the SOC, the classical ECMS formula (B.11) is used.

The stationarity condition is expressed on the quantity $\tilde{H}_1$ (in power unit)[2] given in (6.23). It is the sum of three quantities: the fuel energy consumed, the inner (electro-chemical) battery power, the thermal powers due to the variation of the after-treatment system temperatures defined by $P_{cat}(t) = -C_c \cdot \dot{\theta}_c$

$$\tilde{H}_1(u, t, \theta_c, s, q) = L(u, t, \theta_e = \theta_h, \theta_c) \cdot H_{lhv} + s \cdot I_b(t) \cdot U_{ocv}(t) + q \cdot P_{cat}(t). \tag{6.23}$$

The control u_1 is given by

$$u_1(t) \in \arg\min_{u \in U^{ad}} \tilde{H}_1(u, t, \theta_c, s(\xi), q(\theta_c)),$$

where $(s,\ q)$ are respectively given by (B.11, 6.22). This defines the ECMS$_1$ strategy.

[2] $\tilde{H}_1$ is equivalent to H_1 defined in Section 4.4.

6.2.2 Tuning ECMS$_1$ with respect to α

As the control strategy depends on α, we study the variation of the parameters d_i with respect to α. For the NEDC cycle, we proceed as follows:

- solve the OCP defined in Section 4.4 for different values of α;
- identify the parameters $d_i,\ i = 1:5$ for each value of α;
- find the relationship between each d_i and α by interpolation.

The obtained results are given in Figures 6.2, 6.3, 6.4 and 6.5. *This tedious work is done once, and offline.* From these figures, each parameter d_i can be approximated by an affine function of α

$$d_i = k_{1,i}\alpha + k_{2,i}.$$

The parameters d_2 and d_5 are determined to ensure the continuity of the equivalence factor q at $\theta_c = 200°\text{C}$ and $\theta_c = 400°\text{C}$. These relations, once identified for NEDC, are used for the other driving cycles.

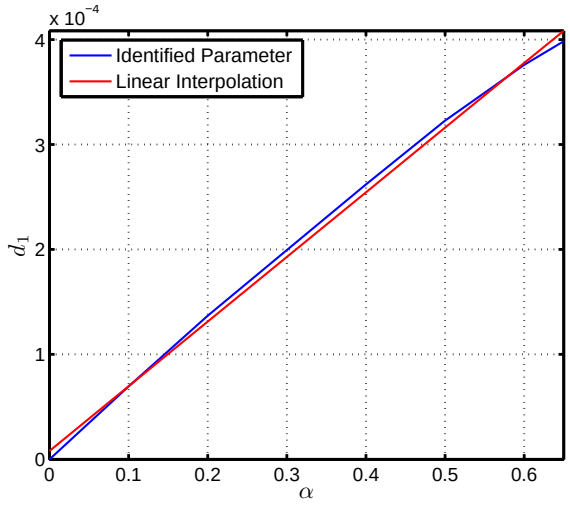

Figure 6.2: d_1 as a function of α for NEDC

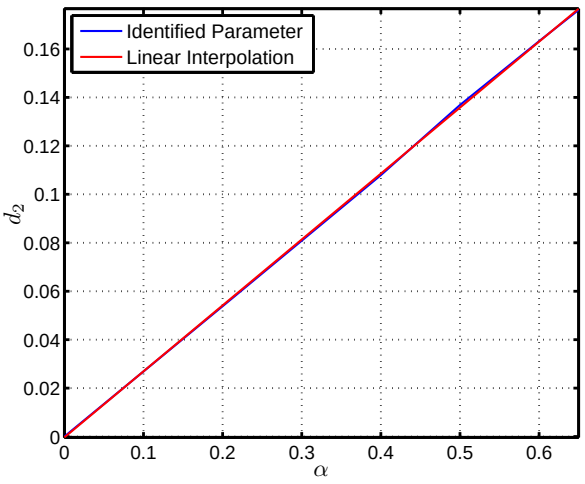

Figure 6.3: d_2 as a function of α for NEDC

6.2.3 Robustness of ECMS$_1$

The proposed rule in (6.22) to update q (or ρ) as a function of θ_c is established for the NEDC for different values of α, and is also tested for the other three driving cycles: FTP, WLTC$_m$ and FHDS. For the equivalence factor s, a single calibration of the parameters s_0 and K_p is used and this calibration does not ensure the satisfaction of the final constraint on the SOC. The initial value s_0 and the gain K_p[3] are the average of the values ensuring the satisfaction of the final constraint on the SOC for the four driving cycles. By taking the average of the parameters s_0 and K_p, the driving cycle is assumed to be unknown.

[3]The relation between k_p (used in the formula of λ) and K_p (used in the formula of s) is given by

$$K_p = \frac{H_{lhv}}{Q_0 \cdot U_{ocv}} k_p.$$

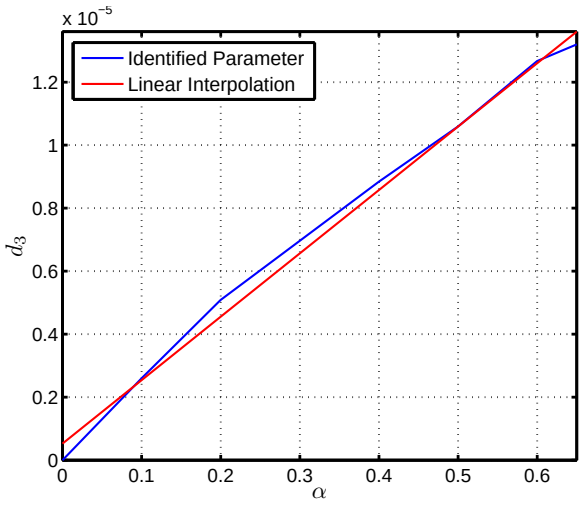

Figure 6.4: d_3 as a function of α for NEDC

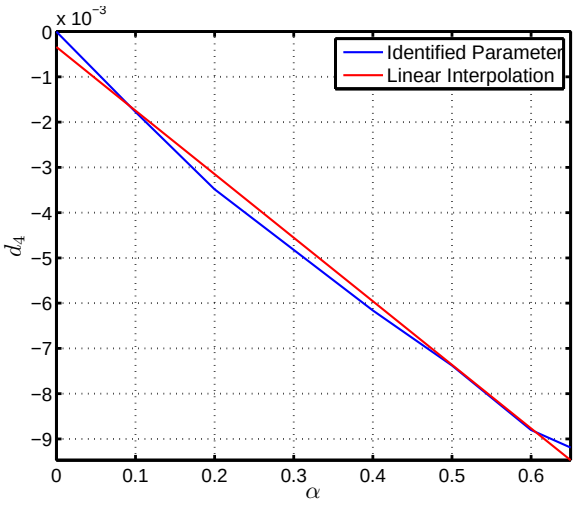

Figure 6.5: d_4 as a function of α for NEDC

The relative errors in terms of fuel consumption, CO emissions and satisfaction of the final SOC constraint (expressed by the error $\xi(T) - \xi(0)$) comparing to the optimal strategy (S_1) by using the strategy ECMS$_1$ are summarized in Figures 6.6, 6.7 and 6.8 respectively.

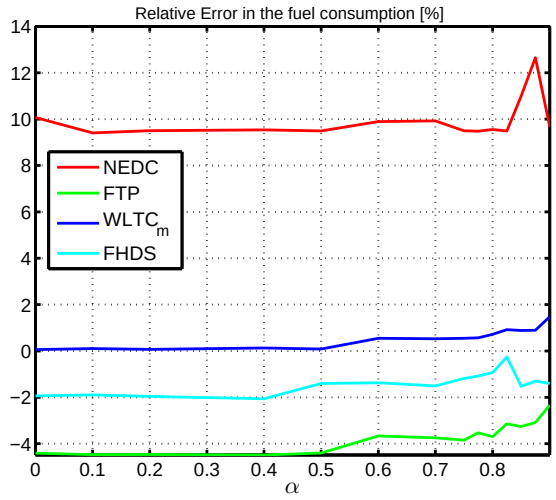

Figure 6.6: Relative error in fuel consumption [%]

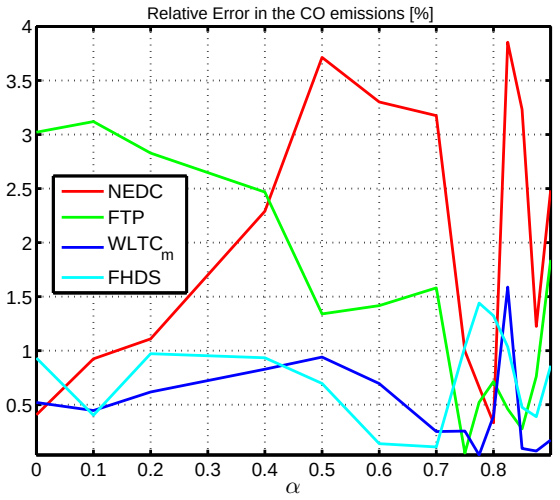

Figure 6.7: Relative error in CO emission [%]

From Figures 6.6 and 6.7, the maximum error in the CO emissions between the strategy (S_1) and ECMS$_1$ is less than 4% while the maximum error in the fuel consumption is more important (10%) for the considered driving cycles. This maximum error depends on the driving cycle and the final constraint satisfaction. For example, in the case of the WLTC$_m$, the error in the final constraint and the fuel consumption are lower than the other driving cycles. The optimality of the solution is strongly related to the choice of the parameters s_0 and K_p, and in most of the cases, the fuel consumption is greatly impacted comparing to the CO emissions. A trade-off between the fuel consumption evaluation and the final SOC constraint satisfaction has to be done.

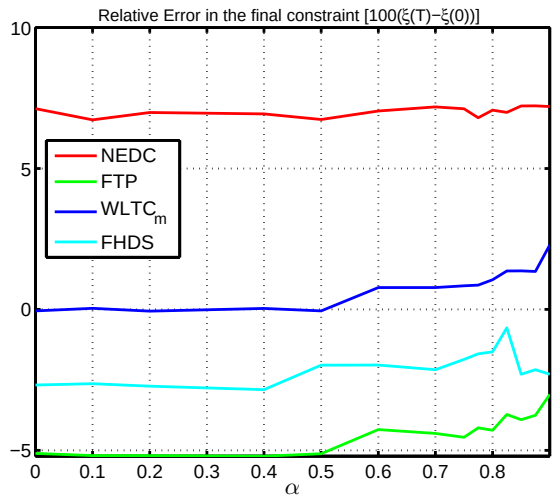

Figure 6.8: Final constraint satisfaction

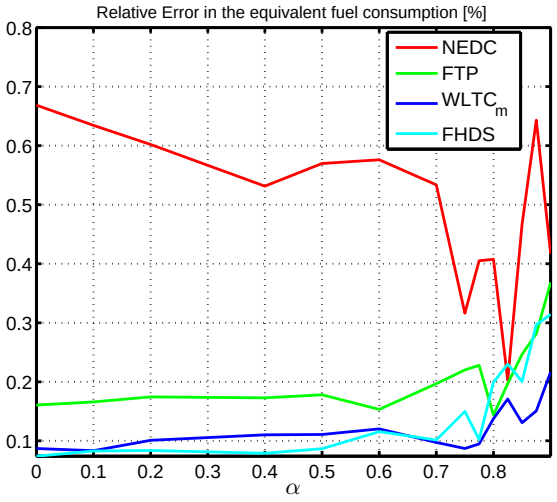

Figure 6.9: Relative error in equivalent fuel consumption [%]

For the reasons mentioned in Section 6.1.3, the equivalent fuel consumption Q_{eq}^{1} [4], defined for $\alpha \neq 0$ in (6.24), must be compared to the optimal fuel consumption obtained by using the strategy (S_1) instead of comparing the fuel consumption and the final constraint satisfaction separately.

$$Q_{eq}^{1} = \frac{1}{\alpha}\left[\int_0^T \alpha \cdot c(u,t)dt + \lambda \cdot (\xi(T) - \xi(0))\right]. \tag{6.24}$$

As the fuel consumption is multiplied by α in the cost function, the conversion factor between the electrical energy and the fuel energy is the optimal adjoint state λ divided by α. The impact of θ_e on the fuel consumption and CO emissions is neglected as the engine is warm. The equivalent fuel consumption Q_{eq}^{1} is compared to the optimal fuel consumption calculated by using the strategy (S_1) for a warm engine start. The obtained relative error in the fuel consumption are summarized in Figure 6.9. These results show that all the used combinations allow to reach a quasi-optimal equivalent fuel consumption with a maximum relative error around 0.7% comparing to the optimal fuel consumption while the error in CO emissions is less than 4%.

6.2.4 Conclusion

The proposed correlation to update q using measurements of θ_c has been shown to be robust against the driving conditions change. The induced sub-optimality, compared to the strategy (S_1), in the equivalent fuel consumption is less than 0.7% while the sub-optimality in CO emissions is less than 4% comparing to the optimal values (if the optimal value of CO emissions is 0.8 g/km, the obtained value by using ECMS_1 is 0.832 g/km). The main problem is to find an efficient way of estimating s, as its calibration has a significant effect on the final SOC constraint.

[4] The superscript ^{1} in Q_{eq}^{1} refers to the use of the control strategy ECMS_1.

6.3 ECMS extension to include engine and catalyst temperature

The engine is cold at the beginning of the driving cycle. The impact of θ_e on the fuel consumption and the CO emissions has to be considered. The OCP formulation is given in Section 4.3. The results will be compared to those given by the strategy (S_2).

6.3.1 Formulation of ECMS$_2$

Following the analysis of the relationships between (p, q) and $(\theta_e,\ \theta_c)$ in Sections B.4.1 and 6.2.1, the proposed relationships to update $(p,\ q)$ are of the form

$$p(\theta_e) = \begin{cases} a_1\theta_e^2 + a_2\theta_e + a_3, \text{ si } \theta_e \leq 80°\text{C}, \\ 0, \text{ si } \theta_e > 80°\text{C}. \end{cases}$$

$$q(\theta_c) = \begin{cases} d_1\theta_c + d_2, \text{ si } \theta_c \leq 200°\text{C}, \\ d_3\theta_c^2 + d_4\theta_c + d_5, \text{ si } 200°\text{C} < \theta_c \leq 400°\text{C}, \\ 0, \text{ si } \theta_c > 400°\text{C}, \end{cases}$$

where the parameters $(a_i,\ d_i)$ have to be identified as in Sections B.4.1 and 6.2.1. The relation between p and θ_e is detailed in Appendix B.4.1 for the fuel consumption minimization case ($\alpha = 0$). For the equivalence factor s, the classical ECMS formula (B.11) is used.

The stationarity condition is expressed on the quantity $\tilde{H}_2$[5] given in (6.25). It is the sum of four quantities: the fuel energy consumed, the inner (electrochemical) battery power, the thermal powers due to the variation of the engine and the after-treatment system temperatures defined by $P_{therm}(t) = -C_e \cdot \dot{\theta}_e$ and $P_{cat}(t) = -C_c \cdot \dot{\theta}_c$

$$\tilde{H}_2 = L(u, t, \theta_e, \theta_c) \cdot H_{lhv} + s \cdot I_b(t) \cdot U_{ocv}(t) + p \cdot P_{therm}(t) + q \cdot P_{cat}(t). \tag{6.25}$$

The optimal control u_2 minimizes $\tilde{H}_2$

$$u_2(t) \in \arg\min_{u \in U^{ad}} \tilde{H}_2(u, t, \theta_e, \theta_c, s(\xi), p(\theta_e), q(\theta_c)).$$

The obtained control strategy is denoted by ECMS$_2$.

6.3.2 Robustness of ECMS$_2$

The proposed rules to update $(p,\ q)$ as functions of $(\theta_e,\ \theta_c)$ are determined for the NEDC for different values of α and they will be tested for the other three driving cycles: FTP, WLTC$_m$ and FHDS. For the equivalence factor s, a single calibration of the parameters s_0 and K_p is used: as it has been highlighted in Sections 6.1.3 and B.4, the final constraint is sensitive to these two parameters. The used calibration does not ensure the satisfaction of the final constraint on the SOC for the considered driving cycles. The relative errors comparing to the optimal strategy (S_2) in terms of fuel consumption, CO emissions and the satisfaction of the final SOC constraint (expressed by the error $\xi(T) - \xi(0)$) for the strategy ECMS$_2$ are summarized in Figures 6.10, 6.11 and 6.12 respectively.

[5] $\tilde{H}_2$ (in power unit) is equivalent to H_2 defined in Section 4.4.

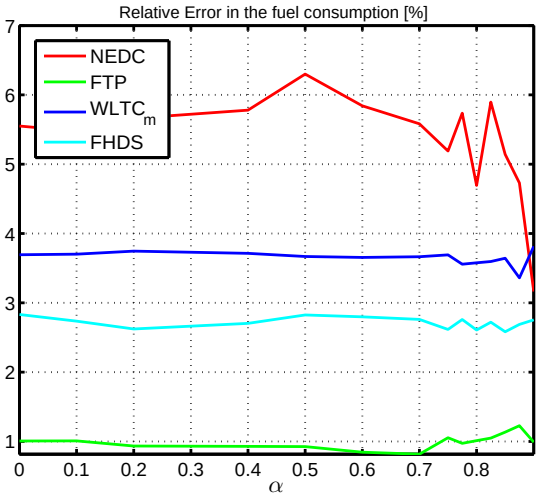

Figure 6.10: Relative error in fuel consumption [%]

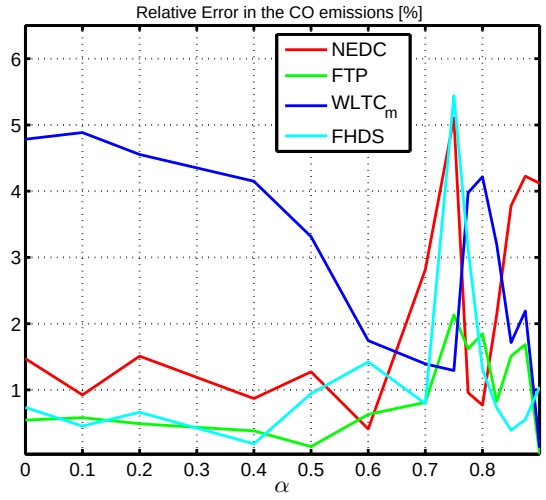

Figure 6.11: Relative error in CO emission [%]

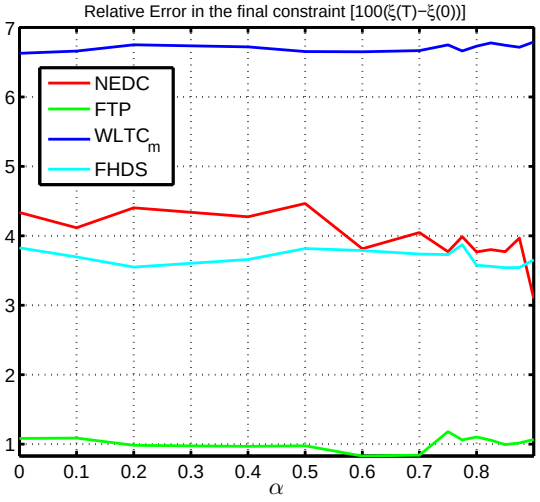

Figure 6.12: Final constraint satisfaction

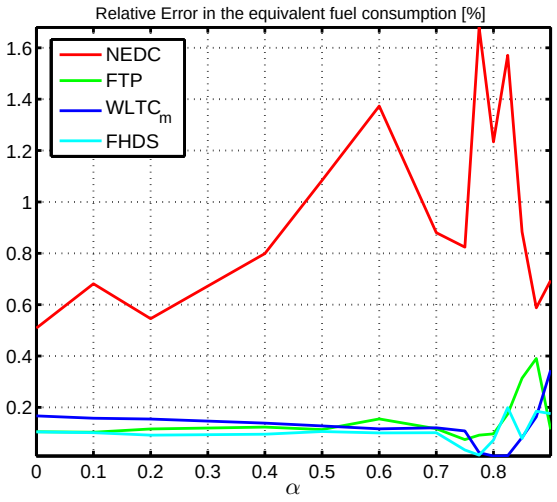

Figure 6.13: Relative error in equivalent fuel consumption [%]

From Figures 6.10 and 6.11, the maximum error in the CO emissions between the strategy (S_2) and ECMS$_2$ is less than 5.5% while the maximum error in the fuel consumption is less than 6% for the considered driving cycles. This maximum error depends on the driving cycle and the final constraint satisfaction. For example, in the case of the FTP cycle, the error in the final constraint and the fuel consumption are lower than the errors for the other driving cycles.

For the reasons mentioned in Section 6.1.3, the equivalent fuel consumption Q_{eq}^{2} [6], defined for $\alpha \neq 0$ in (6.26), must be compared to the optimal fuel consumption obtained by using the strategy (S_2) instead of comparing the fuel consumption and the final constraint satisfaction separately. The formula (6.26) is the general expression to calculate the equivalent fuel consumption. The previous formulas given in (6.8, 6.24, B.12) can be

[6] The superscript ^{2} in Q_{eq}^{2} refers to the use of the control strategy ECMS$_2$ for cold start conditions.

easily deduced from the expression (6.26)[7].

$$Q_{eq}^2 = \frac{1}{\alpha}\left[\int_0^T \alpha \cdot c(u,t)e(\theta_e)dt + \lambda \cdot (\xi(T) - \xi(0))\right]. \tag{6.26}$$

The obtained relative errors in the equivalent fuel consumption are summarized in Figure 6.13. From these numerical comparisons, the maximum relative error in the equivalent fuel consumption Q_{eq}^2 is less than 1.8% comparing to the optimal strategy (S_2).

To illustrate the added value of the strategies ECMS_1 and ECMS_2, the fuel consumption and CO emissions obtained using ECMS_1 and ECMS_2 are compared to their optimal values calculated by using the strategies (S_1) and (S_2) for cold-start conditions for NEDC see Figure 6.14. In this case, the parameters $(s_0,\ K_p)$ are tuned to satisfy the final constraint on the SOC. The full simulation model (3.2, 4.1, 4.3, 4.4) is used for the comparison.

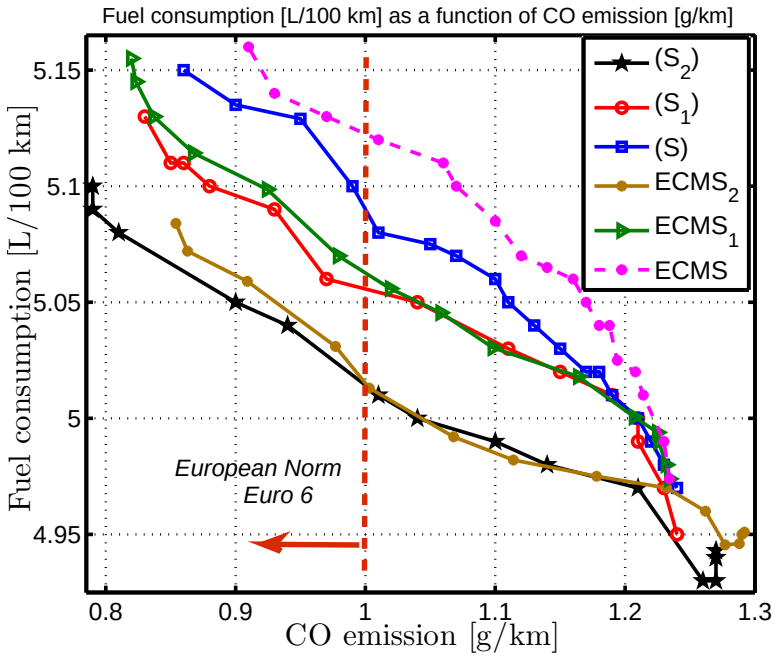

Figure 6.14: Fuel consumption [L/100 km] and CO emissions [g/km] for NEDC

These numerical results show that the strategies ECMS, ECMS_1 and ECMS_2 are close to the strategies (S), (S_1) and (S_2), respectively, in terms of fuel consumption and CO emissions. The three real-time strategies allow the CO emissions to be reduced in order to satisfy the European legislation with an acceptable extra-fuel consumption comparing to the optimal strategy (S_2).

6.3.3 Conclusion

The proposed correlations to update $(p,\ q)$ using the measurements of $(\theta_e,\ \theta_c)$ have been shown to be robust against the driving conditions change. The induced sub-optimality in the equivalent fuel consumption is less than 2% while sub-optimality in CO emissions is less than 6%.

[7]For the formula (6.8), $\alpha = 1$ and the engine is warm at the beginning of the driving cycle. For the formula (6.24), $\alpha \in [0,\ 1]$ and the engine is warm at the beginning of the driving cycle. For the formula (B.12), $\alpha = 1$ and the engine is cold at the beginning of the driving cycle.

6.4 Discussion

The proposed correlations to update $(p,\ q)$ using measurements of $(\theta_e,\ \theta_c)$ seems promising for the pollutant emissions reduction with an acceptable extra-fuel consumption compared to the optimal strategy (S_2). These correlations are *identified* from the optimal trajectories given by the PMP (DP can be also used). The presented results in the previous sections illustrate also the sensitivity of the control strategy to the parameters s_0 and K_p used for the adaptation of the equivalence factor s associated to the SOC. The fuel consumption and the final constraint are greatly impacted by the choice of s_0 and K_p. The separate comparison of these two quantities jeopardize the analysis. The use of the equivalent fuel consumption in the comparison avoids such difficult situation.

The strategies ECMS_1 and ECMS_2 can be seen as closed loop strategies. In fact, under certain assumptions, see [1], the PMP allows the optimal control to be written as a function of the state $x(t)$ and of the adjoint state $\lambda(t)$ from the stationarity condition:

$$u^* = W(x(t), \lambda(t)),\ t \in [0,\ T].$$

In the three proposed strategies, λ is given by a function of the state $x(t)$

$$\lambda(t) = \frac{\partial \Im}{\partial x}(x^*, t) = F(x(t)),\ t \in [0,\ T],$$

where $\Im$ is the cost-to-go function. By combining these two quantities, the formula of the optimal control u^* becomes of the form

$$u^* = L(x(t)),\ t \in [0,\ T].$$

The main difficulty of this procedure is the relation between $\lambda(t)$ and $x(t)$. In our case, this relation is carried out numerically from the optimal solution calculated using the PMP.

Chapter 7

Experimental tests

Chapitre 7 Le système considéré dans ce chapitre est un véhicule hybride de type parallèle équipé d'un moteur diesel. Comme le plupart des moteurs diesel modernes, le système de dépollution est composé de trois sous-systèmes en cascade : un catalyseur d'oxydation diesel (DOC) pour traiter les HC et CO, un filtre à particules diesel (FAP) pour traiter les PM, et un système de réduction sélective catalytique (SCR) par l'urée pour la réduction des NO_x.

D'après la conclusion du chapitre 4, l'EMS mono-état optimal permet de réduire les émissions polluantes avec une surconsommation du carburant acceptable par rapport à la solution optimale (autour de 3%). En outre, les résultats numériques présentés dans la section 6.3 suggèrent que l'ECMS, si soigneusement réglé, donne des performances proches de celles de l'EMS mono-état optimal. Dans ce chapitre, nous souhaitons établir expérimentalement ce résultat avec un accent particulier sur les NO_x.

Dans ce chapitre, la description du banc d'essai et les caractéristiques du véhicule sont données. Ensuite, l'identification des dynamiques thermiques et la formulation du problème de commande optimale sont détaillées. Enfin, les résultats expérimentaux sont discutés.

Contents

For the diesel engine under consideration in the presented application, four pollutants are regulated by current standards: hydrocarbons (HC), carbon monoxide (CO), nitrogen oxides (NO_x), and particulate matter (PM).

Like most of modern engines, our engine is equipped with an after-treatment system composed of three sub-systems: diesel oxidation catalyst (DOC) to treat HC and CO, diesel particulate filter (DPF) to treat PM, and urea selective catalytic reduction (SCR) for NO_x reduction. NO_x and PM are the most problematic issues for diesel after-treatment systems.

Following the conclusion of Chapter 4, the optimal single-state EMS allows the pollutant emissions to be reduced with an acceptable extra-fuel consumption compared to the optimal solution. Additionally, the numerical results presented in Section 6.3 for real-time strategies suggest that the ECMS, if carefully tuned, gives performance close to the optimal single-state EMS. In this chapter, we wish to establish this fact, experimentally with a focus on the NO_x emissions.

This chapter is organized as follows: first, the test bench description and the characteristics of the vehicle are given; then the thermal dynamics identification and the optimization problem formulation are detailed, followed by a description of the simulation platform. Finally, the simulation and the experimental results are discussed.

7.1 Test bench description

In order to reduce the total development cycle of a complete hybrid powertrain and the on-board vehicle calibration, dynamic engine test benches are used. The aim of this kind of bench is to provide an environment where the driver and vehicle behavior can be reproduced. Based on this idea, a dynamic test bench dedicated to hybrid powertrains was developed at IFP Energies nouvelles [17].

This testing tool is able to experimentally represent various hybrid architectures through the hardware-in-the-loop (HiL) concept used in the development and the validation of complex real-time embedded systems. It provides an effective platform by adding the complexity of the plant under control to the test platform. The Hybrid HiL (Hy-HiL) test bench under consideration couples a real engine test bench with mathematical models running in real-time to emulate the electric system, the driver and the vehicle. The rationale for testing a real engine combined with simulated components is to evaluate the fuel consumption and pollutant emissions of the vehicle, taking into account thermal and transient phenomena that are not fully reproduced in a completely simulated system. The high accuracy of the selected models allows Hy-HiL to test either a single component or the whole system in a realistic environment [16, 17].

Figures 7.1 and 7.2 describe the Hy-HiL arrangement. The test bench is controlled in such a way that the torque $T_{eng,mes}$ at the engine output shaft is the response to the driver's requests $T_{wh,sp}$ (i.e., to follow a prescribed driving cycle defined by the vehicle

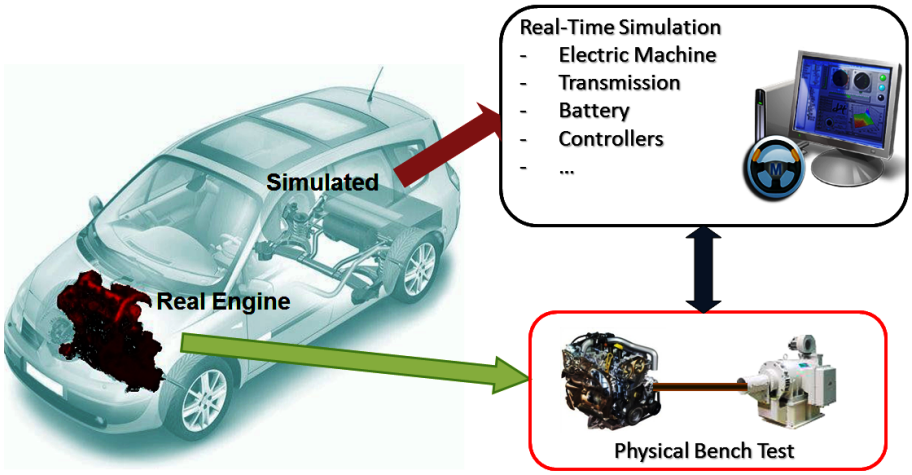

Figure 7.1: Schematics of the Hy-HiL concept

speed $v_{wh,sp}$) and the output of the supervisory controller (EMS) that splits such requests $T_{wh,sp}$ between the engine and the electric machine. In particular, the hybrid driveline model delivers the engine speed set-point to the dynamo-meter control, and the driver model delivers the position of the accelerator and the brake pedals to the powertrain control. The engine speed ω_{eng} and the electric machine speed ω_{el} are related to the vehicle speed at wheels $\omega_{wh,mes}$ by the relations

$$\begin{cases} \omega_{eng}(t) = R_{gb}(t) \cdot \omega_{wh,mes}(t), \\ \omega_{el}(t) = R_{el} \cdot \omega_{wh,mes}(t), \end{cases}$$

where R_{gb} is the gear-box ratio. A more detailed description of the test bench is given in [53]. Photos of the used test bench during the HYDIVU project at IFPEN [69] are given in Figure 7.3. This test bench is equipped with a diesel engine. The after-treatment system is composed of three cascaded sub-systems: DOC, DPF and SCR. Details are given in next sections.

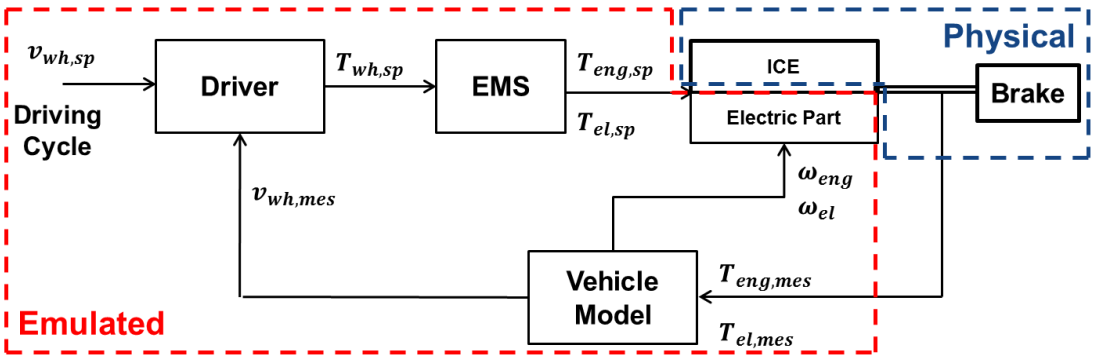

Figure 7.2: Outline of signals flow in the Hy-HiL test bench

7.2 Vehicle description

The architecture under consideration is a parallel HEV equipped with a diesel engine. The electric machine allows power assist, including purely electric drive and battery recharge.

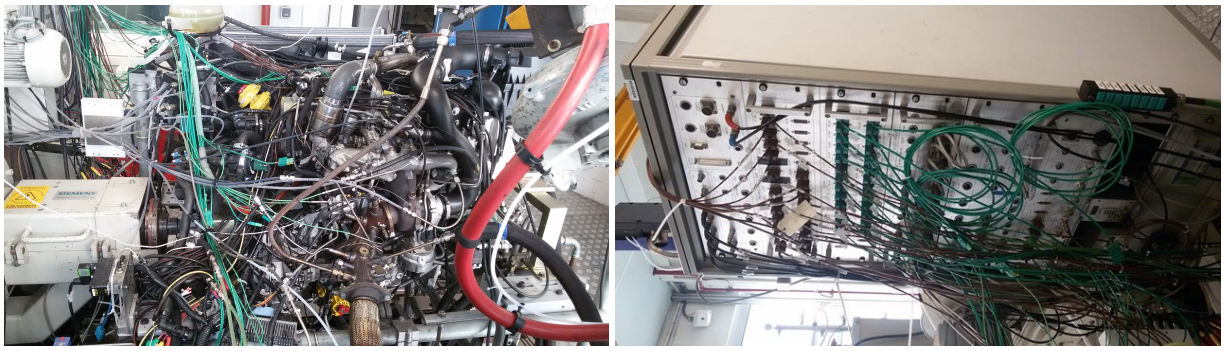

Figure 7.3: Test bench at IFP Energies nouvelles

The transmission ratio between the electric machine and the wheel is constant. The vehicle specifications are summarized in Table 7.1. The fuel consumption and NO_x maps are reported in Figures 7.4 and 7.5 as functions of the engine rotational speed and the indicated engine torque. The engine friction torque map, depending on the engine speed and the engine (water) temperature is given in Figure 7.6 and it is used to calculate the engine effective torque[1]. All reported data were obtained from experimental tests conducted during the HYDIVU project at IFPEN [69].

Table 7.1: Vehicle characteristics

Vehicle weight	2772 kg
Engine max. power	120 kW
Electric machine max. power	50 kW
Battery capacity	4000 Wh

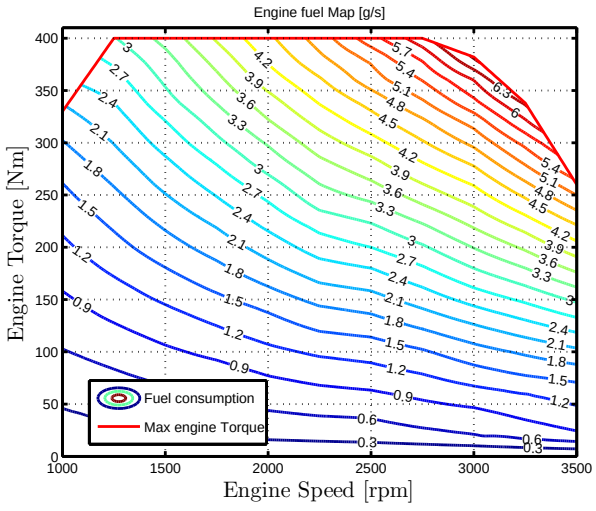

Figure 7.4: Fuel consumption map $c(.)$ [g/s]

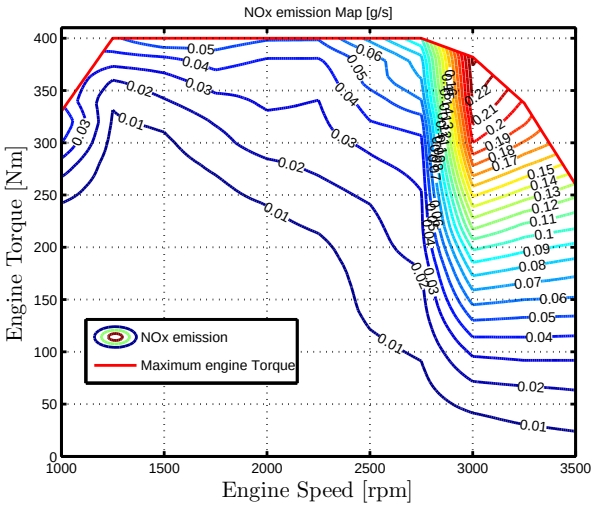

Figure 7.5: NO_x map [g/s]

Figure 7.7 shows the electric power P_m and the speed-dependent torque limits of

[1]The maps of fuel consumption and NO_x emissions are given as a function of the indicated engine torque. The EMS calculate the indicated engine torque and the engine friction torque map is used to deduce the effective torque from the formula: Effective Torque=Indicated Torque−Friction Torque

the electric machine used in the vehicle. The open-circuit voltage U_{ocv} and the internal resistance of the battery R_b are given in Figures 7.8 and 7.9.

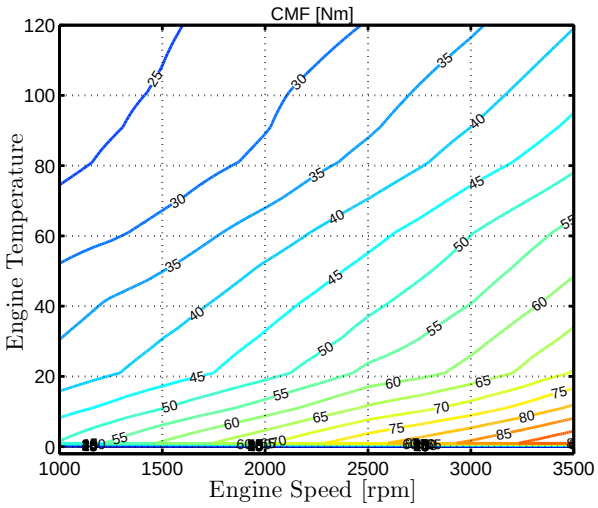

Figure 7.6: Engine friction torque [Nm]

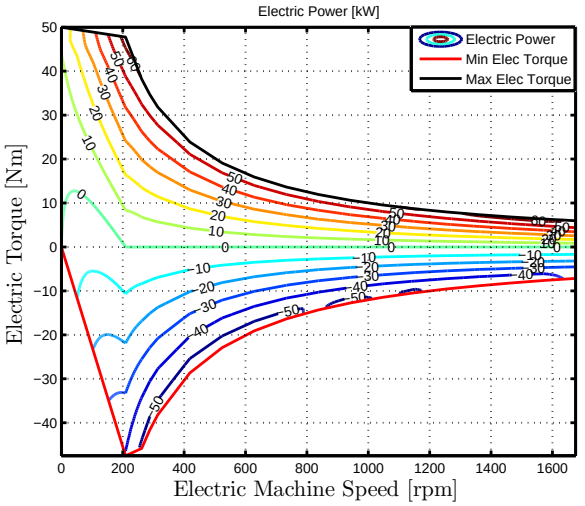

Figure 7.7: Electric power map P_m [kW]

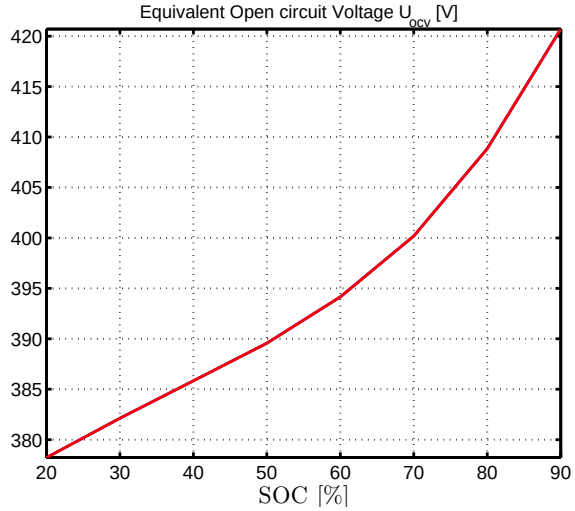

Figure 7.8: Battery open-circuit voltage U_{ocv} [V]

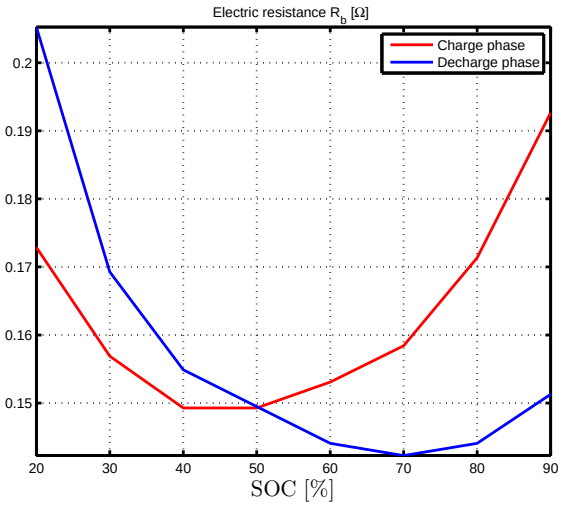

Figure 7.9: Battery internal resistance R_b [Ω]

7.3 Identification of thermal dynamics

7.3.1 Engine temperature

The engine temperature is the coolant temperature (water temperature). The ICE cooling system consists of a thermostat, a coolant temperature sensor, a radiator, and a coolant circulatory pump [41]. In accordance with Chapter 4, the model considered is

$$l_1 \cdot \frac{d\theta_e}{dt} = l_2 \cdot P_{\text{th,e}}(T_{eng}, w_{eng}, \theta_e) - l_3 \cdot (\theta_e - \theta_0), \tag{7.1}$$

where the parameters l_1, l_2 and l_3 have to be identified from experiments. The power $P_{\text{th,e}}$ represents the sum of friction power dissipated into heat and thermal power transferred

Table 7.2: HEV parameters

Parameter	Symbol	Value
Constant coefficient of the road load	c_0	253.26 N
Linear coefficient of the road load	c_1	3.4654 N/(m/s)
Quadratic coefficient of the road load	c_2	1.1677 N/(m/s)^2
Wheel radius	r_{tire}	0.3756 m
Number of wheels	n_{tire}	4
Motor-to-wheel transmission ratio	R_{el}	12.5625
Gear-box efficiency	η_{gb}	0.96
Charging efficiency	η_c	1
Fuel lower heating value	H_{lhv}	42600000 J/kg
Cylinder volume	V_{cyl}	2.300 L

from the engine to the coolant available in a look-up table as a function of the engine speed, the engine torque and the engine temperature. The look-up table used in Chapter 4 has been modified and adapted for the new system. Since the external cooling system (thermostat) is not modeled, the temperature θ_e is assumed to be limited by a maximum value $\theta_{e,max} = 82°C$ at which the thermostat is activated. Informally,

$$\theta_e(t) = \min(\text{solution of equation (7.1)}, 82). \tag{7.2}$$

For the identification, the Matlab solver *pem* is used to estimate the three parameters describing the dynamics of θ_e. This solver estimates model parameters using iterative prediction-error minimization method.

The driving cycle under consideration is the Worldwide harmonized Light vehicles Test Cycle (WLTC). The corresponding speed and gear-box profiles are reported in Figure A.4 (see Appendix A). The engine speed and torque set points are given in Appendix G.1.

The part of the driving cycle in which the thermostat is not activated represents the dynamics of the coolant temperature, and is used in the parameter identification process. The measured and the simulated trajectories of θ_e are shown in Figure 7.10. The maximum error in the water temperature estimation is:

- $\pm 3°C$ for $t \in [0, 800]$s (transient phase).
- $+5°C$ otherwise (steady state). This error is due to the weakness of the model of the thermostat in (7.2).

To validate the model, data from other three experimental tests for the same driving cycle are deployed. The engine speed and torque set points for these experimental tests are given in Appendix G.1. The corresponding trajectories of the water temperature are given in Figures 7.11, 7.12 and 7.13. The maximum error in the estimation of the temperature in the transient phase is less than $\pm 4°C$. The results presented above demonstrate a good agreement between the simplified model and the experimental data.

[2]Ie-Test (identification test) refers to the experimental test data (the driving cycle) used for the identification of the engine temperature dynamics.

[3]Ve$_i$-Test (validation test number i) refers to the experimental test data (the driving cycle) used in the validation of the engine temperature dynamics. The engine torque and speed set points for the three validation tests are given in Appendix G.1.

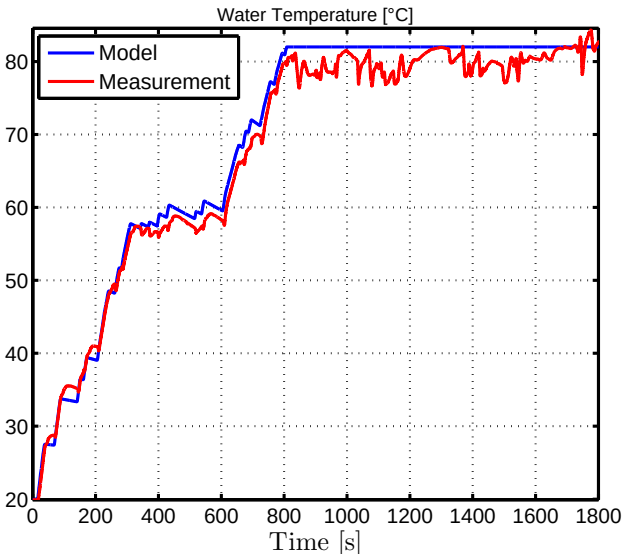

Figure 7.10: Temperature θ_e [°C] trajectories for Ie-Test[2]

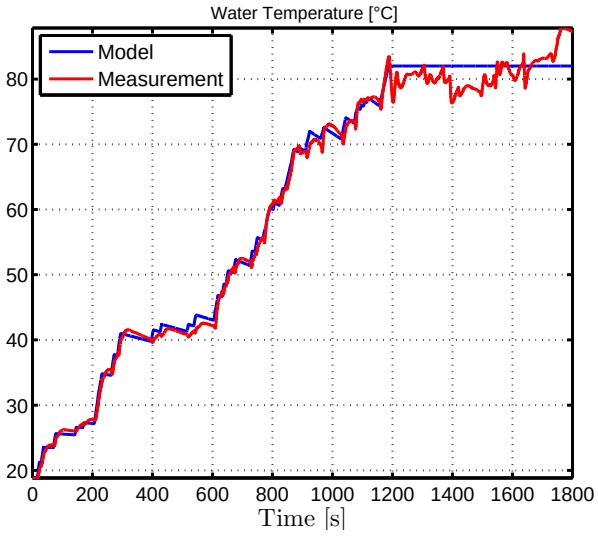

Figure 7.11: Temperature θ_e [°C] for Ve_1-Test[3]

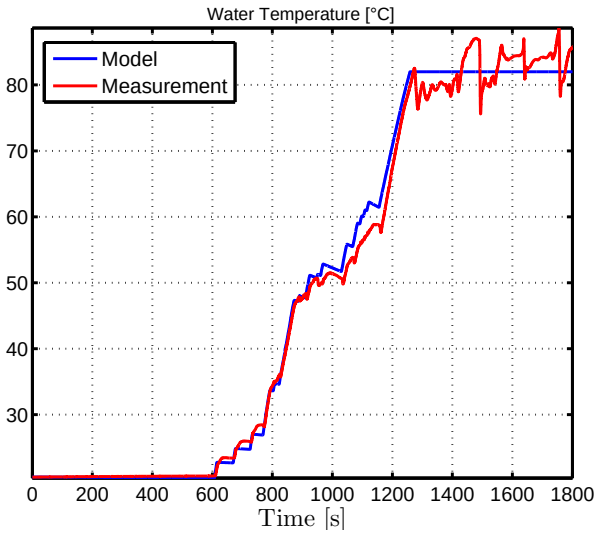

Figure 7.12: Temperature θ_e [°C] for Ve_2-Test

7.3.2 After-treatment system temperatures

As mentioned above, the after-treatment system consists of three sub-systems: DOC, DPF and SCR, cascaded as pictured in Figure 7.14. For each sub-system, a zero-dimensional model based on physical equations is considered. Usually, the physical phenomena are described by partial differential equations involving the three space dimensions. Here, these equations are simplified by considering a uniform distribution of the temperature (spatially averaged). Additionally, the rate of heat released by the chemical reactions in each sub-system is neglected for simplicity. We refer to works in [10, 42] for discussion on this assumption. The energy balance for each sub-system yields a first order differential

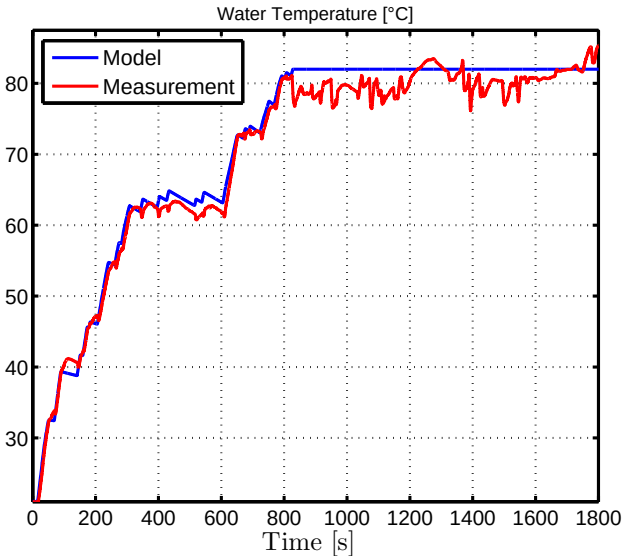

Figure 7.13: Temperature θ_e [°C] for Ve$_3$-Test

equation of the form [81]

$$k_{11} \cdot \frac{d\theta_{doc}}{dt} = k_{12} \cdot \dot{m}_{in} \cdot \theta_{exh} - k_{13} \cdot \dot{m}_{in} \cdot \theta_{doc} - k_{14} \cdot (\theta_{doc} - \theta_0), \tag{7.3}$$

$$k_{21} \cdot \frac{d\theta_{dpf}}{dt} = k_{22} \cdot \dot{m}_{in} \cdot \theta_{doc} - k_{23} \cdot \dot{m}_{in} \cdot \theta_{dpf} - k_{24} \cdot (\theta_{dpf} - \theta_0), \tag{7.4}$$

$$k_{31} \cdot \frac{d\theta_c}{dt} = k_{32} \cdot \dot{m}_{in} \cdot \theta_{dpf} - k_{33} \cdot \dot{m}_{in} \cdot \theta_c - k_{34} \cdot (\theta_c - \theta_0), \tag{7.5}$$

where $\dot{m}_{in}$ is the gas inlet-flow rate, θ_{exh} is the exhaust gas temperature, θ_{doc} is the

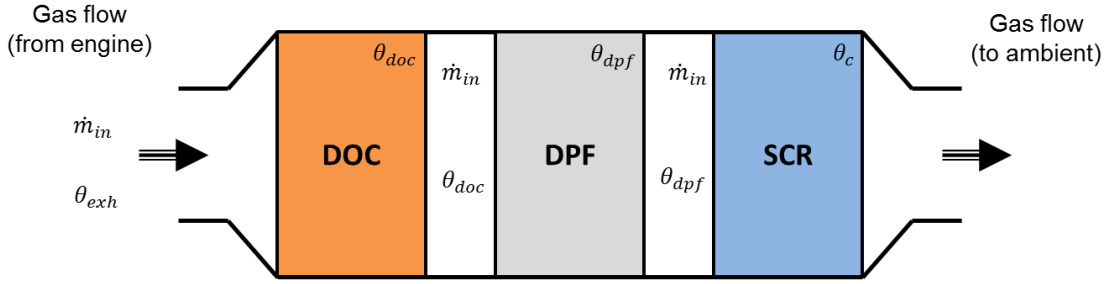

Figure 7.14: Configuration of after-treatment devices in the exhaust line

DOC temperature, θ_{dpf} is the DPF temperature, θ_c is the SCR temperature and θ_0 is the ambient temperature. There also, the parameters k_{ij} are identified using the Matlab solver *pem*.

To identify the model parameters, the vehicle is used in the thermal mode (engine only). The temperature sensors measure the gas temperature: if the power-assist mode is chosen, the engine would be shut down and there would be no gas flow coming from the engine. Therefore, the measured temperature would not represent the gas temperature. This problem is illustrated in the model validation below. The engine torque and speed set points for the identification test Ic-Test are given in Appendix G.2.

7.3.2.1 Diesel oxidation catalysts (DOC)

The inputs of the DOC temperature model are the gas flow from the engine and the exhaust gas temperature θ_{exh}, given by a quasistatic map of the engine torque and speed. The measured and the simulated trajectories of the DOC temperature using the identified parameters are given in Figure 7.15. The maximum error in the temperature estimation is $\pm 20°C$, which considering the model simplicity, can be seen as reasonable.

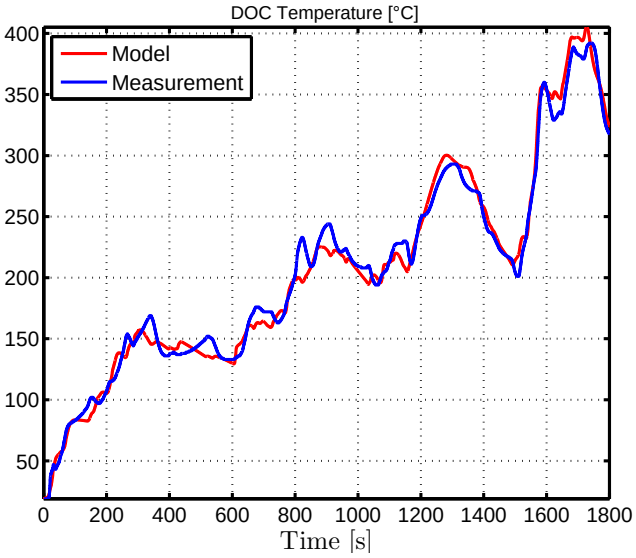

Figure 7.15: Temperature θ_{doc} [°C] for Ic-Test[4]

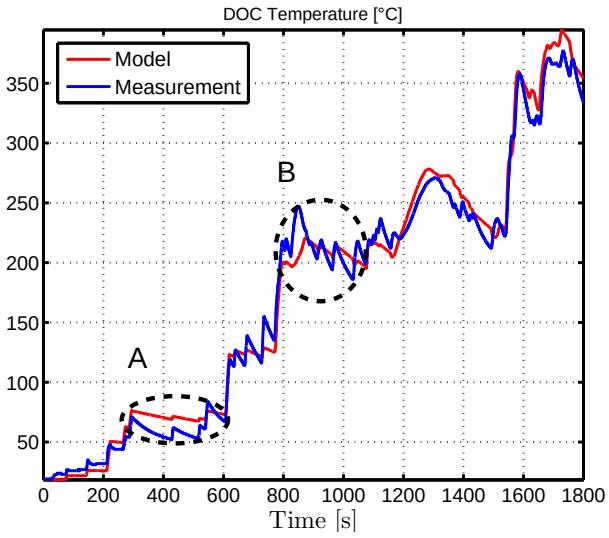

Figure 7.16: Temperature θ_{doc} [°C] for Vc_1-Test[5]

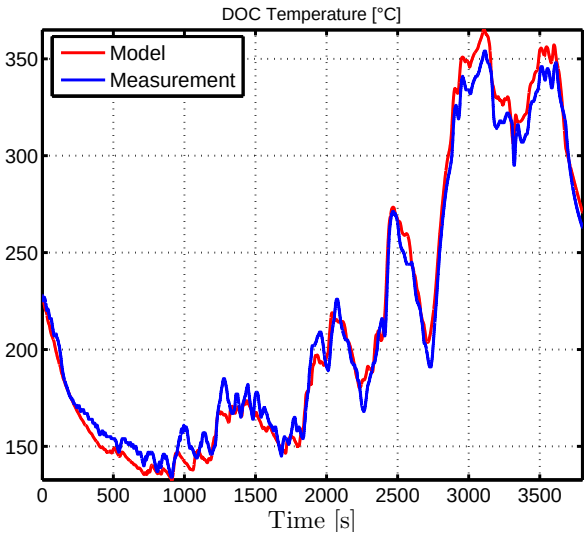

Figure 7.17: Temperature θ_{doc} [°C] for Vc_2-Test

[4]Ic-Test (identification test) refers to the experimental test data (the driving cycle) used in the identification of the after-treatment temperature dynamics.

[5]Vc_i-Test (validation test number i) refers to the experimental test data (the driving cycle) used in the validation of the after-treatment temperature dynamics. The same data are used for the identification of the DOC, DPF and the SCR temperature.

To validate the obtained model, data from other experimental tests are used. The engine torque and speed set points for the Vc_1-Test and the Vc_2-Test are given in Appendix G.2. The corresponding trajectories of the DOC temperature are given in Figures 7.16 and 7.17. For the right figure, the engine and the after-treatment system are warm at the beginning of the driving cycle. The error in the estimation of the temperature is less than ±40°C in the left-hand graph and less than ±20°C for the right-hand graph. In these two examples, the operation mode of the vehicle is the power assist mode: the engine can be turned off (depending on the control strategy) and there is no gas flow from the engine in the corresponding time intervals. Because the employed sensors measure the gas temperature, the data does not represent the true temperature of the DOC and the significant drops in temperature (see area surrounded by a black circle in Figure 7.16) are, in fact, unrealistic. More details about these drops in the temperature are given in Appendix G.3. Generally, the results presented above indicate a good agreement between the model and experimental data.

7.3.2.2 Diesel particulate filters (DPF)

The inputs of the DPF temperature model are the gas flow from the DOC and the DOC temperature estimated above. The measured and the simulated trajectories of the DPF temperature using the identified parameters are given in Figure 7.18. The maximum error in the estimated temperature is ±20°C.

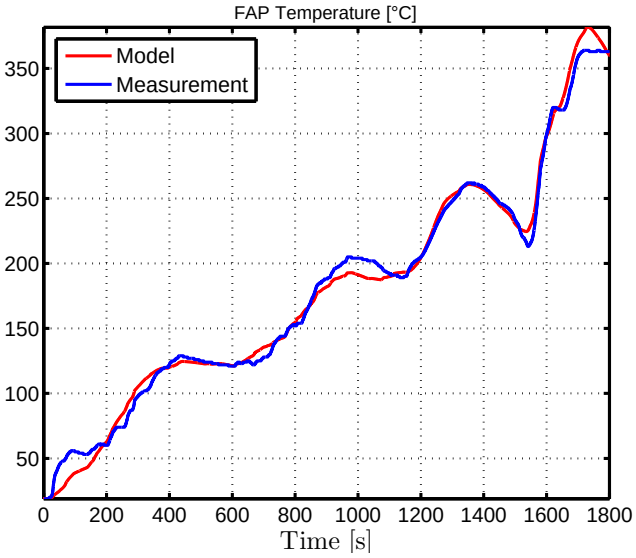

Figure 7.18: Temperature θ_{dpf} [°C] for Ic-Test

To validate the model, the same experimental data from Vc_1-Test and Vc_2-Test are used. The corresponding trajectories of the DPF temperature are given in Figures 7.19 and 7.20. The maximum error in the temperature estimation is less than ±40°C for the left-hand graph and less than ±30°C for the right-hand graph. A similar temperature-drop problem (area surrounded by a black circle in Figure 7.19 and 7.20) appears when the engine is turned off[6], but it is more obvious than in the DOC case. Indeed, the DPF is further from the engine than the DOC and the gas takes more time to reach it.

[6]The engine state for the surrounded regions is given in Appendix G.3.

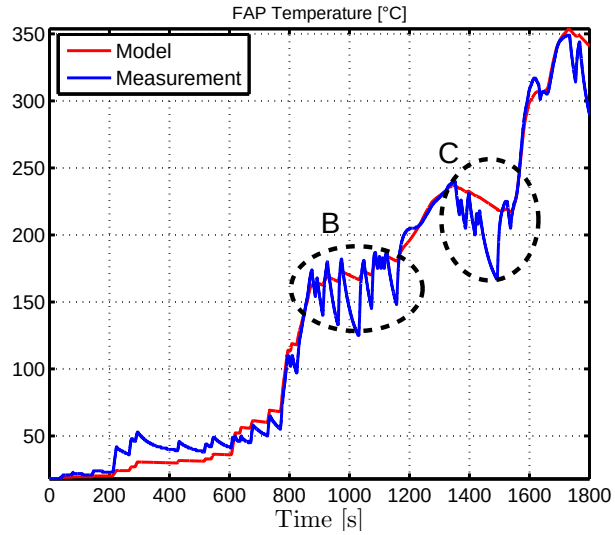

Figure 7.19: Temperature θ_{dpf} [°C] for Vc_1-Test

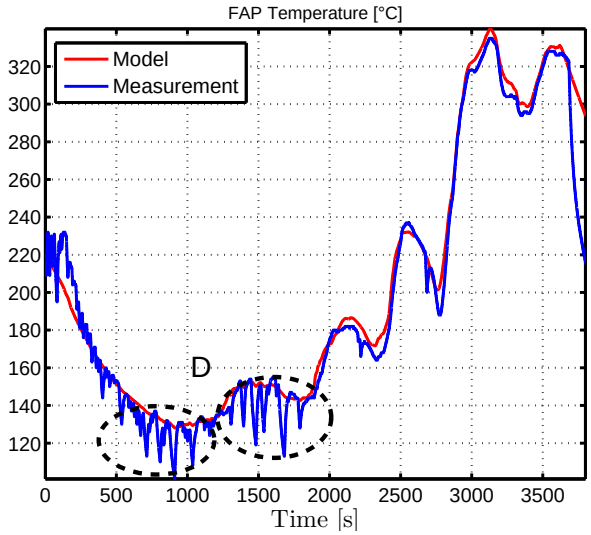

Figure 7.20: Temperature θ_{dpf} [°C] for Vc_2-Test

7.3.2.3 Selective catalytic reduction (SCR)

The inputs of the SCR temperature model are the gas flow coming from the DPF and the DPF temperature. The measured and the simulated trajectories of the SCR temperature for the identified parameters are given in Figure 7.21.

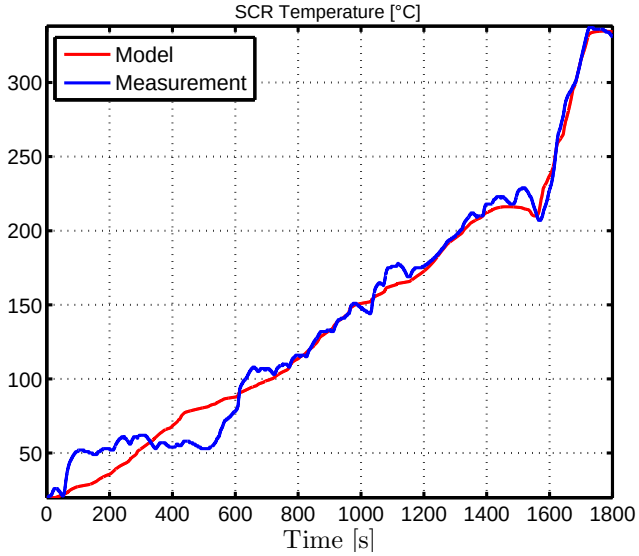

Figure 7.21: Temperature θ_c [°C] for Ic-Test

The maximum error in the estimated temperature is ±30°C. The large difference apparent in the first part of the driving cycle ($t \in [0, 600]$ s), may be due to the limits of the model: zero-dimensional model and neglecting the rate of heat released by the chemical reactions. In this phase, the SCR is not activated and the difference in temperature does not affect the NO_x emission rate out of the SCR. In the second part of the driving cycle, the error in the estimated temperature is less than ±15°C.

[7]Explanations about the drops in the DOC, the DPF and the SCR temperatures in the surrounded regions A, B, C and D are given in Appendix G.3.

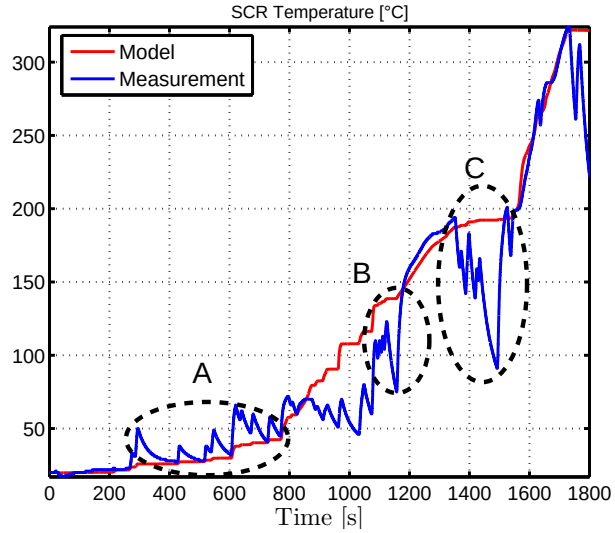

Figure 7.22: Temperature θ_c [°C] for Vc_1-Test[7]

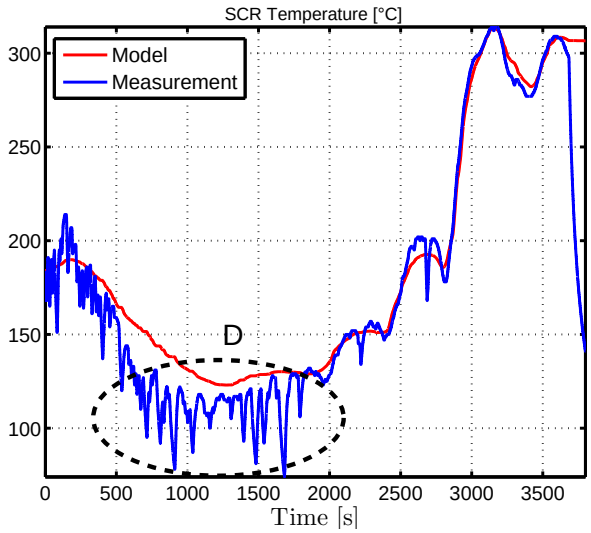

Figure 7.23: Temperature θ_c [°C] for Vc_2-Test

For the model validation, the same experimental data from Vc_1-Test and Vc_2-Test are used. The corresponding trajectories of the SCR temperature are given in Figures 7.22 and 7.23. The error in the estimated temperature is less than ±50°C for the left-hand graph. As explained above for the DOC and DPF models, the temperature-drop phenomenon (surrounded area by a black circle in Figure 7.22 and 7.23) occurs when the engine is turned off. The temperature-drop problem is more obvious than for the two previous cases (see Appendix G.3). Indeed, the SCR is located further from the engine than the DOC and the DPF and the gas takes more time to reach the SCR. Additionally, the characteristics of the sensors used for the SCR are different from those used for the DOC and the DPF. The measured temperature in these phases do not represent the true situation.

7.4 Simulation Tools

The control strategies presented in Section 7.5 are coded in Matlab/ Simulink. The obtained controller is coupled with a simulator aimed at representing the system dynamics in a more accurate way than the simple models used to design the optimization laws. The simulator is distributed between several sub-models as shown in Figure 7.24:

1. The driver model is executed at 100 Hz. It enables the vehicle speed on a given driving cycle to be follow, and reproduce the behavior of a real driver. The driver controller is based on predictive control.

2. The transmission model is integrated in the AMESIM platform. It executes the model at 1 kHz frequency and it includes the sliding of the tire and a 1-D vehicle. This model provides essential information for the good representativeness of the complete platform: it enables the level of predictability of the fuel consumption to be increased and the evaluation of the driving agreement.

3. The models of the electric components include: a quasi-static model of an electric machine and a battery represented with an equivalent-circuit model. The two models are executed at 100 Hz.

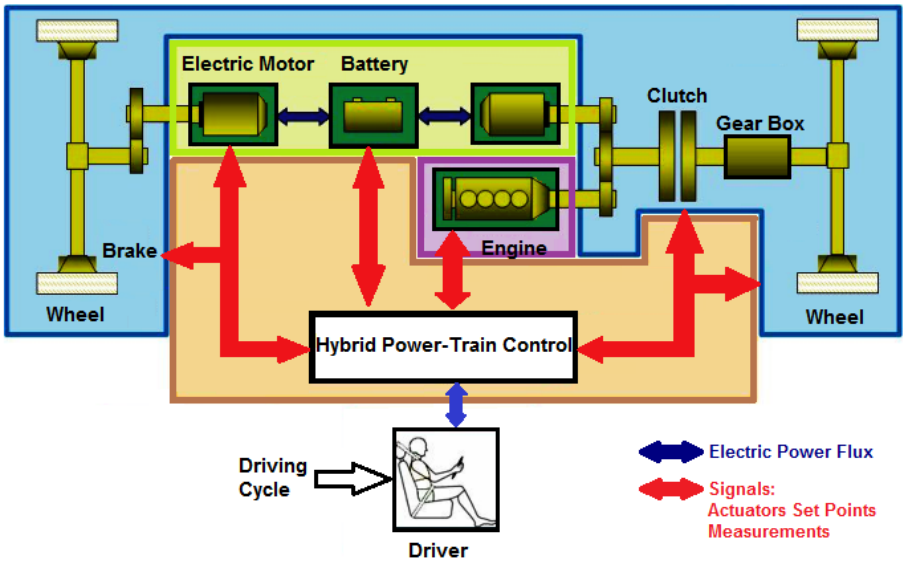

Figure 7.24: Simulation architecture

4. The engine model is based on quasi-static maps giving the fuel consumption and the pollutant emissions. This model does not represent the effect of the engine transient behavior on the whole system. The purpose of this simplified model is to calibrate the control strategies.

The simulations are done in two steps:

- The first step is carried out in Simulink: a simplified model based on look-up tables is used to tune the control strategies. The simulation platform has been developed at IFP and it is called HOT (Hybrid Optimization Tool) [75]. It includes models of the different part of the HEV and a controller where the PMP and the ECMS formula given in (6.1) are implemented [17]. The simulation time is about 10 s. The calibration of the ECMS parameters is performed in order to satisfy the final constraint on the SOC. *The simulation platform in Simulink is used for the control strategy design.*

- The second step is in xMOD [5, 6]: the model described in Section 7.4 is used, so it is more realistic than the model used in HOT. The only missing point is that the engine was represented by a look-up table. This model does not reproduce the effect of the engine transient behavior on the system. The software xMOD is used to optimize model execution time (accelerating the simulation from eight hours using Simulink to thirty minutes using xMOD [5]: Multi-core, multi-solver and multi-rate execution to boost the simulations performance). The adjoint state λ is determined using the ECMS formula in (6.1) where the ECMS parameters are well tuned to fulfill the final constraint on the SOC. *The simulation platform in xMOD is used to validate the control strategy calculated in the first step before testing it in the test bench (Rapid prototyping).*

It is important to highlight that the two simulators have the same models for the thermal dynamics (of the engine and the after-treatment system).

7.5 Optimization strategies

The objective of the study conducted in this section is to find a control strategy based on optimal control that would be suitable for a real-time implementation, as it was carried out in Chapter 6 for CO emissions reduction. This simplified strategy should yield a reduction of NO_x emissions to below 80 mg/km corresponding to the European norm Euro 6 with an acceptable extra-fuel consumption compared to a control strategy that minimizes only the fuel consumption.

7.5.1 Problem formulation

7.5.1.1 Cost function

The cost function (7.6) to be minimized is a weighted sum of the fuel consumption rate and the NO_x emission rate out of the SCR, over a fixed time window corresponding to a driving cycle of a duration T. That is, similarly to equation (4.1)

$$J(u) = \int_0^T \left[(1-\alpha)\cdot c(u,t,\theta_e) + \alpha m_{\mathrm{NO}_x}(u,t,\theta_e,\theta_c)\right] dt, \tag{7.6}$$

where u is the control variable (the engine torque), θ_e is the engine temperature and θ_c is the SCR temperature.

The instantaneous fuel consumption rate $c(u,t,\theta_e)$ is given by a quasi-static map depending on the engine rotational speed, the engine indicated-torque, the engine temperature because the engine friction torque depends on it (see Figure 7.6). The NO_x emission rate out of the SCR system $m_{\mathrm{NO}_x}(.)$ is of the form

$$m_{\mathrm{NO}_x}(u,t,\theta_e,\theta_c) = m_{\mathrm{NO}_x,\mathrm{e}}(u,t,\theta_e)\cdot(1-\eta_{\mathrm{NO}_x}(\theta_c)),$$

where $m_{\mathrm{NO}_x,\mathrm{e}}$ is the emission rate out of the engine given by a quasi-steady map as a function of the engine speed and torque. The term η_{NO_x} is the SCR conversion efficiency

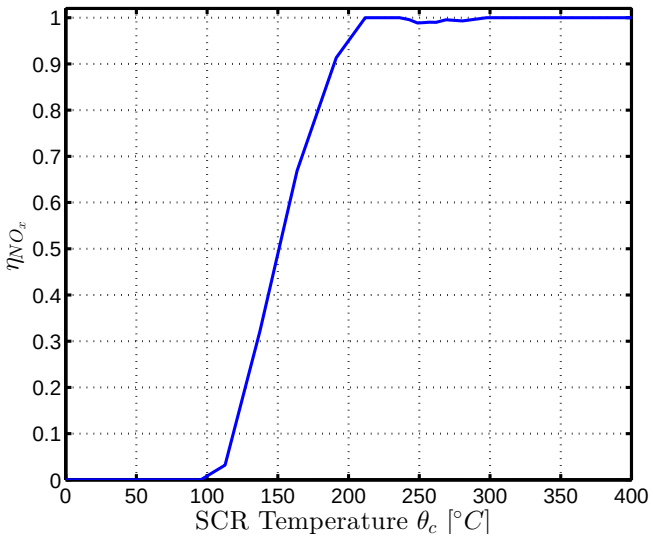

Figure 7.25: SCR conversion efficiency η_{NO_x}

(see Figure 7.25) depending on the SCR temperature θ_c. This latter temperature depends

on the DOC and DPF temperatures calculated using the models proposed in (7.3, 7.4). As in Chapter 4, the parameter $\alpha \in [0, 1]$ is used to set the trade-off between the fuel consumption and the NO_x emissions. The NO_x map is normalized such that its mean value remains close to the mean value of the fuel map. The same approach can be extended to the other pollutant emissions (HC emissions). For convenience, we note

$$L(u, t, \theta_e, \theta_c) = (1 - \alpha) \cdot c(u, t, \theta_e) + \alpha m_{\mathrm{NO}_x}(u, t, \theta_e, \theta_c).$$

7.5.1.2 Dynamics

Five states are taken into account. The first one is the SOC, which is governed by the differential equation in (3.2) with the final constraint on the SOC in (3.3). The second state variable is the engine temperature θ_e whose dynamics is described by equation (7.1). The third dynamics is the SCR temperature whose dynamics is given by equation (7.5). This temperature depends on the DOC and DPF temperatures θ_{doc} and θ_{dpf} whose dynamics are given in equations (7.3, 7.4) respectively. When $\alpha = 0$, only the fuel consumption is minimized and the temperature of the SCR can be neglected in formulating the optimization problem as it has no impact on the cost function nor on the constraints.

7.5.1.3 Input Constraints

The control u is constrained to belong to U^{ad} defined by (3.4).

7.5.2 OCP summary

To summarize, the OCP is defined by

$$\min_{u \in U^{ad}} J(u) \tag{7.7}$$

under the final constraint (3.3) and the state dynamics (3.2, 7.1, 7.3, 7.4, 7.5) where the set U^{ad} is defined in equation (3.4).

7.5.3 Strategies for $\alpha \neq 0$

Following the conclusion given in Chapter 4, the single-state strategies described in Table 7.3 are tested.

The strategy (S) assumes that the engine temperature is constant (fixed at an initial value $\theta_{e,0}$), the SCR is never activated (its temperature is fixed at $\theta_{c,0}$) and its efficiency η_{NO_x} is fixed. The tested values of $\theta_{e,0}$ are 20°C (cold engine start) and 90°C (warm engine start). The tested values of $\theta_{c,0}$ are 20°C (the SCR is not activated and the control strategy minimizes the NO_x emissions out of the engine) and 150°C (the SCR is partially activated but its temperature is constant). These are the only information given to solve (S). These tests are performed only on simulation with the full model (five states) described above to study the sensitivity of the strategy (S) to the provided information. Two additional heuristic strategies based on optimization are considered:

- The first strategy, denoted as (HS_1), is a pseudo-solution of the OCP (7.7) where the engine is warm (the cost function is independent of θ_e and its adjoint state $\mu(t) \equiv 0$) while $\rho(t) \equiv 0$ is arbitrarily imposed in the Hamiltonian.

Table 7.3: Control strategies description for $\alpha \neq 0$

Strategy	Control
(S)	$u^*(t) = \arg\min_{u \in U^{ad}} (L(u,t,\theta_{e,0},\theta_{c,0}) + \lambda \frac{d\xi}{dt})$
(HS_1)	$u_1^h(t) = \arg\min_{u \in U^{ad}} (L(u,t,90,\theta_c) + \lambda \frac{d\xi}{dt})$
(HS_2)	$u_2^h(t) = \arg\min_{u \in U^{ad}} (L(u,t,\theta_e,20) + \lambda \frac{d\xi}{dt})$

- The second strategy, denoted as (HS_2), assumes that the SCR is never activated $\eta_{\mathrm{NO}_x} = 0$ (the cost function is independent of θ_c and its adjoint state $\rho(t) \equiv 0$) while the adjoint state $\mu(t)$ (associated to the engine temperature) is arbitrarily set to zero in the Hamiltonian.

Online adaptation of λ The adjoint state λ is determined using the ECMS formula in (6.1). Following the conclusion drawn in Section 6.1.3, the ECMS parameters (λ_0, k_p) are tuned to satisfy the final constraint on the SOC. The online strategies corresponding to S, HS_1 and HS_2 are referred to ECMS, HECMS$_1$ and HECMS$_2$, respectively.

7.5.4 Strategies for $\alpha = 0$

Here, the fuel consumption is the cost function to be minimized. Two dynamics have to be considered: the SOC dynamics and the water temperature θ_e. The two strategies described in Table 7.4 have been tested. In this case ($\alpha = 0$), the strategy (HS_1) is equivalent to the strategy (S).

Table 7.4: Control strategies description ($\alpha = 0$)

Strategy	Control
$(S^{\alpha=0})$	$u_0^*(t) = \arg\min_{u \in U^{ad}} (c(u,t,90) + \lambda \frac{d\xi}{dt})$
$(HS_2^{\alpha=0})$	$u_2^h(t) = \arg\min_{u \in U^{ad}} (c(u,t,\theta_e) + \lambda \frac{d\xi}{dt})$

The strategy $(S^{\alpha=0})$ refers to the solution of the problem (7.7) for $\alpha = 0$, in which the engine temperature is assumed to be constant (around 90°C). Following [55], the heuristic strategy $(HS_2^{\alpha=0})$ is a pseudo solution of the problem (7.7), where the adjoint state associated to the engine temperature is arbitrary set to $\mu(t) = 0, \ \forall t$ in the Hamiltonian. This simplification reduces the number of the unknown variables from 2 to 1.

Online adaptation of λ As mentioned above for the real-time application, the adjoint state λ is determined using the ECMS formula in (6.1). The ECMS parameters (λ_0, k_p) are tuned to satisfy the final constraint on the SOC.

7.6 Simulation results

The WLTC cycle is used for the simulations. This driving cycle is more representative of real driving conditions and it will be used instead of the NEDC as a validation driving cycle by car manufacturers in Europe from 2017. *For all the simulations, the engine, the DOC, the DPF and the SCR are cold at the beginning of the driving cycle.*

7.6.1 Case of $\alpha \neq 0$

The parameter α is changed in $]0,\ 1]$. For each value of α, the control strategies described in Table 7.3 are tested in simulation.

7.6.1.1 Simulation using HOT

7.6.1.1.1 Offline case Figure 7.26 details the variation of the fuel consumption as a function of the NO_x emissions (out of the engine and out of the SCR) for various values of α where the adjoint state λ is determined using the PMP (λ is constant).

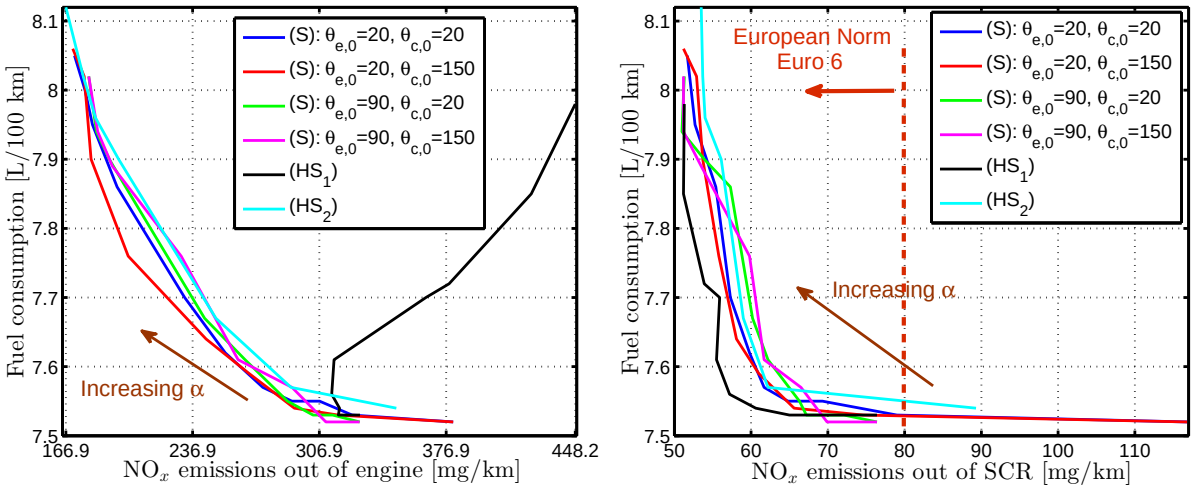

Figure 7.26: Fuel consumption [L/100 km] as a function of NO_x emissions [mg/km] out of the engine (left) and out of the SCR (right) for offline strategies simulated with HOT.

The strategies (S) and (HS_2) reduce the NO_x emissions out of the engine while they increase the fuel consumption when α increases. This behavior leads to a reduction of the NO_x emissions out of the SCR. From the plots of Figure 7.26, the maximum NO_x emissions reduction out of the engine using the strategies (S) and (HS_2) is 50% and the maximum NO_x emissions reduction out of the SCR is about 33% while the extra-fuel consumption is 7% comparing to the strategy minimizing only the fuel consumption (for $\alpha = 0$). On the other hand, the strategy (HS_1) reduces only the NO_x emissions out of the SCR. The maximum NO_x emissions reduction is 33% while the extra-fuel consumption is around 6% comparing to the strategy minimizing only the fuel consumption.

The trajectories of the SOC and the SCR temperature by using the strategies (S) and (HS_1) for increasing values of α are given in Figures 7.27, 7.28, 7.29 and 7.30, respectively. From Figures 7.27 and 7.28 (where the strategy (S) assumes $\theta_{e,0} = 90$ and $\theta_{c,0} = 20$ without loss of generality), when α is increased, the control strategy (S) improves the

SCR efficiency by warming it up promptly. To achieve this improvement, the engine is overused and the additional resulting power is stored in the battery (the SOC trajectories are higher when α increases). Globally, the efficiency improvement decreases the pollutant emissions out of the SCR and the fuel consumption increases.

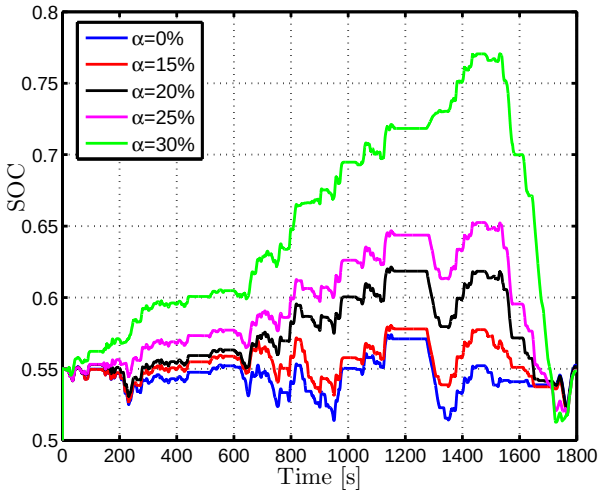

Figure 7.27: SOC trajectories [%] using (S)

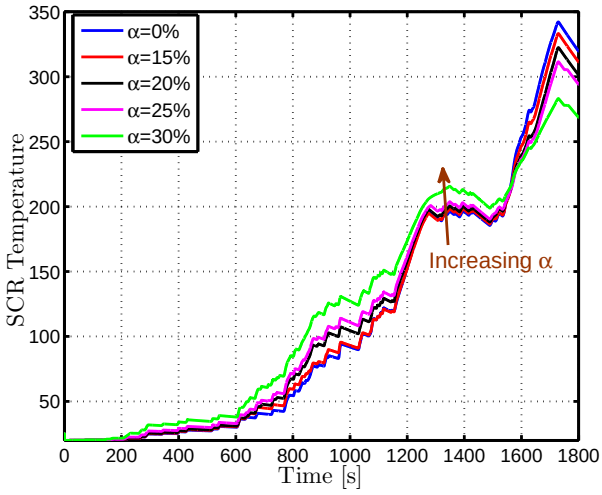

Figure 7.28: SCR temperature [°C] using (S)

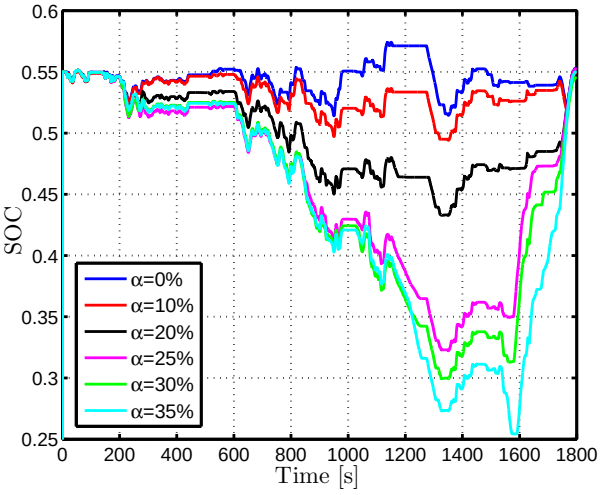

Figure 7.29: SOC [%] trajectories using (HS_1)

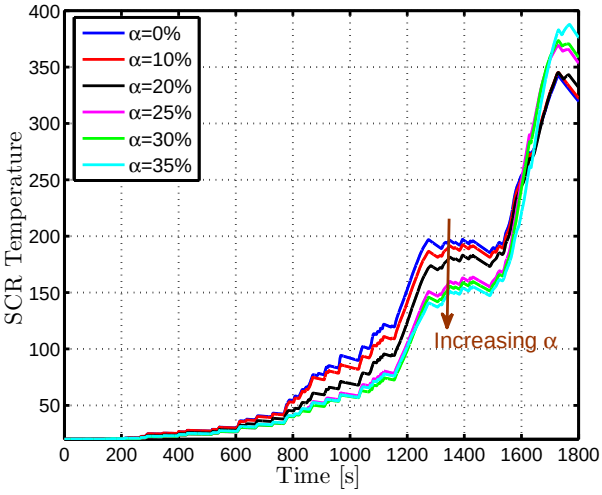

Figure 7.30: SCR temperature [°C] using (HS_1)

According to Figures 7.29 and 7.30 (compared to Figures 7.27 and 7.28 respectively), when α is increased, the control strategy (HS_1) behaves differently from the strategy (S). The electric mode is used at the beginning of the driving cycle. This behavior is observed from the SOC trajectories where the minimum SOC value decreases when α is increased. As the engine is less and less used, the SCR efficiency remains poor at the beginning of the driving cycle. Because of the final constraint on the SOC, strategy (HS_1) favors the use of the engine to bring the final SOC to its target value. The SCR temperature increases quickly. This kind of behavior needs a large battery or a high energy available in the battery at the beginning of the driving cycle in contrast to the strategy (S).

7.6.1.1.2 Online case Figure 7.31 details the variation of the fuel consumption as a function of the NO_x emissions (out of the engine and out of the SCR) for various values of α where the adjoint state λ is determined using the ECMS formula in (6.1). The ECMS parameters (λ_0, k_p) are tuned to satisfy the final constraint on the SOC.

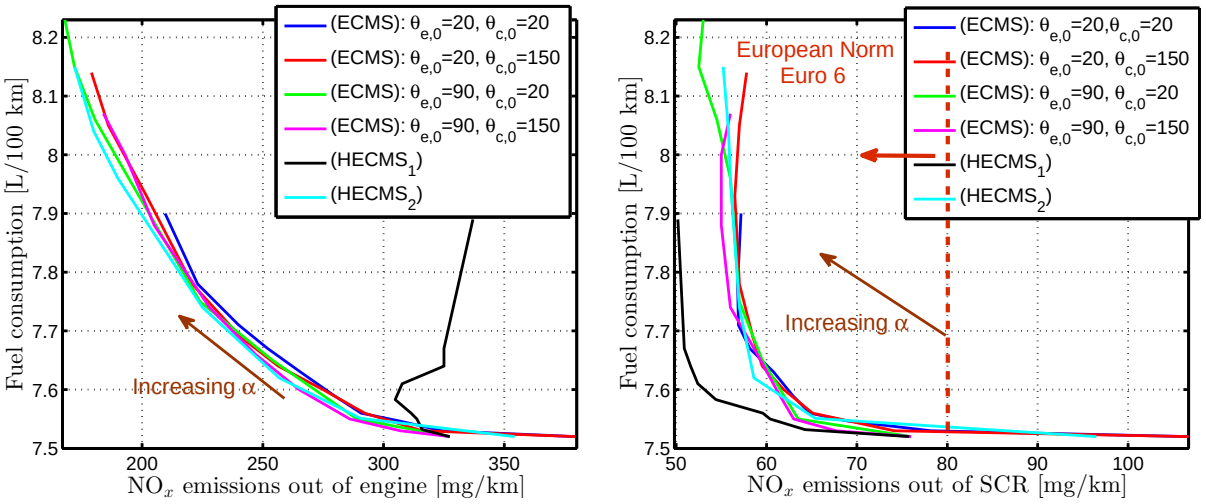

Figure 7.31: Fuel consumption [L/100 km] as a function of NO_x emissions [mg/km] out of the engine (left) and out of the SCR (right). Online strategies tested with HOT.

From the plots of Figure 7.31, when α increases, the strategies ($ECMS$) and ($HECMS_2$) reduce the NO_x emissions out of the engine and the SCR while they increase the fuel consumption. On the other hand, the strategy ($HECMS_1$) reduces only the NO_x emissions out of the SCR. Comparing to the case where λ is constant (optimal value), the maximum reduction of the NO_x emissions out of the SCR is 29% for the strategies ($ECMS$, $HECMS_2$) and 33% for the strategy ($HECMS_1$).

7.6.1.2 Simulation using xMOD

In this section, the xMOD platform is used. The differences between this platform and HOT are the driver and the transmission models which are more realistic. This platform is used for the experimental tests on the test bench.

Figure 7.32 details the variation of the fuel consumption as a function of NO_x emissions (out of the engine and out of the SCR) for various values of α where the adjoint state λ is determined using the ECMS formula in (6.1). The ECMS parameters (λ_0, k_p) are tuned to satisfy the final constraint on the SOC. From this figure, the obtained results have the same tendency as the previous results obtained by HOT in Section 7.6.1.1. The NO_x emissions out of the SCR are reduced by the different tested strategies: the maximum NO_x emissions reduction out of the engine is 50% and out of the SCR is 34% while the maximum extra-fuel consumption is about 7% comparing to the strategy minimizing only the fuel consumption. The same remarks as the ones drawn from HOT about the SOC and the SCR trajectories can be formulated from Figures 7.33 and 7.34: when α is increased, the strategy ($ECMS$) recharges the battery at the beginning of the driving cycle by overusing the engine to provide the power requested by the driver at the wheel while the strategy ($HECMS_1$) discharges the battery at the beginning of the driving cycle by using the electric machine to provide the needed power to follow the driving cycle speed set points.

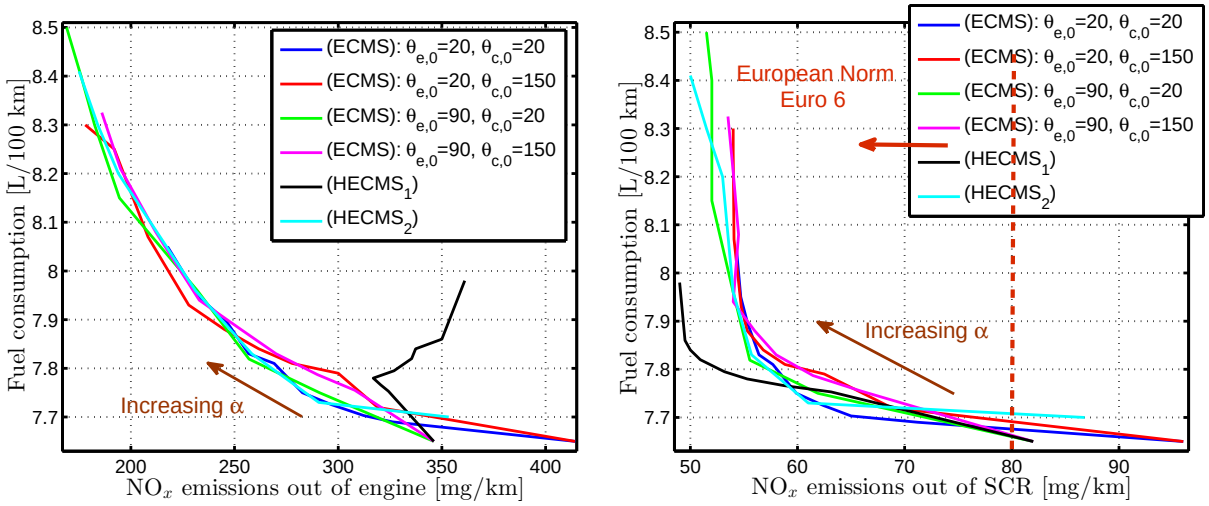

Figure 7.32: Fuel Consumption [L/100 km] as a function of NO_x emissions [mg/km] out of the engine (left) and out of the SCR (right) from ECMS (xMOD platform).

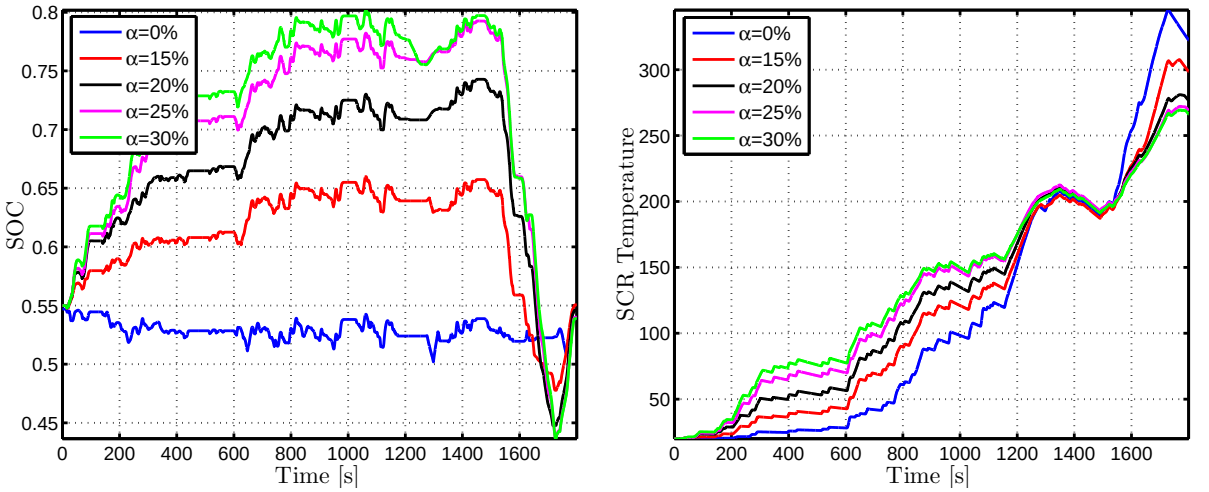

Figure 7.33: SOC trajectories [%] and SCR temperature [°C] using $(ECMS)$

7.6.2 Case of $\alpha = 0$

The fuel consumption obtained with the various control strategies defined in Table 7.4 are given in Table 7.5. The final constraint on the SOC is satisfied for the tested strategies.

From this table, the two strategies appears as close in terms of fuel consumption for the different simulations (using HOT and xMOD platforms). The difference between the strategies $(S^{\alpha=0})$ and $(HS_2^{\alpha=0})$ is less than 0.7%).

7.7 Experimental results

Simulation results of Section 7.6 have been shown great accordance of the results of offline and online strategies. In experiment, we now test ECMS strategies. For the experimental tests, the adjoint state λ is determined by using the ECMS formula. The calibration of the ECMS parameters is carried out in order to satisfy the final constraint on the SOC. The determination of the optimal constant value of λ for the test bench needs some work as

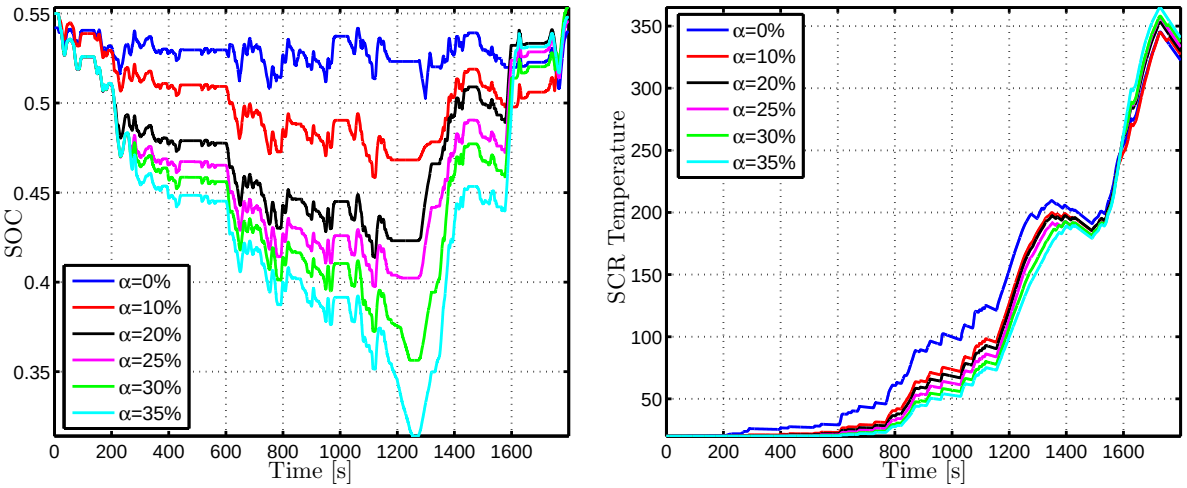

Figure 7.34: OC [%] trajectories and SCR temperature [°C] using ($HECMS_1$)

Table 7.5: Fuel Consumption [L/100 km] for $\alpha = 0$ (Simulation results)

Strategies	$(S^{\alpha=0})$	$(HS_2^{\alpha=0})$
HOT Simulation (offline)	7.52	7.54
HOT Simulation (online)	7.52	7.55
xMOD Simulation (online)	7.65	7.70

the models used in the simulation are not exact and the engine torque set point requested by the EMS are not fulfilled[8]. *For all tests, the engine, the DOC, the DPF and the SCR are cold at the beginning of the driving cycle (around* $20°C$*).*

7.7.1 Case of $\alpha = 0$

The obtained fuel consumption on the test bench for the different control strategies defined in Table 7.4 are given in the first line of Table 7.6 (the line corresponding to $\alpha = 0$). From Table 7.6, the difference between the two tested strategies is less than 1% comparing to the fuel consumption for a warm start of the engine (8.17 L/100 km). The strategy ($ECMS$) gives the lowest fuel consumption for a cold-start of the engine. The obtained results is not surprising. Even in the purely thermal mode (using only the engine), the difference between the fuel consumption for warm and cold start of the engine is less than 2% on the test bench (the fuel consumption for a warm start is 9.85 L/100 km and for cold start is 10.02 L/100 km).

As it has been concluded from the simulation, these experimental tests suggest that the impact of the engine temperature on the calculation of EMS minimizing the fuel consumption can be neglected. This suggestion confirms the conclusion made in Section B.3 for a gasoline engine where the impact of the engine temperature on the fuel consumption were more important than for the diesel engine considered in this chapter.

[8]The torque provided at the shaft by the engine is always lower than the set points generated by the EMS and the driver model based on a model predictive controller modifies the torque requested at the wheels in order to follow the driving cycle defined by the vehicle speed.

7.7.2 Case of $\alpha \neq 0$

Due to some technical problems, the experimental tests concerning the NO_x emissions reduction are limited. Only two tests for each strategy are presented in order to show the possible reduction of the NO_x emissions and its cost in term of fuel consumption. The results are summarized in Tables 7.6, 7.7 and 7.8, respectively. From these tables, the

Table 7.6: Fuel consumption [L/100 km] (experiments of proposed online strategies)

Strategy	$(ECMS)$	$(HECMS_1)$	$(HECMS_2)$
$\alpha = 0$	8.23	8.23	8.30
$\alpha = 0.35$	8.65	8.72	8.90
Extra-fuel consumption	+4.85%	+5.6%	+6.7%

Table 7.7: NO_x emissions [mg/km] out of engine (experiments of proposed online strategies)

Strategy	$(ECMS)$	$(HECMS_1)$	$(HECMS_2)$
$\alpha = 0$	435	435	445
$\alpha = 0.35$	249	450	261
NO_x reduction	−43%	+3.3%	−41.3%

Table 7.8: NO_x emissions [mg/km] out of the SCR (experiments of proposed online strategies)

Strategy	$(ECMS)$	$(HECMS_1)$	$(HECMS_2)$
$\alpha = 0$	120	120	106
$\alpha = 0.35$	68	55	80
NO_x reduction	−43.3%	−54.1%	−24.5%

tested strategies allow the NO_x emissions reduction comparing to the strategy minimizing only the fuel consumption ($\alpha = 0$). The strategies $(ECMS)$ and $(HECMS_2)$ reduce the NO_x emissions out of the engine and out of the SCR while the strategy $(HECMS_1)$ reduces only the NO_x emissions out of the SCR:

- The strategy $(HECMS_1)$ reduces the NO_x emissions out of the SCR by 54% while the extra-fuel consumption is 5.6% compared to the case for $\alpha = 0$ (fuel consumption minimization).
- The strategy $(ECMS)$ also reduces the NO_x emissions out of the SCR by 43% while the extra-fuel consumption is lower (about 4.85%) than in the case of the strategy $(HECMS_1)$.
- The strategy $(HECMS_2)$ is less efficient in NO_x emissions reduction (25%).

The conclusion of these experiments is that the $(HECMS_1)$ and $(ECMS)$ are two good candidates for an EMS of the considered vehicle. The two strategies generate very different trajectories through. The SOC, the engine and the SCR temperatures using the strategies $(ECMS)$ and $(HECMS_1)$ for $\alpha = 0.35$ are given in Figures 7.35 and 7.36, respectively. These figures show that the strategy $(HECMS_1)$ uses only the electric machine at the

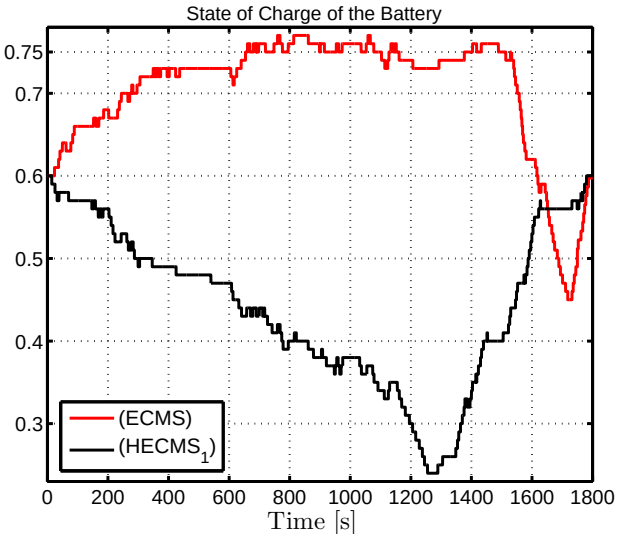

Figure 7.35: SOC [%] trajectories from the experimental tests

beginning of the driving cycle until 600 s (see the engine and the catalyst temperatures, they are constant until 600 s). Later, the strategy uses the engine and the electric machine in order to bring the SOC to its target value at the end of the driving cycle by recharging the battery. The engine and the SCR temperatures increase. On the other hand, the strategy ($ECMS$) chooses to overuse the engine at the beginning of the driving cycle (recharge the battery) and warm-up quickly the engine and the SCR. The battery is discharged at the end of the driving cycle in order to meet the final constraint on the SOC. Despite the difference in the behavior of the two strategies, they reduce the NO_x emissions out of the SCR. These results illustrate that it is not necessary to warm-up quickly the SCR at the beginning of the driving cycle in order to reduce the NO_x emissions.

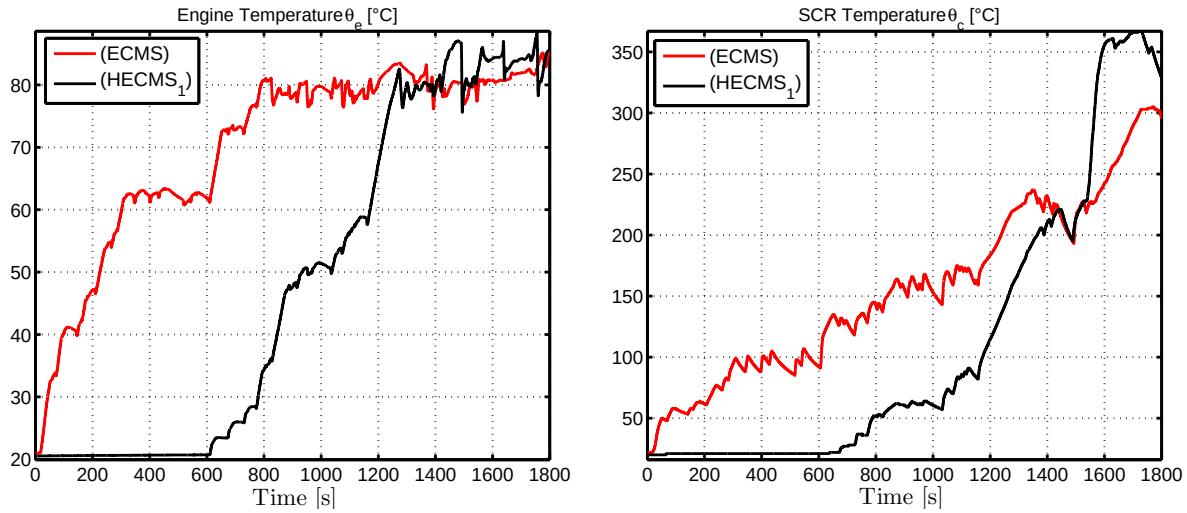

Figure 7.36: Temperatures θ_e [°C] (left) and θ_c [°C] (right) from experimental tests

7.8 Conclusion

For a parallel HEV equipped with a diesel engine and a SCR system, the impact of the engine and the SCR temperatures on the calculation of an EMS aiming at minimizing the a trade-off between fuel consumption and NO_x emissions has been studied.

For the engine temperature, the simulations and the experimental results indicate that it is not necessary to take it into account in the optimization of the fuel consumption. This result confirms the conclusion of Chapter 4 where the engine is of gasoline type.

For the SCR temperature, the simplest strategies ($ECMS$) and ($HECMS_1$) guarantee a good level of NO_x emissions reduction between 40% and 50% with an extra-fuel consumption of $4.9 - 6\%$ on the test bench. The presented results from the strategy ($HECMS_1$) show also that it is not necessary to warm-up quickly the SCR at the beginning of the driving cycle to reduce the NO_x emissions out of the SCR as the strategy ($ECMS$) did.

Conclusion

In this thesis, the design of an EMS for a parallel HEV by taking into account the impact of internal temperatures (engine and/or catalyst temperatures) has been addressed. The objective of this EMS is to reduce pollutant emissions in order to satisfy the European requirements for regulated emissions with an acceptable extra-fuel consumption. This question has been studied in Part I from a model complexity viewpoint: the number of state variables in the optimization problem. Based on results presented in Chapter 4 and Chapter 7, the single-state model, considering only the SOC dynamics, is an effective way to calculate control strategies allowing the pollutant emissions (CO for a gasoline engine and NO_x in the case of diesel engine) to satisfy the demanding standard on emissions with an acceptable extra-fuel consumption stemming from simplification and lack of knowledge on future vehicle's path.

Considering various (increasingly) levels of complexity in the modeling has given us the opportunity to study the question of perturbation in optimal control. Thereafter in Part II, the general concept of regular perturbations in optimal control problems (OCPs) under input constraints has been explored. The various problems studied in Part I are examples of successive model simplifications which can be recast into this concept. The results of Bensoussan [7] about the robustness of cost, control and state with respect to model errors has been extended to include input constraints using the results of [47] about interior penalty approach. Then, we have ended up with a quadratic upper bound on the error in the cost function of the form $K\varepsilon^2$. The estimation of the value of K as a function of the system parameters has been studied and illustrated via numerical examples. The presented results show that the estimated upper bound is conservative. Once K is estimated, we show how its value can be used as a tool to analyze the cost of simplifying OCPs.

Finally in Part III, real-time strategies for EMS have been investigated. Generalizations of the feedback law of ECMS were performed in Chapter 6 by using relationships between the thermal states and their corresponding adjoint states. These correlations have been identified along extremal calculated in Part I. The proposed strategies give satisfactory results for the pollutant emissions reduction with an acceptable extra-fuel consumption compared to optimal strategies.

Part IV

Bibliography and appendices

Bibliography

[1] A. Agrachev and Y. Sachkov. *Control theory from the geometric view-point.* Springer, 2004.

[2] D. Ambühl, O. Sundström, A. Sciarretta, and L. Guzzella. Explicit optimal control policy and its practical application for hybrid electric powertrains. *Control Engineering Practice*, 18:1429–1439, 2010.

[3] G-E. Andrews, J-R. Harris, and A. Ounzain. SI engine warm-up: water and lubricating oil temperature influences. *SAE Technical Paper*, 1989.

[4] F. Badin. *Hybrid vehicles.* Editions TECHNIP, 2013.

[5] M-E. Ben Gaïd, G. Corde, A. Chasse, and B. Léty et al. Heterogeneous model integration and virtual experimentation using xmod: application to hybrid powertrain design and validation. *7th EUROSIM Congress on Modeling and Simulation*, 2010.

[6] A. Ben Khaled. *Distributed real-time simulation of numerical models: application to powertrain.* PhD thesis, Université de Grenoble, 2014.

[7] A. Bensoussan. *Perturbation methods in optimal control.* Wiley, 1988.

[8] G. Bertotti, A. Boglietti, M. Chiampi, D. Chiarabaglio, F. Fiorillo, and M. Lazzari. An improved estimation of iron losses in rotating electrical machines. *IEEE Transactions on Magnetics*, 27:5007–5009, 1991.

[9] D. Bertsekas. *Dynamic programming and optimal control.* Athena Scientific, 2012.

[10] A. Bonfils. *Experimental closed-loop control of SCR aftertreatment systems using NOx sensors cross-sensitive to NH3.* PhD thesis, Ecole Nationale Supérieure des Mines de Paris, 2013.

[11] J-F. Bonnans and Th. Guilbaud. *Using logarithmic penalties in the shooting algorithm for optimal control problems.* Research Report INRIA, 2001.

[12] J-F. Bonnans and A. Hermant. Stability and sensitivity analysis for optimal control problems with a first-order state constraint and application to continuation methods. *ESAIM: COCV*, 14:825–863, 2008.

[13] H-A. Borhan, A. Vahidi, A-M. Phillips, and M-L. Kuang. Predictive energy management of a power-split hybrid electric vehicle. *in Proc. of the American Control Conference*, pages 3970–3976, 2009.

[14] A-E. Bryson and Y-C. Ho. *Applied optimal control.* Ginn and Company: Waltham, MA, 1969.

[15] A. Chasse, G. Corde, A-D. Mastro, and F. Perez. Hyhil: online optimal control of a parallel hybrid with after treatment constraint integration. *In Proc. of IEEE Vehicle Power and Propulsion Conference*, pages 1–6, 2010.

[16] A. Chasse, P. Pognant-Gros, and A. Sciarretta. Online implementation of an optimal supervisory control for a parallel hybrid powertrain. *SAE Technical Paper*, pages 1630–1638, 2009.

[17] A. Chasse and A. Sciarretta. Supervisory control of hybrid powertrains: an experimental benchmark of offline optimization and online energy management. *Control Engineering Practice*, 19:1253–1265, 2011.

[18] J-S. Chen and M. Salman. Learning energy management strategy for hybrid electric vehicles. *In Proc. of IEEE Vehicle Power and Propulsion Conference*, pages 68–73, 2005.

[19] B. De Jager, T. van Keulen, and J. Kessels. *Optimal control of hybrid vehicles.* Springer-Verlag London, 2013.

[20] S. Delprat, T-M. Guerra, and J. Rimaux. Control strategies for hybrid vehicles: synthesis and evaluation. *Proc. of the Vehicular Technology Conference*, 5:3246–3250, 2003.

[21] S. Delprat and T. Hofman. Hybrid vehicle optimal control: linear interpolation and singular control. *IEEE Vehicle Power and Propulsion Conference*, pages 1–6, 2014.

[22] W. Dib, A. Chasse, P. Moulin, A. Sciarretta, and G. Corde. Optimal energy management for an electric vehicle in eco-driving applications. *Control Engineering Practice*, 29:299–307, 2014.

[23] A-L. Dontchev. Perturbations, approximations and sensitivity analysis of optimal control systems. *Lecture Notes in Control and Information Sciences*, 52:1–153, 1983.

[24] R. Dutta, L. Chong, and F-M. Rahman. Analysis and experimental verification of losses in a concentrated wound interior permanent magnet machine. *Progress In Electromagnetics Research B*, 48:221–248, 2013.

[25] L. Eriksson. Mean value models for exhaust system temperatures. *SAE Technical Paper*, 2002.

[26] L. Eriksson and L. Nielsen. *Modeling and control of engines and drivelines.* Wiley, 2014.

[27] A-V. Fiacco and G-P. McCormick. Nonlinear programming: sequential unconstrained minimization techniques. *Wiley : New York*, 1968.

[28] J-P. Gao, G. Zhu, E-G. Strangas, and F-C. Sun. Equivalent fuel consumption optimal control of a series hybrid electric vehicle. *Journal of Automobile Engineering*, 223:1003–1018, 2009.

[29] Y. Gaoua, S. Caux, P. Lopez, and J-D. Salvany. On-line HEV energy management using a fuzzy logic. *12th International Conference on Environment and Electrical Engineering*, pages 46–51, 2013.

[30] K. Graichen. *Feedforward control design for finite time transition problems of nonlinear systems with input and output constraints.* PhD thesis, University of Stuttgart, 2006.

[31] K. Graichen, A. Kugi, N. Petit, and F. Chaplais. Handling constraints in optimal control with saturation functions and system extension. *Systems and Control Letters*, 59:671–679, 2010.

[32] K. Graichen and N. Petit. Constructive methods for initialization and handling mixed state-input constraints in optimal control. *AIAA Journal of Guidance Control and Dynamics*, 31:1334–1343, 2008.

[33] L. Guzzella and A. Sciarretta. *Vehicle propulsion systems.* Springer, 2013.

[34] C-R. Hargraves and S-W. Paris. Direct trajectory optimization using nonlinear programming and collocation. *Journal of Guidance, Control and Dynamics*, 10:338–342, 1987.

[35] N. Karmarkar. A new polynomial-time algorithm for linear programming. *Combinatorica*, 4:373–395, 2008.

[36] S. Kermani, S. Delprat, R. Trigui, and T-M. Guerra. Predictive energy management of hybrid vehicle. *Control Engineering Practice*, 20:408–420, 2012.

[37] J. Kessels, M. Koot, P. Van den Bosch, and D. Kok. Online energy management for hybrid electric vehicles. *IEEE Transactions on Vehicular Technology*, 57(6):3428–3440, 2008.

[38] H. Khalil. *Nonlinear systems.* Prentice Hall, 2002.

[39] U. Kiencke and L. Nielsen. *Automotive control systems: for engine, driveline, and vehicle.* Springer, 2005.

[40] N. Kim, S. Cha, and H. Peng. Optimal control of hybrid electric vehicles based on Pontryagin's minimum principle. *IEEE Transactions on Control Systems Technology*, 19:1279–1287, 2011.

[41] I. Kwang Yoo, K. Simpson, M. Bell, and S. Majkowski. An engine coolant temperature model and application for cooling system diagnosis. *SAE Technical Paper*, 2000.

[42] O. Lepreux. *Model-based temperature control of a Diesel Oxidation Catalyst.* PhD thesis, Ecole Nationale Supérieure des Mines de Paris, 2009.

[43] J. Lescot, A. Sciarretta, Y. Chamaillard, and A. Charlet. On the integration of optimal energy management and thermal management of hybrid electric vehicles. *In Proc. of IEEE Vehicle Power and Propulsion Conference*, 2010.

[44] C-C. Lin, H. Peng, J-W. Grizzle, and J-M Kang. Power management strategy for a parallel hybrid electric truck. *IEEE Transactions on Control Systems Technology*, 11:839–849, 2003.

[45] D. Maamria, F. Chaplais, N. Petit, and A. Sciarretta. Numerical optimal control as a method to evaluate the benefit of thermal management in hybrid electric vehicles. *Proc. of the IFAC World Congress*, pages 4807–4812, 2014.

[46] D. Maamria, F. Chaplais, N. Petit, and A. Sciarretta. On the impact of model simplification in input constrained optimal control: application to HEV energy-thermal management. *53rd IEEE Conference on Decision and Control*, pages 2529–2535, 2014.

[47] P. Malisani. *Dynamic control of energy in buildings using constrained optimal control by interior penalty.* PhD thesis, Ecole Nationale Supérieure des Mines de Paris, 2012.

[48] P. Malisani, F. Chaplais, and N Petit. Design of penalty functions for optimal, control of linear dynamical systems under state and input constraints. *50th IEEE Conference on Decision and Control and European Control Conference*, pages 6697–6704, 2011.

[49] P. Malisani, F. Chaplais, and N. Petit. A constructive interior penalty method for non linear optimal control problems with state and input constraints. *in Proc. of the American Control Conference*, pages 2669–2676, 2012.

[50] P. Malisani, F. Chaplais, and N. Petit. An interior penalty method for optimal control problems with state and input constraints of non-linear systems. *Optimal Control, Applications and Methods*, 2014.

[51] N. Marc, E. Prada, A. Sciarretta, S. Anwer, F. Vangraefschepe, F. Badin, A. Charlet, and P. Higelin. Sizing and fuel consumption evaluation methodology for hybrid light duty vehicles. *World Battery, Hybrid and Fuel Cell Electric Vehicle Symposium & Exhibition*, 4:249–258, 2010.

[52] C. Martínez. Energy efficiency in the automotive industry evidence from germany and colombia. *Environment, Development and Sustainability*, 13:367–383, 2011.

[53] A. Mastro, A. Chasse, P. Pognant-Gros, and G. Corde et al. Advanced hybrid vehicle simulation: from virtual to HyHiL test bench. *SAE Technical Paper*, 2009.

[54] F. Mensing, E. Bideaux, R. Trigui, J. Ribet, and B. Jeanneret. Eco-driving: an economic or ecologic driving style? *Transportation Research Part C: Emerging Technologies*, 38:110–121, 2014.

[55] F. Merz, A. Sciarretta, J-C. Dabadie, and L. Serrao. On the optimal thermal management of hybrid-Electric vehicles with heat recovery systems. *Oil & Gas Science and Technology*, 67(4):601–612, 2012.

[56] P. Michel, A. Charlet, G. Colin, Y. Chamaillard, C. Nouillant, and G. Bloch. Energy management of HEV to optimize fuel consumption and pollutant emissions. *Proc. of International Symposium on Advanced Vehicule Control*, 2012.

[57] P. Michel, A. Charlet, G. Colin, Y. Chamaillard, C. Nouillant, and G. Bloch. 3 WCC temperature integration in a gasoline-HEV optimal energy management strategy. *Advances in Mechanical Engineering*, 2014.

[58] P. Michel, A. Charlet, G. Colin, Y. Chamaillard, C. Nouillant, and G. Bloch. Catalytic converter modeling for optimal gasoline-HEV energy management. *Proc. of the IFAC World Congress*, pages 6636–6641, 2014.

[59] T. Morel and R. Keribar. Warm-up characteristics of a spark ignition engine as a function of speed and load. *SAE Technical Paper*, 1990.

[60] C. Musardo, G. Rizzoni, and B. Staccia. A-ECMS: an adaptive algorithm for hybrid electric vehicle energy management. *44th IEEE Conference on Decision and Control, and the European Control Conference*, pages 1816–1823, 2005.

[61] S-C. Oh and A-J. Hildreth. Estimating the technical improvement of energy efficiency in the automotive industry: stochastic and deterministic frontier benchmarking approaches. *Energies*, 7:6196–6222, 2014.

[62] S. Onori and L. Serrao. On adaptive-ECMS strategies for hybrid electric vehicles. *Proc. of the International Scientific Conference on Hybrid and Electric Vehicles*, pages 1–7, 2011.

[63] T-M. Padovani, M. Debert, G. Colin, and Y. Chamaillard. Optimal energy management strategyincluding battery health through thermal management for hybrid vehicles. *IFAC Symposium on Advances in Automotive Control*, pages 384–389, 2013.

[64] G. Paganelli, S. Delprat, T-M. Guerra, J. Rimaux, and J-J. Santin. Equivalent consumption minimization strategy for parallel hybrid powertrains. *55th IEEE Vehicular Technology Conference*, pages 2076–2081, 2002.

[65] G. Paganelli, G. Ercole, A. Brahma, Y. Guezennec, and G. Rizzoni. General supervisory control policy for the energy optimization of charge-sustaining hybrid electric vehicles. *JSAE Review*, 22:511–518, 2001.

[66] E. Philipp. *Noncausal and causal optimization strategies for hybrid electric vehicles*. PhD thesis, ETH Zurich, 2014.

[67] Clean Power Plan. http://www2.epa.gov/cleanpowerplan.

[68] L-S. Pontryagin, V-G. Boltyanskii, R-V. Gamkrelidze, and E-F. Mishchenko. *The mathematical theory of optimal processes*. Interscience Publishers John Wiley & Sons, Inc. New York, London, 1962.

[69] HYDIVU Project. http://www.ademe.fr/hydivu-groupe-motopropulseur-hybride-diesel-vehicule-utilitaire-leger-inter-urbain.

[70] S. Roberts and J. Shipman. Two-point boundary value problems: shooting methods. *American Elsevier Pub, New York*, 1972.

[71] G. Rousseau, D. Sinoquet, and P. Rouchon. Constrained optimization of energy management for a mild-hybrid vehicle. *Oil & Gas Science and Technology*, 62:623–634, 2007.

[72] G. Rousseau, D. Sinoquet, A. Sciarretta, and Y. Milhau. Design optimisation and optimal control for hybrid vehicles. *Proc. of International Conference on Engineering Optimization*, 2008.

[73] S-B. Ebbesen. *Optimal sizing and control of hybrid electric vehicles*. PhD thesis, ETH Zurich, 2012.

[74] A. Sciarretta, M. Back, and L. Guzzella. Optimal control of parallel hybrid electric vehicles. *IEEE Transactions on Control Systems Technology*, 12:352–363, 2004.

[75] A. Sciarretta, J-C. Dabadie, and G. Font. Automatic model-based generation of optimal energy management strategies for hybrid powertrains. *Proc. of the SIA Powertrain Conference*, 2015.

[76] A. Sciarretta, D. di Domenico, P. Pognant-Gros, and G. Zito. *Optimal energy management of automotive battery systems including thermal dynamics and ageing*. Optimization and Optimal Control in Automotive Systems, Springer Lecture Notes in Control Science, 2014.

[77] A. Sciarretta and L. Guzzella. Control of hybrid electric vehicles. *IEEE Control Systems Magazine*, 27:60–70, 2007.

[78] A. Sciarretta and N. Petit. Optimal drive of electric vehicles using an inversion-based trajectory generation approach. *18th IFAC World Congress*, 18:14519–14526, 2011.

[79] L. Serrao, S. Onori, and G. Rizzoni. ECMS as a realization of Pontryagin's minimum principle for HEV control. *in Proc. of the American Control Conference*, pages 3964–3969, 2009.

[80] L. Serrao, S. Onori, A. Sciarretta, Y. Guezennec, and G. Rizzoni. Optimal energy management of hybrid electric vehicles including battery aging. *in Proc. of the American Control Conference*, pages 2125–2130, 2011.

[81] L. Serrao, A. Sciarretta, O. Grondin, A. Chasse, Y. Creff, D. di Domenico, P. Pognant-Gros, C. Querel, and L. Thibault. Open issues in supervisory control of hybrid electric vehicles: a unified approach using optimal control methods. *Proc. of RHEVE, Int. Scient. Conf. on Hybrid and Electric Vehicles*, 2011.

[82] L. Shampine, J. Kierzenka, and M. Reichelt. *Solving boundary value problems for ordinary differential equations in Matlab with bvp4c*.

[83] P. Shayler, S. Christian, and T. Ma. A model for the investigation of temperature, heat flow and friction characteristics during engine warm-up. *SAE Technical Paper*, pages 667–675, 1993.

[84] E. Silvas, T. Hofman, and M. Steinbuch. Review of optimal design strategies for hybrid electric vehicles. *IFAC Workshop on Engine and Powertrain Control, Simulation and Modeling*, pages 57–64, 2012.

[85] M. Sivertsson and L. Eriksson. Design and evaluation of energy management using map-based ECMS for the PHEV benchmark. *Oil & Gas Science and Technology*, 70:195–211, 2014.

[86] G. Tamai, T. Hoang, J. Taylor, and C. Skaggs et al. Saturn engine stop-start system with an automatic transmission. *SAE Technical Paper*, 2001.

[87] K. Van Berkel, W. Klemm, T. Hofman, B. Vroemen, and M. Steinbuch. Optimal energy management for a mechanical-hybrid vehicle with cold start conditions. *European Control Conference*, pages 452–457, 2013.

[88] K. Van Berkel, W. Klemm, T. Hofman, B. Vroemen, and M. Steinbuch. Optimal control of a mechanical hybrid powertrain with cold start conditions. *IEEE Transactions on Vehicular Technology*, 63:1555–1566, 2014.

[89] A-B Vasilieva and M-G. Dmitriev. Singular perturbations in optimal control problems. *Journal of Mathematical Sciences*, 34:1579–1629, 1986.

[90] S-N. Vukosavic. *Electrical machines*. Springer, 2012.

[91] L. Yong-chen and S. Li. City bus idle stop-start system simulation analysis. *International Conference on Mechatronic Science, Electric Engineering and Computer*, pages 763–766, 2011.

[92] Y. Zhu, Y. Chen, G. Tian, H. Wu, and Q. Chen. A four-step method to design an energy management strategy for hybrid vehicles. *in Proc. of the American Control Conference*, pages 156–161, 2004.

Appendix A

Description of driving cycles

A driving cycle is a series of data points representing the speed and the road gradient profiles as functions of time, to be followed by a vehicle. It provides a basis of comparison to assess the performance of vehicles, for example with respect to fuel consumption and pollutant emissions. In practice, these cycles are often used on chassis dynamometers where the force at the wheels emulates the vehicle energy losses. These tests are carried out in controlled environments (in terms of temperature, humidity), with strict procedures being followed in order to reach defined thermal initial conditions for the vehicle [33]. Another use of standard driving cycles is found in vehicle simulations. More precisely, they are used, in propulsion system simulations, to predict performance of the various powertrain components: internal combustion engine, transmission, electric drive system and battery.

Driving cycles are either built arbitrarily by defining steady-state speed phases and accelerations/decelerations to link these phases (as with NEDC cycle), or from statistical data collected in real use of vehicles. This driving cycle resulting from the second technique is considered to fairly reproduce true vehicle usages. The driving cycles used in this thesis are pictured in the following figures. The WLTC cycle is used in Chapter 7 for the experimental tests. The gear-box ratios are calculated according to a law based on the vehicle performance requirements.

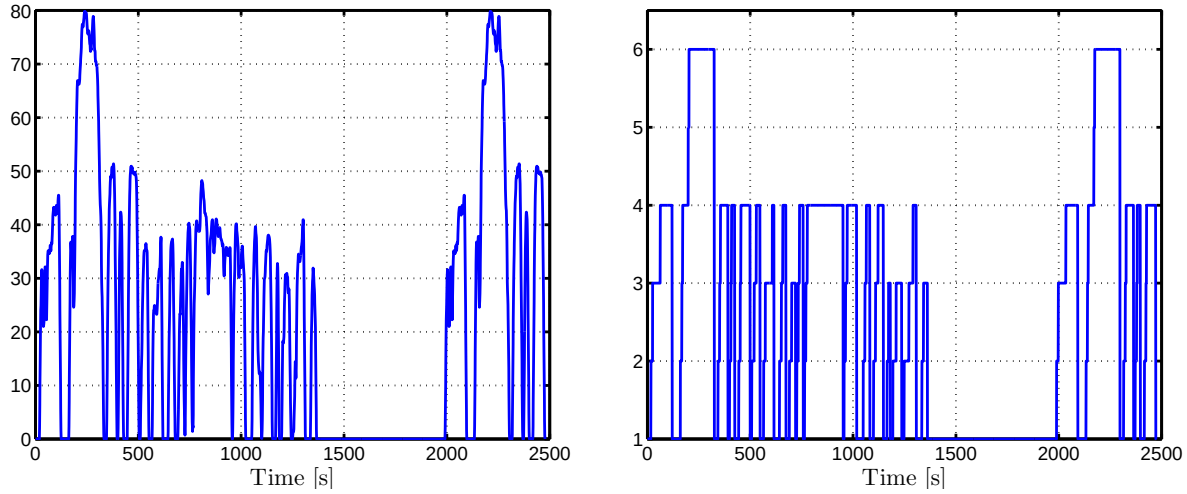

Figure A.1: Wheel speed [km/h] (left) and gear-box ratio (right) for FTP-75 cycle

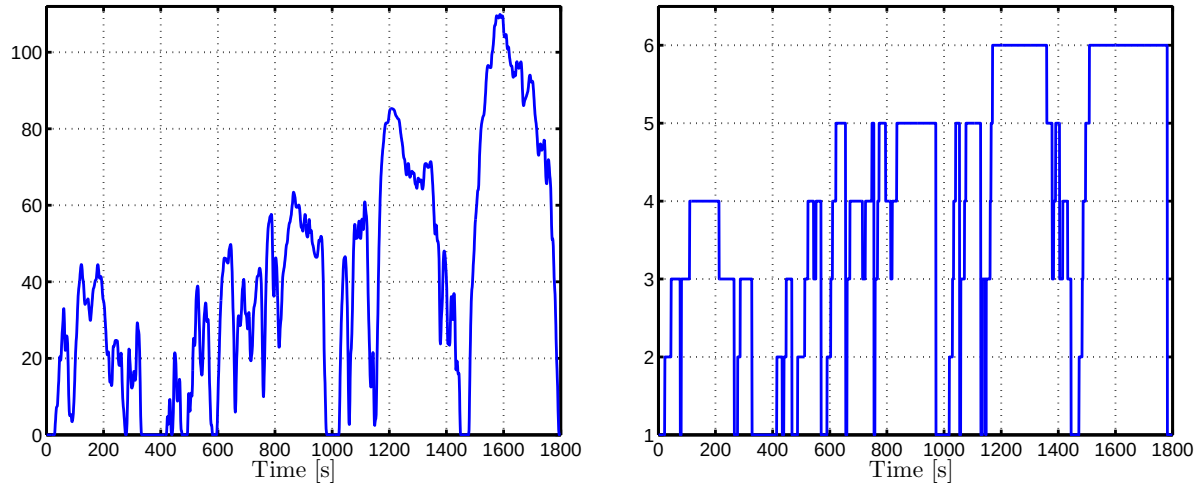

Figure A.2: Wheel speed [km/h] (left) and gear-box ratio (right) for WLTC$_m$ cycle

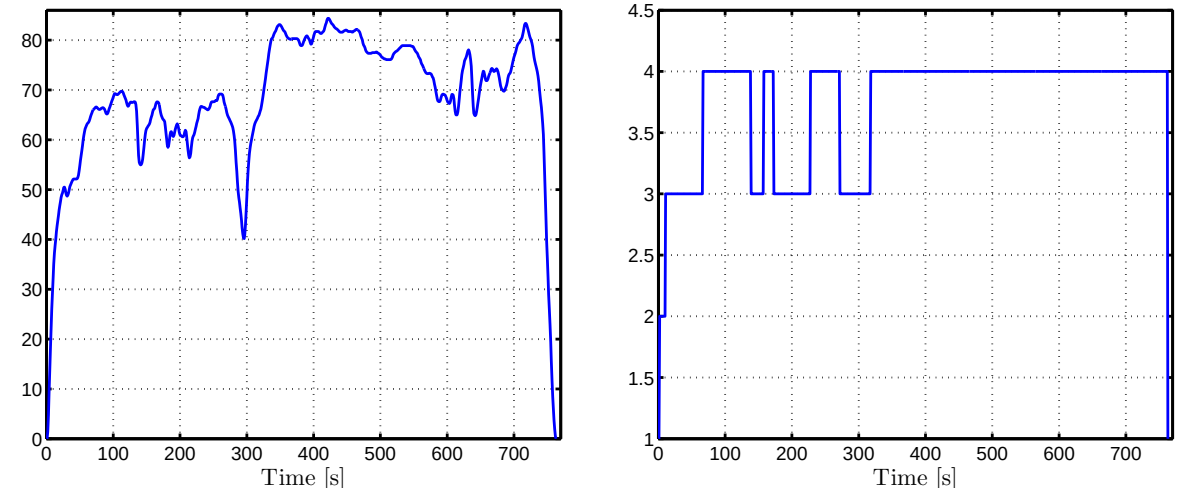

Figure A.3: Wheel speed [km/h] (left) and gear-box ratio (right) for FHDS cycle

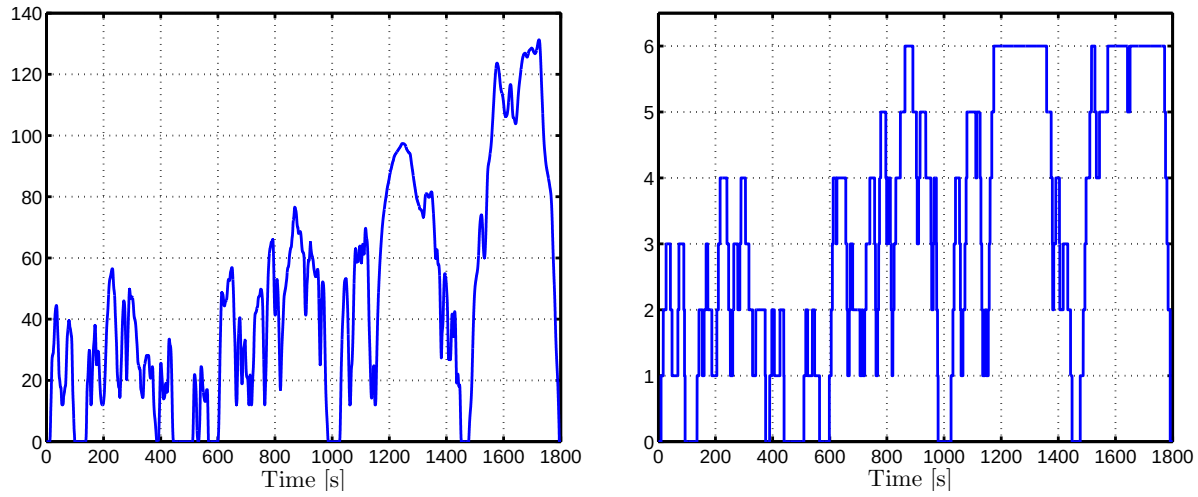

Figure A.4: Wheel speed [km/h] (left) and gear-box ratio (right) for WLTC

Appendix B

Fuel consumption minimization case

The cost function (B.1) to be minimized is the fuel consumption over a fixed time window corresponding to a given driving cycle of a duration T:

$$J_2^0(u) = \int_0^T c_f(u, t, \theta_e)dt, \tag{B.1}$$

where u is the control variable (the engine torque), θ_e is the engine temperature state and $c_f(u, t, \theta_e)$ is the fuel consumption rate when the engine is cold given in equation (4.2).

Two dynamics are taken into account. The first one is the SOC dynamics. It is governed by the differential equation (3.2) with the final constraint (3.3). The second state variable is the engine temperature θ_e described by the differential equation (4.3). The OCP discussed here is defined by

$$\min_{u \in U^{ad}} J_2^0(u),$$

under the final constraint (3.3), the instantaneous constraint on the SOC (3.5) and the dynamics (3.2, 4.3). This OCP can be obtained from (OCP_2) by setting $\alpha = 0$ in the cost function J_2 defined in equation (4.1).

B.1 PMP solution and numerical solving

B.1.1 Without instantaneous SOC constraints

Based on the PMP [68], the Hamiltonian H_2^0 is defined by

$$H_2^0(u, t, \theta_e, \lambda, \mu) = c(u, t)e(\theta_e) + \lambda f(u, t) + \mu g(u, t, \theta_e),$$

where λ and μ are the adjoint variables associated to ξ and θ_e respectively[1]. For a given control u_2^{*0}, the adjoint states $\lambda(t)$ and $\mu(t)$ are defined by

$$\frac{d\lambda}{dt} = -\frac{\partial H_2^0}{\partial \xi} = 0, \tag{B.2}$$

$$\frac{d\mu}{dt} = -\frac{\partial H_2^0}{\partial \theta_e} = -c(u_2^{*0}, t)\frac{\partial e}{\partial \theta_e} - \mu\frac{\partial g(u_2^{*0}, t, \theta_e)}{\partial \theta_e}, \tag{B.3}$$

[1] In the naming of the Hamiltonian, the superscript indicates the value of α in the Hamiltonian H_2 defined in equation (4.5).

with

$$\mu(T) = 0, \tag{B.4}$$

since the final temperature is free and the final time T is fixed. If u_2^{*0} is an optimal control, then, for every t, $u_2^{*0}(t)$ minimizes the Hamiltonian H_2^0 in the set defined by (3.4),

$$u_2^{*0}(t) \in \arg\min_{u \in U^{ad}} H_2^0(u, t, \theta_e(t), \lambda(t), \mu(t)). \tag{B.5}$$

Equations (3.2, 3.3, B.2, B.3, B.4, B.5) constitute a TPBVP denoted by (P_1), where the final condition $\lambda(T)$ is unknown. The control strategy obtained is denoted as (S_2^0).

For the numerical method, a specifically tailored single shooting-related method was used. Classically, the idea of this algorithm is to consider the initial conditions of the adjoint states (λ_0, μ_0) as unknown variables and the vector function, which associates $[\xi(T) - \xi(0)]$ and $\mu(T)$ and (λ_0, μ_0), where $(\xi, \theta_e, \lambda, \mu)$ are the solution of the following system in $[0, T]$

$$\begin{cases} \dfrac{d\xi}{dt} = f(u_2^{*0}, t), \quad \xi(0) = \xi_0, \\ \dfrac{d\theta_e}{dt} = g(u_2^{*0}, t, \theta_e), \quad \theta_e(0) = \theta_0, \\ \dfrac{d\lambda}{dt} = 0, \quad \lambda(0) = \lambda_0, \\ \dfrac{d\mu}{dt} = -c(u_2^{*0}, t)\dfrac{\partial e}{\partial \theta_e} - \mu \dfrac{\partial g(u_2^{*0}, t, \theta_e)}{\partial \theta_e}, \quad \mu(0) = \mu_0. \end{cases}$$

Then, the problem is re-cast into finding zeros of this function from $\mathbb{R}^2$ into $\mathbb{R}^2$. This is achieved using Newton's method implemented in the popular `fsolve` Matlab function. The solution given by `bvp4c` (which is not accurate enough) is used to initialize the `fsolve` algorithm.

B.1.2 With instantaneous SOC constraints

To take the SOC constraints into account, the algorithm proposed in [47] was used. A new cost function parametrized by the penalty weight r is defined

$$\bar{J}_2^0(u, r) = \int_0^T [c(u, t)e(\theta_e) + r \cdot \gamma(\xi)]\, dt,$$

where $\gamma(.)$ is given by (3.11). For simplicity, and as the SOC trajectories are always below ξ_{max} for the considered driving cycles, only the constraint $\xi(t) \geq \xi_{min}$ is considered. To solve this OCP, the PMP was used and the associated Hamiltonian H_{2r}^0 is defined by

$$H_{2r}^0(u, t, \xi, \lambda, r) = c(u, t)e(\theta_e) + r \cdot \gamma(\xi) + \lambda f(u, t) + \mu g(u, t, \theta_e).$$

Only the dynamics of the adjoint state λ is modified by comparison with the unconstrained case presented in the previous section. The new dynamics of λ is given by

$$\dot{\lambda} = \frac{r.n_g}{(\xi(t) - \xi_{min})^{n_g+1}}, \tag{B.6}$$

where $\lambda(T)$ is free since the final SOC is constrained. The optimal control $u_1^r(t)$ minimizes the Hamiltonian H_{2r}^0 in the set defined by (3.4):

$$u_1^r(t) \in \arg\min_{u \in U^{ad}} H_{2r}^0(u, t, \xi, \lambda, r). \tag{B.7}$$

Equations (3.2, 3.3, B.3, B.4, B.6, B.7) constitute a TPBVP denoted by (P_1^r) where the final condition $\lambda(T)$ is unknown. The parameter n_g is set at 1.1. The weight r is initialized with $r_0 = 2 \cdot 10^{-6}$ for the NEDC, and is then decreased.

B.2 Numerical results

An equivalence factor that is positive and dimensionless, denoted by p, is used instead of using μ (which is negative). The relationship between the two parameters is given by

$$p(t) = -\frac{H_{lhv}}{C_e}\mu(t), \tag{B.8}$$

where H_{lhv} is the lower heating value of the fuel. The stationarity condition of the PMP is expressed on the quantity $\tilde{H}_2^0$ given in (B.9) (in power units). $\tilde{H}_2^0$ is the sum of three quantities: the consumed fuel power, the inner (electrochemical) battery power and a thermal power defined by the engine temperature variation $P_{therm}(t) = -C_e \cdot \dot{\theta}_e$,

$$\tilde{H}_2^0(u, t, \theta_e, s, p) = c(u, t)e(\theta_e) \cdot H_{lhv} + s(t) \cdot I_b(t) \cdot U_{ocv}(t) + p(t) \cdot P_{therm}(t), \tag{B.9}$$

where s is the equivalence factor associated to the SOC defined in (3.15). In the case of instantaneous constraints on the SOC, the equivalent quantity of H_{2r}^0 in power units is

$$\tilde{H}_{2r}^0(u, t, \theta_e, s, p) = [c(u, t)e(\theta_e) + r \cdot \gamma(\xi)] \cdot H_{lhv} + s(t) \cdot I_b(t) \cdot U_{ocv}(t) + p(t) \cdot P_{therm}(t).$$

B.2.1 Without instantaneous SOC constraints

The two strategies (S^0) and (S_2^0) calculated by solving the two TPBVP (P_0) (described in Section 3.4.2.1) and (P_1) (described in Section B.1.1) will be compared[2]. Table B.1 summarizes the results obtained in terms of fuel consumption for five driving cycles: NEDC, FUDS, FHDS, FTP and a modified cycle based on WLTC cycle, denoted by WLTC_m. Fuel consumption for a warm engine start is given in the second column corresponding to the strategy (S^0). The optimal trajectories of the SOC, the temperature θ_e and the equivalence factor p for the NEDC are given in the Figures B.1 and B.2 respectively. In the right-hand graph in Figure B.1, the red curve represents the simulated trajectory of θ_e using the control calculated from the strategy (S^0).

The optimal temperature trajectories in Figure B.1 show that the optimal control strategy (S_2^0) improves the engine efficiency by warming up the engine in the first phase of the driving cycle (corresponding to the time interval [0, 800] s). In this phase, the SOC trajectory is higher than the trajectory corresponding to the strategy (S^0). The price paid for achieving this efficiency improvement is an increased fuel consumption due to the excessive use of the engine. This observation means that the control u_2^{*0} anticipates the influence of the low engine temperature on the fuel consumption and improves engine efficiency in the first part of the driving cycle.

[2]In the naming of the control strategies, the superscript indicates the value of α in the corresponding Hamiltonian.

Table B.1: Fuel consumption [L/100 km]

Driving cycle	S_2^0	S^0 (Warm start)
NEDC	4.94	4.38
FUDS	4.54	4.01
FHDS	5.48	5.10
FTP	4.40	4.01
WLTC_m	5.215	4.94

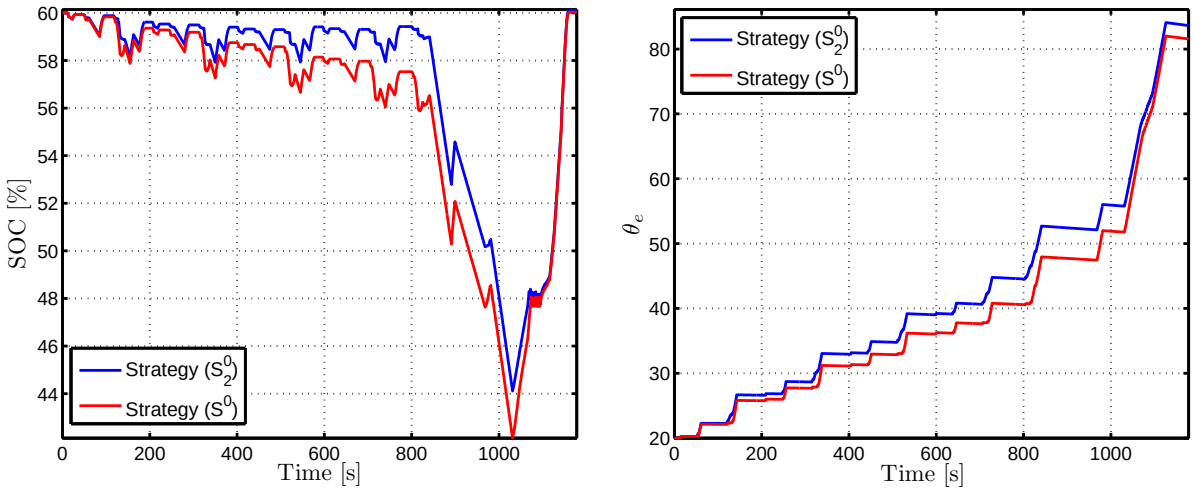

Figure B.1: SOC [%] trajectories (left) and simulated θ_e [°C] trajectories (right) for NEDC in the unconstrained case

The equivalence factor p associated to θ_e for NEDC, shown in Figure B.2, decreases with time and becomes null when the engine is warm ($\theta_e \geq \theta_w$). This is due to the increase in the engine temperature and, consequently, the fuel consumption becomes independent of θ_e after a certain time (corresponding to the time when the thermostat is activated).

B.2.2 Relation between $p(0)$ and $\theta_e(0)$

The behavior of the equivalence factor p depends on the initial value of the engine temperature $\theta_e(0)$. While the SOC equivalence factor is constant, the temperature equivalence factor varies substantially in time, tending to zero when $\theta_e(t)$ tends to 80 °C (the temperature at which the thermostat is activated). The relationship between $p(0)$ and $\theta_e(0)$ is identified here in view of a possible estimation of $p(0)$ for real-time application. To do that, the initial condition of θ_e is changed and the corresponding optimal solution of (P_1) is calculated. This operation was done for the five driving cycles being considered. The results, summarized in Figure B.3, show that the relationship between $p(0)$ and $\theta_e(0)$ is monotonic and that $p(0)$ tends to zero when $\theta_e(0)$ goes to 80°C. The optimal value of $p(0)$ can be identified by a quadratic function in $\theta_e(0)$

$$p(0) = l_1 \cdot \theta_e^2(0) + l_2 \cdot \theta_e(0) + l_3,$$

where the parameters $l_i,\ i = 1,\ 2,\ 3$ depend on the driving cycle. These results can be used for a real-time implementation.

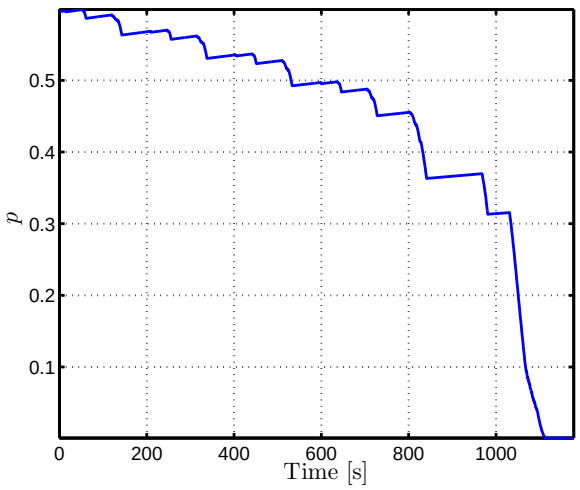

Figure B.2: Equivalence factor p for NEDC

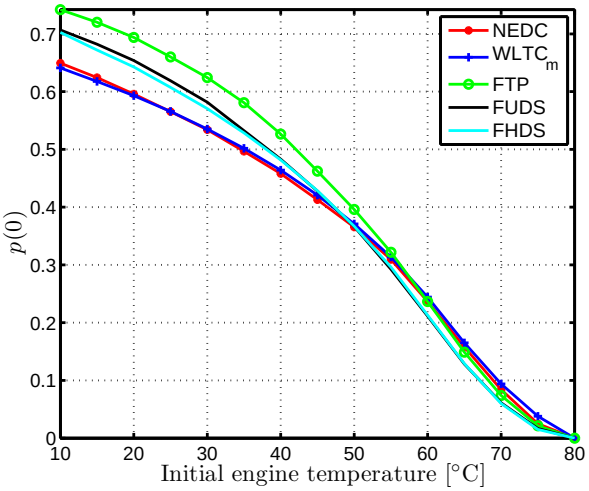

Figure B.3: Relation between $p(0)$ and $\theta_e(0)$

B.2.3 With instantaneous SOC constraints

For each value of r in a decreasing sequence, the TPBVP (P_1^r) is solved. The state and the corresponding costate trajectories for NEDC are shown in Figures B.4 and B.5. The obtained fuel consumptions are summarized in Table B.2.

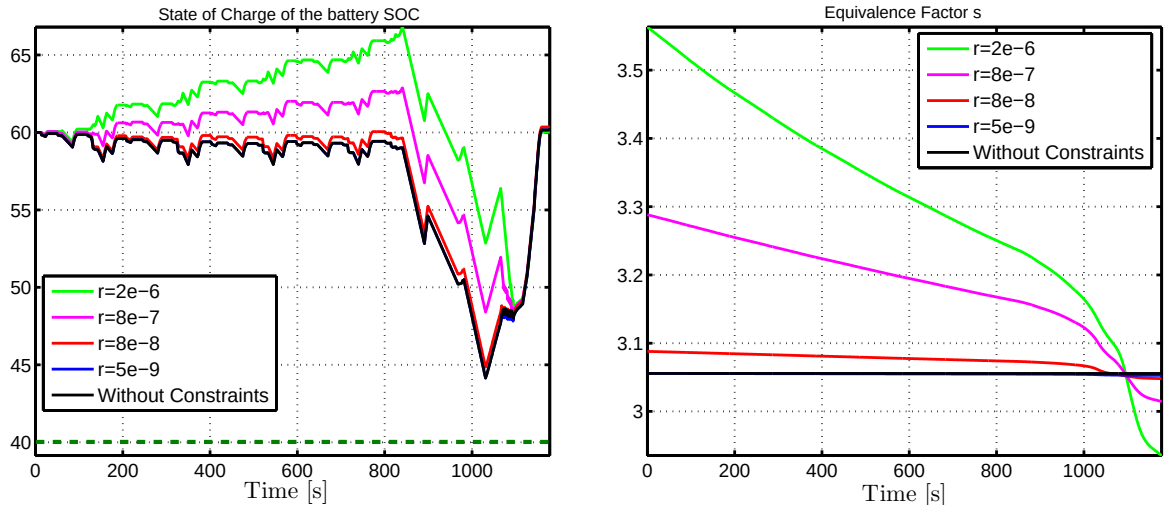

Figure B.4: SOC [%] trajectories (left) and equivalence factor $s(t)$ (right) for NEDC in the constrained case

Table B.2: $J_2^0(u_1^r)$ [L/100 km] for NEDC

r	$J_2^0(u_1^r)$	$100 \cdot \min(\xi(t) - \xi_{min})$
$2e^{-6}$	4.973	8.59
$8e^{-7}$	4.961	8.30
$8e^{-8}$	4.957	4.84
$5e^{-9}$	**4.947**	**4.14**
Without constraints	**4.94**	/

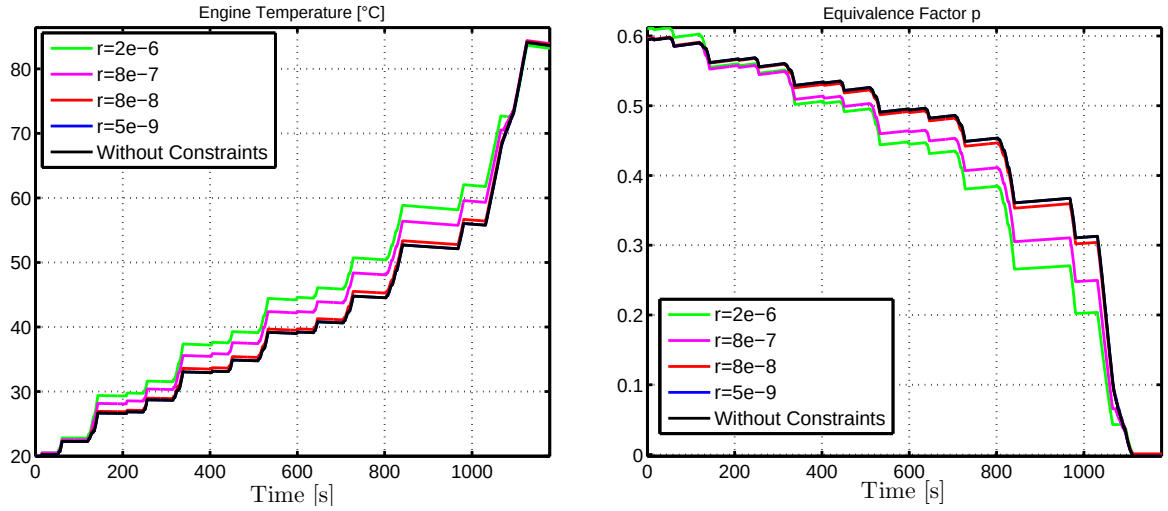

Figure B.5: Engine temperature θ_e [°C] (left) and equivalence factor p (right) for NEDC in the constrained case

When r decreases, Figure B.4 shows that the SOC trajectories approach the state constraints and the engine temperature trajectories are affected. The parameter r has some impact on the history of the SOC (the use of the engine and the electric machine): for high value of r, the control strategy recharges the battery at the beginning of the driving cycle by overusing the engine. To minimize the term $r \cdot \gamma(\xi)$, $\xi(t)$ has to be far from its lower bound (ξ_{min}). This use of the engine at the beginning of the driving cycle increases the engine temperature quickly (see Figure B.5). When r tends to zero, the strategy has more flexibility and the SOC moves close to the constraints. The term $\gamma(\xi)$ increases.

The trajectories of equivalence factors s and p given in Figures B.4 and B.5 (right-hand figures) illustrate the monotonic relation between the initial conditions ($s(0)$, $p(0)$) and the value of r. When r goes to zero, ($s(0)$, $p(0)$) converge to their initial values in the unconstrained case (the black and the cyan trajectories in Figures B.4 and B.5). This convergence is quite logical as the SOC constraints are never activated even in the unconstrained case.

To illustrate the usefulness of the interior penalty approach in the presence of active state constraints, the combined cycle (see Figure 3.12) is considered. The weight r for this cycle is initialized with $r_0 = 5 \cdot 10^{-7}$. The control strategies obtained for various values of r are compared in Table B.3 to the unconstrained strategy in terms of fuel consumption. The SOC and the equivalence factor s trajectories are given in Figures B.6.

Table B.3: $J_2^0(u_1^r)$ [L/100 km] for the combined cycle

r	$J_2^0(u_1^r)$	$100 \cdot \min(\xi(t) - \xi_{min})$
$5e^{-7}$	5.089	8.19
$1e^{-7}$	5.064	5.43
$5e^{-8}$	5.058	1.85
$8e^{-9}$	**5.054**	**0.39**
Without constraints	**5.053**	/

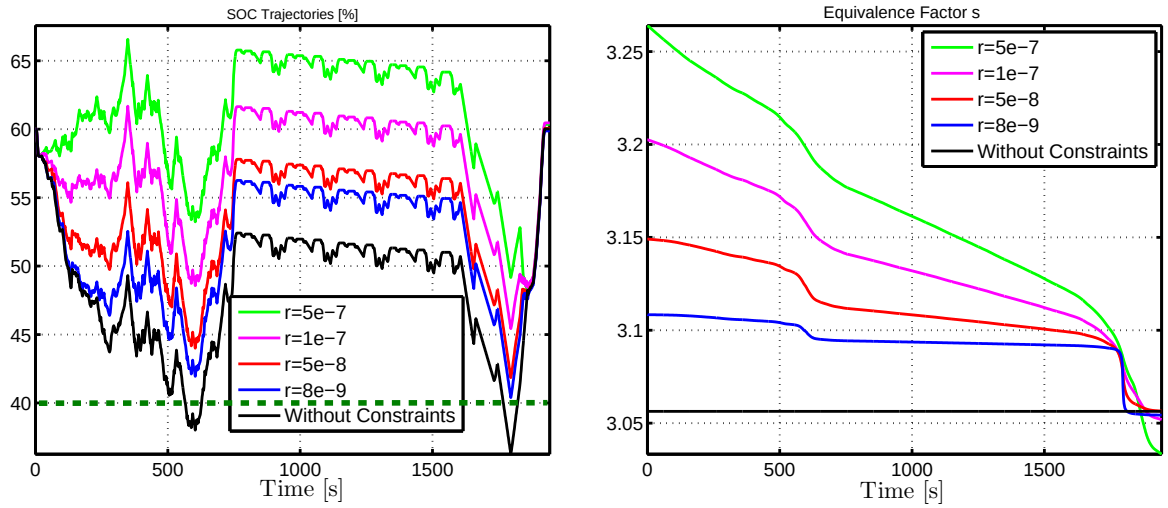

Figure B.6: SOC [%] (left) and equivalence factor $s(t)$ (right) for the combined cycle in the constrained case

The SOC trajectory approaches the state constraints and the constraints are always satisfied. When r tends to zero, the minimum distance between the SOC and its lower bound decreases. After a certain threshold of r for which ξ is very close to ξ_{min}, a jump in the value of the equivalence factor s appears.

The fuel consumptions given in Table B.3 show that the difference in terms of fuel consumption for different values of r is less than 2% compared to the unconstrained strategy. This remark is discussed in Section 5.9 from a theoretical viewpoint.

B.3 Simplified model for EMS minimizing fuel consumption

The objective is to find a trade-off between the order of the model used to calculate the optimal control (i.e., number of state variables) and the optimality of the used strategy. The constraints (3.5) on the SOC are omitted.

B.3.1 Control strategies description

The idea presented here is based on simplifying the model used to calculate the optimal control. Three control strategies are defined:

- The strategy (S^0) refers to the solution of the TPBVP (P_0) where $e(\theta_e)$ is constant, $e \equiv 1$.
- The strategy (S_2^0) corresponds to the solution of the TPBVP (P_1). It represents the optimal solution.
- Following the work in [55], the strategy (HS_2^0) is a pseudo-solution of the TPBVP (P_1) where $\mu(t) = 0, \quad \forall t$ is imposed in the Hamiltonian. This simplification reduces the number of the unknown variables from 2 to 1.

The control strategies are formulated in Table B.4. The strategies (S^0) and (HS_2^0) are single state strategies where the only unknown variable, the adjoint state λ, is determined to satisfy the final constraint (3.3).

Table B.4: Control strategies description[3]

Strategy	Unknown	Control	Opt/Heur
(S_2^0)	2 (λ, μ)	$u_2^{*0}(t) = \arg\min_{u\in U^{ad}}(c(u,t)e(\theta) + \lambda\frac{d\xi}{dt} + \mu\frac{d\theta}{dt})$	Optimal
(S^0)	1 (λ)	$u^{*0}(t) = \arg\min_{u\in U^{ad}}(c(u,t) + \lambda\frac{d\xi}{dt})$	Optimal
(HS_2^0)	1 (λ)	$u_1^h(t) = \arg\min_{u\in U^{ad}}(c(u,t)e(\theta) + \lambda\frac{d\xi}{dt})$	Heuristic

Note that these strategies are only used to calculate the control. The comparison will be done using the full model described by (3.2, 4.3, B.1).

B.3.2 Numerical results

The three strategies described above have been implemented and tested in simulation. Tables B.5 and B.6 summarize the obtained results for five driving cycles: NEDC, FUDS, FHDS, FTP and WLTC$_m$ in terms of fuel consumption (Table B.5) and the satisfaction of the final constraint (Table B.6). The discussions will be about the NEDC.

Table B.5: Fuel consumption [L/100 km]

	S_2^0	S^0	HS_2^0
NEDC	4.94	4.97 (+0.6%)	5.16 (+4.4%)
FUDS	4.54	4.55 (+0.2%)	4.79 (+5.5%)
FHDS	5.48	5.50 (+0.4%)	5.77 (+4.9%)
FTP	4.40	4.42 (+0.5%)	4.99 (+13.4%)
WLTC$_m$	5.21	5.22 (+0.2%)	5.39 (+3.5%)

Table B.6: Constraint violation of the SOC $[\xi(T) - \xi(0)] \times 100$

	S^0	HS_2^0	S_2^0
NEDC	0.02	-0.30	0.13
FUDS	-0.06	0.11	-0.05
FHDS	0.06	0.25	-0.10
FTP	-0.02	-0.31	0.08
WLTC$_m$	-0.03	0.07	0.09

The SOC and the temperature θ_e trajectories for the NEDC are shown in Figure B.7. The accumulated fuel consumption is shown in Figure B.8.

From Table B.5, the strategy (HS_2^0) is far from the strategies (S^0) and (S_2^0) which are very close in terms of fuel consumption as well as in the state trajectories (see Figure B.7).

[3]In the naming of the control strategies, the superscript indicates the value of α in the corresponding control strategies (without a superscript) described in Table 4.1.

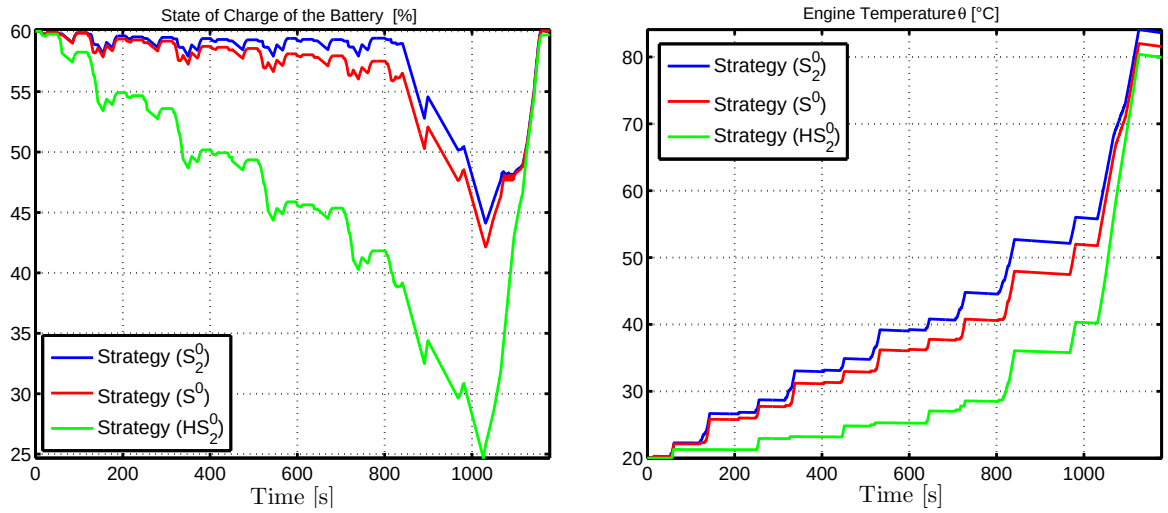

Figure B.7: SOC [%] (left) and engine temperature θ_e [°C] (right) trajectories for NEDC

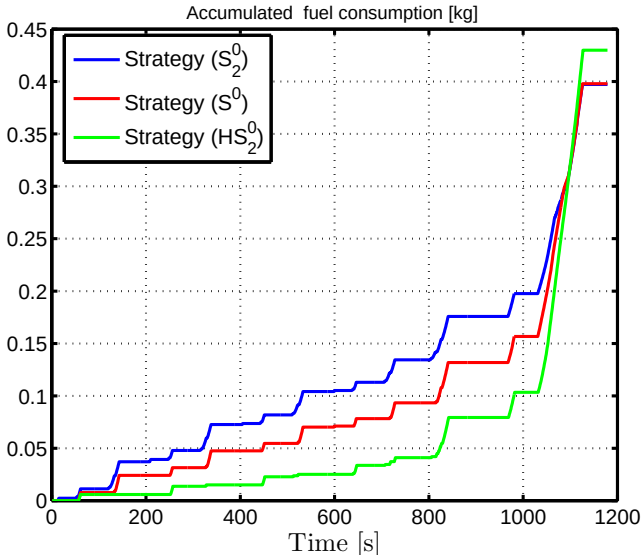

Figure B.8: Accumulated fuel consumption [kg] for NEDC

The strategy (HS_2^0) uses the electric mode in a first part of the cycle as the engine use is more costly in this part than the electric machine, and the battery is discharged to provide the power at the wheels requested by the driver (see Figure B.7). Due to the presence of the final constraint on the SOC, the control strategy will promote the use of the engine (thermal mode) in order to bring the final SOC to its target value. Because of the large SOC excursions, this pattern of behavior requires a large battery, or a high energy available in the battery at the beginning of the driving cycle in contrast to the strategies (S^0) and (S_2^0) (see Figure B.7 for the SOC trajectories) . Note that the disparity between the strategies (S^0), (S_2^0) and (HS_2^0) in terms of fuel consumption and state trajectories would be less noticeable if the value of b_0 in the correction factor $e(\theta_e)$ were lower than the value given in Table 4.2.

The optimal temperature trajectory in Figure B.7 shows that the optimal control of solution (S_2^0) improves the engine efficiency by warming up the engine in the first phase of the driving cycle. The price to be paid for achieving this improvement is an increased

fuel consumption, as seen in Figure B.8. In the second phase, the engine is warmer and more efficient and the fuel consumption obtained by using the control u_2^{*0} is less than when using the control u^{*0}. However, the control cannot fully exploit the temperature-dependent efficiency improvement of the engine because it must meet the final constraint $\xi(T) = \xi(0)$. Globally, this might explain why thermal management does not significantly improve fuel consumption in comparison with simply using control u^{*0} obtained by solving the problem (P_0), which ignores the influence of the engine temperature on the fuel consumption. More explanation of these results from a mathematical viewpoint are given in Section 5.7.

The behavior of the SOC and the engine temperature for the three control strategies is given in Figures B.9 for FUDS driving cycles.

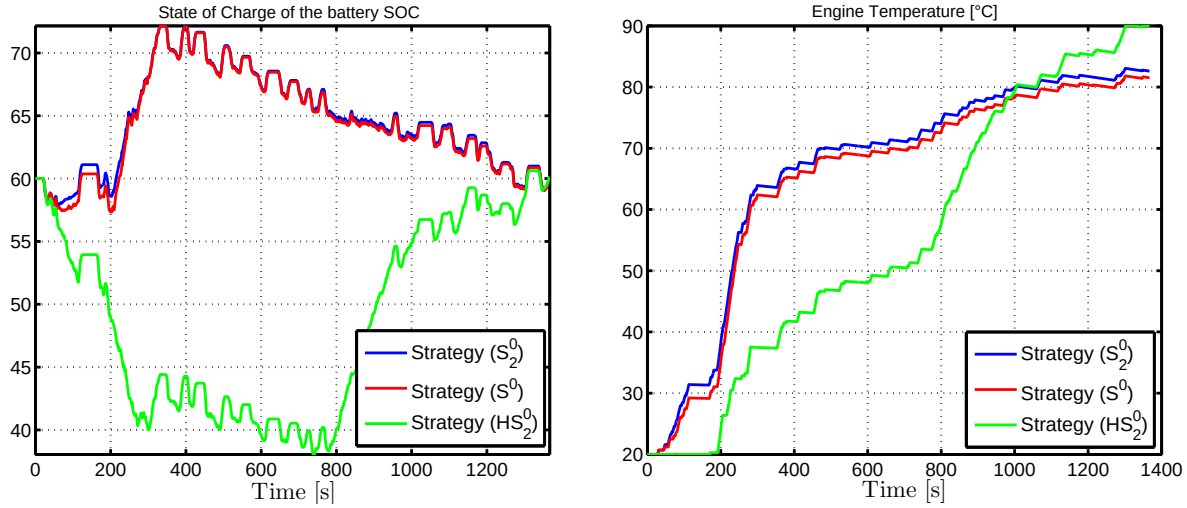

Figure B.9: FUDS trajectories: SOC [%] (left);engine temperature θ_e [°C] (right)

These figures show that the state trajectories resulting from the control strategy (S^0) are closer to the optimal trajectories obtained using the strategy (S_2^0), whereas those for strategy (HS_2^0) are far from optimal.

B.3.3 Conclusion

The numerical results presented above suggest that it may be sufficient to use the strategy (S^0) to compute the optimal torque split minimizing the fuel consumption, even although engine temperature impacts fuel consumption. Results presented in [87, 88] have suggested a similar conclusion, where it was shown that the optimal control calculated for a warm engine start is close to the optimal control calculated for a cold-engine start.

B.4 ECMS extension to include engine temperature

The optimization problem considered has the objective of minimizing the fuel consumption under the dynamics of the SOC and the engine temperature θ_e.

B.4.1 Formulation of θ_e-ECMS

The TPBVP (P_1) described in Section B.1.1 requires the driving cycle to be known in advance, as the initial values of the adjoint variables λ and μ depend on the future driving conditions. The objective is to find a relationship between μ and θ_e which is assumed to be measured or at least estimated. This relation will be used for a real-time controller and it has to be robust for driving condition variations.

The proposed method is based on post-analysis of the PMP results. In what follows, the equivalence factors $(s,\ p)$ defined in (3.15, B.8) are used instead of $(\lambda,\ \mu)$. Figure B.10 shows the relationship between p and θ_e on the optimal trajectories calculated using the PMP for the five driving cycles. This relationship seems monotonic and has the same tendency as that between $p(0)$ and $\theta_e(0)$ described in Section B.2.2 (see Figure B.3).

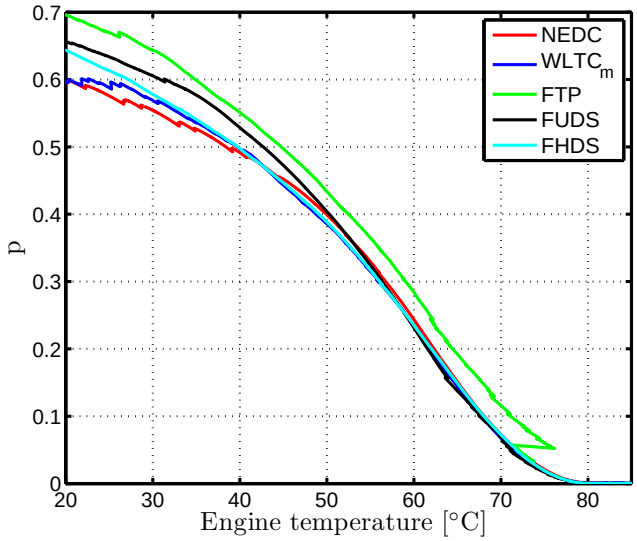

Figure B.10: Equivalence factor p as a function of θ_e

The proposed formula is of the form

$$p(\theta_e) = \begin{cases} a_1\theta_e^2 + a_2\theta_e + a_3, \text{ if } \theta_e \leq 80°\text{C}, \\ 0, \text{ if } \theta_e > 80°\text{C}, \end{cases} \tag{B.10}$$

where the parameters a_i have to be identified. The threshold 80°C from which the adjoint state vanishes is justified by the fact that fuel consumption is independent of θ_e beyond this value. The p trajectory as a function of θ_e ($\theta_e \in [0, 80]\ °C$) for the FHDS driving cycle is shown in Figure B.11. The proposed relation seems to fit the optimal trajectory of p well.

Table B.7: Identified parameters from the FHDS cycle

a_1	a_2	a_3
-0.0001509	0.00212265	0.654553

For the equivalence factor s (equivalent to the adjoint state λ), the classical ECMS formula with a proportional gain is used:

$$s(t) = s_0 - K_p \cdot (\xi(t) - \xi(0)), \tag{B.11}$$

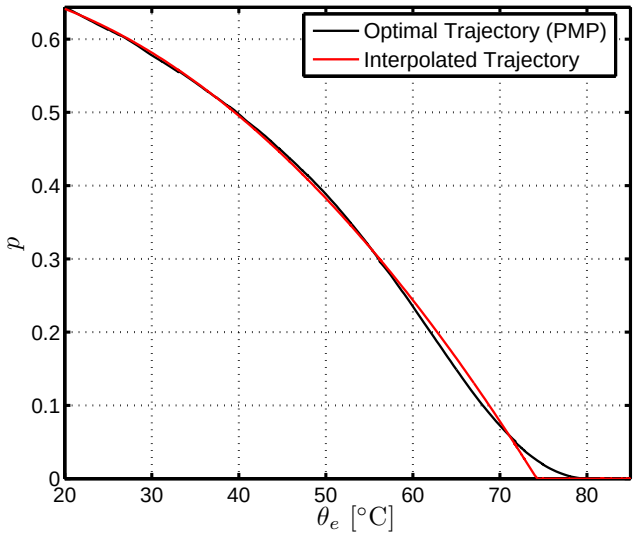

Figure B.11: Equivalence factor p as a function of θ_e for FHDS diving cycle

where the parameters s_0 and K_p are fixed[4]. The optimal control u_2^0 minimizes the Hamiltonian $\tilde{H}_2^0$ in the set defined by (3.4),

$$u_2^0 \in \arg\min_{u \in U^{ad}} \tilde{H}_2^0(u, t, \theta_e, s(\xi), p(\theta_e)),$$

where $\tilde{H}_2^0$ is defined in (B.9) and the equivalence factors $(s,\ p)$ are given by (B.10, B.11) respectively. The obtained control strategy is denoted θ_e-ECMS.

B.4.2 Robustness of θ_e-ECMS

As a real-time strategy has to be robust for all the driving condition changes, the proposed rule to update p as a function of θ_e is tested for other four driving cycles. The obtained fuel consumption was compared to its optimal value calculated using the PMP. For the equivalence factor p, the same identified parameters were used for all the driving cycles. For the adjoint state associated to the SOC, the same procedure described in Section 6.1.3 is used:

- Calibrate $(s_0,\ K_p)$ for each driving cycle such that the obtained performance in terms of fuel consumption are close to the optimal strategy;
- use each combination of the (calibrated) parameters to simulate other cycles;
- compare the obtained fuel consumption to its optimal value.

The results in terms of fuel consumption and satisfaction of the final SOC constraint (expressed by the error $\xi(T) - \xi(0)$) for the strategy θ_e-ECMS are summarized in Tables B.8 and B.9. From these two tables, the optimality of the solution is strongly related

[4]The relation between k_p (used in the formula of λ) and K_p (used in the formula of s) is given by

$$K_p = \frac{H_{lhv}}{Q_0 \cdot U_{ocv}} k_p.$$

to the choice of the parameters s_0 and K_p. In most of the cases, a trade-off between fuel consumption minimization and final SOC constraint satisfaction has to be made.

Table B.8: Fuel consumption in [L/100 km] using different combinations of ECMS parameters

Tuning	**PMP**	**NEDC**	**FHDS**	**FTP**	**WLTC$_m$**
NEDC	4.946	4.949 (+0.1%)	5.29 (+6.9%)	5.43 (+9.8%)	5.25 (+6.1%)
FHDS	5.48	5.30 (-3.3%)	5.495 (+0.3%)	5.57 (+1.6%)	5.44 (-0.7%)
FTP	4.40	4.15 (-5.7%)	4.32 (-1.8%)	4.40 (+0%)	4.30 (-2.3%)
WLTC$_m$	5.215	5.15 (-1.2%)	5.29 (+1.4%)	5.31 (+1.8%)	5.22 (+0.1%)

For the reasons explained in Section 6.1.3, comparisons must be made between the equivalent fuel consumption Q^e_{eq} [5] when using the different parameter combinations rather than the fuel consumption and the final constraint satisfaction separately:

$$Q^e_{eq} = \int_0^T c(u,t)e(\theta_e)dt + \lambda \cdot (\xi(T) - \xi(0)). \tag{B.12}$$

Table B.9: Percentage difference between final value and target value of ξ ($\xi(T) - \xi(0)$) [%]

Tuning	**PMP**	**NEDC**	**FHDS**	**FTP**	**WLTC$_m$**
NEDC	-0.13	0.1	5.76	8	4.8
FHDS	-0.16	-4.7	0.08	2.01	-1.4
FTP	0.08	-7.51	-2.52	-0.21	-2.92
WLTC$_m$	0.09	-2.21	2.63	3.25	-0.05

The values of the equivalent fuel consumption obtained in this way, listed in Table B.10, show that all the combinations have allowed a quasi-optimal equivalent fuel consumption to be reached.

Table B.10: Equivalent fuel consumption (Q^e_{eq}) in [L/100 km] using different ECMS parameters

Tuning	**PMP**	**NEDC**	**FHDS**	**FTP**	**WLTC$_m$**
NEDC	4.938	4.943 (+0.1%)	4.96 (+0.4%)	4.96 (+0.4%)	4.96 (+0.4%)
FHDS	5.488	5.49 (+0.05%)	5.492 (+0.07%)	5.495 (+0.1%)	5.49 (+0.05%)
FTP	4.40	4.415 (+0.35%)	4.41 (+0.2%)	4.41 (+0.2%)	4.41 (+0.2%)
WLTC$_m$	5.213	5.22 (+0.1%)	5.22 (+0.1%)	5.23 (+0.3%)	5.22 (+0.1%)

The state trajectories ξ, θ_e, the equivalence factor p and the accumulated fuel consumption for the FTP driving cycle are given in Figures B.12, B.13, B.14 and B.15 respectively. The parameters s_0 and K_p used for these trajectories have been calibrated to satisfy the final constraint on the SOC. The state and the equivalence factor p trajectories for the optimal strategy (S^0_2) and the θ_e-ECMS are close. From the SOC and θ_e trajectories, the θ_e-ECMS strategy uses the engine less than the optimal strategy in the first part of the driving cycle. This behavior leads to a lower fuel consumption (see Figure B.15) and

[5] The superscript ^{e} in Q^e_{eq} refers to the use of the control strategy θ_e-ECMS for cold-engine start.

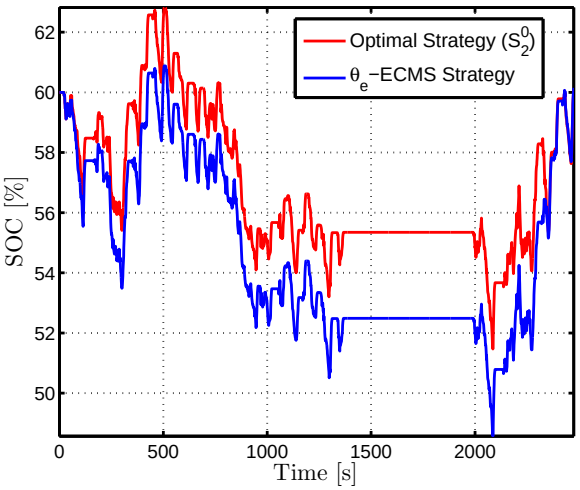

Figure B.12: SOC [%] trajectories for FTP

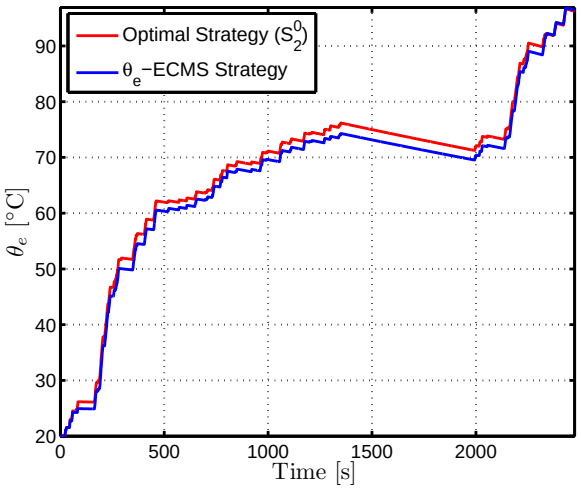

Figure B.13: Temperature θ_e [°C] trajectories

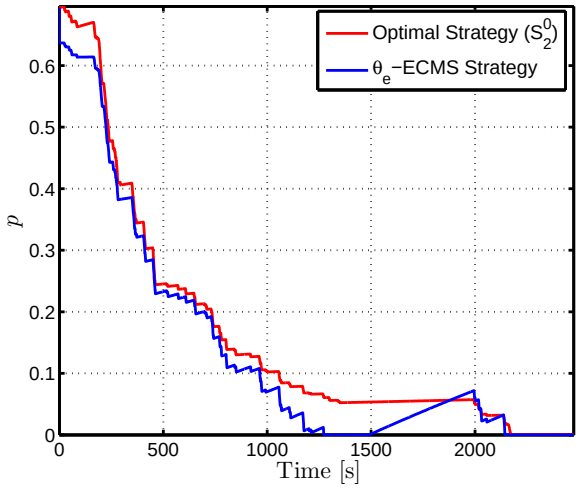

Figure B.14: Equivalence factor p

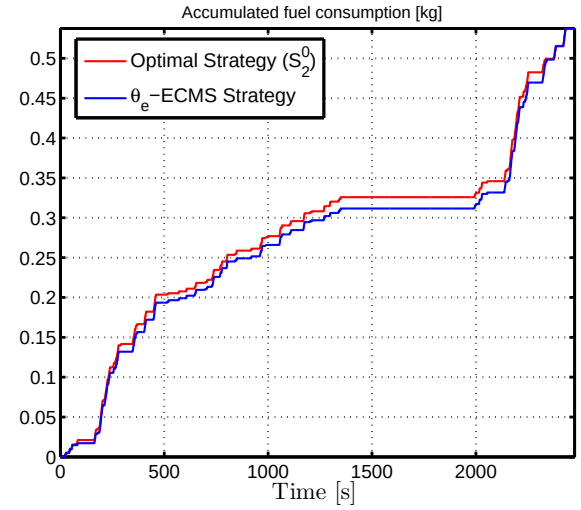

Figure B.15: Accumulated fuel consumption [kg]

a lower SOC. At the end of the driving cycle and because of the final constraint on the SOC, the difference between the two solutions is small. The overall fuel consumption over the driving cycle is almost the same.

B.4.3 Conclusion

The proposed correlation to update p using measurements of θ_e in (B.10) has been shown to be robust against the driving conditions change, as the induced sub-optimality in the equivalent fuel consumption is less than 0.5% and the parameters a_i have been calibrated (identified) for one driving cycle. The main problem is to find an efficient way of estimating λ, as its calibration greatly impacts the final SOC constraint.

Appendix C

Additional numerical results for Chapter 4

C.1 Details about the solutions of OCP_2 and OCP_1

To solve the (OCP_2), two scenarios are possible: engine warm-start and engine cold-start conditions. In the case of warm start conditions, fuel consumption and CO emissions become independent of θ_e and thus its associated equivalence factor p is zero for $t \in [0,\ T]$. The number of the state variables is reduced to two (ξ and θ_c). For cold-start conditions, the number of the state variables is three (ξ, θ_e and θ_c).

For convenience, an equivalence factor that is positive and dimensionless, denoted by q, is used instead of using ρ (which is negative). The relationship between the two parameters is given by

$$q(t) = -\frac{H_{lhv}}{C_c}\rho(t).$$

C.1.1 Engine warm-start case

The engine is assumed to be warm at the beginning of the driving cycle (a temperature around 80° C). The number of the state variables is two (ξ and θ_c). The associated OCP is described in Section 4.4.

The obtained results (fuel consumption and CO emissions) are summarized in Figure C.1 for five driving cycles: NEDC, FUDS, FHDS, FTP and $WLTC_m$ for different values of α. For each cycle, each point is obtained as follows: first, the value of α is fixed and then the (OCP_1) is solved. The corresponding fuel consumption and CO emissions are presented.

The results have been normalized with respect to the fuel consumption and CO emission obtained for $\alpha = 0$ (fuel consumption minimization strategy): the fuel consumption increases when α increases while CO emissions decreases. These numerical results show that it is possible to reduce pollutant emissions by 15% to 28% with an extra-fuel consumption of 2.1% compared to a strategy that minimizes only the fuel consumption. The maximum emission reduction depends on the driving cycle and the weight factor α.

The variations of the initial values of s and q with respect to α for the five considered cycles are given in plots of Figure C.2. The relationship between ($s(0)$, $q(0)$) and α for the considered cycles appears linear and their values for those driving cycles are not scattered.

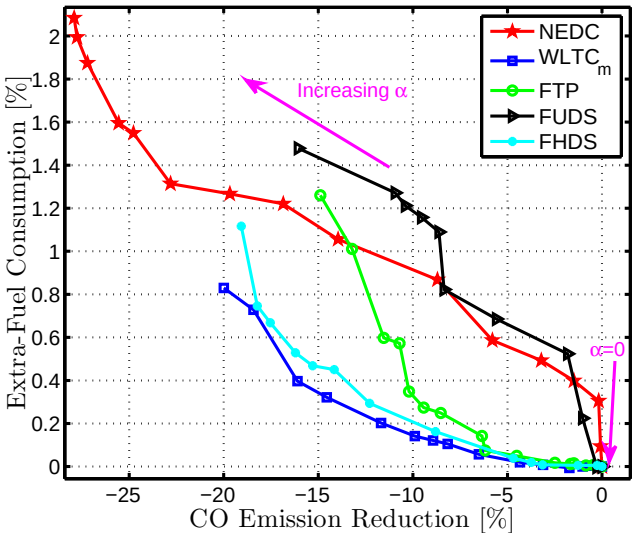

Figure C.1: Extra-fuel consumption [%] as a function of CO emissions reduction [%] for engine warm-start conditions

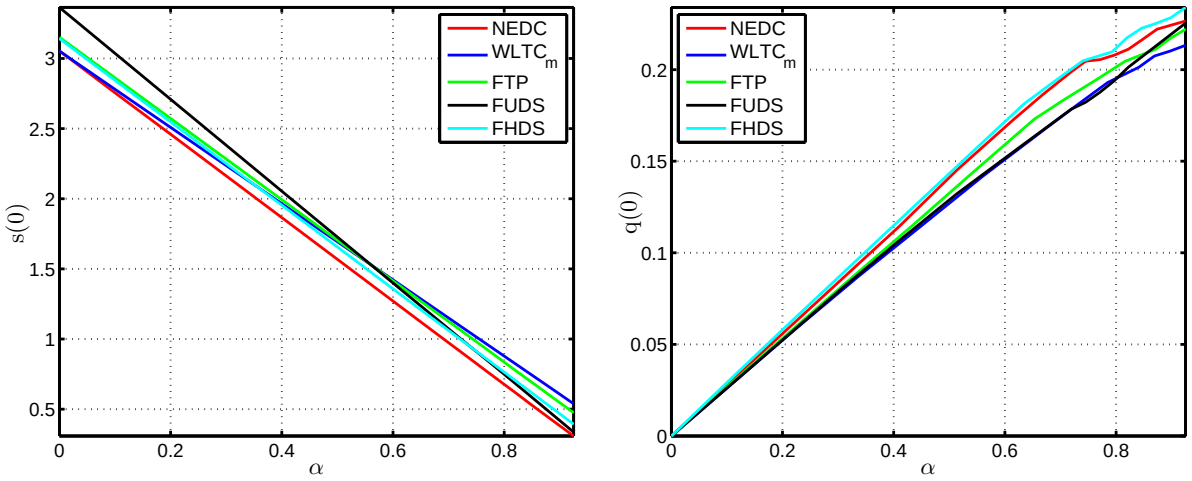

Figure C.2: $s(0)$ (left) and $q(0)$ (right) as functions of α for engine warm-start conditions

C.1.2 Engine cold-start conditions

In this case, the engine is cold at the beginning of the driving cycle. The (OCP_2) has been solved for the five driving cycles considered. Fuel consumption and CO emissions variation for different values of α are summarized in Figure C.3.

The results have been normalized with respect to the fuel consumption and CO emission obtained for $\alpha = 0$ as done for warm-start conditions above. These results show that it is possible to reduce pollutant emissions of 20% to 35% with an extra-fuel consumption of 2.5%, compared to a strategy minimizing only the fuel consumption. The emissions reduction obtained depends on the driving cycle and α.

To illustrate the influence of the parameter α on the thermal behavior of the ATS, the catalyst temperature trajectories for different values of α for NEDC and FHDS cycles are given in Figures C.4. This shows that, when α is increased, the control strategy improves

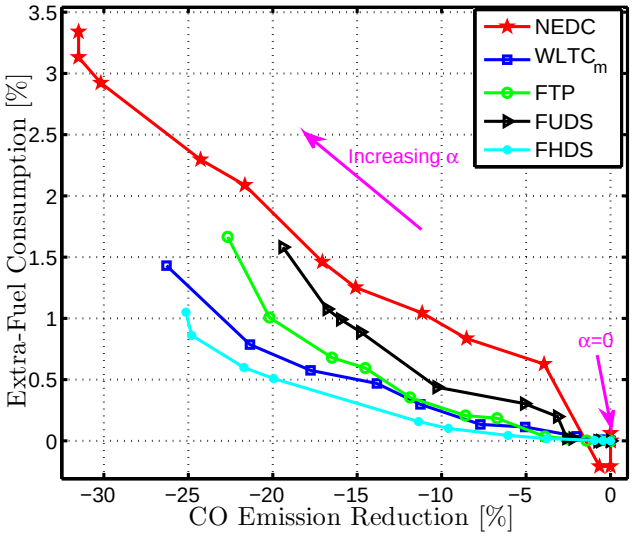

Figure C.3: Extra-fuel consumption [%] as a function of CO emissions reduction [%] for engine cold-start conditions

the catalyst efficiency by warming it up promptly, which decreases the pollutant emissions out of the catalyst. The price to pay for achieving this improvement is an increase in fuel consumption.

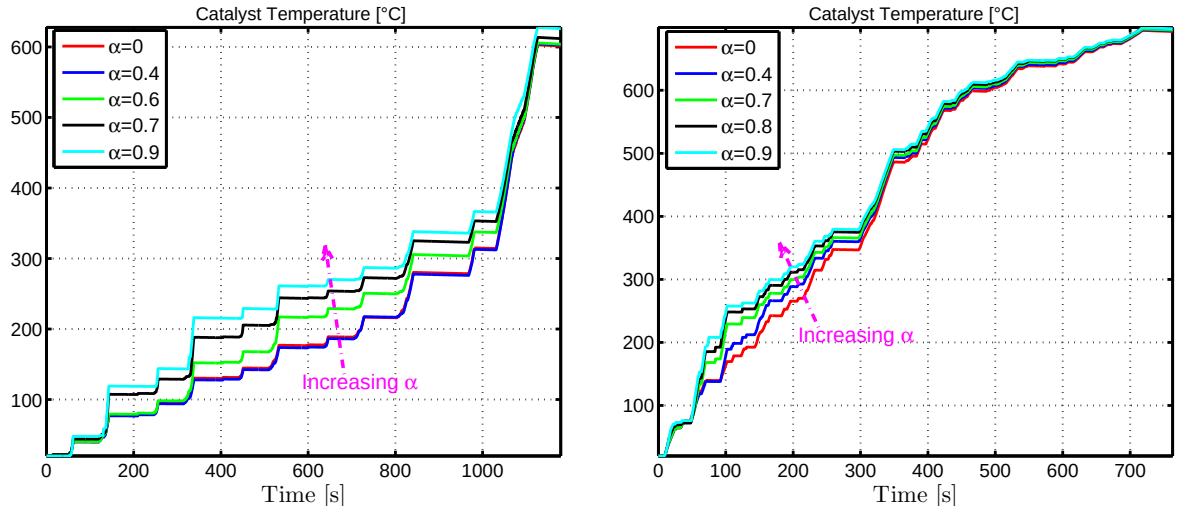

Figure C.4: Catalyst temperature trajectories θ_c [°C] for NEDC (left) and FHDS (right) for engine cold-start conditions

The equivalence factors p and q associated to θ_e and θ_c are given in Figures C.5 for different values of α for NEDC. Similar behaviors of p and q have been obtained for the other considered driving cycles. The equivalence factor p decreases with time for different values of α and it becomes null when the engine becomes warm ($\theta_e \geq \theta_w$). This behavior is due to the fact that fuel consumption and CO emissions are independent of θ_e after θ_w. For the equivalence factor q, three phases are distinguished.

1. For $\theta_c \leq 200$ °C: the cost function is independent of θ_c, and q increases with time until it reaches the catalyst activation temperature of 200 °C.

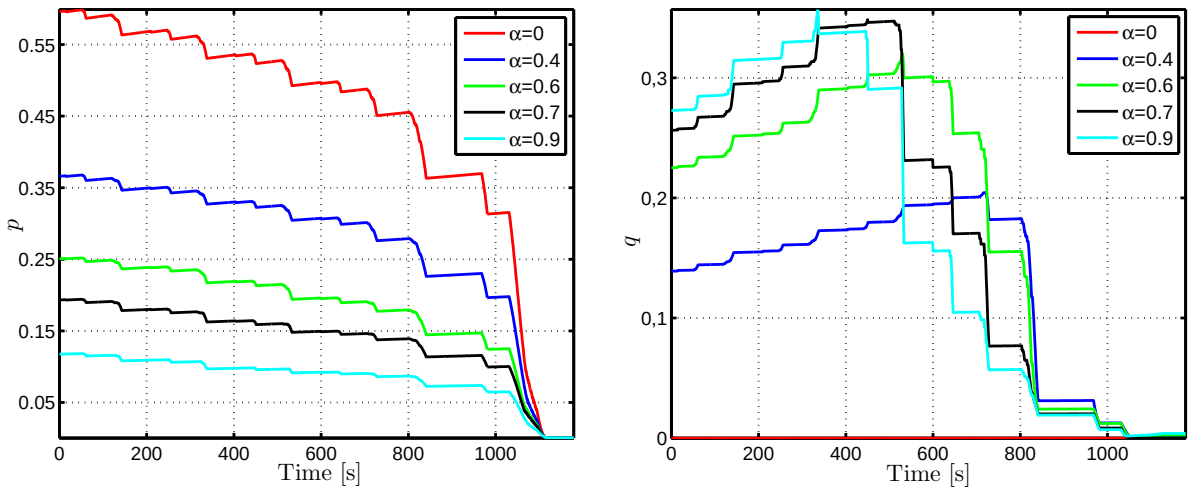

Figure C.5: Equivalence factors p (left) and q (right) for NEDC in the case of engine cold-start conditions

2. For 200 °C$\leq \theta_c \leq$ 400 °C: the cost function depends on θ_c and an additional term related to the derivative of η_{CO} with respect to θ_c modified the dynamics of q. It becomes a decreasing function of time.

3. For $\theta_c \geq$ 400 °C: the cost function becomes independent of θ_c and as the final temperature $\theta_c(T)$ is free, q is equal to zero.

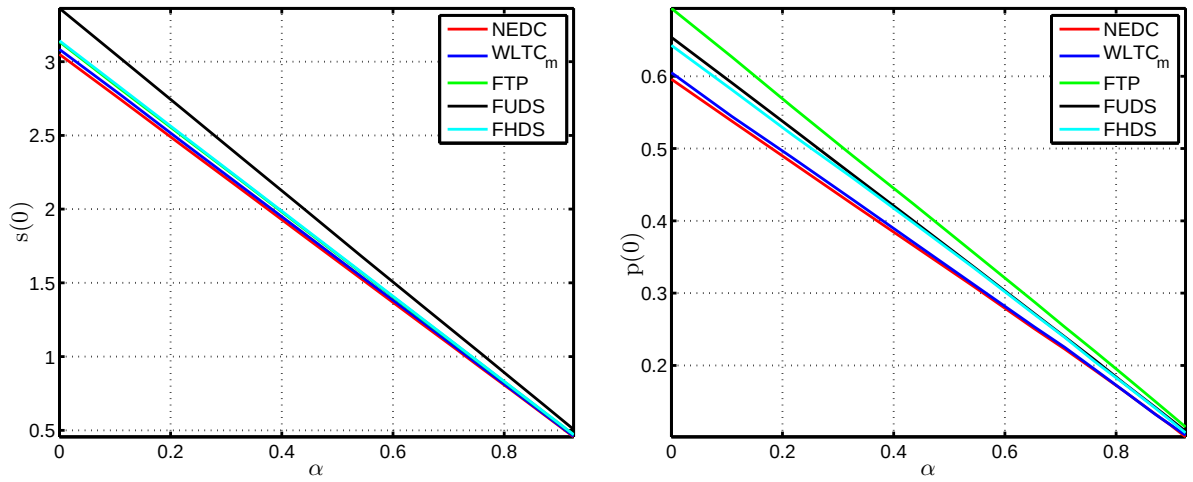

Figure C.6: $s(0)$ (left) and $p(0)$ (right) as functions of α for engine cold-start conditions

The variations of the initial values of s, p and q with respect to α for the five considered cycles are given in Figures C.6 and C.7 respectively. From these figures, the behavior of the equivalence factors p and q is interpreted as follows:

- the initial value of p decreases when α increases and the resulting control strategy becomes less sensitive to the engine temperature;
- the initial value of q increases when α increases and the resulting control strategy becomes more sensitive to the catalyst temperature.

The relation between $(s(0),\ p(0))$ and α for the considered cycles seems linear while the relation between $q(0)$ and α is not linear for $\alpha \geq 0.7$. For the linear part, $s(0)$ and $p(0)$) can be approximated by

$$s(0) = s_{01}\alpha + s_{02},\ p(0) = p_{01}\alpha + p_{02},$$

where the constants $(s_{01},\ s_{02},\ p_{01},\ p_{02})$ have to be identified.

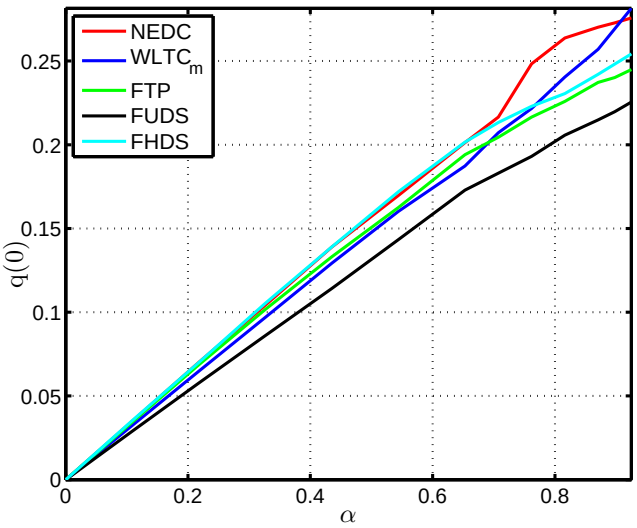

Figure C.7: $q(0)$ as a function of α for engine cold-start conditions

C.2 Additional numerical results for reduced order EMS including engine and catalyst temperatures

To illustrate the conclusions given in Section 4.6 regarding the simplified control strategy for pollutant emissions reduction, four driving cycles are considered: FUDS, FHDS, FTP and WLTC$_m$. In contrast to the NEDC case, where the objective is to meet the European norm for CO emissions, the objective here is to show that the simplified control strategies proposed to reduce CO (close to the optimal solution) with an acceptable extra-fuel consumption remain valid.

The control strategies $(S_2,\ S_1,\ S)$ are tested for the considered driving cycles. The results in terms of fuel consumption and CO emissions are shown in Figures C.8 and C.9. The two-state strategy (S_1) is very close to the optimal strategy (S_2). Strategy (S) reduces the CO emissions close to their optimal value, with an extra-fuel consumption of the order of 1% comparing to the strategy (S_2). These results confirm that the single-state strategy (S) is a good candidate to generate a control trajectory allowing the CO emissions to be reduced with a quasi-optimal fuel consumption.

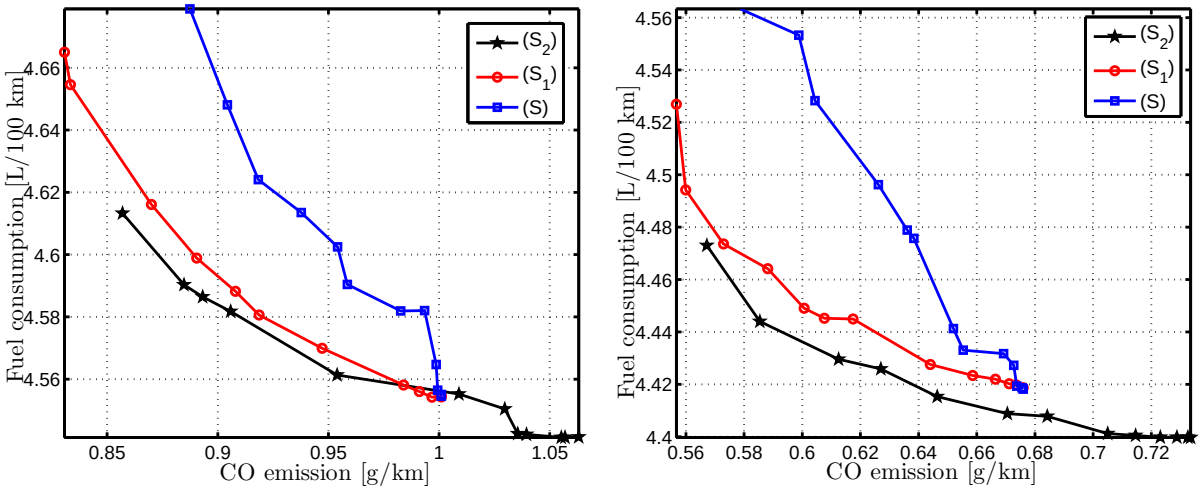

Figure C.8: Fuel consumption [L/100 km] as a function of CO emissions [g/km] for FUDS (left) and FTP(right)

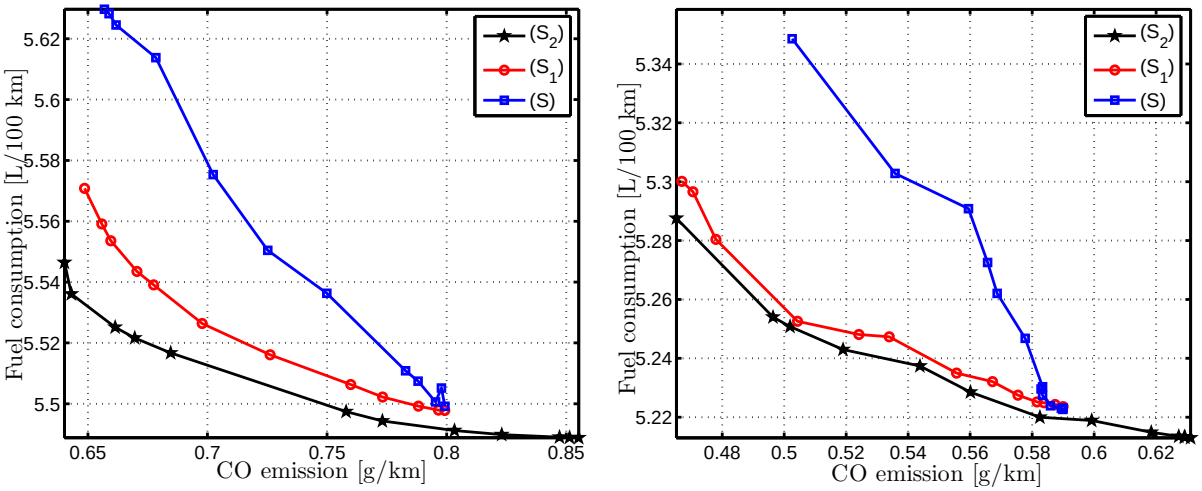

Figure C.9: Fuel consumption [L/100 km] as a function of CO emissions [g/km] for FHDS (left) and WLTC$_m$ (right)

Appendix D

Proofs of some results of Chapter 5

D.1 Proof of Proposition 2

For any control u, $J_\varepsilon^r(u)$ can be written

$$\begin{aligned} J_\varepsilon^r(u) = & \int_0^T \left[H_\varepsilon^r(\sigma_0^r, p_0^r) - p_0^{rT}\dot{x}_0^r\right] dt + \varepsilon \int_0^T \left[N^0(t)\cdot\delta u^r + N^1(t)\cdot\delta x^r\right] dt \\ & + \int_0^T\int_0^1\int_0^1 \lambda\partial_{\sigma\sigma}H_\varepsilon^r(\sigma_0^r + \lambda\mu\delta\sigma^r, p_0^r)(\delta\sigma^r)^2 d\lambda d\mu dt, \end{aligned}$$

where

$$N^0(t) \triangleq \partial_u H_1(\sigma_0^r, p_0^r),\ \ N^1(t) \triangleq \partial_x H_1(\sigma_0^r, p_0^r).$$

Proof For any smooth function F of a variable y, its Taylor expansion can be written as

$$F(y) = F(y_0) + \partial_y F(y_0)(y - y_0) + \int_0^1\int_0^1 \lambda\partial_{yy}F(y_0 + \lambda\mu(y - y_0))(y - y_0)^2 d\lambda d\mu. \quad \text{(D.1)}$$

Using this expansion, $J_\varepsilon^r(u)$ can be written

$$\begin{aligned} J_\varepsilon^r(u) = & \int_0^T [L_\varepsilon(\sigma_0^r) + \partial_x L_\varepsilon(\sigma_0^r)\delta x^r + \partial_u L_\varepsilon(\sigma_0^r)\delta u^r]dt + r\int_0^T [P(u_0^r) + \partial_u P(u_0^r)\delta u^r]dt \\ & + \int_0^T\int_0^1\int_0^1 \lambda\partial_{\sigma\sigma}L_\varepsilon(\sigma_0^r + \lambda\mu\delta\sigma^r)(\delta\sigma^r)^2 d\lambda d\mu dt \\ & + r\int_0^T\int_0^1\int_0^1 \lambda\partial_{uu}P(u_0^r + \lambda\mu\delta u^r)(\delta u^r)^2 d\lambda d\mu dt. \end{aligned} \quad \text{(D.2)}$$

Denote by S

$$S \triangleq \partial_x L_\varepsilon(\sigma_0^r)\delta x^r + \partial_u L_\varepsilon(\sigma_0^r)\delta u^r + r\partial_u P(u_0^r)\delta u^r.$$

Using equation (5.5) given the adjoint state and the stationarity condition (5.6), S may be written

$$\begin{aligned} S &= [-\dot{p}_0^{rT} - p_0^{rT}\partial_x f_\varepsilon(\sigma_0^r) + \varepsilon\partial_x L_1(\sigma_0^r) + \varepsilon p_0^{rT}\partial_x f_1(\sigma_0^r)]\delta x^r \\ &+ [-p_0^{rT}\partial_u f_\varepsilon(\sigma_0^r) + \varepsilon\partial_u L_1(\sigma_0^r) + \varepsilon p_0^{rT}\partial_u f_1(\sigma_0^r)]\delta u^r. \end{aligned}$$

By integrating S, we get

$$\begin{aligned}\int_0^T S(t)dt = & - \int_0^T \dot{p}_0^{rT}\delta x^r dt - \int_0^T p_0^{rT}\partial_\sigma^r f_\varepsilon(\sigma_0^r)\delta\sigma^r dt \\ & + \varepsilon\int_0^T \left[(\partial_x L_1(\sigma_0^r) + p_0^{rT}\partial_x f_1(\sigma_0^r))\delta x^r + (\partial_u L_1(\sigma_0^r) + p_0^{rT}\partial_u f_1(\sigma_0^r))\delta u^r\right] dt,\end{aligned}$$

which, using integration by parts, can be rewritten as

$$\begin{aligned}\int_0^T S(t)dt = & - \left[\underbrace{p_0^{rT}(T)}_{=0}\delta x^r(T) - p_0^r\underbrace{\delta x^r(0)}_{=0} - \int_0^T p_0^{rT}(\dot{x}^r - \dot{x}_0^r)dt\right] - \int_0^T p_0^{rT}\partial_\sigma f_\varepsilon(\sigma_0^r)\delta\sigma^r dt \\ & + \varepsilon\int_0^T \left[(\partial_x L_1(\sigma_0^r) + p_0^{rT}\partial_x f_1(\sigma_0^r))\delta x^r + (\partial_u L_1(\sigma_0^r) + p_0^{rT}\partial_u f_1(\sigma_0^r))\delta u^r\right] dt,\end{aligned}$$

that is,

$$\int_0^T S(t)dt = \varepsilon\int_0^T \partial_\sigma H_1(\sigma_0^r, p_0^r)\delta\sigma^r dt + \int_0^T p_0^{rT}(\dot{x}^r - \dot{x}_0^r - \partial_\sigma f_\varepsilon(\sigma_0^r)\delta\sigma^r)dt.$$

From expansion (D.1), the term $\dot{x}^r - \dot{x}_0^r - \partial_\sigma f_\varepsilon(\sigma_0^r)\delta\sigma^r$ can be written

$$\dot{x}^r - \dot{x}_0^r - \partial_\sigma f_\varepsilon(\sigma_0^r)\delta\sigma^r = \varepsilon f_1(\sigma_0^r) + \int_0^1\int_0^1 \lambda\partial_{\sigma\sigma} f_\varepsilon(\sigma_0^r + \lambda\mu\delta\sigma^r)(\delta\sigma^r)^2 d\lambda d\mu. \quad \text{(D.3)}$$

Using equation (D.3), the expression of S becomes of the form

$$\begin{aligned}\int_0^T S(t)dt = & \ \varepsilon\int_0^T \partial_\sigma H_1(\sigma_0^r, p_0^r)\delta\sigma^r dt + \varepsilon\int_0^T p_0^{rT} f_1(\sigma_0^r(t))dt \\ & + \int_0^T\int_0^1\int_0^1 \lambda p_0^{rT}\cdot\partial_{\sigma\sigma} f_\varepsilon(\sigma_0^r + \lambda\mu\delta\sigma^r)(\delta\sigma^r)^2 d\lambda d\mu dt. \quad \text{(D.4)}\end{aligned}$$

Recalling that, from the definition of H_ε^r, the term $L_\varepsilon(\sigma_0^r) + rP(u_0^r)$ can be written

$$\begin{aligned}L_\varepsilon(\sigma_0^r) + rP(u_0^r) = & \ H_\varepsilon^r(\sigma_0^r, p_0^r) - p_0^{rT}\frac{dx_0^r}{dt} - \varepsilon p_0^{rT} f_1(\sigma_0^r), \\ = & \ H_\varepsilon^r(\sigma_0^r, p_0^r) - p_0^{rT} f_\varepsilon(\sigma_0^r). \quad \text{(D.5)}\end{aligned}$$

Replacing (D.3, D.4, D.5) in the expansion (D.2), the expression of $J_\varepsilon^r(u)$ becomes

$$\begin{aligned}J_\varepsilon^r(u) = & \int_0^T [H_\varepsilon^r(\sigma_0^r, p_0^r) - p_0^{rT}\frac{dx_0^r}{dt} - \varepsilon p_0^{rT} f_1(\sigma_0^r)]dt + \varepsilon\int_0^T \partial_\sigma H_1(\sigma_0^r, p_0^r)\delta\sigma^r dt \\ & + \varepsilon\int_0^T p_0^{rT} f_1(\sigma_0^r(t))dt + \int_0^T\int_0^1\int_0^1 \lambda p_0^{rT}\cdot\partial_{\sigma\sigma} f_\varepsilon(\sigma_0^r + \lambda\mu\delta\sigma^r)(\delta\sigma^r)^2 d\lambda d\mu dt \\ & + \int_0^T\int_0^1\int_0^1 \lambda\left[\partial_{\sigma\sigma} H_\varepsilon^r(\sigma_0^r + \lambda\mu\delta\sigma^r, p_0^r) - p_0^{rT}\partial_{\sigma\sigma} f_\varepsilon(\sigma_0^r + \lambda\mu\delta\sigma^r)\right](\delta\sigma^r)^2 d\lambda d\mu dt.\end{aligned}$$

The terms $\varepsilon p_0^{rT} f_1(\sigma_0^r)$ and $p_0^{rT}\partial_{\sigma\sigma} f_\varepsilon(.)$ appear in the expression of $J_\varepsilon^r(u)$ with positive and negative sign and they cancel. The formula (5.9) is proven where

$$N^0(t) \triangleq \partial_u H_1(\sigma_0^r, p_0^r), \ \ N^1(t) \triangleq \partial_x H_1(\sigma_0^r, p_0^r).$$

In the formula (5.9), the penalty disappears from the first order variation. This concludes the proof. ■

D.2 Proof of Proposition 3

Proof The solutions $\xi_0^r(t)$ and $x_0^r(t)$, for the initial condition $x(0)$, are given by

$$\begin{aligned} \xi_0^r(t) &= x(0) + \int_0^t f_\varepsilon(\xi_0^r(\tau), u_0^r(\tau))d\tau, \\ x_0^r(t) &= x(0) + \int_0^t f_0(x_0^r(\tau), u_0^r(\tau))d\tau. \end{aligned}$$

Subtracting the two equations and taking norms yield

$$\|\xi_0^r(t) - x_0^r(t)\| \leq \int_0^t \|f_\varepsilon(\xi_0^r(\tau), u_0^r(\tau)) - f_\varepsilon(x_0^r(\tau), u_0^r(\tau))\|\, d\tau + \varepsilon \int_0^t \|f_1(x_0^r(\tau), u_0^r(\tau))\|\, d\tau.$$

Note that $\xi_0^r(t)$ and $x_0^r(t)$ have the same control input u_0^r and the same initial conditions. As f_ε is Γ-Lipschitz and f_1 is bounded, the upper bound on $\xi_0^r - x_0^r$ implies

$$\|\xi_0^r(t) - x_0^r(t)\| \leq \Gamma \int_0^t \|\xi_0^r(\tau) - x_0^r(\tau)\| + \varepsilon F_1 t,$$

for some positive constant F_1 defined by

$$F_1 = \sup_{t\in[0,T]} \|f_1(\sigma_0^r(t))\|.$$

Using Gronwall's lemma [38], the upper bound on $\|\xi_0^r(t) - x_0^r(t)\|$ is given by

$$\|\xi_0^r(t) - x_0^r(t)\| \leq \varepsilon F_1 \int_0^t e^{\Gamma(t-\tau)} d\tau.$$

This concludes the proof. ■

D.3 Proof of Proposition 4

There exist positive constants $(\alpha_3,\ \alpha_4)$ and time functions $(\alpha_1,\ \alpha_2)$ such that

$$\begin{aligned} \|\delta x_\varepsilon^r(t)\|^2 &\leq \alpha_1(t) \int_0^T \int_0^1 \int_0^1 \lambda \|z(\lambda,\mu,t)\|^2 \, d\lambda d\mu dt + \alpha_2(t) F_1^2 \varepsilon^2, \\ \int_0^T \|\delta u_\varepsilon^r(t)\|^2 \, dt &\leq \alpha_3 \int_0^T \int_0^1 \int_0^1 \lambda \|z(\lambda,\mu,t)\|^2 \, d\lambda d\mu dt + \alpha_4 F_1^2 \varepsilon^2, \end{aligned}$$

where the variable z is defined in (5.17) and

$$\delta x^r = x - x_0^r,\ \delta u^r = u - u_0^r,\ \delta\sigma^r = \sigma - \sigma_0^r.$$

Proof The dynamic of the error on the state trajectories δx_ε^r can be written as

$$\frac{d(\delta x_\varepsilon^r)}{dt} = f_\varepsilon(\sigma_\varepsilon^r) - f_\varepsilon(\sigma_0^r) + \varepsilon f_1(\sigma_0^r).$$

As $\delta x_\varepsilon^r(0) = 0$, we can write

$$\delta x_\varepsilon^r(t) = \int_0^t \left[f_\varepsilon(\sigma_\varepsilon^r) - f_\varepsilon(\sigma_0^r)\right] dt + \varepsilon \int_0^t f_1(\sigma_0^r) dt.$$

Since f_ε is Γ-Lipschitz, this formula yields

$$\|\delta x_\varepsilon^r(t)\| \leq \Gamma \int_0^t \left[\|\delta x_\varepsilon^r(t)\| + \|\delta u_\varepsilon^r(t)\|\right] dt + \varepsilon \left\| \int_0^t f_1(\sigma_0^r) dt \right\|. \tag{D.6}$$

From the expression of z in equation (5.17), δu_ε^r can be written as

$$\begin{aligned} \delta u_\varepsilon^r &= z - [\partial_{uu} H_0^r(.)]^{-1} \partial_{ux} H_0^r(.) \delta x_\varepsilon^r, \\ &= z - W(.) \delta x_\varepsilon^r. \end{aligned}$$

As the term $[\partial_{uu} H_0^r(.)]^{-1}$ is bounded by $\dfrac{1}{\beta}$ (from Assumption 3) and $\partial_{ux} H_0^r(.)$ is bounded independently of $rP(.)$ [1], the bound on $W(.)$, denoted by γ_1, is independent of $rP(.)$

$$\gamma_1 = \sup_{t \in [0,T]} \|W(.)\|,$$

and we can write the upper bound on δu_ε^r as follows

$$\|\delta u_\varepsilon^r\| \leq \|z(\lambda, \mu, t)\| + \gamma_1 \|\delta x_\varepsilon^r\|. \tag{D.7}$$

By replacing this inequality in equation (D.6) and using the fact that f_1 is bounded, the upper bound on δx_ε^r implies

$$\|\delta x_\varepsilon^r(t)\| \leq \Gamma(1+\gamma_1) \int_0^t \|\delta x_\varepsilon^r(t)\| dt + \Gamma \int_0^t \|z(\lambda, \mu, s)\| ds + \varepsilon F_1 t.$$

Using Gronwall's lemma [38], the upper bound on $\delta x_\varepsilon^r(t)$ is of the form

$$\|\delta x_\varepsilon^r(t)\| \leq \Gamma \int_0^t e^{\Gamma(1+\gamma_1)(t-s)} \|z(\lambda, \mu, s)\| ds + \varepsilon F_1 \int_0^t e^{\Gamma(1+\gamma_1)(t-s)} ds. \tag{D.8}$$

From Cauchy-Schwarz inequality for any two real integrable functions $f(t)$ and $g(t)$ in $[0,\ s]$,

$$\int_0^s f(t)g(t)dt \leq \sqrt{\int_0^s f^2(t)dt} \sqrt{\int_0^s g^2(t)dt},$$

applied to the first term of (D.8), the upper bound on $\delta x_\varepsilon^r(t)$ can be written

$$\|\delta x_\varepsilon^r(t)\| \leq \Gamma \sqrt{\int_0^t e^{2\Gamma(1+\gamma_1)(t-s)} ds} \sqrt{\int_0^t \|z(\lambda, \mu, s)\|^2 ds} + \frac{\varepsilon F_1}{\Gamma(1+\gamma_1)} (e^{\Gamma(1+\gamma_1)t} - 1)$$

As $(x+y)^2 \leq 2x^2 + 2y^2$ and $\int_0^t \|z(\lambda, \mu, \tau)\|^2 d\tau \leq \int_0^T \|z(\lambda, \mu, \tau)\|^2 d\tau$, we can write the following inequality

$$\|\delta x_\varepsilon^r(t)\|^2 \leq \left[\Gamma \frac{e^{2\Gamma(1+\gamma_1)t} - 1}{1+\gamma_1}\right] \int_0^T \|z(\lambda, \mu, s)\|^2 ds + 2\varepsilon^2 F_1^2 \left[\frac{e^{\Gamma(1+\gamma_1)t} - 1}{\Gamma(1+\gamma_1)}\right]^2.$$

[1] $\partial_{ux} H_0^r(\sigma) = \partial_{ux} L_0(\sigma) + p^T \partial_{ux} f_0(\sigma)$ as $r \partial_{ux} P(u) = 0$.

To express the upper bound on $\delta x_\varepsilon^r(t)$ as a function of R, the two sides of this inequality are multiplied by λ and integrated twice with respect to λ and μ

$$\int_0^1\int_0^1 \lambda \left\|\delta x_\varepsilon^r(t)\right\|^2 d\lambda d\mu \leq \left[\Gamma\frac{e^{2\Gamma(1+\gamma_1)t}-1}{1+\gamma_1}\right] R + \varepsilon^2 F_1^2 \left[\frac{e^{\Gamma(1+\gamma_1)t}-1}{\Gamma(1+\gamma_1)}\right]^2,$$

where R is given by

$$R = \int_0^T\int_0^1\int_0^1 \lambda \left\|z(\lambda,\mu,t)\right\|^2 d\lambda d\mu dt.$$

As δx_ε^r is independent of λ and μ, the upper bound on $\delta x_\varepsilon^r(t)$ can be written

$$\left\|\delta x_\varepsilon^r(t)\right\|^2 \leq 2\left[\Gamma\frac{e^{2\Gamma(1+\gamma_1)t}-1}{1+\gamma_1}\right] R + 2\varepsilon^2 F_1^2 \left[\frac{e^{\Gamma(1+\gamma_1)t}-1}{\Gamma(1+\gamma_1)}\right]^2.$$

By defining

$$\alpha_1(t) \triangleq 2\Gamma\frac{e^{2\Gamma(1+\gamma_1)t}-1}{1+\gamma_1},\ \alpha_2(t) \triangleq 2\left[\frac{e^{\Gamma(1+\gamma_1)t}-1}{\Gamma(1+\gamma_1)}\right]^2, \tag{D.9}$$

the upper bound on $\delta x_\varepsilon^r(t)$ in (5.15) is proven.

Using $(x+y)^2 \leq 2x^2+2y^2$, we can write from the relation (D.7) that

$$\left\|\delta u_\varepsilon^r\right\|^2 \leq 2\left\|z(\lambda,\mu,t)\right\|^2 + 2\gamma_1^2\left\|\delta x_\varepsilon^r\right\|^2,$$

yielding

$$\int_0^T \left\|\delta u_\varepsilon^r\right\|^2 dt \leq 2\int_0^T \left\|z(\lambda,\mu,t)\right\|^2 dt + 2\gamma_1^2\int_0^T \left\|\delta x_\varepsilon^r\right\|^2 dt. \tag{D.10}$$

Multiplying by λ and integrating twice with respect to λ and μ, equation (D.10) implies

$$\frac{1}{2}\int_0^T \left\|\delta u_\varepsilon^r\right\|^2 dt \leq 2R + \gamma_1^2\int_0^T \left\|\delta x_\varepsilon^r\right\|^2 dt.$$

By replacing the upper bound on $\left\|\delta x_\varepsilon^r\right\|^2$ given by (5.15) in this equation, the relationship (5.16) is proven where

$$d_1 \triangleq \int_0^T \alpha_1(s)ds,\ d_2 \triangleq \int_0^T \alpha_2(s)ds,\ \alpha_3 \triangleq 2\left[2+\gamma_1^2 d_1\right],\ \alpha_4 \triangleq 2\gamma_1^2 d_2. \tag{D.11}$$

This concludes the proof. ■

D.4 Proof of Proposition 5

There exist positive constants c_0 and c_1 such that

$$\left|J_\varepsilon^r(u_0^r) - \int_0^T \left[H_\varepsilon^r(\sigma_0^r,p_0^r) - p_0^{rT}\dot{x}_0^r\right] dt\right| \leq (c_0F_1^2 + c_1)\varepsilon^2,$$

where

$$\begin{aligned} c_0 &= \frac{1}{2}(\sup_{t\in[0,T]} \partial_{xx}H_0^r(.) + m)\int_0^T q^2(t)dt + \frac{1}{2}\sup_{t\in[0,T]}\partial_{xx}H_1(.)\int_0^T q^2(t)dt, \\ c_1 &= \frac{1}{2m}\int_0^T k_1^2(t)dt, \end{aligned}$$

where the parameter m is positive constant, q is given in (5.14), F_1 is an upper bound on $f_1(.)$ and k_1 is an upper bound on $N^1(t)$. In particular, the upper bound given in (5.22) is independent of $rP(.)$.

Proof The proof is based on the second-order decomposition in Proposition 2. The upper bound given in (5.22) is independent of the penalty, as the input constraints are still always satisfied. This remark is not true in the presence of state constraints where the perturbation in the dynamics may lead to violation of the state constraints.

From Proposition 2, the penalized cost function J_ε^r for u_0^r can be written in the form

$$\begin{aligned} J_\varepsilon^r(u_0^r) \quad - \quad & \int_0^T \left[H_\varepsilon^r(\sigma_0^r, p_0^r) - p_0^{rT}\dot{x}_0^r\right] dt = \varepsilon \int_0^T N^1(t)\cdot(\xi_0^r - x_0^r)dt \\ + \quad & \int_0^T \int_0^1 \int_0^1 \lambda \partial_{xx} H_\varepsilon^r(x_0^r + \lambda\mu(\xi_0^r - x_0^r), u_0^r, p_0^r)(\xi_0^r - x_0^r)^2 d\lambda d\mu dt. \end{aligned} \tag{D.12}$$

Since the first derivatives of L_1 and f_1 are bounded by assumption, N^1 and N^0 are bounded as follows

$$\left|N^1(t)\right| \leq k_1(t), \quad \left|N^0(t)\right| \leq k_2(t).$$

Indeed, terms $N^1(t)$ and $N^0(t)$ depend only on the nominal trajectories and they can be bounded by functions of time. To find an upper bound on M_0, the following inequality, for any a and b is used:

$$2ab \leq \frac{1}{m}a^2 + mb^2,$$

where m is a positive constant. The upper bound on $N^1(t)\cdot(\xi_0^r - x_0^r)$ can be written as

$$\varepsilon \int_0^T N^1(t)\cdot(\xi_0^r - x_0^r)dt \leq \frac{\varepsilon^2}{2m}\int_0^T (N^1(t))^2 dt + \frac{m}{2}\int_0^T (\xi_0^r - x_0^r)^2 dt. \tag{D.13}$$

Since $\xi_0^r - x_0^r$ is bounded by $F_1 q(t)\varepsilon$ from equation (5.13), the relation (D.13) yields

$$\begin{aligned} \varepsilon \int_0^T N^1(t)\cdot(\xi_0^r - x_0^r)dt \quad &\leq \quad \frac{\varepsilon^2}{2m}\int_0^T k_1^2(t)dt + \frac{\varepsilon^2 m}{2}F_1^2\int_0^T q^2(t)dt, \\ &\leq \quad \frac{\varepsilon^2}{2}\left(\frac{1}{m}\int_0^T k_1^2(t)dt + mF_1^2\int_0^T q^2(t)dt\right). \end{aligned}$$

From the decomposition in equation (5.7), we have

$$\partial_{xx}H_\varepsilon^r(.) = \partial_{xx}H_0^r(.) + \varepsilon\partial_{xx}H_1(.).$$

The term $\varepsilon\partial_{xx}H_1(.)(\xi_0^r - x_0^r)^2$ in equation (D.12) leads to ε^3. As the second derivatives of L_0 and f_0 are assumed to be bounded and the term $\partial_{xx}H_0^r$ is independent of the penalty $P(.)$, we can write

$$\gamma_0 = \sup_{t\in[0,T]} \partial_{xx}H_0^r(.).$$

By using the relation (5.13), we derive that

$$\left|\int_0^T \int_0^1 \int_0^1 \lambda\partial_{xx}H_0^r(x_0^r + \lambda\mu(\xi_0^r - x_0^r), u_0^r, p_0^r)(\xi_0^r - x_0^r)^2 d\lambda d\mu dt\right| \leq \frac{\varepsilon^3}{2}\gamma_0 F_1^2\int_0^T q^2(t)dt. \tag{D.14}$$

As ε is in $[0,\ 1]$, $\varepsilon^3 \leq \varepsilon^2$, and we can write the following upper bound

$$|\int_0^T \int_0^1 \int_0^1 \lambda \partial_{xx} H_0^r(x_0^r + \lambda\mu(\xi_0^r - x_0^r), u_0^r, p_0^r)(\xi_0^r - x_0^r)^2 d\lambda d\mu dt| \leq \frac{\varepsilon^2}{2}\gamma_0 F_1^2 \int_0^T q^2(t)dt.$$

From equation (D.12), M_0 is thus bounded by

$$|J_\varepsilon^r(u_0^r) - \int_0^T \left[H_\varepsilon^r(\sigma_0^r, p_0^r) - p_0^{rT}\dot{x}_0^r\right] dt| \leq (c_0 F_1^2 + c_1)\varepsilon^2.$$

The constants c_0 and c_1 are independent of $rP(.)$

$$\begin{aligned} c_0 &= \frac{1}{2}(\sup_{t\in[0,T]} \partial_{xx} H_0^r(.) + m)\int_0^T q^2(t)dt + \frac{1}{2}\sup_{t\in[0,T]} \partial_{xx} H_1(.)\int_0^T q^2(t)dt, \\ c_1 &= \frac{1}{2m}\int_0^T k_1^2(t)dt. \end{aligned}$$

This concludes the proof. ■

D.5 Proof of Proposition 6

There exists a constant c_2 such that

$$\int_0^T \int_0^1 \int_0^1 \lambda \left\|z(\lambda,\mu,t)\right\|^2 d\lambda d\mu dt \leq c_2\varepsilon^2,$$

where c_2 is independent of the penalty $rP(.)$.

Proof Essentially, the proof is based on the decomposition suggested in Proposition 2 and the convexity conditions given in Assumption 3.

Since u_ε^r is the optimal control of the perturbed problem, it satisfies

$$J_\varepsilon^r(u_\varepsilon^r) \leq J_\varepsilon^r(u_0^r),$$

which is equivalent to

$$J_\varepsilon^r(u_\varepsilon^r) - \int_0^T \left[H_\varepsilon^r(w_0^r) - p_0^{rT}\dot{x}_0^r\right] dt \leq J_\varepsilon^r(u_0^r) - \int_0^T \left[H_\varepsilon^r(w_0^r) - p_0^{rT}\dot{x}_0^r\right] dt \leq (c_0 F_1^2 + c_1)\varepsilon^2. \tag{D.15}$$

By using Proposition 2, $J_\varepsilon^r(u_\varepsilon^r)$ can be rewritten in the form

$$\begin{aligned} J_\varepsilon^r(u_\varepsilon^r) - \int_0^T \left[H_\varepsilon^r(\sigma_0^r, p_0^r) - p_0^{rT}\dot{x}_0^r\right] dt &= \varepsilon\int_0^T \left[N^0(t)\delta u_\varepsilon^r + N^1(t)\delta x_\varepsilon^r\right] dt \\ &+ \int_0^T \int_0^1 \int_0^1 \lambda \partial_{\sigma\sigma} H_\varepsilon^r(., p_0^r)(\delta\sigma_\varepsilon^r)^2 d\lambda d\mu dt. \end{aligned}$$

By combining this expression with (D.15), we obtain

$$(c_0 F_1^2 + c_1)\varepsilon^2 \geq \varepsilon\int_0^T \left[N^0\delta u_\varepsilon^r + N^1\delta x_\varepsilon^r\right] dt + \int_0^T \int_0^1 \int_0^1 \lambda \partial_{\sigma\sigma} H_\varepsilon^r(\sigma_0^r + \lambda\mu\delta\sigma_\varepsilon^r, p_0^r)(\delta\sigma_\varepsilon^r)^2 d\lambda d\mu dt. \tag{D.16}$$

From the expression of H_ε^r in (5.7),

$$\partial_{\sigma\sigma} H_\varepsilon^r(.) = \partial_{\sigma\sigma} H_0^r(.) + \varepsilon \partial_{\sigma\sigma} H_1(.).$$

To find a bound on $\partial_{\sigma\sigma} H_0^r(\sigma_0^r + \lambda\mu\delta\sigma_\varepsilon^r, p_0^r)(\delta\sigma_\varepsilon^r)^2$, every factor of δu_ε^r in the second-order variation of the cost $J_\varepsilon^r(u_\varepsilon^r)$ is substituted by terms in z and δx_ε^r. This allows us to handle a diagonal quadratic form in terms of z and δx_ε^r. The expression of $\partial_{\sigma\sigma} H_0^r(\sigma_0^r + \lambda\mu\delta\sigma_\varepsilon^r, p_0^r)(\delta\sigma_\varepsilon^r)^2$ is

$$\partial_{\sigma\sigma} H_0^r(\sigma_0^r + \lambda\mu\delta\sigma_\varepsilon^r, p_0^r)(\delta\sigma_\varepsilon^r)^2 = \delta x_\varepsilon^{rT} \partial_{xx} H_0^r(\sigma_0^r + \lambda\mu\delta\sigma_\varepsilon^r, p_0^r)\delta x_\varepsilon^r$$

$$+\delta u_\varepsilon^{rT} \partial_{uu} H_0^r(\sigma_0^r + \lambda\mu\delta\sigma_\varepsilon^r, p_0^r)\delta u_\varepsilon^r + 2\delta u_\varepsilon^{rT} \partial_{ux} H_0^r(\sigma_0^r + \lambda\mu\delta\sigma_\varepsilon^r, p_0^r)\delta x_\varepsilon^r,$$

which can be written using the variable z as

$$\partial_{\sigma\sigma} H_0^r(.)(\delta\sigma_\varepsilon^r)^2 = z^T \partial_{uu} H_0^r(.) z + \delta x_\varepsilon^{rT} \left[\partial_{xx} H_0^r - \partial_{xu} H_0^r [\partial_{uu} H_0^r]^{-1} \partial_{ux} H_0^r\right](.)\delta x_\varepsilon^r.$$

The term $\partial_{\sigma\sigma} H_0^r(\sigma_0^r + \lambda\mu\delta\sigma_\varepsilon^r, p_0^r)(\delta\sigma_\varepsilon^r)^2$ is written as the sum of terms whose signs are known from the second order optimality conditions given in Assumption 3, and a lower bound on $\partial_{\sigma\sigma} H_0^r(.)(\delta\sigma_\varepsilon^r)^2$ is of the form

$$\partial_{\sigma\sigma} H_0^r(.)(\delta\sigma_\varepsilon^r)^2 \geq \beta \left\| z(\lambda, \mu, t) \right\|^2.$$

Thus, equation (D.16) implies

$$\begin{aligned}(c_0 F_1^2 + c_1)\varepsilon^2 \quad &\geq \quad \varepsilon \int_0^T \left[N^0 \delta u_\varepsilon^r + N^1 \delta x_\varepsilon^r\right] dt + \beta R \\ &\quad +\varepsilon \int_0^T \int_0^1 \int_0^1 \lambda \partial_{\sigma\sigma} H_1(\sigma_0^r + \lambda\mu\delta\sigma_\varepsilon^r, p_0^r)(\delta\sigma_\varepsilon^r)^2 d\lambda d\mu dt. \quad \text{(D.17)}\end{aligned}$$

By using the formula (holding for any a, b and $m > 0$)

$$2ab \geq -\frac{1}{m} a^2 - m b^2,$$

the term $\varepsilon \int_0^T \left[N^0 \delta u_\varepsilon^r(t) + N^1 \delta x_\varepsilon^r(t)\right] dt$ is lower bounded as follows

$$\begin{aligned}\varepsilon \int_0^T \left[N^0 \delta u_\varepsilon^r + N^1 \delta x_\varepsilon^r\right] dt \quad &\geq \quad -\int_0^T \left[\frac{\varepsilon^2}{2m} \left\{(N^0)^2 + (N^1)^2\right\} + \frac{m}{2} \left\{\|\delta x_\varepsilon^r\|^2 + \|\delta u_\varepsilon^r\|^2\right\}\right] dt, \\ &\geq \quad -\frac{\varepsilon^2}{2m} \int_0^T (k_2^2(t) + k_1^2(t)) dt - F_1^2 \frac{\varepsilon^2 m}{2} \left(\alpha_4 + \int_0^T \alpha_2(s) ds\right) \\ &\quad -\frac{m}{2} \left[\alpha_3 + \int_0^T \alpha_1(s) ds\right] R.\end{aligned}$$

The inequality (D.17) becomes

$$\begin{aligned}(c_0 F_1^2 + c_1)\varepsilon^2 \quad &\geq \quad -\varepsilon^2 \left[\frac{1}{2m} \int_0^T (k_2^2(t) + k_1^2(t)) dt + \frac{m}{2} F_1^2 (\alpha_4 + d_2)\right] - \frac{m}{2} [\alpha_3 + d_1] R \\ &\quad +\beta R + \varepsilon \int_0^T \int_0^1 \int_0^1 \lambda \partial_{\sigma\sigma} H_1(\sigma_0^r + \lambda\mu\delta\sigma_\varepsilon^r, p_0^r)(\delta\sigma_\varepsilon^r)^2 d\lambda d\mu dt. \quad \text{(D.18)}\end{aligned}$$

The term $\varepsilon \int_0^T \int_0^1 \int_0^1 \lambda \partial_{\sigma\sigma} H_1(\sigma_0^r + \lambda\mu\delta\sigma_\varepsilon^r, p_0^r)(\delta\sigma_\varepsilon^r)^2 d\lambda d\mu dt$ gives rise to a term in ε^3 (where we bound ε^3 by ε^2 as $\varepsilon \leq 1$). By combining the fact that $\partial_{\sigma\sigma} H_1$ is bounded with the two inequalities (5.15, 5.16) and $\varepsilon^3 \leq \varepsilon^2$, we obtain for the last term of (D.18)

$$\varepsilon \int_0^T \int_0^1 \int_0^1 \lambda \partial_{\sigma\sigma} H_1(.)(\delta\sigma_\varepsilon^r)^2 d\lambda d\mu dt \leq \frac{1}{2} \sup_{t\in[0,T]} \|\partial_{\sigma\sigma} H_1(.)\| \left[F_1^2(\alpha_4 + d_2)\varepsilon^2 + \varepsilon(\alpha_3 + d_1)R\right].$$

Inequality (D.18) can be written

$$\begin{aligned} & \left[\beta - \frac{m}{2}(\alpha_3 + d_1) + \frac{\varepsilon}{2} \sup \|\partial_{\sigma\sigma} H_1\| (\alpha_3 + d_1)\right] R \\ \leq & \left[c_0 + \frac{m}{2}(\alpha_4 + d_2) - \frac{1}{2} \sup_{s\in[0,T]} \|\partial_{\sigma\sigma} H_1\| (\alpha_4 + d_2)\right] F_1^2 \varepsilon^2 \\ & + \left[c_1 + \frac{1}{2m} \int_0^T (k_2^2(t) + k_1^2(t)) dt\right] \varepsilon^2, \end{aligned} \tag{D.19}$$

where $(d_1,\ d_2,\ \alpha_3,\ \alpha_4)$ are defined in (D.11) .The parameter m can be chosen such that

$$\beta - \frac{m}{2}\left(\alpha_3 + \int_0^T \alpha_1(s) ds\right) = \frac{\beta}{2} > 0,$$

which is satisfied if

$$m = \sqrt{\frac{\beta}{\alpha_3 + \int_0^T \alpha_1(s) ds}} > 0.$$

The parameter m is well defined because the term $\left[\alpha_3 + \int_0^T \alpha_1(s) ds\right]$ in the denominator is strictly positive. Consider the following notations

$$\begin{aligned} s_1 &= \frac{1}{2} \sup_{s\in[0,T]} \|\partial_{\sigma\sigma} H_1(.)\| (\alpha_3 + d_1), \\ s_{2a} &= c_0 + \frac{m}{2}(\alpha_4 + d_2) - \frac{1}{2} \sup_{s\in[0,T]} \|\partial_{\sigma\sigma} H_1(.)\| (\alpha_4 + d_2), \\ s_{2b} &= c_1 + \frac{1}{2m} \int_0^T (k_2^2(t) + k_1^2(t)) dt. \end{aligned}$$

Inequality (D.19) can be written as

$$(\frac{\beta}{2} + s_1\varepsilon)R \leq (s_{2a}F_1^2 + s_{2b})\varepsilon^2,$$

where the constant s_1 is strictly positive. Finally, the upper bound on R is given by

$$R \leq 2\frac{s_{2a}F_1^2 + s_{2b}}{\beta + 2s_1\varepsilon}\varepsilon^2 \leq \frac{2}{\beta}\left(s_{2a}F_1^2 + s_{2b}\right)\varepsilon^2 \triangleq c_2\varepsilon^2. \tag{D.20}$$

From the two inequalities (5.15, 5.16), the upper bounds on δx_ε^r and δu_ε^r are of the form

$$\begin{aligned} \|\delta x_\varepsilon^r(t)\|^2 &\leq \left[\alpha_1(t)c_2 + \alpha_2(t)F_1^2\right]\varepsilon^2 = c_x^2(t)\varepsilon^2, \\ \int_0^T \|\delta u_\varepsilon^r(t)\|^2 dt &\leq \left[\alpha_3 c_2 + \alpha_4 F_1^2\right]\varepsilon^2 = c_u^2\varepsilon^2, \end{aligned}$$

and the inequalities (5.18) and (5.19) are proven. This concludes the proof. ■

D.6 Proof of Proposition 8

We consider a state constraints of the form $g(x(t)) \leq 0$ for all $t \in [0, T]$. Let a positive constant s and a given $\bar{\gamma}(r)$ such that

$$\bar{\gamma}(r) \geq \int_{t_1}^{t_2} \gamma_g(g(x(\tau)))d\tau.$$

Proposition 8 gives the upper bound on $c(r)$ of the form

$$c(r) \leq -\sqrt[n_g]{\frac{s}{\bar{\gamma}(r)\Gamma(1+s)^{(n_g+1)}}},$$

where the constant $\bar{\gamma}(r)$, depending on r, increases when the penalty weight r goes to zero and Γ is the Lipschitz constant of the function f_0.

Proof

We consider a control $u \in U^{ad}$, where U^{ad} is defined in (5.3), x^u is the solution of the following differential equation

$$\frac{dx^u}{dt} = f_0(x^u, u), \;\; x(0) = X_0,$$

and $M = \max\limits_{t\in[0,\ T]}(g(x^u(t))) \leq 0$. As the solution x^u is continuous with respect to time, we have

$$\exists t_1 : t_1 = \inf_{t\in[0,\ T]}(g(x^u(t)) = M).$$

Let N a constant in $]X_0, M[$. As the function $x^u(t)$ is continuous with respect to time, there exists t_2 such that

$$t_2 = \sup_{t\in[0,\ t_1]}(g(x^u(t)) = N).$$

The function f_0 is Lipschitz (by assumption) and from the continuous differentiability of the function g, there exists a positive constant Γ such that, for all $u \in U^{ad}$, we have

$$\exists \Gamma > 0 : \quad g(x^u(t_1)) - g(x^u(t_2)) \leq \Gamma(t_1 - t_2),$$

yielding

$$t_1 - t_2 \geq \frac{M - N}{\Gamma}. \tag{D.21}$$

The penalty $\gamma_g(.)$ is positive and increasing, we can write

$$\forall \tau \in [t_2,\ t_1] : \quad \gamma_g(g(x^u(\tau))) \geq \gamma_g(N).$$

By integrating this inequality, we get

$$\int_{t_2}^{t_1} \gamma_g(g(x^u(\tau)))d\tau \geq \gamma_g(N)(t_1 - t_2).$$

By using the relation (D.21), this inequality becomes

$$\int_{t_2}^{t_1} \gamma_g(g(x^u(\tau)))d\tau \geq \gamma_g(N)\frac{M - N}{\Gamma}. \tag{D.22}$$

As N is free in $]X_0, M[$, we choose $N = (1+s)M$ where s is positive constant. Equation (D.22) becomes

$$\bar{\gamma}(r) \geq \int_{t_2}^{t_1} \gamma_g(g(x^u(\tau)))d\tau \geq -\gamma_g((1+s)M)\frac{sM}{\Gamma}.$$

By using the expression of $\gamma_g(.)$ in (3.11), we can write

$$\bar{\gamma}(r) \cdot (-M)^{ng} \geq \frac{s}{\Gamma(1+s)^{ng+1}},$$

and the formula (5.28) is proven for a given $\bar{\gamma}(r)$ where $M = c(r)$. This concludes the proof.

■

Appendix E

K estimation details

For the toy NL problem and the eco-driving problem described in Section 5.6, the following notations are used:

- The nominal state and costate trajectories for $\varepsilon = 0$: $(y_1,\ y_2,\ \lambda_1,\ \lambda_2)$.
- The solutions of the dynamics equations for the nominal control $u = u_0$ and for $\varepsilon > 0$: $(x_1,\ x_2)$.
- The optimal state and costate trajectories for $\varepsilon > 0$: $(x_1^*,\ x_2^*,\ \lambda_1^*,\ \lambda_2^*)$.
- The error in the state and the control trajectories $\delta X_1 = x_1 - y_1,\ \delta X_2 = x_2 - y_2,\ \delta x_1 = x_1^* - y_1,\ \delta x_2 = x_2^* - y_2,\ \delta u = u_\varepsilon - u_0$.

The estimation of K is done in four steps:

1. estimate an upper bound on δX_i,
2. estimate an upper bound on δx_i,
3. estimate an upper bound on R,
4. estimate an upper bound on ΔJ.

E.1 NL problem

Consider the following OCP

$$\begin{cases} \min\limits_u \left[J_\varepsilon(u) = \displaystyle\int_0^T \left(0.3u^2 + 5(1+\frac{\varepsilon}{4})x_1^2\right) dt, \right], \\ \dot{x}_1 = (1+\frac{\varepsilon}{5})x_1 - x_1 x_2,\ x_1(0) = 4, \\ \dot{x}_2 = -x_2 + \frac{1}{10}(1+\frac{\varepsilon}{4})u,\ x_2(0) = 5, \\ u_{min}(t) \leq u(t) \leq u_{max}(t). \end{cases}$$

Upper bounds on δX_i

The dynamics of δX_1 and δX_2 are approximated by the tangent linear system

$$\begin{aligned}\frac{d(\delta X_1)}{dt} &\approx (1+\frac{\varepsilon}{5}-y_2(t))\delta X_1 - y_1(t)\delta X_2 + \frac{\varepsilon}{5}y_1,\ \delta X_1(0)=0,\\ \frac{d(\delta X_2)}{dt} &\approx -\delta X_2 + \frac{\varepsilon}{40}u_0,\ \delta X_2(0)=0.\end{aligned}$$

The transition matrix Φ of this linear system for $\varepsilon = 1$ calculated numerically is of the form

$$\Phi(t,\tau) = \begin{bmatrix} \Phi_{11}(t,\tau) & \Phi_{12}(t,\tau) \\ \Phi_{21}(t,\tau) & \Phi_{22}(t,\tau) \end{bmatrix}. \tag{E.1}$$

By using the expression of Φ, δX_1 and δX_2 can be written as

$$\|\delta X_1(t)\| \le \varepsilon \left| \int_0^t (\Phi_{11}(t,\tau)\frac{y_1(\tau)}{5} + \Phi_{12}(t,\tau)\frac{u_0(\tau)}{40})d\tau \right|,$$

$$\|\delta X_2(t)\| \le \varepsilon \left| \int_0^t (\Phi_{21}(t,\tau)\frac{y_1(\tau)}{5} + \Phi_{22}(t,\tau)\frac{u_0(\tau)}{40})d\tau \right|,$$

where y_1 and y_2 are the nominal state trajectories (calculated using the nominal control). The upper bounds on $\delta X_1(t)$ and $\delta X_2(t)$ are of the form

$$\|\delta X_1(t)\| \le \varepsilon\alpha_{21}(t),\ \|\delta X_2(t)\| \le \varepsilon\alpha_{22}(t).$$

The quantities $\alpha_{21}(t)$ and $\alpha_{22}(t)$ depend only on the nominal trajectories and they are evaluated numerically.

Upper bounds on δx_i

The dynamics of δx_1 and δx_2 can be approximated by

$$\begin{aligned}\frac{d(\delta x_1)}{dt} &\approx (1+\frac{\varepsilon}{5}-y_2(t))\delta x_1 - y_1(t)\delta x_2 + \frac{\varepsilon}{5}y_1,\ \delta x_1(0)=0,\\ \frac{d(\delta x_2)}{dt} &\approx -\delta x_2 + \frac{1}{10}(1+\frac{\varepsilon}{4})\delta u + \frac{\varepsilon}{40}u_0,\ \delta x_2(0)=0.\end{aligned}$$

From the transition matrix $\Phi(t,\tau)$ given in equation (E.1), the solution of this system is of the form

$$\begin{aligned}\delta x_1(t) &\approx \int_0^t \frac{1}{10}(1+\frac{\varepsilon}{4})\Phi_{12}(t,\tau)\delta u(\tau)d\tau + \varepsilon\int_0^t (\Phi_{11}(t,\tau)\frac{y_1(\tau)}{5} + \Phi_{12}(t,\tau)\frac{u_0(\tau)}{40})d\tau,\\ \delta x_2(t) &\approx \int_0^t \frac{1}{10}(1+\frac{\varepsilon}{4})\Phi_{22}(t,\tau)\delta u(\tau)d\tau + \varepsilon\int_0^t (\Phi_{21}(t,\tau)\frac{y_1(\tau)}{5} + \Phi_{22}(t,\tau)\frac{u_0(\tau)}{40})d\tau.\end{aligned}$$

By using Cauchy-Schwarz inequality and from the expressions of $\delta x_1(t)$ and $\delta x_2(t)$, upper bounds on $\delta x_1(t)$ and $\delta x_1(t)$ are of the form

$$|\delta x_1(t)| \le \sqrt{\int_0^t k_1^2(t,\tau)d\tau}\sqrt{\int_0^t \delta u^2(\tau)d\tau} + \varepsilon\alpha_{21}(t) = \alpha_{11}(t)\sqrt{\int_0^t \delta u^2(\tau)d\tau} + \varepsilon\alpha_{21}(t),$$

$$|\delta x_2(t)| \leq \sqrt{\int_0^t k_2^2(t,\tau)d\tau}\sqrt{\int_0^t \delta u^2(\tau)d\tau} + \varepsilon\alpha_{22}(t) = \alpha_{12}(t)\sqrt{\int_0^t \delta u^2(\tau)d\tau} + \varepsilon\alpha_{22}(t).$$

The upper bounds on $\delta x_1(t)$ and $\delta x_2(t)$ can be written as follows

$$|\delta x_1(t)| \leq \alpha_{11}(t)\sqrt{R} + \varepsilon\alpha_{21}(t),$$
$$|\delta x_2(t)| \leq \alpha_{12}(t)\sqrt{R} + \varepsilon\alpha_{22}(t),$$

where

$$k_1(t,\tau) = \frac{1}{8}\Phi_{12}(t,\tau),\ k_2(t,\tau) = \frac{1}{8}\Phi_{22}(t,\tau),\ R = \int_0^T \delta u^2(\tau)d\tau,$$
$$M = \int_0^T \left[H_\varepsilon(y_1, y_2, u_0, \lambda_1, \lambda_2) - \lambda_1\dot{y}_1 - \lambda_2\dot{y}_2\right] dt.$$

Upper bound on R

From Proposition 2, $J(u_0)$ can be written in the form

$$J_\varepsilon(u_0) = M + \varepsilon\int_0^T \left[N_1(t)\delta X_1(t)\right] dt + \int_0^T \left[5(1+\frac{\varepsilon}{4})\delta X_1^2 - \lambda_1\delta X_1(t)\delta X_2(t)\right] dt,$$

where $N_1(t) = \dfrac{5y_1(t)}{2} + \dfrac{\lambda_1(t)}{5}$ and we can easily derive

$$|J_\varepsilon(u_0) - M| \leq \left|\varepsilon\int_0^T \left[N_1(t)\delta X_1(t)\right] dt + \int_0^T \left[5(1+\frac{\varepsilon}{4})\delta X_1^2 - \lambda_1\delta X_1(t)\delta X_2(t)\right] dt\right|,$$

yielding

$$|J_\varepsilon(u_0) - M| \leq c\varepsilon^2,$$

where c, that depends only on the nominal trajectories, is given by

$$c = \left[\left|\int_0^T (\frac{5}{2}y_1(\tau) + \frac{1}{5}\lambda_1(\tau))\alpha_{21}(\tau)d\tau + \int_0^T \left(\frac{25}{4}\alpha_{21}^2(\tau) - \lambda_1(\tau)\alpha_{21}(\tau)\alpha_{22}(\tau)\right) d\tau\right|\right].$$

The same approach allows $J(u_\varepsilon)$ to be written from Proposition 2

$$J_\varepsilon(u_\varepsilon) = M + \varepsilon\int_0^T \left[N_1(t)\delta x_1(t) + N_0(t)\delta u\right] dt + \int_0^T (0.3\delta u^2 + 5(1+\frac{\varepsilon}{4})\delta x_1^2 - \lambda_1\delta x_1\delta x_2)dt, \tag{E.2}$$

where $N_0 = \dfrac{\lambda_2}{40}$. As u_ε is the optimal control of the perturbed problem and from equation (E.2), we can write

$$c\varepsilon^2 \geq \varepsilon\int_0^T \left[N_1(t)\delta x_1(t) + N_0(t)\delta u\right] dt + \int_0^T (0.3\delta u^2 + 5(1+\frac{\varepsilon}{4})\delta x_1^2 - \lambda_1\delta x_1\delta x_2)dt.$$

By using the decomposition $xy \geq -\frac{x^2}{2m} - \frac{m}{2}y^2$ (holding for any x, y and $m > 0$), we obtain

$$\begin{aligned} c\varepsilon^2 &\geq -\frac{\varepsilon^2}{2m}\int_0^T [N_1^2(t) + N_0^2(t)]dt - \frac{m}{2}\int_0^T [\delta x_1^2(t) + \delta u^2(t)]dt \\ &+ \int_0^T (0.3\delta u^2 + 5(1+\frac{\varepsilon}{4})\delta x_1^2 - \lambda_1\delta x_1\delta x_2)dt. \end{aligned} \tag{E.3}$$

In the following, the notations used are

$$\begin{aligned} H_1(t) &= \alpha_{11}^2(t) + \alpha_{12}^2(t), \\ H_2(t) &= \alpha_{21}^2(t) + \alpha_{22}^2(t), \\ D_1 &= 0.3 + 10\int_0^T \alpha_{11}^2(\tau)d\tau + \int_0^T \lambda_1(\tau)H_1(\tau)d\tau, \\ D_2 &= 0.5 + \int_0^T \alpha_{11}^2(\tau)d\tau. \end{aligned}$$

From the upper bounds on δx_1 and δx_2, we derive

$$\begin{aligned} \delta x_1^2(t) &\leq 2\alpha_{11}^2(t)R + 2\varepsilon^2\alpha_{21}^2(t), \\ \delta x_2^2(t) &\leq 2\alpha_{12}^2(t)R + 2\varepsilon^2\alpha_{22}^2(t), \\ -\delta x_1(t)\delta x_2(t) &\leq H_1(t)R + H_2(t)\varepsilon^2. \end{aligned}$$

The inequality (E.3) can be written

$$\begin{aligned} \left[D_1 - mD_2 + \frac{5\varepsilon}{2}\int_0^T \alpha_{11}^2(\tau)d\tau\right] R &\leq \frac{\varepsilon^2}{2m}\int_0^T \left[N_1^2(t) + N_0^2(t)\right] dt + c\varepsilon^2 \\ &+ \left[(m - 10 - \frac{5\varepsilon}{2})\int_0^T \alpha_{21}^2(\tau)d\tau - \int_0^T \lambda_1(\tau)H_2(\tau)d\tau\right]\varepsilon^2, \end{aligned}$$

yielding to the following upper bound on R as

$$R \leq \frac{c\varepsilon^2 + \frac{\varepsilon^2}{2m}\int_0^T \left[N_1^2(t) + N_0^2(t)\right] dt + (m - 10 - \frac{5\varepsilon}{2})\varepsilon^2\int_0^T \alpha_{21}^2(\tau)d\tau - \varepsilon^2\int_0^T \lambda_1(\tau)H_2(\tau)d\tau}{D_1 - mD_2 + \frac{5\varepsilon}{2}\int_0^T \alpha_{11}^2(\tau)d\tau},$$

where m is chosen to be equal to

$$\frac{D_1}{2D_2}.$$

As $\varepsilon \geq 0$, the upper bound on R is

$$R \leq c_1\varepsilon^2,$$

where

$$c_1 \triangleq \frac{c + \frac{1}{2m}\int_0^T \left[N_1^2(t) + N_0^2(t)\right] dt + (m - 10)\int_0^T \alpha_{21}^2(\tau)d\tau - \int_0^T \lambda_1(\tau)H_2(\tau)d\tau}{D_1 - mD_2}.$$

The upper bounds on δx_1 and δx_2 become of the form

$$\begin{aligned} |\delta x_1(t)| &\leq \left(\alpha_{11}(t)\sqrt{c_1} + \alpha_{21}(t)\right)\varepsilon \triangleq c_{x1}(t)\varepsilon, \\ |\delta x_2(t)| &\leq \left(\alpha_{12}(t)\sqrt{c_1} + \alpha_{22}(t)\right)\varepsilon \triangleq c_{x2}(t)\varepsilon. \end{aligned}$$

Upper bound on ΔJ

The final step is to find an upper bound on $\Delta J = J_\varepsilon(u_0) - J_\varepsilon(u_\varepsilon) > 0$. For this, we proceed as follows

$$\Delta J = J_\varepsilon(u_0) - J_\varepsilon(u_\varepsilon) \leq \left|J_\varepsilon(u_0) - M\right| + \left|J_\varepsilon(u_\varepsilon) - M\right|.$$

From equation (E.2), and by using the state upper bounds, we have

$$\begin{aligned}
|J_\varepsilon(u_\varepsilon) - M| &= \left|\varepsilon \int_0^T [N_1 \delta x_1(t) + N_0 \delta u]\, dt + \int_0^T (0.3\delta u^2 + 5(1+\frac{\varepsilon}{4})\delta x_1^2 - \lambda_1 \delta x_1 \delta x_2) dt\right|, \\
&\leq \int_0^T \left[\varepsilon^2 N_1(t) c_{x1}(t) + \frac{\varepsilon^2}{2m_1} N_0^2(t)\right] dt + \frac{m_1}{2} c_1 \varepsilon^2 \\
&\quad + \left|5(1+\frac{\varepsilon}{4})\varepsilon^2 \int_0^T c_{x1}^2(\tau) dt + 0.3 c_1 \varepsilon^2 - \varepsilon^2 \int_0^T \lambda_1(\tau) c_{x1}(\tau) c_{x2}(\tau) d\tau\right|, \\
&\leq K_1 \varepsilon^2.
\end{aligned}$$

The parameter m_1 is chosen to minimize the term

$$\frac{1}{2m_1} \int_0^T N_0^2(t) dt + \frac{m_1}{2} c_1,$$

and the upper bound on ΔJ is

$$\Delta J \leq (c + K_1)\varepsilon^2. \tag{E.4}$$

E.2 Eco-driving problem

The nominal problem is obtained for $\varepsilon = 0$. The associated TPBVP is

$$\begin{cases}
\dot{x}_1 = h_1 u_0^* - h_0,\ x_1(0) = 0, \\
\dot{x}_2 = x_1,\ x_2(0) = 0, \\
\dot{\lambda}_1 = -\lambda_2 - b_1 u_0^*,\ x_1(T) = 0, \\
\dot{\lambda}_2 = 0,\ \lambda_2(T) = \beta_0(x_2(T) - D), \\
u_0^* = -\dfrac{(h_1\lambda_1 + b_1 x_1)}{2b_2},
\end{cases} \tag{E.5}$$

where λ_1 and λ_2 are the adjoint states associated to x_1 and x_2 respectively. The corresponding Hamiltonian in this case is

$$H_0(x_1, x_2, \lambda_1, \lambda_2, u) = b_1 u x_1 + b_2 u^2 + \lambda_1(h_1 u - h_0) + \lambda_2 x_1.$$

The perturbed problem is for $\varepsilon \neq 0$. The associated TPBVP is

$$\begin{cases}
\dot{x}_1^* = h_1 u_1^* - h_0,\ x_1^*(0) = 0, \\
\dot{x}_2^* = x_1^*,\ x_2^*(0) = 0, \\
\dot{\lambda}_1^* = -\lambda_2^* - b_1 u_1^*,\ x_1^*(T) = 0, \\
\dot{\lambda}_2^* = 0,\ \lambda_2^*(T) = (\beta_0 + \varepsilon\beta_1)(x_2^*(T) - D), \\
u_1^* = -\dfrac{(h_1\lambda_1^* + b_1 x_1^*)}{2b_2},
\end{cases} \tag{E.6}$$

where λ_1^* and λ_2^* are the adjoint states associated to x_1^* and x_2^* respectively. The difference between the two TPBVP described above is the final value of the adjoint state λ_2. Note that

$$\delta u = u_1^* - u_0^*,\ \delta x_1 = x_1^* - x_1,\ \delta x_2 = x_2^* - x_2,\ \sigma = [x_1,\ x_2,\ u].$$

Upper bound on δx_i

The first step is to find an upper bound on δx_1 and δx_2 as a function of z defined by

$$z = \delta u + \frac{b_1}{2b_2}\delta x_1.$$

From equations (5.27), the dynamics of δx_1 and δx_2 are given by

$$\begin{cases} \delta\dot{x}_1 = h_1\delta u, \ \delta x_1(0) = 0, \\ \delta\dot{x}_2 = \delta x_1, \ \delta x_2(0) = 0. \end{cases} \tag{E.7}$$

By using the expression of z, the dynamics of δx_1 can be written

$$\delta\dot{x}_1 = h_1 z - \frac{h_1 b_1}{2b_2}\delta x_1, \ \delta x_1(0) = 0.$$

The solution of this differential equation is

$$\delta x_1(t) = h_1 \int_0^t e^{-k(t-\tau)} z(\tau) d\tau, \ k = \frac{h_1 b_1}{2b_2}.$$

By using the Cauchy-Schwarz inequality, this equation can be written

$$\|\delta x_1(t)\| \ \leq \ h_1 \sqrt{\int_0^t e^{-2k(t-\tau)} d\tau} \sqrt{\int_0^T z(\tau)^2 d\tau}.$$

From the dynamics of δx_2, we obtain

$$\|\delta x_2(t)\| \leq h_1 \left[\int_0^t \sqrt{\frac{1 - e^{-2k(t-\tau)}}{2k}} d\tau\right] \sqrt{\int_0^T z(\tau)^2 d\tau}.$$

The upper bounds on δx_1 and δx_2 become of the form

$$\|\delta x_1(t)\| \leq c_1(t)\sqrt{R},$$

$$\|\delta x_2(t)\| \leq c_2(t)\sqrt{R},$$

where

$$R = \int_0^T z(\tau)^2 d\tau,$$

$$c_1(t) = h_1 \sqrt{\frac{1 - e^{-2kt}}{2k}}, \ c_2(t) = h_1 \int_0^t \sqrt{\frac{1 - e^{-2k\tau}}{2k}} d\tau,$$

$$d_1 = b_2 + \frac{\beta_0}{2} c_2^2(T) - \frac{b_1^2}{4b_2} \int_0^T c_1^2(\tau) d\tau,$$

$$d_2 = \frac{1}{2}\beta_1 c_2^2(T), \ d_3 = \frac{\beta_1^2}{2}(x_2(T) - D)^2.$$

The functions c_1 and c_2 are calculated numerically.

Upper bound on R

The cost function $J_\varepsilon(u_1^*)$ can be written using Proposition 2 in the form

$$\begin{aligned} J_\varepsilon(u_1^*) &= J_\varepsilon(u_0^*) + \int_0^T (b_1 u_0^* \delta x_1 + (2b_2 u_0^* + b_1 x_1)\delta u)dt + (\beta_0 + \varepsilon\beta_1)(x_2(T) - D)\delta x_2(T) \\ &\quad + \frac{1}{2}\int_0^T (2b_1 \delta u \delta x_1 + 2b_2 \delta u^2)dt + \frac{1}{2}(\beta_0 + \varepsilon\beta_1)\delta x_2^2(T). \end{aligned}$$

Note that S is the following quantity

$$S = \int_0^T (b_1 u_0^* \delta x_1 + (2b_2 u_0^* + b_1 x_1)\delta u)dt.$$

From equations (E.5), given the formula of u_0^*, we can write

$$2b_2 u_0^* + b_1 x_1 = -h_1 \lambda_1.$$

By replacing this expression in the formula of S, we have

$$S = \int_0^T (b_1 u_0^* \delta x_1 - h_1 \lambda_1 \delta u)dt.$$

From equations (E.7), the term $h_1 \delta u$ is equal to $\delta \dot{x}_1$. Integrating by parts gives the formula of S in the form

$$S = \int_0^T b_1 u_0^* \delta x_1 dt - \lambda_1(T) \cdot \underbrace{\delta x_1(T)}_{=0} + \lambda_1(0) \cdot \underbrace{\delta x_1(0)}_{=0} + \int_0^T \dot{\lambda}_1 \delta x_1 dt.$$

The term $\delta x_1(T)$ is equal to zero, since the final constraint on x_1 at time $t = T$ is satisfied for the two OCP (E.5) and (E.6). The expression of S is

$$S = \int_0^T (b_1 u_0^* + \dot{\lambda}_1)\delta x_1 dt.$$

From the equation given the dynamics of λ_1 in equations (E.5), the formula of S becomes

$$S = -\int_0^T \lambda_2 \cdot \delta x_1 dt.$$

From the dynamics of δx_2 in equations (E.7), S can be written

$$S = -\int_0^T \lambda_2 \cdot \delta \dot{x}_2 dt.$$

As λ_2 is constant, $\delta x_2(0) = 0$ and from equations (E.5), S can be simplified to

$$S = -\beta_0(x_2(T) - D)\delta x_2(T),$$

yielding to the following expression for $\Delta J = J_\varepsilon(u_1^*) - J_\varepsilon(u_0^*)$

$$\Delta J = \frac{1}{2}\int_0^T (2b_1 \delta u \delta x_1 + 2b_2 \delta u^2)dt + \varepsilon\beta_1(x_2(T) - D)\delta x_2(T) + \frac{1}{2}(\beta_0 + \varepsilon\beta_1)\delta x_2^2(T). \quad \text{(E.8)}$$

As u_1^* is the optimal control, it satisfies

$$J_\varepsilon(u_1^*) \leq J_\varepsilon(u_0^*),$$

and from equation (E.8), we can write

$$\frac{1}{2}\int_0^T (2b_1\delta u\delta x_1 + 2b_2\delta u^2)dt + \varepsilon\beta_1(x_2(T) - D)\delta x_2(T) + \frac{1}{2}(\beta_0 + \varepsilon\beta_1)\delta x_2^2(T) \leq 0. \quad \text{(E.9)}$$

From the relationship between δu and z, we have

$$2b_1\delta u\delta x_1 + 2b_2\delta u^2 = 2b_2 z^2 - \frac{b_1^2}{2b_2}\delta x_1^2.$$

From the inequality $xy > -\frac{x^2}{2a} - \frac{a}{2}y^2$ and the upper bounds on δx_1 and δx_2, inequality (E.9) becomes of the form

$$\left[d_1 - \frac{\alpha}{2}c_2^2(T) + \varepsilon d_2\right] R \leq \frac{\varepsilon^2}{\alpha}d_3,$$

where α is chosen such that $\alpha c_2^2(T) = d_1$. Finally, as $\varepsilon \geq 0$, the upper bound on R is

$$R \leq \frac{d_3\varepsilon^2}{\alpha d_1 - \frac{1}{2}\alpha^2 c_2^2(T)} \triangleq f\varepsilon^2,$$

and the upper bounds on δx_1 and δx_2 are of the form

$$\|\delta x_1(t)\| \leq c_1(t)\sqrt{f}\varepsilon, \ \ \|\delta x_2(t)\| \leq c_2(t)\sqrt{f}\varepsilon.$$

Upper bound on ΔJ

From equation (E.8), the upper bound on ΔJ is $K\varepsilon^2$ where K is give by

$$K = \beta_1(D - x_2(T))c_2(T)\sqrt{f} + \frac{1}{2}(\beta_0 + \varepsilon\beta_1)c_2^2(T)f + b_2 f + \frac{b_1^2}{4b_2}f\int_0^T c_1^2(t)dt. \quad \text{(E.10)}$$

E.3 Thermal management problem for HEV

The Hamiltonian associated to the perturbed problem (OCP_ε) is

$$H_\varepsilon(\theta_e, u, \lambda, \mu, t) = e(\theta_e, \varepsilon)c(u, t) + \lambda f(u, t) + \mu g(\theta_e, u, t),$$

where λ and μ are the adjoint states associated respectively to the SOC and θ_e. From the optimality conditions, the associated TPBVP is

$$\begin{cases} e(\theta_1, \varepsilon)\partial_u c(u_1^*, t) + \lambda_1\partial_u f(u_1^*, t) + \mu_1\partial_u g(\theta_1, u_1^*, t) = 0, \\ \dot{\lambda}_1 = 0, \quad \lambda_1(T) = 2\beta(\xi_1(T) - \xi_1(0)), \\ -\dot{\mu}_1 = c(u_1^*, t)\partial_\theta e(\theta_1, \varepsilon) + \mu_1\partial_\theta g(\theta_1, u_1^*, t), \quad \mu_1(T) = 0, \end{cases}$$

where $(\xi_1,\ \theta_1)$ are solutions of (3.2, 4.3) for the control u_1^*. For the nominal problem, the associated TPBVP is of the form

$$\begin{cases} \partial_u c(u_0^*, t) + \lambda_0\partial_u f(u_0^*, t) = 0, \\ \dot{\lambda}_0 = 0, \quad \lambda_0(T) = 2\beta(\xi_0(T) - \xi_0(0)), \end{cases}$$

where $(\xi_0,\ \theta_0)$ are solutions of (3.2, 4.3) for the control u_0^*. The following notations will be used

$$\delta\xi = \xi_1 - \xi_0,\ \ \delta\theta = \theta_1 - \theta_0,\ \ \delta u = u_1^* - u_0^*.$$

As the perturbation terms are only present in the cost function, the errors on the state trajectories can be written in the form

$$\begin{aligned} |\delta\xi(t)|^2 &\leq c_\xi^2(t)\int_0^T |\delta u(\tau)|^2\, d\tau, \\ |\delta\theta(t)|^2 &\leq c_\theta^2(t)\int_0^T |\delta u(\tau)|^2\, d\tau, \end{aligned}$$

where c_ξ and c_θ are functions of time and the nominal control u_0^*. Using Proposition 2, the optimal cost $J_\varepsilon(u_1^*)$ can be written as

$$\begin{aligned} J_\varepsilon(u_1^*) &= J_\varepsilon(u_0^*) + \varepsilon\int_0^T [(1-\frac{\theta_0}{\theta_w})\partial_u c(u_0^*,t)\cdot\delta u(t) - \frac{c(u_0^*,t)}{\theta_w}\cdot\delta\theta]dt + \beta\cdot\delta\xi(T)^2 \\ &\quad + \int_0^T\int_0^1\int_0^1 \rho\partial_{\sigma\sigma}H_1(\sigma_0+\rho k(\sigma_1-\sigma_0),\lambda_0,0,t)(\sigma_1-\sigma_0)^2 d\rho dk dt, \quad \text{(E.11)} \end{aligned}$$

where $\sigma = [\theta\ , u]$. As u_1^* is the optimal control for the perturbed problem, it satisfies

$$J_\varepsilon(u_1^*) \leq J_\varepsilon(u_0^*).$$

From equation (E.11), we can write

$$\begin{aligned} &\varepsilon\int_0^T [(1-\frac{\theta_0}{\theta_w})\partial_u c(u_0^*,t)\cdot\delta u(t) - \frac{c(u_0^*,t)}{\theta_w}\cdot\delta\theta]dt + \beta\cdot\delta\xi(T)^2 \\ &+ \int_0^T\int_0^1\int_0^1 \rho\partial_{\sigma\sigma}H_1(\sigma_0+\rho k(\sigma_1-\sigma_0),\lambda_0,0,t)(\sigma_1-\sigma_0)^2 d\rho dk dt \leq 0. \quad \text{(E.12)} \end{aligned}$$

Consider the notations

$$S_1(t) = (1-\frac{\theta_0}{\theta_w})\partial_u c(u_0^*,t),\ \ S_2(t) = \frac{c(u_0^*,t)}{\theta_w},\ \ S_3(\theta_e,u,t) = (1-\frac{\theta_e}{\theta_w})c(u,t).$$

The quantities S_1 and S_2 are calculated numerically from the nominal trajectories. From the definition of H_ε, we can write

$$H_\varepsilon(\theta_e,u,\lambda_0,0,t) = H_0(u,\lambda_0,t) + \varepsilon(1-\frac{\theta_e}{\theta_w})c(u,t).$$

Equation (E.12) becomes of the form

$$\begin{aligned} &\varepsilon\int_0^T S_1(t)\delta u(t)dt + \beta\delta\xi^2(T) + \int_0^T\int_0^1\int_0^1 \rho\partial_{uu}H_0(u_0+\rho k\delta u,\lambda_0,t)\delta u^2(t)d\rho dk dt \\ &+\varepsilon\int_0^T\int_0^1\int_0^1 \rho\partial_{\sigma\sigma}S_3(\sigma_0+\rho k(\sigma_1-\sigma_0),t)(\sigma_1-\sigma_0)^2 d\rho dk dt \leq \varepsilon\int_0^T S_2(t)\delta\theta(t)dt. \end{aligned}$$

The part $\varepsilon \int_0^T \int_0^1 \int_0^1 \rho \partial_{\sigma\sigma} S_3(\sigma_0 + \rho k(\sigma_1 - \sigma_0), t)(\sigma_1 - \sigma_0)^2 d\rho dk dt$ leads to a term in ε^3 (as ε is less than one, $\varepsilon^3 \leq \varepsilon^2$). We can write from the previous equation that

$$\begin{aligned} &\varepsilon \int_0^T S_1(t)\delta u(t)dt + \beta \delta\xi^2(T) + \int_0^T \int_0^1 \int_0^1 \rho \partial_{uu} H_0(u_0 + \rho k \delta u, \lambda_0, t)\delta u^2(t) d\rho dk dt \\ &\leq \varepsilon \int_0^T S_2(t)\delta\theta(t)dt. \end{aligned} \tag{E.13}$$

Assume that there exists a positive constant γ such that

$$\partial_{uu} H_0(u, \lambda_0, t) \geq \gamma I, \quad \text{uniformly in } u, \tag{E.14}$$

where H_0 is the Hamiltonian associated to the nominal problem. From the condition (E.14), we derive

$$\int_0^T \int_0^1 \int_0^1 \rho \partial_{uu} H_0(u_0 + \rho k \delta u, \lambda_0, t)\delta u(t)^2 d\rho dk dt \geq \frac{\gamma}{2} \int_0^T \delta u(t)^2 dt.$$

Using the inequalities, for any x, y and $\alpha > 0$,

$$-\frac{x^2}{2\alpha^2} - \frac{\alpha^2 y^2}{2} \leq xy \leq \frac{x^2}{2\alpha^2} + \frac{\alpha^2 y^2}{2},$$

equation (E.13) can be written as

$$\begin{aligned} &-\frac{\varepsilon^2}{2\alpha^2} \int_0^T S_1^2(t)dt - \frac{\alpha^2}{2} \int_0^T \delta u^2(t)dt + \beta \delta\xi^2(T) + \frac{\gamma}{2} \int_0^T \delta u^2(t)dt \\ &\leq \frac{\varepsilon^2}{2\alpha^2} \int_0^T S_2^2(t)dt + \frac{\alpha^2}{2} \int_0^T \delta\theta^2(t)dt. \end{aligned} \tag{E.15}$$

Equation (E.15) becomes of the form

$$\left[\frac{\gamma}{2} + \beta c_\xi^2(T) - \frac{\alpha^2}{2}\left[1 + \int_0^T c_\theta^2(t)dt\right]\right] \int_0^T \delta u^2(t)dt \leq \frac{\varepsilon^2}{2\alpha^2} \int_0^T (S_1^2(t) + S_2^2(t))dt. \tag{E.16}$$

The parameter α is chosen such that

$$\frac{\gamma}{2} + \beta c_\xi^2(T) - \frac{\alpha^2}{2}\left[1 + \int_0^T c_\theta^2(t)dt\right] = \frac{\gamma}{4} + \frac{1}{2}\beta c_\xi^2(T) \triangleq q,$$

and we get

$$\alpha = \sqrt{\frac{\frac{\gamma}{2} + \beta c_\xi^2(T)}{1 + \int_0^T c_\theta^2(t)dt}}.$$

The parameter α is well defined. From equation (E.16), one derives that

$$\int_0^T \delta u^2(t)dt \leq \frac{\varepsilon^2}{2q\alpha^2} \int_0^T (S_1^2(t) + S_2^2(t))dt = c_u^2 \varepsilon^2,$$

and the upper bounds on the state trajectories error become of the form

$$\begin{aligned} \delta\xi^2(T) &\leq c_\xi^2 c_u^2 \varepsilon^2, \\ \delta\theta^2(t) &\leq c_\theta^2(t) c_u^2 \varepsilon^2. \end{aligned}$$

The final step is to find an upper bound of ΔJ. From the expression of $J_\varepsilon(u_1^*)$ given in (E.11), we can write

$$\begin{aligned}
\Delta J &= \left| \varepsilon \int_0^T [S_1(t)\delta u - S_2(t)\delta\theta]dt + \int_0^T \int_0^1 \int_0^1 \rho \partial_{uu} H_0(., \lambda_0, t)\delta u^2 d\rho dk dt + \beta \delta\xi(T)^2 \right|, \\
&\leq \left[\frac{1}{2\alpha_1} \int_0^T (S_1^2(t) + S_2^2(t))dt + \frac{\alpha_1}{2} c_u^2 (1 + \int_0^T c_\theta^2(t)dt) + \frac{1}{2} \sup_{[0T]} \partial_{uu} H_0 c_u^2 + \beta c_\xi^2 c_u^2 \right] \varepsilon^2, \\
&\leq K\varepsilon^2,
\end{aligned}$$

where α_1 is given by

$$\alpha_1 = \sqrt{\frac{\int_0^T (S_1^2(t) + S_2^2(t))dt}{c_u^2 + c_u^2 \int_0^T c_\theta^2(t)dt}}.$$

The formula of K is

$$K = \frac{1}{2\alpha_1} \int_0^T (S_1^2(t) + S_2^2(t))dt + \frac{\alpha_1}{2} c_u^2 + \frac{\alpha_1}{2} c_u^2 \int_0^T c_\theta^2(t)dt + \frac{1}{2} \sup \partial_{uu} H_0(.) c_u^2 + \beta c_\xi^2 c_u^2. \quad \text{(E.17)}$$

Appendix F

Details of the proof about the ECMS stability

The objective here is to study the stability of the following time-variant system with a time-varying perturbation G

$$\begin{aligned} \dot{x} &= -D_1(t) \cdot [k_p x + y], \\ \dot{y} &= k_i x + \dot{G}. \end{aligned}$$

The study is divided into three parts.

F.1 LTI system

In the first step, the following LTI system without perturbation is studied ($\dot{G} = 0$)

$$\dot{x} = -d \cdot [k_p x + y], \tag{F.1}$$
$$\dot{y} = k_i x. \tag{F.2}$$

The purpose of this analysis is to find a Lyapunov function [38] to be used in the following. The stability of the system (F.1, F.2) can easily be checked by taking a quadratic Lyapunov function

$$V = \begin{bmatrix} x & y \end{bmatrix} P \begin{bmatrix} x \\ y \end{bmatrix},$$

where P is a symmetric positive definite matrix solution of the following Lyapunov equation

$$A^T P + PA = -\begin{bmatrix} \alpha & 0 \\ 0 & \beta \end{bmatrix},$$

where α and β are positive constants. The matrix A is the dynamic matrix of the system (6.14, 6.15). The matrix P is given by

$$P = \frac{1}{2d}\begin{bmatrix} p_1 & p_2 \\ p_2 & p_3 \end{bmatrix} = \frac{1}{2d}\begin{bmatrix} \dfrac{\alpha}{k_p} + \dfrac{\beta k_i}{k_p d} & \beta \\ \beta & \dfrac{\alpha d}{k_p k_i} + \dfrac{\beta d k_p}{k_i} + \dfrac{\beta}{k_p} \end{bmatrix}.$$

The Lyapunov matrix P is definite positive if the following two inequalities are satisfied

$$\begin{cases} p_1 + p_3 > 0, \\ p_1 p_3 - p_2^2 > 0. \end{cases}$$

The first inequality is satisfied if $(k_i > 0)$ and $(k_p > 0)$. The second inequality can be written as follow

$$\frac{\alpha^2 d}{k_i k_p^2} + \frac{k_i \beta^2}{d k_p^2} + \alpha\beta\left[\frac{d}{k_i} + \frac{2}{k_p^2}\right] > 0.$$

The left side of this inequality is a polynomial of degree 2 with respect to α and β where the coefficients are positives as $k_i > 0$ and $k_p > 0$: this means that if this polynomial has roots, they will be < 0. So, this inequality is always satisfied for any α and β positives. Thus, P is positive definite if the gains k_p and k_i are strictly positive

$$k_p > 0, \quad k_i > 0.$$

In what follows, α and β are set to 1 without loss of generality.

F.2 Time-varying system without source terms

The next step is to introduce a perturbation term $\delta(t) = D_1(t) - d$ in the dynamics (F.1, F.2),

$$\dot{x} = -(d + \delta(t)) \cdot [k_p x + y], \tag{F.3}$$
$$\dot{y} = k_i x. \tag{F.4}$$

The dynamic matrix A_1 of the system (F.3, F.4) can be written as a linear function of A defined for the LTI system

$$A_1 = A + \begin{bmatrix} -k_p\delta(t) & -\delta(t) \\ 0 & 0 \end{bmatrix}. \tag{F.5}$$

The objective in this second step is to find sufficient conditions on perturbation term $\delta(t)$ so that the system (F.3, F.4) remains stable by using the above Lyapunov matrix P.

Lemma 2 *If $\delta(t)$ satisfies the two inequalities*

$$\begin{cases} \dfrac{\delta(t)}{d} < r_1, \\ \dfrac{\delta(t)}{d} > \max(\dfrac{-2d}{2d + k_i}, r_2), \end{cases} \tag{F.6}$$

where $k_i > 0$, $k_p > 0$, r_1 (resp. r_2) is the positive (resp. the negative) root of

$$\Pi(q) = -\frac{1}{4}\left[k_p - \frac{k_i}{k_p d} - \frac{1}{k_p}\right]^2 q^2 + \left[2 + \frac{k_i}{d}\right] q + 1,$$

the system (F.3, F.4) will be stable. The case $\delta = 0$ satisfies the condition (F.6).

Proof The derivative of (V) along the trajectories of (F.3, F.4) is given by

$$\dot{V} = \begin{bmatrix} x & y \end{bmatrix} \left[A^T P + PA + \begin{bmatrix} -k_p\delta(t) & -\delta(t) \\ 0 & 0 \end{bmatrix}^T P + P \begin{bmatrix} -k_p\delta(t) & -\delta(t) \\ 0 & 0 \end{bmatrix} \right] \begin{bmatrix} x \\ y \end{bmatrix}.$$

For convenience, the following notation is used

$$s = \frac{1}{k_p} + \frac{k_i}{dk_p}.$$

The derivative of V can be written

$$\dot{V} = \begin{bmatrix} x & y \end{bmatrix} \begin{bmatrix} -1 - \frac{\delta(t)}{d}k_p s & -\frac{\delta(t)}{2d}(k_p + s) \\ -\frac{\delta(t)}{2d}(k_p + s) & -\frac{\delta(t)}{d} - 1 \end{bmatrix} \begin{bmatrix} x \\ y \end{bmatrix}.$$

Let's suppose that

$$F = \begin{bmatrix} -f_1 & -f_2 \\ -f_2 & -f_3 \end{bmatrix} = \begin{bmatrix} -1 - \frac{\delta(t)}{d}k_p s & -\frac{\delta(t)}{2d}(k_p + s) \\ -\frac{\delta(t)}{2d}(k_p + s) & -\frac{\delta(t)}{d} - 1 \end{bmatrix}. \tag{F.7}$$

We look for conditions on $\delta(t)$ that's make the matrix F negative definite, which is equivalent to

$$\begin{cases} -f_1 - f_3 < 0, \\ f_1 f_3 - f_2^2 > 0. \end{cases} \tag{F.8}$$

The first inequality leads to the condition

$$\frac{\delta(t)}{d} > \frac{-2d}{2d + k_i},$$

while the second condition leads to

$$-\frac{1}{4}\left[k_p - \frac{k_i}{k_p d} - \frac{1}{k_p}\right]^2 \frac{\delta^2}{d^2} + \left[2 + \frac{k_i}{d}\right]\frac{\delta}{d} + 1 > 0,$$

which is equivalent to

$$\Pi(\frac{\delta}{d}) > 0.$$

The two roots of $\Pi(.)$ are

$$\begin{aligned} r_1 &= 2\frac{k_p s + 1}{(k_p - s)^2}\left(1 + \sqrt{1 + \frac{(s - k_p)^2}{(sk_p + 1)^2}}\right) > 0, \\ r_2 &= 2\frac{k_p s + 1}{(k_p - s)^2}\left(1 - \sqrt{1 + \frac{(s - k_p)^2}{(sk_p + 1)^2}}\right) < 0. \end{aligned}$$

The condition on $\delta(t)$ such that $\Pi(\frac{\delta}{d}) > 0$ is

$$r_2 < \frac{\delta(t)}{d} < r_1.$$

The inequalities (F.6) are proven. So, if $\delta(t)$ satisfies the conditions (F.6), the system (F.3, F.4) will be stable for any $k_p > 0$ and $k_i > 0$. It's clear that $\delta(t) = 0$ is included in this domain with strict inequalities. This concludes the proof. ■

F.3 Time-varying system with source terms

In this case, the dynamic of the system (6.11, 6.12) can be written

$$\begin{bmatrix} \dot{x} \\ \dot{y} \end{bmatrix} = A_1 \begin{bmatrix} x \\ y \end{bmatrix} + \begin{bmatrix} 0 \\ \dot{G}(t) \end{bmatrix}, \tag{F.9}$$

where A_1 is defined in (F.5).

Proposition 10 *Assuming that the conditions on $\delta(t)$ in (F.6) are satisfied. There exists a set defined by*

$$f_1 \left[x + \frac{f_2}{f_1} y - \frac{\dot{G}(t)}{2df_1} \right]^2 + (f_3 - \frac{f_2^2}{f_1}) \left[y - \frac{\dot{G}(t)}{2d} \frac{f_1 s_1 - f_2}{f_3 f_1 - f_2^2} \right]^2 \leq \frac{\dot{G}^2(t)}{4d^2 f_1} \left[1 + \frac{(f_1 s_1 - f_2)^2}{f_3 f_1 - f_2^2} \right]$$

outside of it, the Lyapunov function (V) calculated above decreases and the origin belongs always to this set. The constant s_1 is given by

$$s_1 = \frac{d}{k_i k_p} + \frac{1}{k_p} + \frac{dk_p}{k_i}.$$

Proof The derivative of the Lyapunov function (V) along the trajectories of the dynamic system (F.9) is

$$\dot{V} = \begin{bmatrix} x & y \end{bmatrix} F \begin{bmatrix} x \\ y \end{bmatrix} + \frac{\dot{G}}{d}(x + s_1 y),$$

where F is defined in equation (F.7). In details, $\dot{V}$ can be written as

$$\dot{V} = -f_1 x^2 - 2f_2 xy - f_3 y^2 + \frac{\dot{G}}{d}(x + s_1 y),$$

yielding

$$\dot{V} = -f_1 \left[x + \frac{f_2}{f_1} y \right]^2 + \frac{\dot{G}(t)}{d}(x + \frac{f_2}{f_1} y) - (f_3 - \frac{f_2^2}{f_1}) y^2 + \frac{\dot{G}(t)}{d}(s_1 - \frac{f_2}{f_1}) y.$$

By gathering the two first terms of the right side, $\dot{V}$ becomes of the form

$$\dot{V} = -f_1 \left[x + \frac{f_2}{f_1} y - \frac{\dot{G}(t)}{2df_1} \right]^2 - (f_3 - \frac{f_2^2}{f_1}) \left[y - \frac{\dot{G}(t)}{2d} \frac{f_1 s_1 - f_2}{f_3 f_1 - f_2^2} \right]^2 + \frac{\dot{G}^2(t)}{4d^2 f_1} \left[1 + \frac{(f_1 s_1 - f_2)^2}{f_3 f_1 - f_2^2} \right],$$

where $f_1 > 0$ and $f_3 - \dfrac{f_2^2}{f_1} > 0$ (the matrix F is negative definite from conditions (F.8)). So, the derivative of the Lyapunov function will be negative in the region of the state space $[x,\ y]$ defined by

$$f_1 \left[x + \frac{f_2}{f_1} y - \frac{\dot{G}(t)}{2df_1} \right]^2 + (f_3 - \frac{f_2^2}{f_1}) \left[y - \frac{\dot{G}(t)}{2d} \frac{f_1 s_1 - f_2}{f_3 f_1 - f_2^2} \right]^2 > \frac{\dot{G}^2(t)}{4d^2 f_1} \left[1 + \frac{(f_1 s_1 - f_2)^2}{f_3 f_1 - f_2^2} \right].$$

The system (F.9), after some finite time, will converge to the set defined by

$$f_1\left[x+\frac{f_2}{f_1}y-\frac{\dot{G}(t)}{2df_1}\right]^2+(f_3-\frac{f_2^2}{f_1})\left[y-\frac{\dot{G}(t)}{2d}\frac{f_1s_1-f_2}{f_3f_1-f_2^2}\right]^2\leq\frac{\dot{G}^2(t)}{4d^2f_1}\left[1+\frac{(f_1s_1-f_2)^2}{f_3f_1-f_2^2}\right],$$

and will not go out of it in the future time as $\dot{V}$ is negative. The origin of the state space is on the boundary of this set When $\dot{G}\neq 0$. When G becomes constant after a certain time, this set is reduced to the origin of the state space $[x,\ y]$.

The main conclusion is the following: we are not sure that the states x and y will converge to the origin, but we know that they will be bounded by some functions of the driving cycle parameters (torque and speed requested at the wheels and parameters of PI controller) after some finite time. This concludes the proof. ■

Appendix G

Experimental data used in the identification of thermal dynamics

The engine torque and speed set points of the experimental tests used for the identification and the validation of the thermal dynamics of the engine, DOC, DPF and the SCR are given in this Appendix.

G.1 Engine temperature

For the engine temperature, the cycle used in the identification of the engine temperature model parameters is the WLTC. The inputs of engine temperature model (7.1) are the engine speed and the engine torque.

G.1.1 Ie-Test: Identification

The engine speed and torque set points are given in Figures G.1 and G.2.

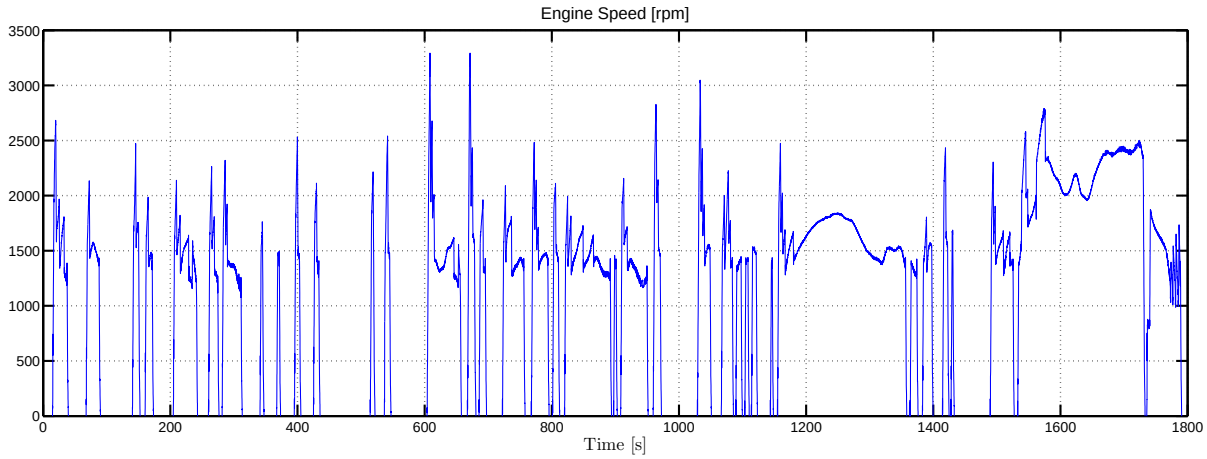

Figure G.1: Engine speed set points [rpm] for Ie-Test

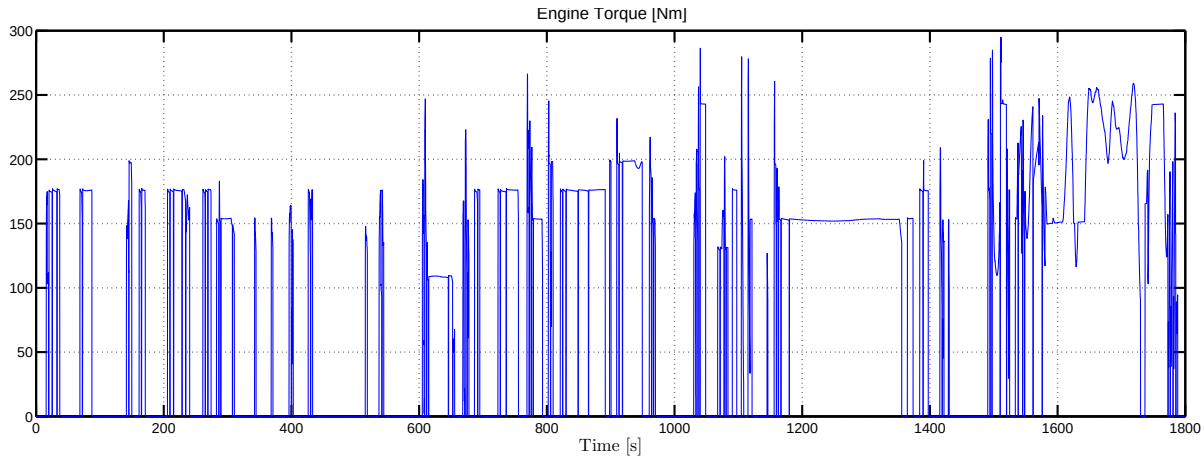

Figure G.2: Engine torque set points [Nm] for Ie-Test

G.1.2 Ve-Tests: Validation

Three tests are considered for the validation of the engine temperature model: Ve_1-Test, Ve_2-Test and Ve_3-Test. The engine speed and torque trajectories are given in Figures G.3, G.4, G.5, G.6, G.7 and G.8. The driving cycle is the WLTC. These tests have been done for the power assist mode where the control strategies of the EMS (to split the power requested at the wheel between the engine and the electric machine) are different.

G.1.2.1 Ve_1-Test

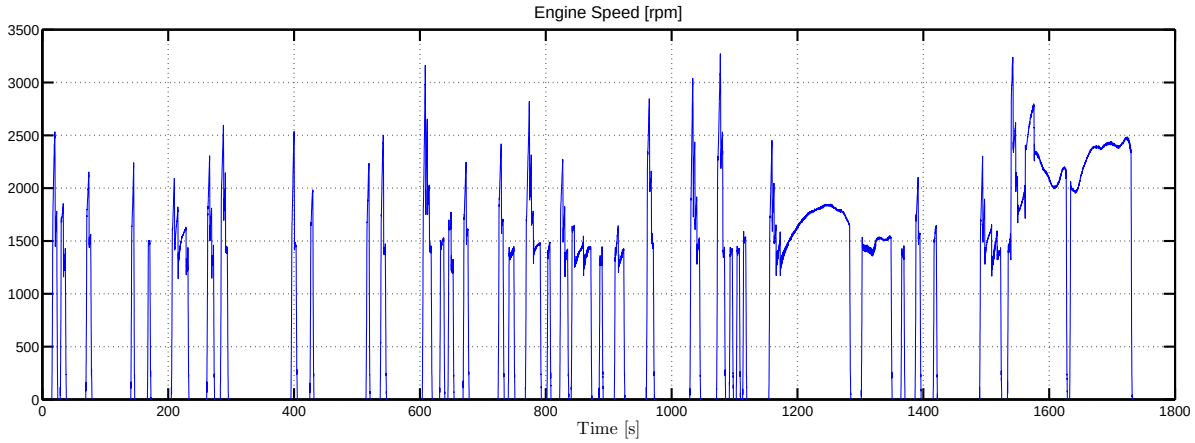

Figure G.3: Engine speed set points [rpm] for Ve_1-Test

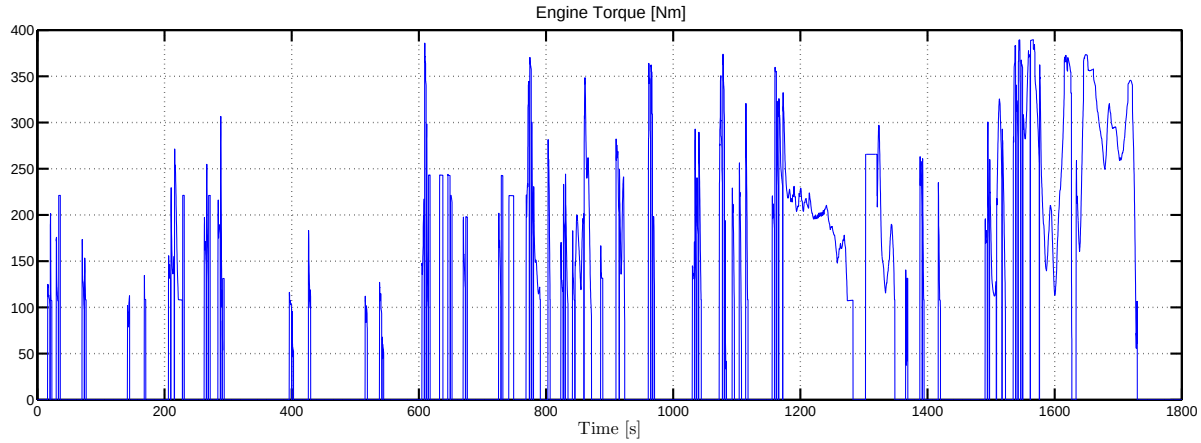

Figure G.4: Engine torque set points [Nm] for Ve_1-Test

G.1.2.2 Ve_2-Test

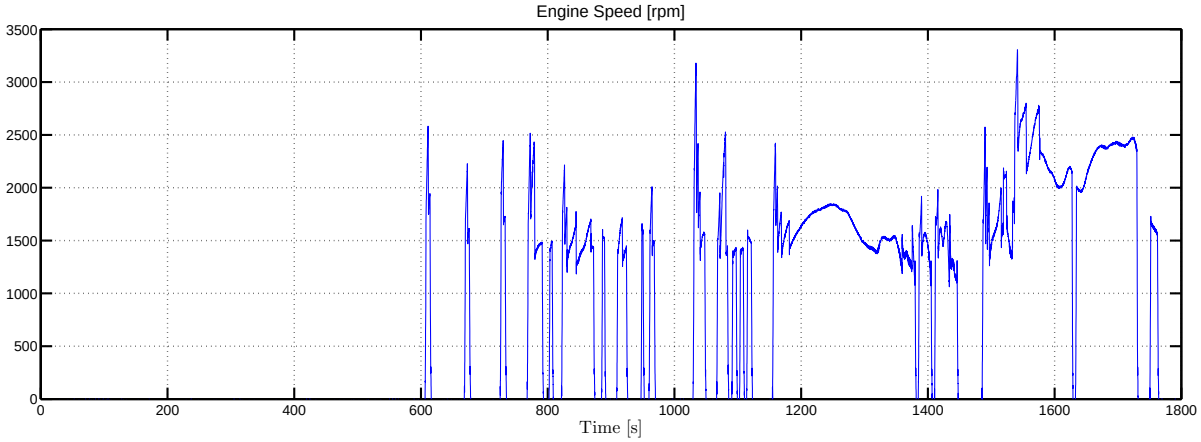

Figure G.5: Engine speed set points [rpm] for Ve_2-Test

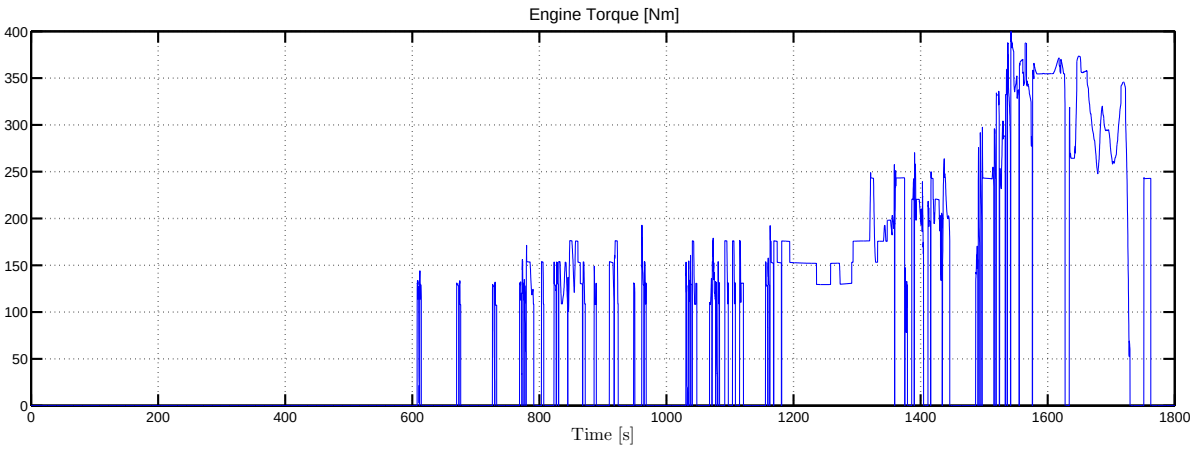

Figure G.6: Engine torque set points [Nm] for Ve_2-Test

G.1.2.3 Ve_3-Test

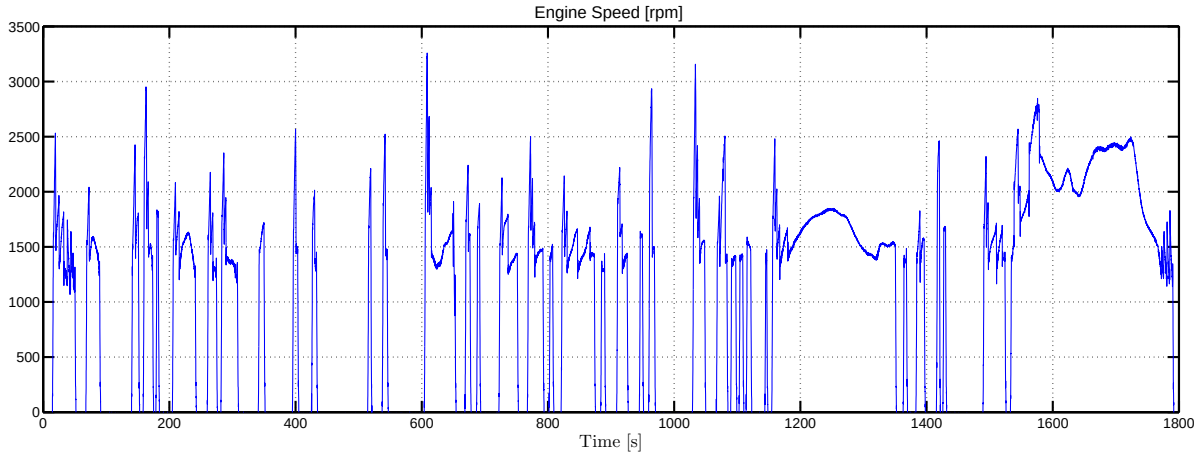

Figure G.7: Engine speed set points [rpm] for Ve_3-Test

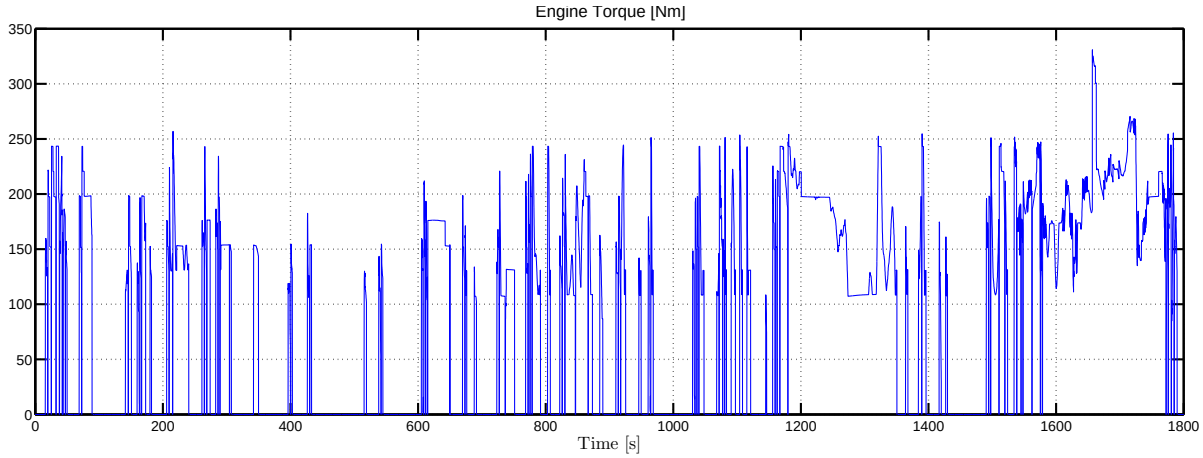

Figure G.8: Engine torque set points [Nm] for Ve_3-Test

G.2 After-treatment system temperatures

The after-treatment system is composed of three sub-systems: DOC, DPF and SCR (see Figure 7.14). For each sub-system, a zero-dimensional model based on physical equations is considered. The main inputs of the DOC model are the gas flow coming from the engine $\dot{m}_{exh}$ and the exhaust temperature θ_{exh}, given by a quasistatic maps as functions of the engine torque and the engine speed. For Ic-Test and Vc_1-Test, the driving cycle is the WLTC.

G.2.1 Ic-Test: Identification

The engine speed and torque are given in Figures G.9 and G.10. The corresponding driving cycle is the WLTC. The operation mode of the vehicle to identify the model

parameters is the thermal mode (engine only). The engine speed is at the idle speed (780 rpm) when the engine torque equals zero.

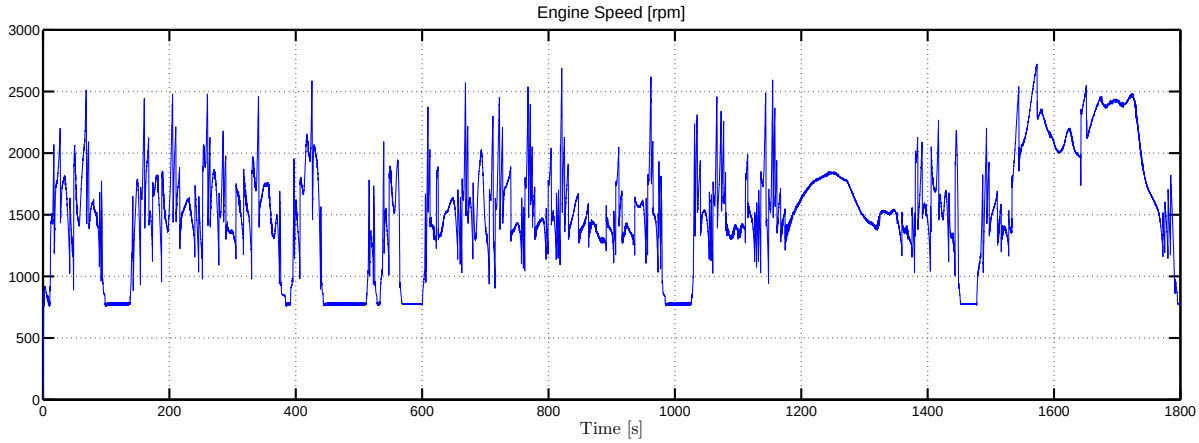

Figure G.9: Engine speed set points [rpm] for Ic-Test

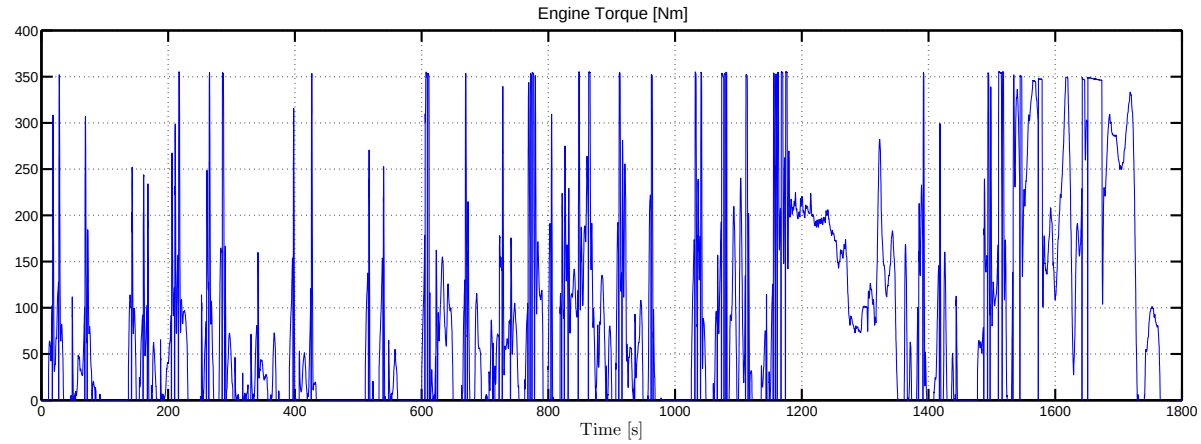

Figure G.10: Engine torque set points [Nm] for Ic-Test

G.2.2 Vc-Tests: Validation

Three tests are considered: Vc_1-Test and Vc_2-Test. The engine speed and torque are given in Figures G.11, G.12, G.13 and G.14.

G.2.2.1 Vc_1-Test

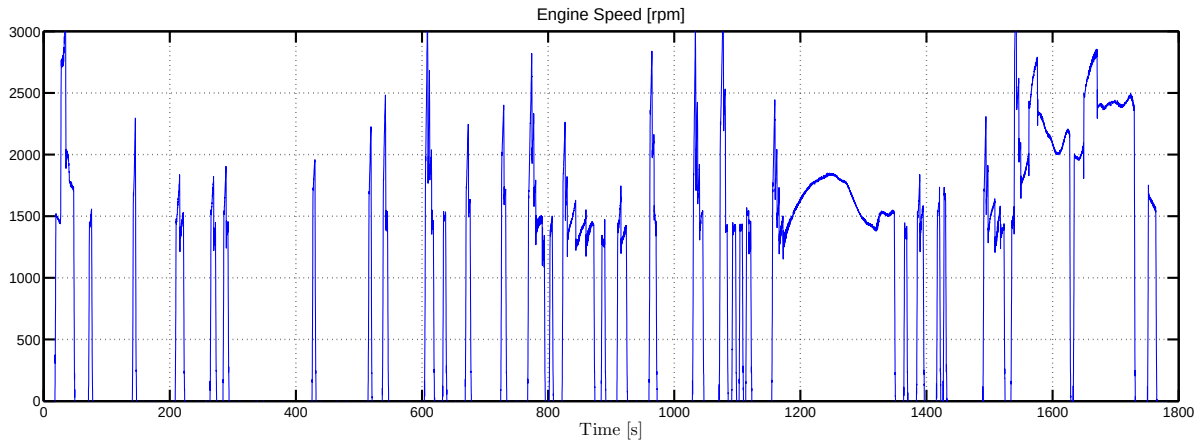

Figure G.11: Engine speed set points [rpm] for Vc_1-Test

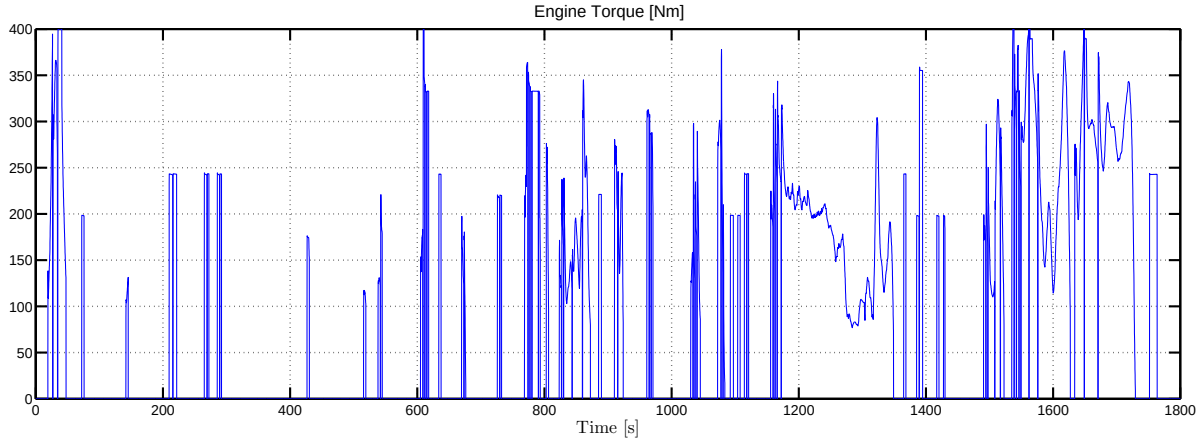

Figure G.12: Engine torque set points [Nm] for Vc_1-Test

G.2.2.2 Vc_2-Test

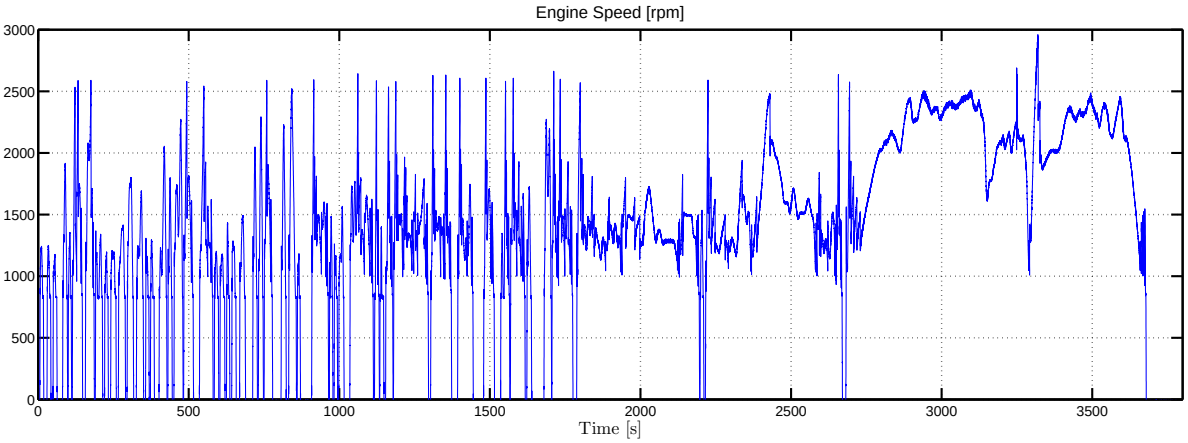

Figure G.13: Engine speed set points [rpm] for Vc_2-Test

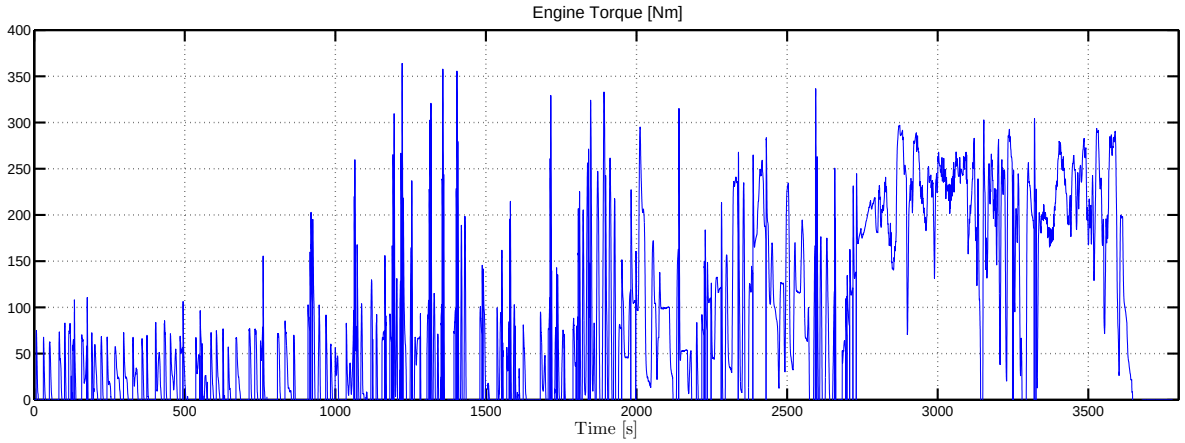

Figure G.14: Engine torque set points [Nm] for Vc_2-Test

G.3 Illustration of the temperature drop problem

As it has been mentioned in Section 7.3.2, the operation mode of the vehicle used for the validation of the DOC, DPF and the SCR temperatures is the "power assist" mode: the engine can be turned off (depending on the control strategy) and there will be no gas flow coming from the engine over the corresponding time intervals. In this case, because the temperature sensors measure the gas temperature, the data in regions A, B, C and D in Figures 7.22 and 7.23 are not representative of the real temperatures. From Figures G.15, G.16, G.17, G.18 and G.19, when the engine is turned off (engine torque and speed are zero), the temperatures of the DOC, DPF and the SCR decrease. In the next engine start, the temperatures increase quickly. Additionally, since the sensors characteristics used for the temperature measurement in the three sub-systems are different, the maximum magnitude of the increase/decrease in the temperatures are different.

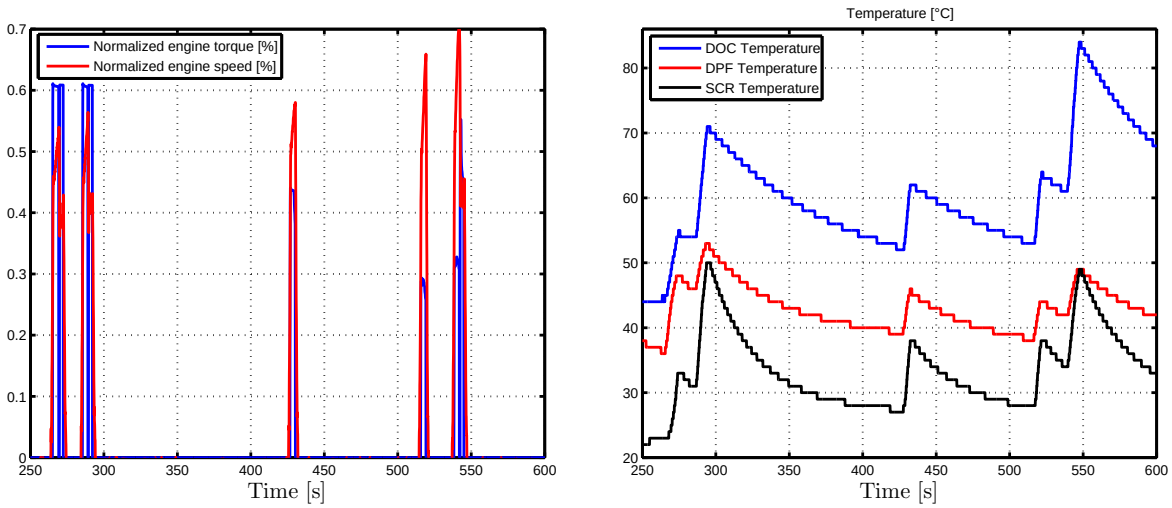

Figure G.15: Zoom on normalized engine torque, normalized engine speed and ATS temperatures for region A

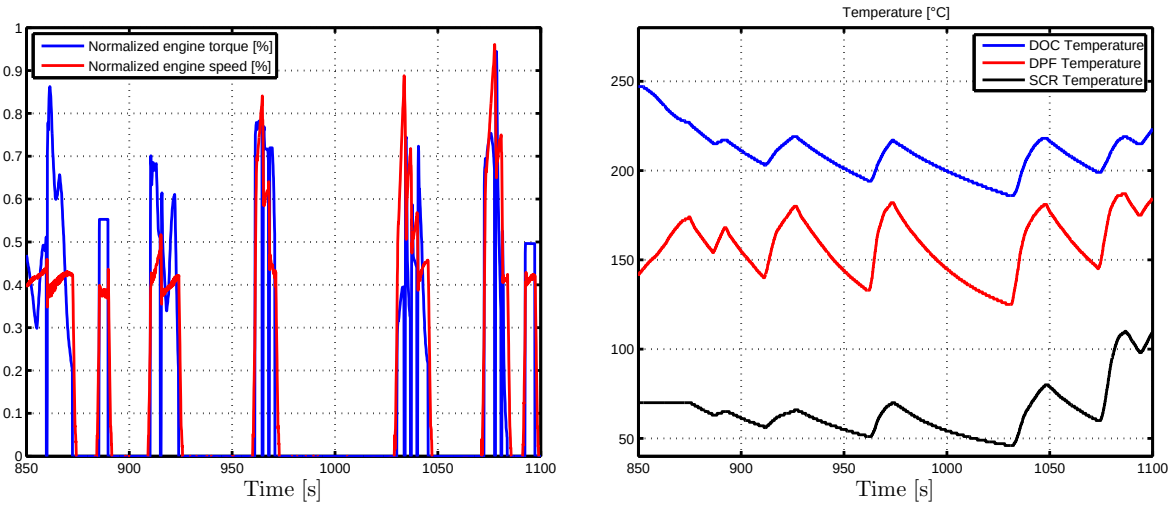

Figure G.16: Zoom on normalized engine torque, normalized engine speed and ATS temperatures for region B

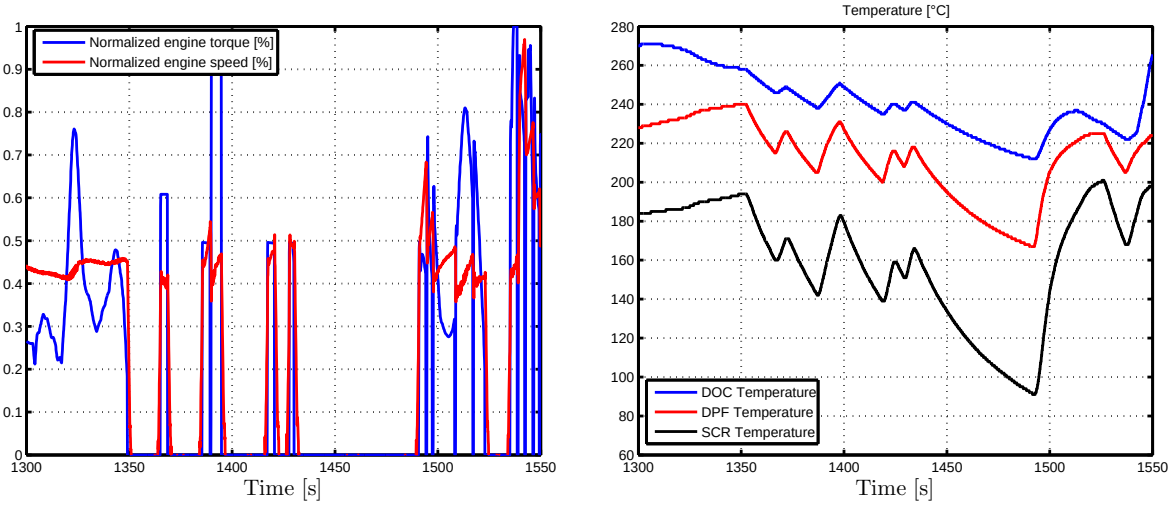

Figure G.17: Zoom on normalized engine torque, normalized engine speed and ATS temperatures for region C

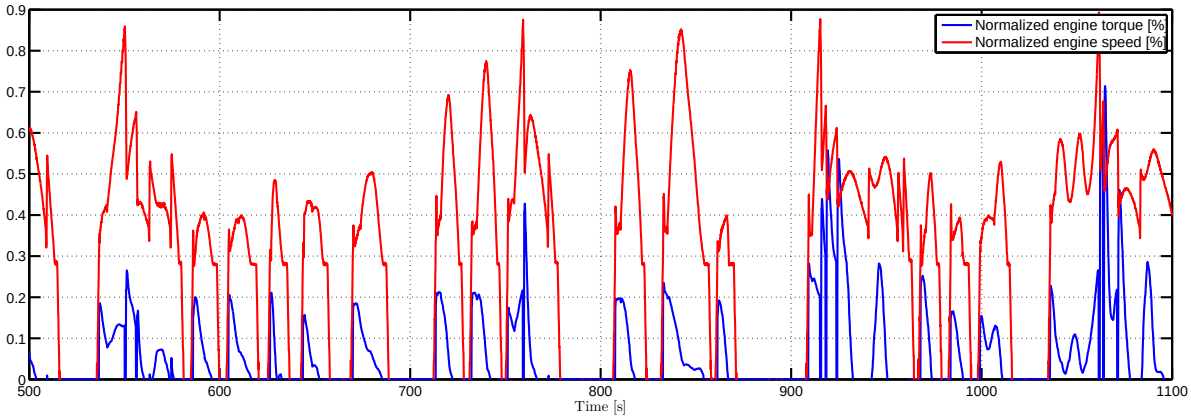

Figure G.18: Zoom on normalized engine torque and normalized engine speed for region D

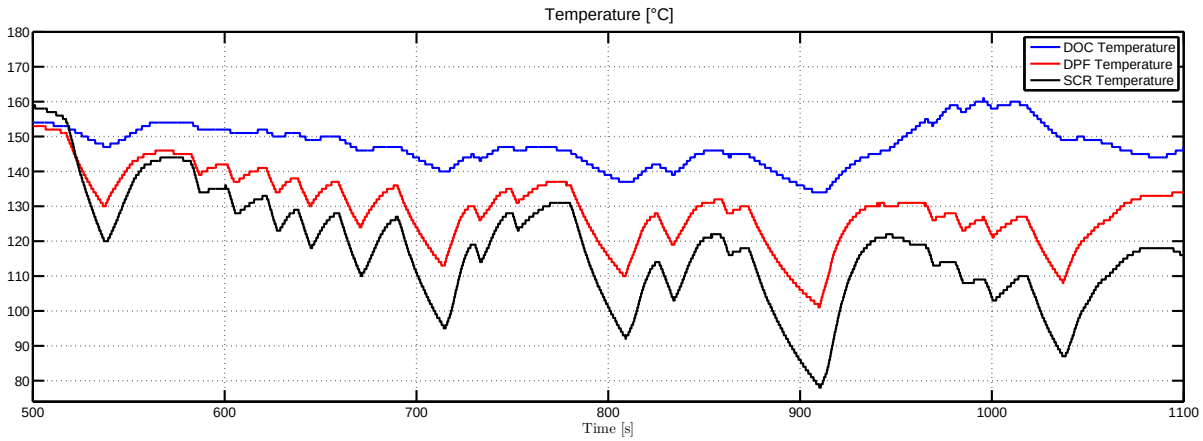

Figure G.19: Zoom on ATS temperatures for region D

Appendix H

Eco-driving

This appendix presents another important problem of optimal control which can be analyzed using the methodology presented in the thesis.

There are different ways of driving during a specific journey, which are not equivalent from an energy consumption viewpoint (see Figure H.1). The so-called eco-driving methodology consists in finding the optimal way to reduce the overall energy consumption [22, 78]. A driver support system calculates and proposes the speed and the gear-box ratio set points to the driver through a human machine interface(HMI) integrated in the dashboard of the vehicles. The aim of vehicle trajectory control is to determine the vehicle speed profile required to minimize the fuel consumption over a given period under various constraints. However, for eco-driving to be environmentally friendly, not only fuel consumption but also pollutant emissions should be considered [54]. It was found in [54] that, while the fuel optimal velocity profile reduces energy consumption, this operation can not be seen as ecological due to the increase in CO and HC emissions. The mathematical formulation of this problem is given below.

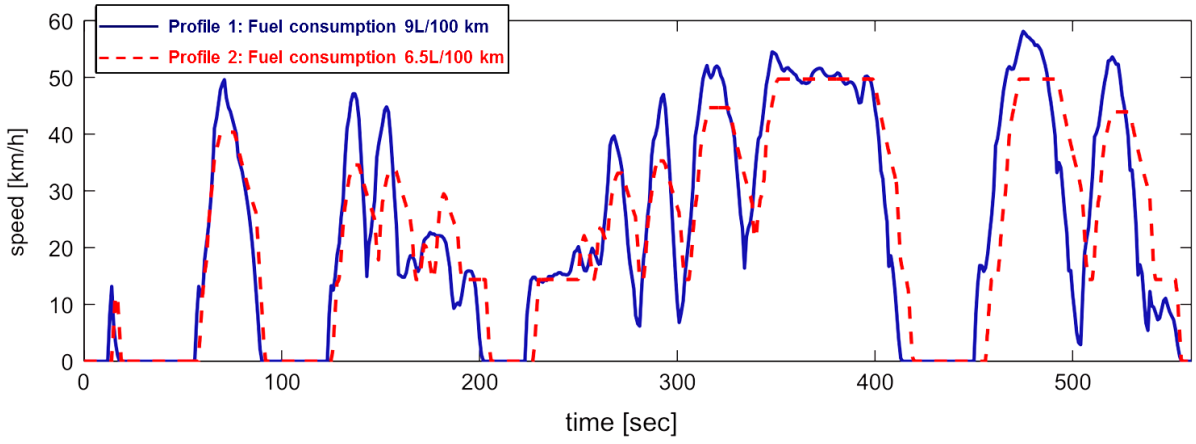

Figure H.1: Profile speeds and their fuel consumptions [54]. The traveled distances are equal. A reduction of 27% is achieved.

Let us consider the example of an individual driving his/her full electric car. The vehicle is powered by a DC electric machine (other kind of primer mover can be considered: internal combustion engine and permanent-magnet synchronous machine). The individual wants to travel from point A to point B in a duration T where the traveled distance D is known in advance and T is fixed. The problem we want to solve is: «*what is the best*

speed profile minimizing the vehicle power consumption knowing that the vehicle starts from point A at rest and must reach the destination point B in a duration T, with a zero velocity?» to answer this question, we define the electric power consumption P_m. The cost function to be minimized is

$$\int_0^T P_m(v(t), u(t))dt,$$

where $v(t)$ is the vehicle speed, u is a percent of torque demand to the maximum torque of the electric machine and it is the control input of the system. This optimization is carried out under the following dynamical constraint

$$\begin{aligned} \dot{v}(t) &= f_1(v(t), x(t), u(t)), \\ \dot{x}(t) &= v(t), \end{aligned}$$

where x is the position of the vehicle. Since the speed and the electric machine torque are limited and the final position and speed are fixed, the optimization must be performed under the following state and input constraints

$$\begin{aligned} x(T) &= D, \\ v(T) &= 0, \\ v(t) &\in [v_{min},\ v_{max}], \\ u(t) &\in [u_{min},\ u_{max}]. \end{aligned}$$

The solution of this optimization problem gives the optimal speed profile minimizing the power consumption of the vehicle from point A to point B. The red curve in Figure H.1 represents the optimal speed profile and the gain in fuel consumption is 27% [54].

Méthodes d'optimisation dynamique de systèmes à plusieurs états pour l'efficacité énergétique automobile

Résumé : La gestion énergétique (EMS) pour véhicules hybrides a pour objectif de déterminer la répartition de puissance entre les différentes sources d'énergie de manière à minimiser la consommation de carburant et/ou les émissions polluantes. L'objectif de cette thèse est de développer un EMS en prenant en compte des températures internes (la température du moteur et/ou la température du système de post-traitement). Dans une première partie et en utilisant une connaissance préalable du cycle de conduite, le calcul d'un EMS est formulé comme un problème de commande optimale. Ensuite, le principe du minimum de Pontryagin (PMP) est utilisé pour résoudre ce problème d'optimisation. En se basant sur les résultats numériques obtenus, un compromis entre les performances de la stratégie de commande et de la complexité du modèle utilisé pour la calculer est établi. Les différents problèmes étudiés dans cette thèse sont des exemples des simplifications successives de modèle qui peuvent être regroupées dans le concept des perturbations régulières en contrôle optimal sous contrainte de commande discuté ici. Dans une deuxième partie, la formulation de l'ECMS a été généralisée pour inclure les dynamiques thermiques. Ces extensions définissent des stratégies sous-optimales que nous avons testées numériquement et expérimentalement.
Mots-clés : Superviseur énergétique, véhicule électrique hybride, commande optimale, PMP, perturbation régulière, généralisation de l'ECMS.

Dynamic optimization in multi-states systems for automobile energy efficiency

Abstract: Energy management system (EMS) for hybrid vehicles consists on determining the power split between the different energy sources in order to minimize the overall fuel consumption and/or pollutant emissions of the vehicle. The objective of this thesis is to develop an EMS taking into account the internal temperatures (engine temperature and/or catalyst temperature). In a first part and using a prior knowledge of vehicle driving cycle, the EMS design is formulated as an optimal control problem. Then, the PMP is used to solve this optimization problem. Based on the obtained numerical results, some trade-off between performance of the control strategy and complexity of the model used to calculate this strategy is established. The various problems studied in this thesis are examples of successive model simplifications which can be recast in the concept of regular perturbations in optimal control under input constraints discussed here. In a second part, the feedback law of ECMS is generalized to include thermal dynamics. This defines sub-optimal feedback strategies which we have tested numerically and experimentally.
Keywords: Energy management, hybrid electric vehicle, optimal control, Pontryagin minimum principle, regular perturbation, ECMS extensions.

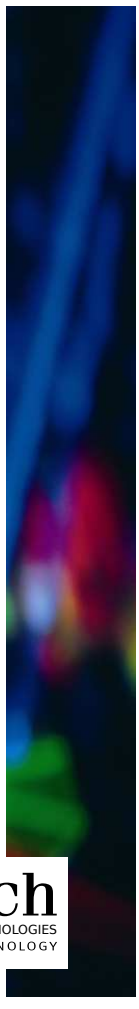

MINES ParisTech

ParisTech
INSTITUT DES SCIENCES ET TECHNOLOGIES
PARIS INSTITUTE OF TECHNOLOGY